
# Diamond based nanoelectronics and imaging

---

A thesis submitted for the degree of Doctor of Philosophy at

University of Technology Sydney

Faculty of Science

School of Mathematical and Physical Sciences

*Author*

**Kerem BRAY**

*Supervisors*

Prof. Igor AHARONOVICH

Dr. Olga Shimoni

Prof. Stella Valenzuela

January 2019

# Certificate of Original Authorship

I, Kerem Bray, certify that the work in this dissertation entitled, "Diamond based nanoelectronics and diagnostics", has not previously been submitted for a degree nor has it been submitted as part of requirements for a degree except as fully acknowledged within the text.

I also attest that the dissertation has been written by myself. Any help that I have received in my research work and the preparation of the dissertation itself has duly been acknowledged. In addition, I certify that all information sources and literature used are indicated in the dissertation.

This research is supported by an Australian Government Research Training Program Scholarship.

Signature of student:

Production Note:
Signature removed prior to publication.

Date: 1 August 2018

# Copyright notice

# Acknowledgments

Firstly, I would like to acknowledge and thank my supervisor, Prof. Igor Aharonovich, for allowing me to undertake my PhD and to be able to partake in the interesting fields of nanophotonics and material fabrication. I am thankful for your guidance and being available to lend aid with my academic difficulties. I have been able to learn a lot from your quick replies to many of my questions over the course of my candidature. Thanks to your mentorship, you have allowed me to grow as an experimental scientist and, for that I am grateful.

I would also like to thank my co-supervisors Dr. Olga Shimoni and Dr. Stella Valenzuela and, in addition Prof. Milos Toth. You have motivated me with your helpful comments and advice. You made time to offer valuable help and encouragement while also allowing me to pursue additional research that has arisen. I thank you for all of your support.

Additionally, I would like to thank Katie McBean for all her help in the lab, by training me on the various instruments around the Micro Analysis Unit (MAU), being available to answer my questions, as well as her invaluable help with the bureaucracy side of research. I also want to thank Geoff McCredie, Angus Gentle for their constant assistance around the MAU and vacuum labs. I am also thankful for Mark Berkahn for his assistance with the AFM and XRD machines.

I would like to acknowledge and thank the collaborators whom I have worked with over the years. I am grateful to Hiromitsu Kato and his group at the National Institute of Advanced Industrial Science and Technology (AIST), Japan for their invaluable help with diamond doping. Additionally, I would like to thank Dr. Kumaravelu Ganesan from the University of Melbourne for his help with diamond implantation. I would also like to thank Prof. Alexander Kubanek from the University of Ulm for hosting me at your lab and collaborating with us over the years. Furthermore, I also would like to thank Asst. Prof. Dirk Englund at the Massachusetts Institute of Technology (MIT) for our fruitful collaboration on a wide variety of research projects.

I would like to show my appreciation my fellow students at the MAU for their consistent support and creating a positive and enjoyable environment to work in. I would like to thank my fellow doctoral students for all the support and shared laughter, even in the most

stressful of times. To the Device & Development (D&D) group for the wonderful nights of imagination where I were able to explore many scenarios, I would like to show my appreciation.

To my partner Freya Whereat, thank you for all your patience through the past couple of years and supporting me through it all. You lifted me up through the stressful times.

Lastly, to my mother Munerva Bray, thank you for your unconditional love and support through all of the years.

# List of Publications

## Refereed journal publications

1) **K. Bray**, R. Previdi, B.C. Gibson, O. Shimoni and I. Aharonovich, "*Enhanced photoluminescence from single nitrogen-vacancy defects in nanodiamonds coated with phenol-ionic complexes*", Nanoscale, Vol 11, issue 11, 4869-4874, 2015

2) **K. Bray**, R. Sandstrom, C. Elbadawi, M. Fischer, M. Schreck, O. Shimoni, C. Lobo, M. Toth, I. Aharonovich, "*Localization of narrowband single photon emitters in nanodiamonds*", ACS Applied Materials & Interfaces, Vol 8, issue 11, 7590-7594, 2016. (Chapter 6)

3) **K. Bray**, H. Kato, R. Previdi, R. Sandstrom, K. Ganesan, M. Ogura, T. Makino, S. Yamasaki, A. P. Magyar, M. Toth, I. Aharonovich, "S*ingle crystal diamond membranes for nanoelectronics",* Nanoscale, Vol. 10, 4028-4035, 2018. (Chapter 4 and Chapter 5)

4) **K. Bray**, A. Trycz, R. Previdi, B. Regan, G. Seniutinas, K. Ganesan, M. Kianinia, S. Kim, I. Aharonovich, *"Single crystal diamond membranes containing germanium vacancy centres"*, (arxiv)

5) **K. Bray**, L. Cheung, K. R. Hossain, I. Aharonovich , S. M. Valenzuela, O. Shimoni, "*Versatile Multicolor Nanodiamond Probes for Intracellular Imaging and Targeted Labeling*", Journal of Materials Chemistry B, Vol. 6, 3078-3084, 2018 (Chapter 7)

6) T. T. Tran, J. Fang, H. Zhang, P. Rath, **K. Bray**, R. Sandstrom, O. Shimoni, M. Toth and I. Aharonovich, "*Facile Self-Assembly of Quantum Plasmonic Circuit Components",* Advanced Materials, Vol. 27, issue 27, 4048-4053, 2015.

7) T. T. Tran, **K. Bray**, M. J. Ford, M. Toth and I. Aharonovich, "*Quantum Emission from Hexagonal Nitride Monolayers*", Nature Nanotechnology, Vol. 11, Issue 1, 37, 2016.

8) T. T. Tran, C. Zachreson, A. M. Berhane, **K. Bray**, R. Sandstrom, L. H. Li, T. Taniguchi, K. Watanabe, I. Aharonovich, and M. Toth, "*Quantum Emission from Defects in Single-Crystalline Hexagonal Boron Nitride*", Physical Review Applied*,* Vol 5, Issue 3, 034005, 2016

9) T. T. Tran, M. Kianinia, **K. Bray**, S. Kim, Z.-Q. Xu, A. Gentle, B. Sontheimer, C. Bradac, I. Aharonovich, *"Nanodiamonds with photostable, sub-gigahertz linewidth quantum emitters",* APL Photonics, Vol. 2, Issue 11, 116103, 2017 (Chapter 6)

10) S. Häußler, J. Benedikter, **K. Bray**, B. Regan, A. Dietrich, J. Twamley, I. Aharonovich, D. Hunger, A. Kubanek, "*A Diamond-Photonics Platform Based on Silicon-Vacancy Centers in a Single Crystal Diamond Membrane and a Fiber-Cavity"*, ArXiv, 2018.

## Conference presentations (Oral)

K. Bray et al., "*Localization of narrowband single photon emitters in nanodiamonds*", Diamond and Carbon Related Materials (DCM), 2016, Montpellier, France.

*Received Young Scholar Award for this presentation.*

K. Bray et al., "*Localization of narrowband single photon emitters in nanodiamonds*", Conference on Optoelectronic and Microelectroni Materials and Devices (COMMAD), 2016, Sydney, Australia.

K. Bray et al., *"Single crystal diamond membranes for nanoelectronics"*, International Conference of Nanoscience and Nanotechnology (ICONN), 2018, Wollongong, Australia.

## Conference presentations (Poster)

K. Bray et al., "Enhanced Photoluminescence from single nitrogen vacancy defects in nanodiamonds coated with phenol ionic complexes", Australian Nanotechnology Network (ANN), 2015, Queensland, Australia.

K. Bray et al., *"*Enhanced Photoluminescence from single nitrogen vacancy defects in nanodiamonds coated with phenol ionic complexes*"*, International Conference of Nanoscience and Nanotechnology (ICONN), 2016, Canberra, Australia.

K. Bray et al., "Enhanced Photoluminescence from single nitrogen vacancy defects in nanodiamonds coated with phenol ionic complexes", Conference on Optoelectronic and Microelectroni Materials and Devices (COMMAD), 2016, Sydney, Australia.

K. Bray et al., "*Localization of narrowband single photon emitters in nanodiamonds*", Conference on New Diamond and Nano-carbons (NDNC), 2016, Cairns, Australia.

K. Bray et al., *"Versatile Nanodiamond Probes for Intracellular Imaging",* Conference on New Diamond and Nano-carbons (NDNC), 2016, Cairns, Australia.

# Contents

# List of Figures

# List of Tables

# List of Abbreviations

| Abbreviation | Meaning |
|---|---|
| AFM | Atomic Force Microscope |
| APD | Avalanche Photo Diode |
| BASD | Bead-Assisted Sonication Disintegration |
| CB | Conductance Band |
| CHO | Chinese Hamster Ovarian |
| CL | Cathodoluminescence |
| CPP | Cell Penetrating Peptide |
| CVD | Chemical Vapour Deposition |
| CW | Continuous Wavelength |
| EBIE | Electron Beam Induced Etching |
| EL | Electroluminescence |
| FIB | Focused Ion Beam |
| FWHM | Full Width at Half Maximum |
| GaN | Gallium Nitride |
| GeV | Germanium Vacancy |
| HBT | Hanbury Brown and Twiss |
| HPHT | High Pressure High Temperature |
| DW | Debye-Waller |
| ICP-RIE | Inductively Coupled Plasma - Reactive Ion Etching |
| IR | Infrared |
| LEDs | Light Emitting Diodes |
| MEM | Micro-Electromechanical System |

| | |
|---|---|
| MPCVD | Microwave Plasma Chemical Vapour Deposition |
| ND | Nanodiamond |
| NIR | Near Infra-Red |
| NV | Nitrogen Vacancy |
| PL | Photoluminescence |
| QDs | Quantum Dots |
| QE | Quantum Efficiency |
| SCR | Space Charge Region |
| SEM | Scanning Electron Microscopy |
| SiC | Silicon Carbide |
| SiV | Silicon Vacancy |
| SnV | Tin-Vacancy |
| SPE | Single Photon Emitter |
| SPS | Single Photon Source |
| SRIM | Stopping and Range of Ions in Matter |
| SIMS | Secondary Ion Mass Spectrometry |
| STED | Stimulated Emission Depletion |
| TEM | Transmission Electron Microscope |
| UV | Ultraviolet |
| VB | Valance Band |
| ZPL | Zero Phonon Line |

# Abstract

To investigate new pathways for numerous quantum technologies it is necessary to efficiently fabricate various interesting materials. Single photon sources that are optically and electrically triggerable are the fundamental building blocks required to push the boundaries of several applications, such as realising secure communication technologies. Accordingly, various platforms are being investigated for generation of single photon emitters (SPEs). Diamond is one platform of great interest, due to its ability to host several photostable, optically active SPE defects that can operate at room temperature. Numerous diamond defects have been studied extensively, including the Nitrogen vacancy (NV), Silicon vacancy (SiV) and, recently, the Germanium vacancy (GeV) colour centres. All were shown to be robust room temperature SPEs. Despite promising reports on quantification and applications of diamond-based defects, the search continues to find an emitter that can excel at most applications.

Another important factor for the utility of colour centres is the method of excitation. While optical pumping is common practice, the ability to electrically excite emitters is highly desired for optoelectronic applications. Several reports exist on the fabrication and characterisation of electrical device structures of various materials, including Gallium Nitride, Silicon Carbide, Zinc Oxide and diamond defects. The central part of the thesis delves into the fabrication of high aspect ratio, thin, nanoscale, conductive diamond membranes hosting SiV colour centres, which demonstrate key advantages, such as being easily transferrable to a variety of structures.

Secondly, I investigate unknown narrowband SPEs in diamond nanocrystals, which are preferable for nanophotonic, quantum communications and bio-imaging applications. The origin of the narrowband emission is determined to be point defects localised at extended morphological defects in individual nanodiamond particles. Furthermore, a highly polarised, narrowband, possessing sub GHz optical linewidths was observed at cryogenic temperatures.

Finally, I exploit the optimal fluorescent, chemical and biocompatibility properties for multi-colour tagging of CHO-K1 and U937 cell lines using both $NV^-$ and, for the first time, SiV diamond colour centres, to investigate their intracellular properties. The non-toxic SiV diamond nanocrystals initially dispersed throughout the cell interior while tagged NV nanocrystals localised close to the nucleus.

Therefore, this work reports new findings in spectroscopic studies of diamond-based colour centres that can be excited optically and electrically. Furthermore, it provides detailed evidence

which forms the building blocks for future investigation into diamond-based devices and SPEs for a wide variety of applications. The results presented in this thesis therefore provide a new and interesting platform for applications using defect based nanophotonics.

# Preface

The following work was performed in collaboration with several researchers in various institutions, as follows:

- The initial growth of the boron doped, and subsequent growth of the phosphor doped diamond was performed in collaboration with H. Kato, M. Ogura, T. Makino and S. Yamasaki at the Advanced Power Electronics Research Center, AIST, in Ibaraki, Japan.
- The ion implantation of helium was performed in collaboration by K. Ganesan at the School of Physics at the University of Melbourne, Victoria, Australia.
- The ion implantation of diamond colour centres was partially carried out in the Australian National University with the assistance of Rob Elliman.

In all the above circumstances I actively participated in the design of the experimental work, performed the measurements, and analysed the data.

In certain places throughout the thesis, figures from other sources have been used. Appropriate references have been inserted in the figure caption to acknowledge the sources of the figure.

# Chapter 1 Introduction

Decades of rapid advances in quantum information technology, especially lasers and light emitting diodes, have led to the development of devices that are high performance, affordable and reliable. New concepts in "top down" or "bottom up" synthesis have driven the discovery and research of new candidates for uses in nano-optics and nanoelectronics [1], [2].

Quantum technology spans numerous applications including quantum metrology, quantum key distribution for secured communications and most ambitiously the quantum computer [3]–[5]. The fast-growing need for stronger and faster computational devices has led to the investigation of using quantum mechanical devices as bits, or qubits, which would enable faster processing speeds when compared to classical bits [6], [7]. Simply, qubits have the possibility of an additional, superimposed state of two bits forming a third state. This allows for simultaneous computations. Furthermore, to fabricate practical devices and components for quantum applications, the material would need to be efficient, reliable, scalable and allow manipulation of individual quantum states at a nanometre scale.

Recently, there has been a lot of interest in non-classical light sources, where an emitter can produce controllable, quantised packets of light. A fundamental building block for these emitters is single photon emitters which are very important for many scalable quantum technologies [8]–[11]. Single photon emission is desirable for quantum applications because it travels at the speed of light, possesses low noise, and allows for free space communication [8], [12], [13].

Promising candidates for single photon applications are diamond colour centres. They possess various outstanding properties such as room temperature operation, photostability and ease of fabrication. Diamond can host several single photon emitters for nanophotonic applications. The most prominently studied defect is the Nitrogen vacancy (NV) defect due to its interesting optical, optical read out and spin properties [14], [15]. However, it possesses a few drawbacks such as a broad photoluminescence spectrum where the zero-phonon line comprises of ~4%. This low emission leads to a low count rate of single photons being emitted from the NV defect. Silicon vacancy (SiV) centres have been suggested as an alternative to NV colour centres, owing to their narrow zero phonon line (ZPL) width of ~ 5 nm at room temperature along with their small phonon-coupling [16]. Furthermore, its emission is in the near infrared at 737 nm and has a short lifetime of 1.2 ns. However, they possess low single photon count rates (~1000

counts/s), a quantum yield of 0.05 and the fluorescence is quenched in the presence of graphite which leads to the need for high quality diamond [17]–[19].

Single crystal diamond containing SiV colour centres is imperative for a range of optoelectrical quantum applications because diamond possess a high breakdown voltage (~$10^7$ $Vcm^{-1}$) and relatively high carrier mobilities (0.2 $m^2V^{-1}s^{-1}$). They have recently been realised for optoelectronic applications, where electroluminescence signal has been observed from SiV colour centres [20], [21]. Electrical excitation of diamond is essential to engineer scalable devices utilising quantum defects to fabricate efficient single chip devices [22]–[24].

Diamond planar or membrane devices are the next stepping stone towards optically integrated circuits. The fabrication of free-standing single crystal diamond membranes has led to high-quality waveguides, ring resonators and nano electromechanical systems (NEMS). The free-standing membranes led to the collection efficiency from single photon emitters embedded in cavity structures (i.e. whispering gallery modes and ring resonators) to be enhanced through the Purcell effect [25], [26]. Free-standing single crystal diamond membranes have been fabricated to be as thin as 200 nm [27]–[29] and numerous devices have been fabricated, including photonic crystals [30], cavities [31], nanomechanical resonators [32], [33], diodes [21] and other novel structures. For quantum applications it is favourable to fabricate structures and devices from high-quality single crystal diamond.

Furthermore, to exploit the optical properties of diamond colour centres, it is imperative to understand their internal energy level structure, in particular SiV colour centres. It was first shown by G. Sittas, *et. al.* [34] that the electron excitation energy for the SiV defect is 1.68 eV. This was determined by photoluminescence excitation (PLE) from 490 nm to 690 nm using a 250 W halogen lamp. PLE measurements provide information about dephasing mechanisms and optical transitions of emitters at cryogenic temperatures (<10K).

Another benefit of using diamond is its biocompatibility and surface tuneability. This feature of diamonds can be exploited for a range of therapeutic and diagnostic applications from targeting various processes, monitoring pathways and even drug delivery. There has been an abundance of research utilising diamonds containing NV colour centres for bio-imaging and drug delivery. However, the NV defects possess a wide fluorescent band emission in the visible range that contributes to tissue absorption and auto-fluorescence [35]–[40]. Therefore, using diamond containing the near-infrared SiV colour centre is ideal.

## 1.1 Summary of thesis

There has been substantial research conducted on diamond colour centres as a platform for quantum technology. The aim of this thesis is the efficient fabrication of diamond that host active colour centres that can be optically and electrically excited.

Chapter 2 presents a brief introduction about diamond as a material including various types of diamond colour centres. The definition and differences between photoluminescence and electroluminescence of quantum emitters and the various pathways for excitation. Finally, it contains a summary of types of diamond devices.

Chapter 3 provides information about experimental methodologies and equipment for the fabrication of differently doped single crystal diamond membranes. Fabrication techniques include the use of microwave plasma chemical vapour deposition and inductively coupled plasma-reactive ion etching.

Chapter 4 and Chapter 5 detail the electrical and optical analysis of diamond membrane-based junctions showing the electrical triggering of SiV colour centres. Chapter 4 is dedicated to the electrical characterisation and analysis of p-doped membranes, p-n and p-i-n diamond membrane diode devices containing SiV colour centres While, Chapter 5 revolves around the electrical triggering of diamond colour centres in p-i-n diamond membrane diode device. Furthermore, it mentions a variety of device configuration challenges and how they can be overcome.

Chapter 6 details the growth and analysis of unknown narrowband single photon emitters originating from point defects in diamond nanocrystal grain boundaries. The single photon emitters were subsequently cooled down to 10K to show sub-GHz optical linewidths with a stable ZPL shown to be blue shifted with increasing excitation power.

Chapter 7 investigates another interesting aspect of diamond nanocrystals, namely their stable fluorescent properties, tuneable surface chemistry and biocompatibility. It details the methodology and analysis for nanodiamonds hosting either NV or SiV colour centres to be successfully up-taken into diverse, cultured cell lines and to target specific areas of individual cells.

Finally, in Chapter 8 the thesis is concluded, and future work is outlined.

# Chapter 2 Background

This thesis reports on the efficient fabrication of single crystal diamond membranes with incorporated diamond defects for optoelectrical applications. Therefore, the introduction is divided into two distinct sections. The first section introduces diamond and the various colour centres it can host. The second section deals with optical and electrical pumping of diamond colour centres and the variety of fabricated devices.

## 2.1 Diamond

Diamond is an allotrope of carbon with a $sp^3$ configuration. It is host to more than 500 luminescent centres, where these centres emit across the visible spectrum from deep ultraviolet (UV) to the far infrared (IR) [41]. Diamond is a unique material and possesses highly sought-after properties, including being chemically inert, biocompatibility and possessing a wide bandgap (5.5 eV). This leads to the ability to host a large variety of vacancy and impurity related optically active defects or colour centres. Out of the 500 colour centres, less than 10 have been identified as bright and stable single photon emitters.

The fields of photonics, bio-imaging and quantum emitters have grown noticeably over the past few years. There has been great interest in the exploitation of nanofabrication techniques to create optically active devices [42]–[45]. Numerous research groups investigate the development of various materials for bio-imaging, diagnostic, optoelectronic (Figure 2.1) and photonic applications, one of which are diamonds and diamond nanocrystals [46]–[49].

The phrase ‘nanodiamond’ (ND) is used to describe diverse diamond structures at the nanoscale (<100 nm in size). This includes diamond crystals, nanocrystalline diamond films, isolated diamond particles and their architectural deviations. There are diverse techniques employed to synthesise diamond, which include ND detonation, high pressure high temperature (HPHT) transformation of $sp^2$ carbon (also referred to as graphite) and chemical vapour deposition (CVD) [50]–[53].

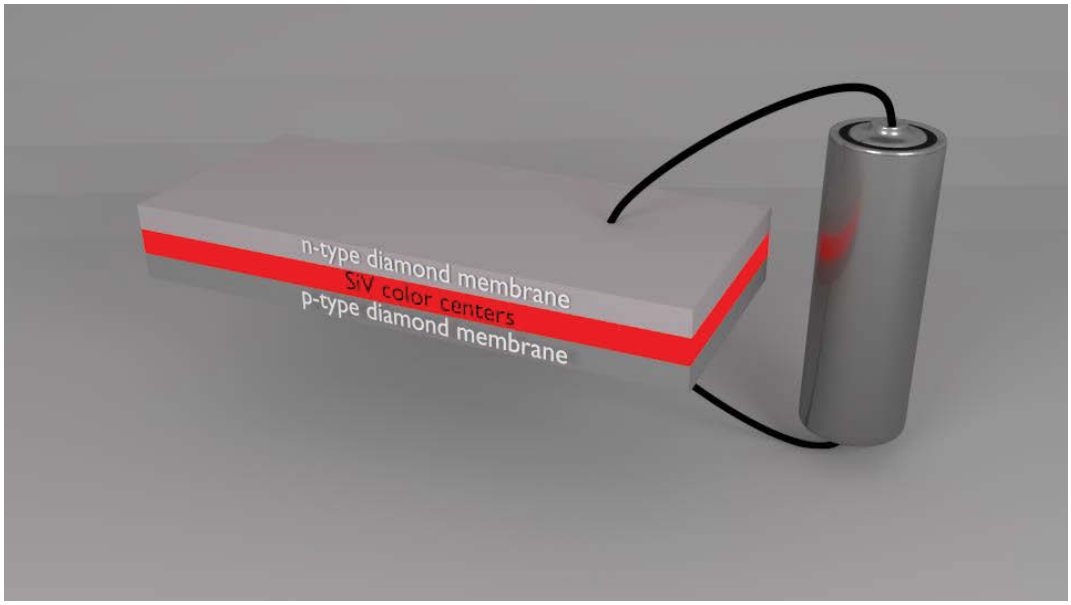


**Figure 2.1**. A graphical representation of a diamond membrane p-i-n diode connected to a power supply. The intrinsic layer contains a uniform optically active layer of SiV defects.

## 2.2 Colour centres for quantum applications

Diamond is a distinctive material enriched with tremendous physical properties. It possesses a relatively large atomic density (3.5 g/cm$^3$) along with a large band gap (5.5 eV at room temperature) (Figure 2.2). This provides the capability to contain numerous colour centres and impurity states with little to no absorption [46], [54], where some are exceedingly bright [55]. If these impurity states, or defects, are created by a foreign atom occupying a regular atomic site it is known as substitutional. However, if it is not related to an atomic site, it is called interstitial. Colour centres are an important feature of crystalline materials.

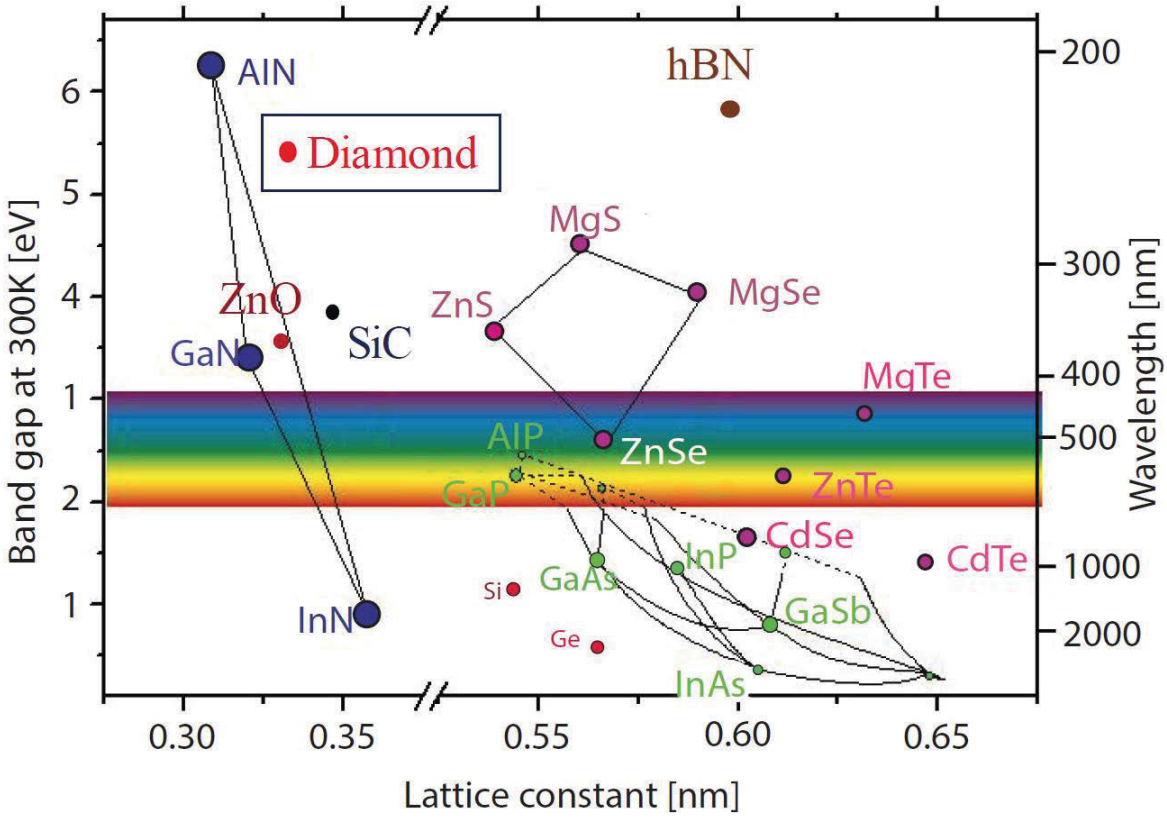


**Figure 2.2.** The bandgap energies and lattice constants of various direct and indirect bandgap semiconductors including III-nitrides [56]. ZnO, SiC, hBN and diamond have been added for comparison.

Defects or impurities are commonplace within the crystallographic lattices of diamonds and they can bring about the abnormalities in the optical properties of diamonds with fluorescence signals ranging from infrared to deep ultra violet [55] . These defects may be produced through several different processes, including diamond growth, and are a direct result of lattice imperfections. When a lattice site, inside a perfect crystal, is not properly occupied due to accommodating a foreign atom or being vacant, it is called a defect [46].

Various defects can be formed through numerous methods, including ion implantation, displacing heat to a crystal while surrounded by a gaseous metal or through induced photo-ionisation by a laser. Impurities that have been created in diamond include silicon, nitrogen and nickel [57].

### 2.2.1 Nitrogen vacancy defect

The NV defect centre is the most abundant impurity in diamond [58]. Nitrogen atoms are readily available during diamond growth [59] and implantation techniques [60], [61] and possess an atomic size comparable to carbon (Figure 2.3a). NV defect centres are fabricated through the incorporation of a substitutional nitrogen atom with an adjacent vacant carbon lattice site [62]. This defect can exist in two different charge states, a neutral charge state, $NV^0$, and a negatively charge state, $NV^-$. The $NV^0$ complex has five unpaired electrons, one of which is from the intrinsic nitrogen atom and the other four are neighbouring the carbon atoms. Since nitrogen atoms have five outer shell electrons (juxtaposed to four electrons in a carbon atom) they may donate an extra electron to generate a donor energy state in the band-gap [57], [63].

The photoluminescence (PL) of the $NV^0$ colour centre exhibits a zero-phonon line (ZPL) at 575 nm with a characteristic broad phonon sideband ranging from ~580 nm to 650 nm. This is shown, in part, in Figure 2.3b. Furthermore, the $NV^-$ colour centre, is one of the most popular diamond defects because it is the only colour centre to demonstrate coherent optical effects including coherent population trapping [64], [65] and electromagnetically induced transparency [66], [67]. Single $NV^-$ colour centres have been studied extensively in bulk diamond [68] and in ND [69], [70] samples. The defects can be easily fabricated by ion implantation techniques or synthesised using CVD. The $NV^-$ complex possesses six unpaired electrons, five of which neighbour the carbon atom and intrinsic nitrogen atom with an additional unpaired electron trapped at the defect site giving rise to the negatively charged state [71] (Figure 2.3b). The $NV^-$ colour centre possesses a ZPL at 637 nm and a large phonon sideband until ~800 nm [72]. Only 4% of the $NV^-$ defect emissions are concentrated in its ZPL and possess a Debye-Waller (DW) factor of 0.04. Furthermore, the fluorescence lifetime of the $NV^-$ defect is dependent on the diamond surrounding material. A single photon emitted from a $NV^-$ defect can produce lifetimes of ~10 ns in bulk material [73], [74] versus ~20 ns in NDs [75]–[77]. The quantum efficiency of the $NV^-$ defect is estimated to be around 0.7 [78], [79]. However, the NV centre also has a permanent dipole moment which makes it highly susceptible to external electromagnetic fluctuations. These fluctuations result in ultrafast spectral diffusion of the NV centres optical transitions, and hinder the generation rate of indistinguishable photons[80], [81].

### 2.2.2 Silicon vacancy defect

Possibly the second most studied diamond defect is the SiV colour centre (Figure 2.3c). It is commonly fabricated using CVD techniques with a silicon source (i.e. a silicon substrate juxtaposed to the creation of NV emitters using ion implantation [17], [82]–[85]). The SiV defect consists of a single silicon atom interstitially sitting in between two vacancy centres as shown in Figure 2.3c and is known as a semi-divacancy defect. Since silicon atoms have four outer shell electrons and sit between two vacancy sites they can donate extra electrons to generate a donor energy state in the band-gap, leading to the overall negative charge. The SiV colour centre possesses a short decay lifetime of ~ 1 ns. Its quantum efficiency is as low as 0.05 [86], [87]. The SiV colour centre is labelled a semi-divacancy centre because the silicon atom moves along the <111> direction of the diamond lattice toward the neighbouring vacancy into the split-vacancy site [88], [89]. The SiV colour centre symmetry is classified as a $D_{3d}$ (as opposed to the NV centres $C_{3v}$) and the ZPL is a transition between $E_u$ and $E_g$ electronic states, which both include an orbital degeneracy. Also, at cryogenic temperatures, the ZPL splits into four components, thus making the level scheme of the SiV centre complex [88].

In comparison to NV colour centres, the SiV colour centre exhibits a near infrared (NIR), highly luminescent, narrow peak at room temperature [17], [90]. Furthermore, silicon doped diamond demonstrates a high signal to noise ratio with a remarkable constant emission upon excitation [37]. The SiV defect possesses a highly luminescent ZPL at 738 nm with a narrow linewidth of < 5 nm, as shown in Figure 2.3d. The NIR emission is also favourable for biological applications because it permits photon excitation by red laser light which diminishes tissue and cell auto-fluorescence [91], allowing their use for *in vitro*, and *in vivo* studies [37], [92], [93].

Engineering diamond containing uniform and bright SiV colour centres is very easy by using CVD. This is because silicon atoms are readily available from the silicon substrates or quartz windows in the CVD chamber. However, fabrication of silicon based single photon emitters into nanodiamonds is incredibly challenging. When the diamonds undergo CVD growth on a silicon or silica substrate, the silicon atoms diffuse simultaneously into the growing crystal. This leads to the formation of large clusters or aggregates of SiV centres, which are difficult to isolate [94], [95]. However, Neu *et al.* has demonstrated that growing nanodiamonds on a 150 nm thick iridium layer deposited on a 40 nm buffer layer of yttria-stabilised zirconia on silicon can produce room temperature ultrabright SiV single photon emitters [18]. In addition, the fabricated single emitting SiV colour centre can shift ZPL >5 nm, and it possesses a DW factor

of ~0.8 [96]. The DW factor, and similarly the Huang-Rhys factor (S), are used to measure the phonon coupling to determine the fraction of the emission into the ZPL and total emission in the bandwidth. The DW factor is defined as:

$$\boldsymbol{DW = \frac{I_{ZPL}}{I_{tot}}} \qquad \textbf{Equation 2.1}$$

While S is defined as:

$$\boldsymbol{\exp(-S) = \frac{I_{ZPL}}{I_{tot}}} \qquad \textbf{Equation 2.2}$$

where $I_{ZPL}$ is the integrated luminescent intensity of the ZPL and $I_{tot}$ is the integrated luminescence intensity of the colour centre [97]–[99]. SiV assembles have an $S = 0.24 \pm 0.02$ [100], [101]. PLE and polarisation measurements at cryogenic temperatures have given insight to the electronic structure of the centre showing that it is composed of a split ground and excited state, which yields four distinct ZPL [101]–[103]. Sipahigil *et al.*, has demonstrated indistinguishable photon generation from two distinct $SiV^-$ centres. This indicates the possibility of two-photon entanglement by exploiting the colour centre, which is a needed for quantum computation using photons [104]. Furthermore, spin-state manipulation by using spin-photon interaction is shown for both the $SiV^-$ and the $SiV^0$ [105], [106].

Due to their unique properties, SiV colour centres are being exploited for optoelectrical devices including light emitting diodes (LEDs), lasers and micro-electromechanical systems (MEMs). Electrical excitation of SiV colour centres has been achieved in polycrystalline [20], single crystalline [21] and more recently in high aspect ratio nanometre diamond devices, which are part of this work. The polycrystalline diamond devices have shown high current output (~60 mA) when a forward bias of 10 V is applied, while their single crystal bulk and nanoscale counterparts show a relatively high current of ~3-4 mA under a similar forward bias. However, under reverse bias the single crystal diamond possesses a far lower current on the order of nanoamps, versus micro-milliamps in polycrystalline diamond. This small current under reverse bias leads to a high rectification ratio of ~$10^6$, which is necessary for electronic and high-power device applications. However, electrically excited single photon fluorescence from SiV is necessary to realise narrowband electrical devices. The pathways behind electroluminescence (EL) of emitters and results demonstrating electrical triggering of SiV defects will be explained in later chapters of the thesis.

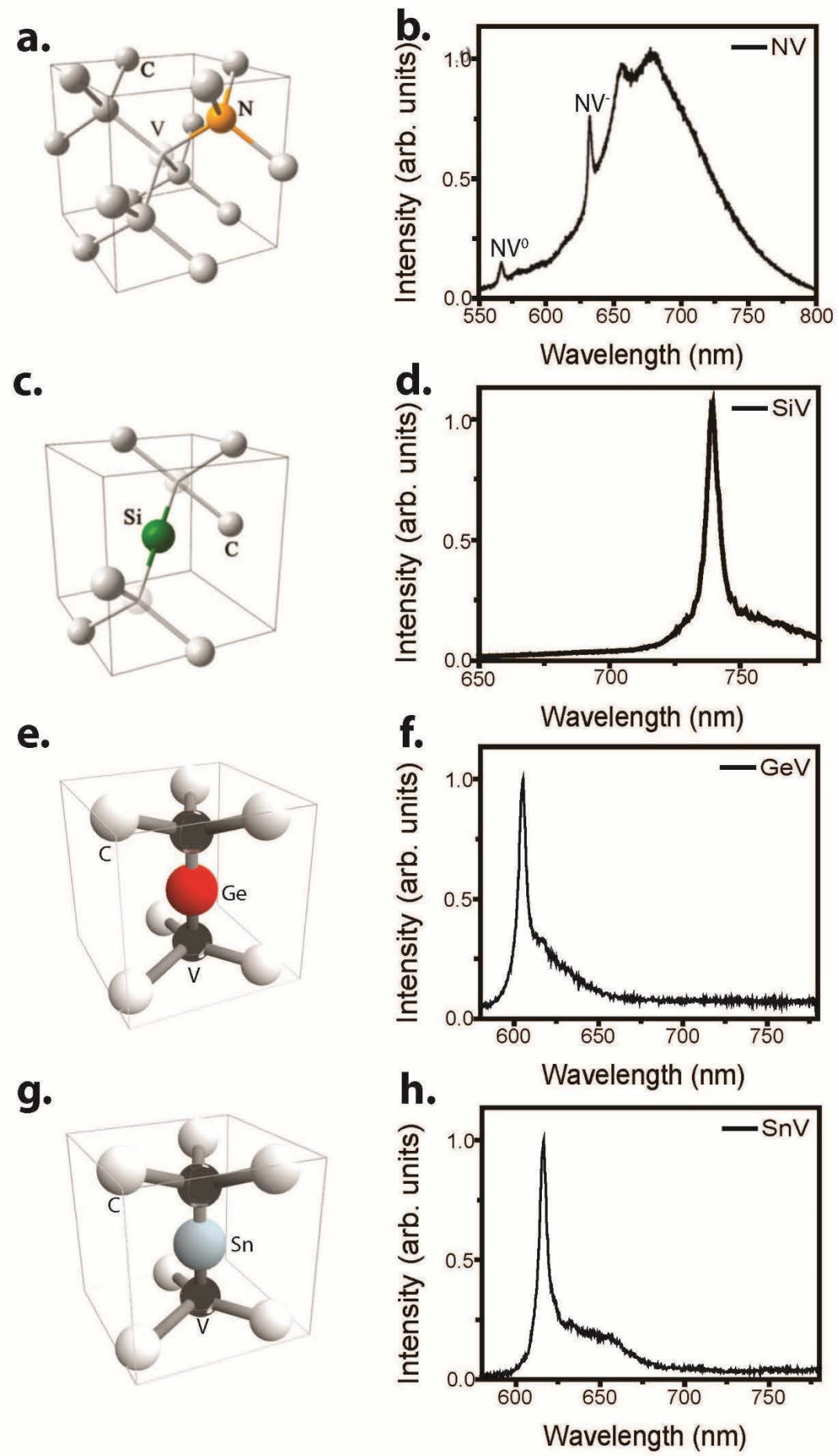
a.
C
V
N
b.
NV
NV-
NV0
Intensity (arb. units)
Wavelength (nm)
c.
Si
C
d.
SiV
Intensity (arb. units)
Wavelength (nm)
e.
C
Ge
V
f.
GeV
Intensity (arb. units)
Wavelength (nm)
g.
C
Sn
V
h.
SnV
Intensity (arb. units)
Wavelength (nm)

**Figure 2.3.** (a) Illustration of a crystallographic lattice model of the NV defect in diamond showing a substitutional nitrogen atom near a vacancy site. (b) A PL spectrum showing the $NV^0$ and $NV^-$ centre ZPL at 575 nm and 637nm, respectively, along with its wide phonon sideband. (c) A crystallographic model of the SiV defect in diamond consisting of a single silicon atom near two vacancies. (d) A PL spectrum showing a ZPL peak at 738 nm with a visible phonon sideband. (e) A crystallographic model of the GeV defect in diamond consisting of a single germanium atom near two vacancies. (f) A PL spectrum showing a ZPL peak at ~602 nm with a visible phonon sideband. (g) A crystallographic model of the SnV defect in diamond consisting of a single tin atom near two vacancies. (h) A PL spectrum showing a ZPL peak at ~619 nm with a visible phonon sideband.[58].

### 2.2.3 NE8 defect

Another prevalent impurity is the, nickel defect in diamond, where it is created primarily through ion implantation and HPHT diamond growth [107]–[109]. With the colour centres ease of fabrication, it has attracted interest over the years to understand its physical and optical properties. One of the most common nickel complexes is the NE8 centre. The NE8 structure is shown in Figure 2.3e, where it consists of a single nickel atom surrounded by four nitrogen atoms. The NE8 centre shows emission in the NIR with a ZPL of 793 nm and has exhibited single photon emission [98], [110], [111]. The NE8 centre possesses a DW factor of 0.7 as most of the emission is emitted through the ZPL. The NE8 centre also exhibits a QE of ~0.7 and is a three level system [98], [110], [111]. The colour centre is difficult to fabricate in large quantities and at localized areas, therefore, leading to difficulties for device fabrication.

### 2.2.4 Germanium vacancy defect

Colour centres in diamond are attractive building blocks for solid state integrated quantum photonics[112], [113]. So far, significant effort has been devoted to studying the NV centre due to its long electron spin coherence time and hence its applicability as a spin qubit and a sensor[14], [114]. However, its optical properties are not ideal as it has a large phonon sideband with only ~ 4% of the fluorescence being emitted into the ZPL.

To overcome these shortfalls, new colour centres with inversion symmetry based on group IV elements in diamond have recently been explored. Following on from detailed investigations

of the $SiV^-$ [18], [88], [102], [115]–[119], other colour centres including the Germanium vacancy (GeV) [120]–[125] and more recently the Tin vacancy (SnV) [126], [127] have been identified. The GeV colour centre is a semi-divacancy and consists of a single germanium atom sitting between two vacancy sites, as shown in Figure 2.3e. The GeV defect possesses a narrow ZPL of ~602 nm (Figure 2.3f) and has been demonstrated to be a single photon emitter at room temperature with an excited state decay lifetime of ~1.4 ns [122]. All the optical characteristics are summarised in Table 2-1 and juxtaposed to other prevalent optical materials including quantum dots (QD) and fluorophores. The defects have an inversion symmetry and therefore are less vulnerable to strain and electromagnetic fluctuations. Indeed, recent reports showed that generation of Fourier Transform limited photons is possible employing SiV centres in both nanodiamonds and bulk, and fabricated nanostructures using a reactive ion etching process [102], [128]–[130]. On the other hand, the advantage of the GeV and the SnV is their larger energy splitting in the ground state that reduces the phonon mediated spin mixing, and perform coherent spin manipulation at liquid Helium temperatures [131], [132]. In addition, the GeV colour centre is believed to have a much higher quantum efficiency compared to the SiV, therefore being advantageous for applications in quantum optics and nanophotonics. To employ these colour centres in integrated nanophotonic devices, an interface between the spin and the emitted photons is needed. To this end, a promising avenue is an integration of these colour centres with photonic resonators [5], [112], [117], [133]–[135].

### 2.2.5 Tin vacancy defects

As stated previously, SnV is an emerging single photon emitting colour centre that has been studied recently [126], [127], [136]. First principle calculations theorise that the SnV defect sits on an interstitial site with two neighbouring vacancies (Figure 2.3g). SnV have been fabricated using tin implantation ($2 \times 10^{13} - 5 \times 10^{13}\ cm^{-2}$ fluence) and subsequent high pressure (7.7 GPa) and high temperature annealing (~2373 K). The SnV colour centre exhibits a strong and sharp ZPL at 619 nm with a full width at half maximum (FWHM) of ~6.2 nm (Figure 2.3h) along with a phonon sideband (PSB). The emitters possess a short radiative decay lifetime of ~6 ns. This centre, although new, provides another option in the visible range and may hold several key properties for the fabrication of quantum devices.

A summary of the spectral properties of a few diamond colour centres is shown in Figure 2.4

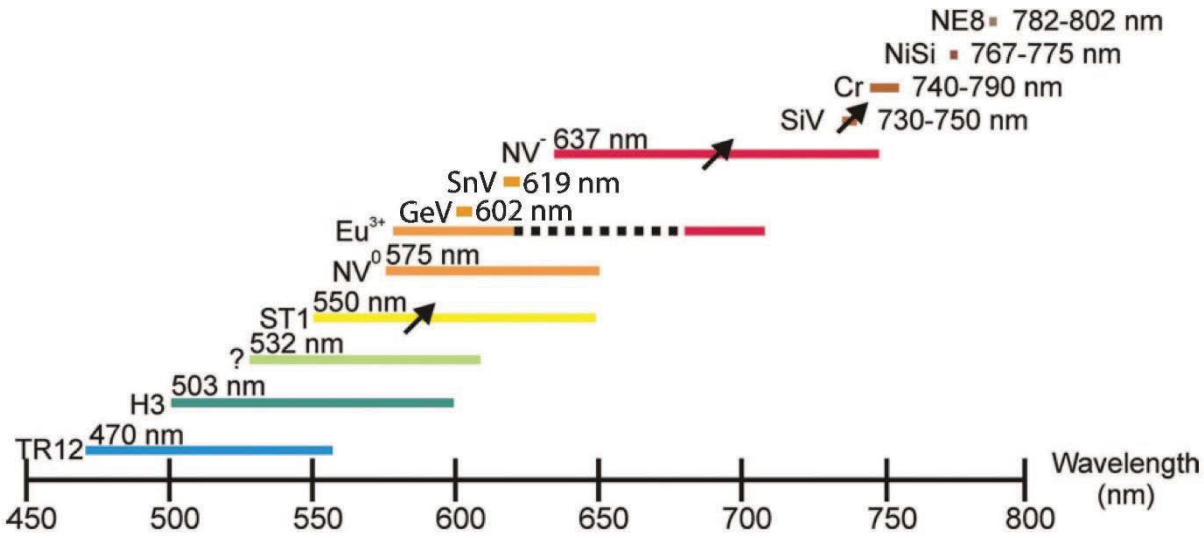


**Figure 2.4.** A spectra map of various diamond colour centres. The length of the lines corresponds to the width of the emitter's emission including the PSB. The intrinsic carbon interstitials (TR12) has a ZPL of ~470 nm while the H3 centre consisted of two nitrogen atoms with a lone vacancy and emits at 503 nm. An unidentified emitter with a ZPL of 532 nm is shown. The so-called ST1 centre is also unidentified defect from the diamond, consisting of a ZPL of ~550 nm and allows optical manipulation of its spin as indicated by the arrow. Two separate ZPLs are observed when europium (Eu3+) is incorporated into the diamond lattice, they correspond to allowed radiative transitions. The NiSi is a Nickel-Silicon complex showing emission with a ZPL between 767-775 nm [137].

**Table 2-1** Comparison of optical and physical properties between Si-Vs, NVs, QDs and fluorophores [138]–[142].

| **Property** | **Si-V** | **NV** | **NE8** | **GeV** | **Fluorophore** | **QD** |
|---|---|---|---|---|---|---|
| Absorption spectra | Red to NIR | Green | NIR | Green | Infra-Red to UV | Infra-Red to UV |
| ZPL (nm) | 738 | 637 | 793 | 602 | - | - |
| FWHM (nm) | ~6 | $> 100$ | ~3 | ~6 | $35 - 100$ | $30 - 90$ |
| Lifetime (ns) | 1 | 20 | ~1.1 | ~1.4 | $1 - 10$ | $10 - 100$ |
| Photostability | Extremely high | Extremely high | Extremely high | Extremely high | Low | High |
| Quantum Yield | $0.7 - 0.8$ | $0.7 - 0.8$ | $0.7 - 0.8$ | NA | $0.5 - 1.0$ | $0.1 - 0.8$ |
| Size (nm) | $> 10$ | $> 10$ | >10 | >500 | $< 1$ | $6 - 60$ |
| Toxicity | Low | Low | Low | Low | Low to High | High |
| Biocompatibility | High | High | High | High | High | Low |

Table 2-1 summarises several photophysical properties of various diamond single photon emitters and compares them to fluorophore and QD samples. SiV emitters exhibit the smallest lifetime decay, followed closely by NE8 and GeV.

## 2.3 Optical characterisation of defects

The previously discussed diamond colour centres in chapter 2.2 were probed using PL techniques to develop a greater understanding of the properties and mechanisms of the defects. The mechanisms behind excitation and further characterisation of single photon emitting defects will be discussed below.

PL of diamond colour centres has been studied for years [143], [144]. It can be described as a bright laser which excites an electron in the colour centre from its electronic ground state to above the lowest excited level. This state is short lived and quickly relaxes to a meta-stable

state, which is soon followed by the colour centre returning to the ground state emitting a photon with an energy:

$$\hbar\omega = E_{|e\rangle} - E_{|g\rangle} \qquad \textbf{Equation 2.3}$$

Therefore, PL only involves the transitions between the ground state and excited states of the colour centre and excludes interactions with the valance and conduction band of the material. This allows the colour centre to be treated as an isolated atom-like system.

The emitted light can be described by their photon statistics by measuring the second order autocorrelation function, $g^{(2)}(\tau)$. The autocorrelation function measures the probability of detecting a photon at a delay time of $\tau$. The function can be described mathematically as:

$$g^{(2)}(\tau) = \langle I(t)I(t+\tau)\rangle / \langle I(t)\rangle^2 \qquad \textbf{Equation 2.4}$$

Where I is the intensity of the photon and $\langle\ \rangle$ denotes the expectation values and can be used as a method to determine if an emitted photon is indeed a single photon or not. $g^{(2)}(\tau)$ can be expressed in terms of photonic creation, $a^\dagger$, and annihilation, a, operators as:

$$g^{(2)}(\tau) = \frac{\langle a^\dagger(t)a^\dagger(t+\tau)a(t)a(t+\tau)\rangle}{\langle a^\dagger(t)a(t)\rangle^2} \qquad \textbf{Equation 2.5}$$

When the bosonic commutation relation is satisfied by a given Frock state $|n\rangle$, $a^\dagger(t_1), a^\dagger t_2 = \delta_{t1,t2}$, the zero-time delay correlation becomes:

$$g^{(2)}(0) = \frac{n(n-1)}{n^2} \qquad \textbf{Equation 2.6}$$

For an explicit single photon emitter, more than one photon cannot be generated at any given time, $n = 1$ and $g^{(2)}(0) = 0$. The generated statistic curve is typically called an antibunching curve. If there is no peak at $g^{(2)}(0) = 0$ or zero-delay time, it shows that the emitter is a single photon source. It should be noted, in experimental work the theoretical value of $g^{(2)}(0) = 0$ can not be easily obtained due to background contribution, for example dark counts and timing jitters. As such, $g^{(2)}(0) < 0.5$ is considered a single photon emitter because a higher photon number, $n \geq 2$, will results in a $g^{(2)}(0) \geq 0.5$. Experimentally, this means that a single photon cannot be observed at two detectors with a zero-delay time. Generally, the emitted light can be defined by the values of $g^{(2)}(\tau)$ as follows: $g^{(2)}(\tau) > 1$ is bunched light, $g^{(2)}(\tau) = 1$ is coherent light and $g^{(2)}(\tau) < 1$ is antibunched light.

A schematic of single photon sources is shown in Figure 2.5a, showing a two-state quantum system with a ground state, $|1\rangle$, and an excited state, $|2\rangle$. When the emitter is excited, from the ground state to an excited state, one photon is emitted and therefore cannot be detected at both the avalanche photodiodes (APDs). Most real-world quantum emitters are not two-level systems but possess additional levels for photons to be trapped and decay. Figure 2.5b shows an illustration of a three-level system. Most single molecules [145], [146] and diamond defects [16], [98], [147] exhibit a metastable state between $|1\rangle$ and $|2\rangle$ states. Figure 2.5c shows an example of a single photon emitter (red curve) and of a bunched light source (black curve).

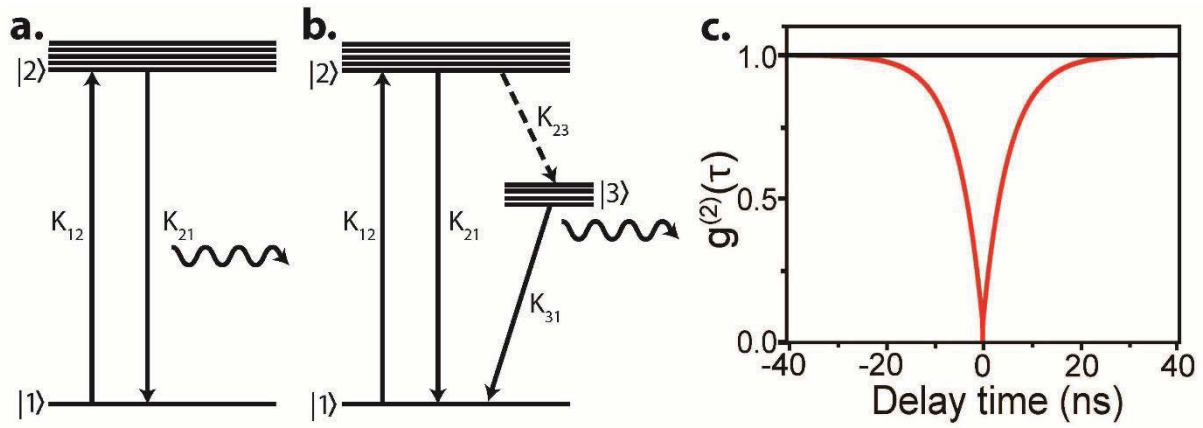


**Figure 2.5.** A schematic diagram of (a) a two-level system and (b) a three-level system, $\kappa_{xy}$ are the transition rates from level x to level y. (c) Is an example of a $g^{(2)}(\tau)$ function where the red curve denotes a single photon emitter, $(g^{(2)}(\tau) < 1)$, and the black curve is when $g^{(2)}(\tau) \geq 1$.

One of the standard methods to determine photo statistics or characteristics is the Hanbury-Brown-Twiss (HBT) interferometer [148]. An example of an HBT interferometer is shown in Figure 2.6 connected to a confocal microscope set-up and spectrometer. Generally, an emitter is excited by a laser (green line), generating photons. The emitted light travels along the beam path (red line) where it is coupled into a fibre coupler and can either be sent to a spectrometer or split evenly by a beam splitter and measured by two photodetectors, specifically APDs. To determine if a source is a single photon emitter or not, an antibunching curve is measured using the HBT interferometer.

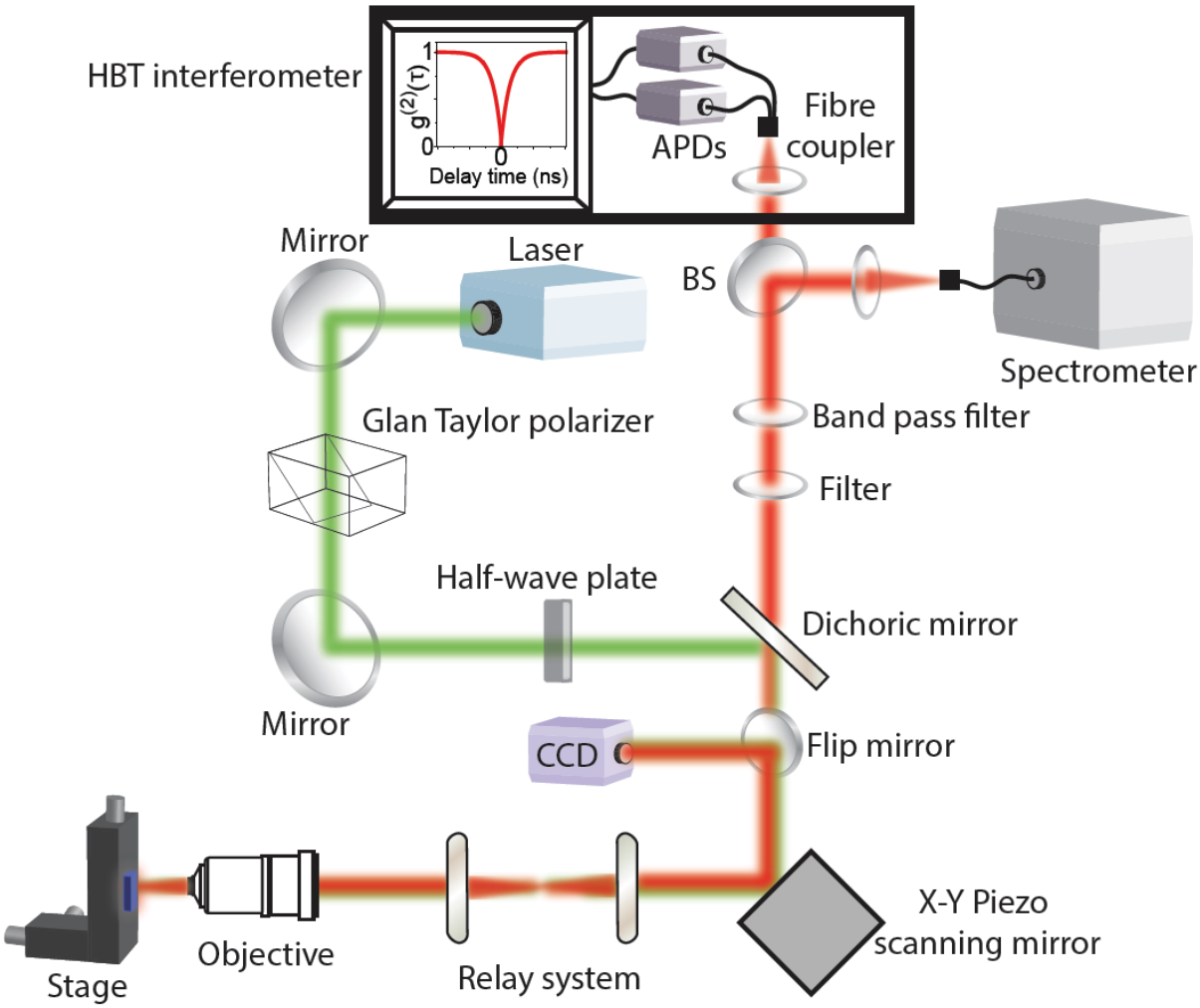


**Figure 2.6.** Schematic diagram of a confocal microscope with a spectrometer and HBT interferometer. BS – Beam splitter, APDs – avalanche photodiodes.

## 2.4 Diamond devices

Diamond materials with hosted colour centres are promising options for myriad of integrated nanophotonics, optoelectronics and quantum information processing applications [14], [137], [149], [150]. As mentioned previously, diamond possesses numerous unique and interesting properties, including a wide bandgap (5.5eV), high breakdown voltage (~$10^7$ V $cm^{-1}$) [151] and a high carrier mobility (~0.2 m $^2V^{-1}$ $s^{-1}$), high thermal conductivities (>2000$Wm^{-1}K^{-1}$) and a breakdown field strength of 10$MVcm^{-1}$ [152]. These properties make diamond ideal for high power, high energy, and high frequency optoelectronic devices. Therefore, diamond holds many advantages over its competitors, namely silicon carbide (SiC) and gallium nitride (GaN) (Table 2-2). The main advantage of using diamond for all the mentioned applications is that it

allows operation under extreme conditions due to its materials hardness, chemical inertness, wear resistance and high thermal conductivity.

To produce EL from a diamond defect, the p-i-n diode device requires fabrication of a high-quality n-type (electron) and p-type (holes) conducting material and an intrinsic (i) layer. Diamonds are generally doped with high concentrations of boron and phosphorous to create the p-type and n-type layer, respectively [153], [154]. The doped diamond layers are typically created using microwave plasma-enhanced CVD (MPCVD) growth techniques [155]–[157]. There has been a lot of research and great progress in diamond electronics, where EL has been observed in NV colour centres [21], [22], [158] and more recently SiV colour centres [159], [160]. However, the fluorescent intensity of the electrically pumped devices is $\leq 10^4$ counts $s^{-1}$, which is significantly lower than if the emitters were optically excited [143], [161]. LEDs fabricated from diamond can be advantageous for biosensors, on-chip applications, and photodetectors. Therefore, it is desirable to possess a narrow EL bandwidth or to increase the EL signal. Electrical excitation of quantum emitters is needed to allow the design, scalability and fabrication of efficient on-chip designs [22]–[24]. Also, electrical excitation allows the study of the charge dynamics and injection pathways between various charge states in a particular defect [158], [159], [162], [163].

**Table 2-2.** Material properties for silicon (Si), 4H-silicon carbide (4H-SiC), gallium nitride (GaN), natural diamond and CVD grown diamond [151], [152].

| Material | Si | 4H-SiC | GaN | Natural Diamond | CVD Diamond |
|---|---|---|---|---|---|
| **Bandgap (eV)** | 1.1 | 3.2 | 3.44 | 5.47 | 5.47 |
| **Breakdown field ($MVcm^{-1}$)** | 0.3 | 3 | 5 | 10 | 10 |
| **Electron saturation velocity ($x10^7$ cm $s^{-1}$)** | 0.86 | 3 | 2.5 | 2 | 2 |
| **Hole saturation velocity ($x10^7$ cm $s^{-1}$)** | n/a | n/a | n/a | 0.8 | 0.8 |
| **Electron mobility ($cm^2$ $V^{-1}$ $s^{-1}$)** | 1450 | 900 | 450 | 200 - 2800 | 4500 |
| **Hole mobility ($cm^2$ $V^{-1}$ $s^{-1}$)** | 480 | 120 | 200 | 1800 - 1200 | 3800 |
| **Thermal conductivity ($Wcm^{-1}$ $K^{-1}$)** | 1.5 | 5 | 1.3 | 22 | 24 |

Photonic crystal cavities are structures that have generated great interest, as it possesses a periodic structure and the ability of confining and manipulating photons [164], [165]. A periodic structure is a repeating pattern with defined dimension, typically circles with a specific radii and distance [149]. Recently there has been exploration into tuneable photonic crystals. By manipulating the structural arrangement or material refractive index, it allows the properties of the bandgap to be tuned. Tuneable structures are necessary for optoelectronic integrated circuits and optical interconnects [166]–[168]. Photonic crystal cavities have been fabricated in silicon and coupled to a graphene layer and triggered using an external bias to reduce the linewidth of the emitter by 1.5 nm and shift the cavity resonance by 1-2 nm [169] and increase the quality factor by 3 fold [170]. Shifts of >70 nm have been observed in silicon photonic crystals when a bias is applied [171]–[173]. Diamond is considered to be a great candidate for photonic crystal cavities due to their optically narrow emission linewidths and long spin

coherence times. Optimal photonic crystal cavity hybrid devices have been fabricated where, for example, NDs or bulk diamonds have been coupled to GaP cavities [174], [175]. The coupling showed enhancement in the $NV^-$ ZPL, but there were limitations such as scattering and losses from the cavity material, spatial mismatch as well as line-broadening mechanisms [174], [176]. Another avenue of fabrication is using bulk single crystal diamond as the base material where colour centres can be implanted at further depths to minimise the influence of surface defects. However, it has been difficult to fabricate due to high absorption and intrinsic scattering losses in the material [149]. To overcome these difficulties, it is imperative to fabricate thin, high quality single crystal diamond membranes [135].

Furthermore, the literature shows a variety of material bases that have been optimised for optoelectronic devices by integrating different single photon emitters in classical LED structures. For instance, by embedding Indium Gallium Nitride (InGaN) QDs into the intrinsic layer of GaN p-i-n diode or, similarly, Indium Arsenide (InAs) QDs in the intrinsic layer of Gallium Arsenide (GaAs), single photon EL has been demonstrated with on-set voltages of ~1.5 - 3.5V and a current density up to ~30 $A/cm^2$ [177], [178]. Single photon EL has also been observed in isolated carbon nanotubes [179], Silicon Carbide (SiC) [180], [181], single molecules [182], monolayer Tungsten di-Selenide ($WSe_2$) with a layer of boron nitride [179] and monolayer Molybdenum di-Sulphide ($MoS_2$) [183], [184]. Nevertheless, EL of single photons from these devices require cryogenic temperatures due to the necessity to confine carriers. In subsequent chapters, I show the realisation of a stable, room-temperature, electrically triggered SiV colour centre in a nanoscale diamond membrane diode structure. After describing a few p-i-n diode devices, I will now move on to describe the mechanisms behind their electrical triggering.

## 2.5 Electroluminescence of diamond

Similarly, to Chapter 2.3, this section describes the techniques and processes behind the electrical triggering of diamond devices.

A valued technique is the EL of optically active materials. EL is where excess carrier are injected into the photon emitting systems resulting in radiative recombination [21], [22], [185]–[188]. This technique allows electrically controlled single photon generation and is integral for the realisation of large-scale integrated quantum devices. Additionally, using an external

voltage supply to inject current into a single photon emitting system provides insight into fundamental properties, for example, charge state switching in active emitters.

Electrically driven excitation of emitters requires photons to incorporate into the active region of a device junction where the emitters will trap the efficient transport of excess carriers. Single photons are emitted upon subsequent decay of trapped carriers with characteristic time.

For electrically driven emission of photons, it is imperative that the recombination of excess charge carriers happens between the energy levels of the emitter. Therefore, incorporation of emitters into devices is unavoidable for excess carriers to be introduced into the neighbourhood of the energy levels. A simplified review of the basics of common semiconductor junctions is covered below to explain the charge flow and driving forces behind excess carrier injection.

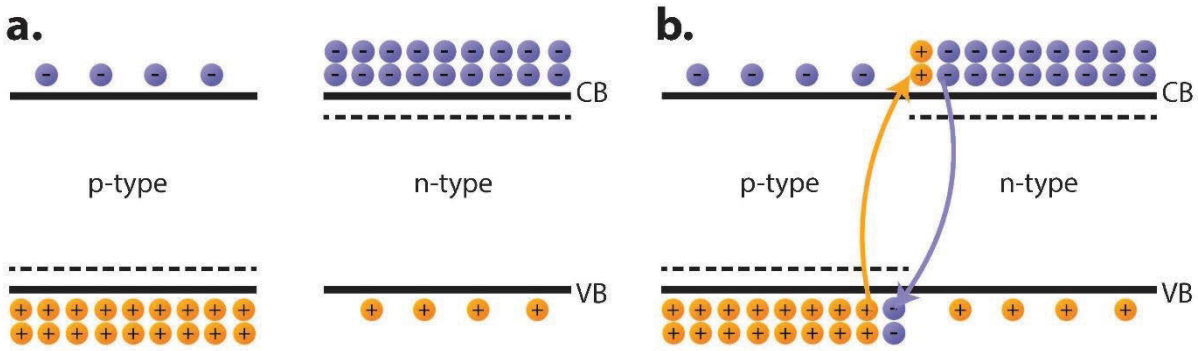


**Figure 2.7.** Energy band schematics of two materials that are p-doped and n-doped. (a) The majority of holes are located in the valance band (VB) of the p-doped material while the majority of electrons reside in the conduction band (CB) of the n-doped material. (b) When the materials come into contact, the majority carrier in the n-doped and p-doped material diffuse to the opposite side, to become minority carrier before they recombine.

Two similar semiconductors that are either n-doped or p-doped, are brought into close contact (Figure 2.7a). The dotted line in the above band diagrams illustrates the Fermi energy levels of the n-doped and p-doped semiconductors which are the majority carrier electrons (donors) and majority carrier holes (acceptors), respectively. The acceptor density is generally denoted as $N_A$ while the donor density is $N_D$. When the differently doped regions are brought into contact, holes can diffuse to the n-doped region, across the junction leaving behind acceptor-impurities in the p-doped region and becoming a minority carrier as shown in Figure 2.7b [88, 89]. Furthermore, current will flow readily in one direction (forward biased) but not in the other

(reverse biased), creating a basic diode. This non-reversing behaviour arises from the nature of the charge transport process. This process lowers the Fermi energy level of the n-doped region and raises it on the p-doped region. Similarly, the electron-minority flow moving towards the p-doped region leaves behind donor-impurities in the n-doped region. This can be expected since holes are the absence of electrons. This diffusion process near the junction will result in recombination of majority carrier to minority carriers resulting in conservation of charge through photon emission as well as momentum.

Due to the electric field build up across the p-n junction between the fixed donor and acceptor impurities, the diffusion of carriers cannot continue indefinitely [90, 91]. This intrinsic field will inspect charge flow, pushing electrons to the n-doped region and holes to p-doped region. This region is referred to as the depletion region or the space charge region (SCR) and it is empty of carriers. The minority carrier flow must overcome a potential barrier, $V_b$, due to the built-in electric field, caused by the work-function difference between the n-type and p-type semiconductors. This leads to band-bending in the band energy schematic (Figure 2.8). At thermal equilibrium, the Fermi level of the system is uniform, as indicated by the broken black line in the centre.

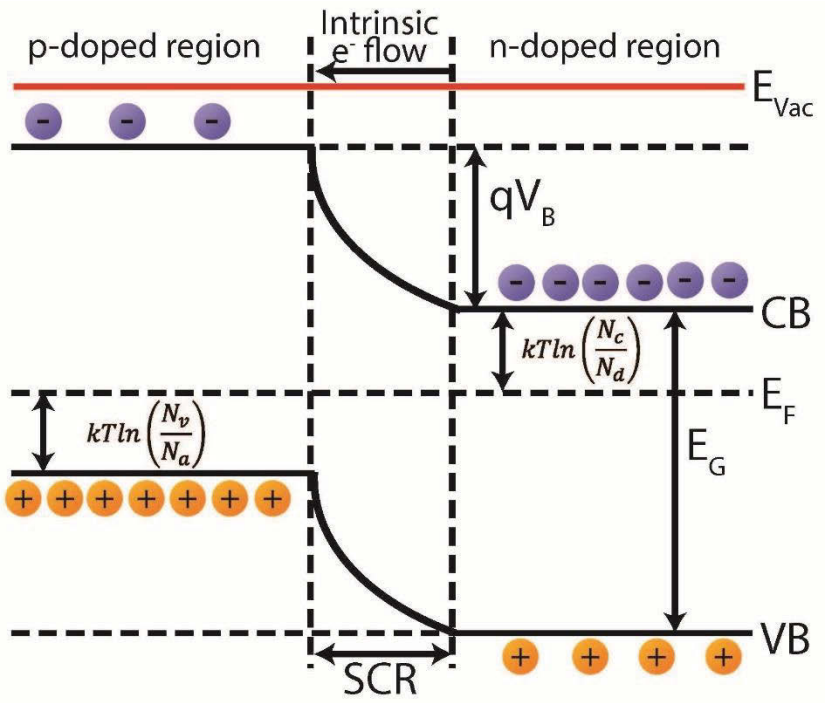


**Figure 2.8.** A band energy schematic showing band bending when an n-doped and p-doped material are in contact and at equilibrium. The space charge region (SCR) is empty of carriers. $E_G$ is the band gap of the material.

The built-in potential can be quantitatively described, at thermal equilibrium, using the difference in the energy between the Fermi level, $E_F$, and the conduction band, $E_C$, and valance band, $E_V$, by[189], [190]:

$$\boldsymbol{E_c - E_F = kTln\left(\frac{N_c}{N_D}\right)} \qquad \textbf{Equation 2.7}$$

and

$$\boldsymbol{E_F - E_v = kTln\left(\frac{N_v}{N_A}\right)} \qquad \textbf{Equation 2.8}$$

Where $kT$ is the Boltzmann constant ($1.38 \times 10^{-23} m^2 kg s^{-2} K^{-1}$) multiplied by room temperature to obtain 25 meV. $N_c$ and $N_v$ are the intrinsic carrier concentration and are dependent on the material properties. $N_D$ is the electron carrier, or donor, density while $N_A$ is the hole carrier, or acceptor, densities. $N_D$ and $N_A$ are reliant on the doping concentrations of the n-type and p-type semiconductors.

Figure 2.8 shows us that:

$$\begin{aligned} \boldsymbol{qV_b} &= \boldsymbol{E_G - (E_c - E_F) - (E_F - E_v)} \\ &= \boldsymbol{E_G - kTln\left(\frac{N_c}{N_D}\right) - kTln\left(\frac{N_v}{N_A}\right)} \\ &= \boldsymbol{E_g - kTln\left(\frac{N_c N_v}{N_D N_A}\right)} \end{aligned} \qquad \textbf{Equation 2.9}$$

Where $q$ is the charge of the minority carriers. This can be used to determine the depletion region, ω, of a p-n junction. The electric field is related to charge density, by using Gauss's law, as:

$$\boldsymbol{E(x) = \frac{1}{\varepsilon}\int \rho(x)\, dx} \qquad \textbf{Equation 2.10}$$

Where $\varepsilon$ is the dielectric constant. Considering a Dirac-delta function assumption for the p-doped region, the integral can be represented as:

$$\boldsymbol{E(x) = \frac{1}{\varepsilon}\int_0^{\omega} qN_D\, dx} \qquad \textbf{Equation 2.11}$$

Therefore, the maximum field in the depletion region can be represented as:

$$E_{max} = \frac{qN_D\omega}{\varepsilon}$$ **Equation 2.12**

If I assume that the maximum electric field is reached in the centre of the depletion region at $\omega/2$, the potential drop due to band bending is:

$$V_b = \frac{E_{max}\omega}{2} = \frac{qN_D\omega^2}{2\varepsilon}$$ **Equation 2.13**

This can be simplified to:

$$\omega = \sqrt{\frac{2\varepsilon V_b}{qN_D}}$$ **Equation 2.14**

Similarly, for a p-n junction:

$$\omega = \sqrt{\frac{2\varepsilon V_b}{q^2}\left(\frac{1}{N_A} + \frac{1}{N_D}\right)}$$

$$\omega = \sqrt{\frac{2\varepsilon V_b}{q^2}\left(\frac{N_D+N_A}{N_AN_D}\right)}$$ **Equation 2.15**

As mentioned previously, p-n junctions can be used to give insight into semiconductor device properties, including current flow and band bending. Numerous other device structures can be manufactured by changing the desired semiconductor material, fabrication technique and application of the device.

It is imperative to ensure that the injected excess carriers will lead to the photon emitting sources avoiding unwanted recombination channels. Therefore, when fabricating junctions, it is important to use a p-i-n device structure where the intrinsic layer contains the photon emitting defects [159], [163], [188], [191].

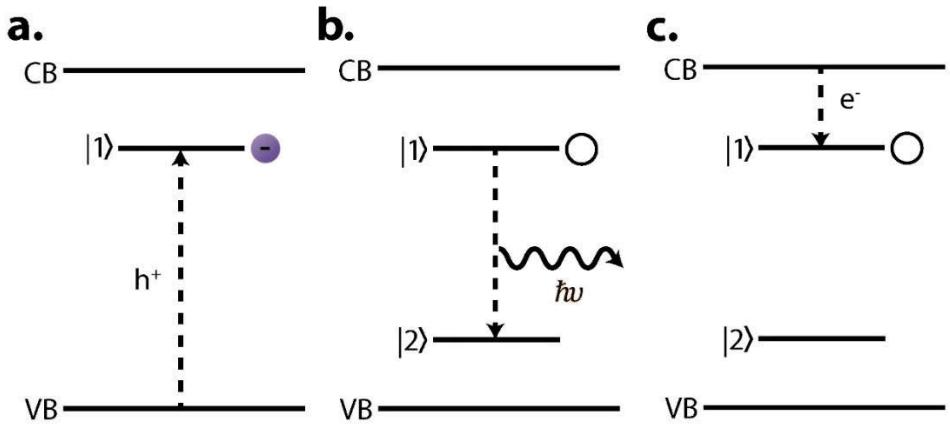


**Figure 2.9.** Schematic illustration of a photon being emitted at a charged defect site. (a) A hole is trapped by a defect state that has an electron in its ground state. (b) An immediate decay from the excited state to the ground state, of the trapped state, emits a photon. This turns the charge state neutral. (c) An electron travels to the decay state, changing it from a neutral to a negatively charged state to repeat the cycle.

Figure 2.9 shows the emission of an electrically triggered photon. A photon may have a defect state in a semiconductor with a single electron in its ground state (for example $NV^-$). This state would cause an excess of minority holes to be attracted to this state and combine as shown in Figure 2.9a. Subsequently, this will cause the state to relax by sending the trapped hole to the ground state. This will lead to EL of the emitter (Figure 2.9b). Radiative recombination causes the electrically triggered photon to lose its electron to the ground state, changing the charge state neutral [192]. This causes the electron to move from the conduction band to the photon defect state, trapping it and turning the state negatively charged (Figure 2.9c).

To summarise optical pumping of an emitter through an external laser source uses sub-bandgap direct excitation that drives electrons to transition into an isolated photon emitter energy state. This is juxtaposed to electrical pumping through excess carrier injection by an external voltage supply, where it involves the valance and conduction bands of the semiconducting material where subsequent trapping of photons can occur.

## 2.6 Diamond photonics

In addition to electrical triggering of diamond, there is a vast field of nanophotonic research, primarily, to understand and manipulate single photon emitters for quantum applications.

Diamond colour centres are highly sought after for quantum information processes, such as for triggering of single photon emitters due to their short lifetime of several nanoseconds. The NV colour centre exhibits a coherent electron spin which can serve as a long lived qubit and enables information of the spin state to be transmitted through single photons [14], [78], [193]. As mentioned previously, the SiV colour centre is highly desirable due to its narrowband emission in the near-infrared (737nm) and can be synthesized with relative ease in CVD reactors with a silicon source. This has led to the engineering of single SiV centres isolated in grown NDs [99] and nano-islands on iridium [194] with single photon emission as high as 6 Mcounts/s [17]. Unfortunately, the emission of the SiV emitter suffers in these systems due to the shift of the ZPL from ~730 to 750 nm from high levels of individual stress in the nanodiamonds. Also, the ZPL of the SiV colour centre is almost fully linearly polarized at room temperature [102], [194], [195]. This allows for the polarization of the emitter to be used to encode information, which is highly useful for quantum cryptography. To utilize single emitting diamond colour centres, it is imperative to efficiently capture their fluorescence and manipulate their photonic properties. This can be achieved through the use of waveguides [196], nanoparticles [197], nano-pillars to enhance their collection efficiency, while nano-cavity structures are utilized to manipulate the bandwidth and lifetime of the emitters [198]. The transmission of information of the source is limited by the collection efficiency and is more apparent for indistinguishable photons. Moreover, it is important to control the lifetimes of colour centres because single photons are emitted at a higher rate for shorter lifetimes. Manipulation of colour centre lifetimes is highly desirable for controlling the spontaneous emission rate through cavity coupling. To control the lifetime of colour centres, sophisticated waveguides need to be engineered. Fabrication of waveguides and cavities in diamond is challenging as it demands sophisticated etching and growth recipes. Furthermore, isolated single crystal diamond films that are <1μm are not readily available. Fabrication of such thin diamond membranes will be discussed in Chapter 3 and Chapter 4.

To utilize the full potential of diamond nanophotonic devices, it is required to fabricate high quality diamond structures that host isolated colour centres with good emission and spin properties. Therefore, free standing, thin single crystal diamond membranes are indispensable

for the engineering of nanophotonic devices. Diamond membranes have been used for a variety of devices including one and two dimensional photonic crystal cavities, ring resonators and resonators coupled to waveguides [31], [150], [199], [200]. A large problem with many photonic devices is that the photonic crystal cavity is often resting on another substrate instead of being suspended in air. This leads to the potential of light scattering and/or absorption by the substrate due the small difference in refractive indices and other material properties. Several techniques have been employed to combat this issue such as using a sacrificial layer of poly (methyl methacrylate) (PMMA) between the diamond and $SiO_2$ layer [30], or the silicon material beneath the device can be removed with an isotropic etch in a reactive ion etching (RIE) chamber [150], [199]. Additionally, fabrication of nanophotonic structures etched into bulk diamond and subsequently undercut using an angled etching technique has also been employed [201].

Furthermore, the ion-assisted lifted-off process has been used for fabrication of diamond nanophotonic devices. The stopping of the fast-implanted ions creates a buried graphite layer that can be subsequently removed to make a thin diamond membrane. Parikh *et al.* originally proposed this idea [202], however, it was only recently diamond membrane based optical resonators have been produced [27], and details of the fabrication are part of Chapter 3 and Chapter 4. The ion implantation technique makes the original diamond material unsuitable for devices, but, recent work has shown that they can be effectively used as templates for pristine single crystal diamond growth for further fabrication of waveguides [203]–[205]. The grown diamond membranes do not show propagation of damage into the regrown material unlike other traditional semiconductors (SiC and GaN). Even though this technique involves multiple steps it still possesses various advantages, which includes the ability to avoid laser cutting of a 20 μm diamond membrane and etching it down and MPCVD overgrowth to intentionally dope the membranes with a variety of colour centres.

In summary, despite the challenges associated with the fabrication of nanoscale diamond devices, progress has been expeditious. Numerous research groups have been able to transform polycrystalline and single crystalline devices into high quality photonic crystal cavities for a variety of nanophotonic quantum applications. New applications are continually being developed, a very recent one is utilizing diamond devices for optoelectronic applications as a part of this thesis. Both these techniques, optical and electrical pumping, are used to investigate the suitability of the diamond devices for several applications.

# Chapter 3 Diamond membrane fabrication

The fabrication of high aspect ratio, single crystal diamond membranes are highly sought after for nanophotonic applications, nanoelectronics and quantum information processes. Diamond membranes are created using a lift-off process after the generation of a damaged layer through ion implantation. This chapter details the lift-off process and removal of the damaged diamond material to yield thin, single crystal diamond membranes with optically active colour centres. These diamond membranes are the stepping stones for the fabrication of high-quality optical resonators and electrical devices. Igor Aharonovich and Kerem Bray conceived the idea. Kerem Bray and Rodolfo Previdi generated the membranes. Andrew P. Magyar contributed to the electrochemical etch. Kumaravelu Ganesan (University of Melbourne, Australia) carried out the ion implantation. Minh Anh Phan assisted with AFM measurements. John Scott measured and analysed the TEM data. Blake Regan assisted with the resonator fabrication. Igor Aharonovich and Milos Toth supervised the work. All the authors discussed and wrote the manuscript.

## 3.1 Diamond membranes

The fabrication of diamond membranes is imperative for a variety of advanced nanophotonics, nanoelectronics and optomechanics applications. Diamond possesses extraordinary properties, which include a wide band-gap, high thermal conductivity, a high refractive index and it is biocompatible [206]. Exploiting these properties for nanophotonic and nanoelectronics applications requires high quality, thin, single crystal diamond membranes containing colour centres [199], [200]. The thickness of single crystal diamond membranes is very important for the confinement of light and should be on the order of nanometres. The ideal thickness is determined by the emitter wavelength divided by the refractive index of the material [207]. For a SiV centre, with a ZPL of 737 nm, and refractive index of diamond as 2.4, the required thickness is ~300 nm. There remain challenges when scalable fabrication of high quality single crystal diamond devices for use in a wide variety of quantum applications.

Our work uses ion implantation and selective etching techniques to fabricate diamond membranes from bulk, single crystal diamond. I make use of a flip and thin etching step to remove damaged material created through the implantation process. This technique results in 300 nm thick single crystal diamond membranes that are up to 1000 μm x 2000 μm. Through

MPCVD, the diamond membranes are able to host a variety of colour centres including NV [27], [208], SiV [160], [209] and GeV [122]. With the availability of various colour centres in the visible to NIR along with a high yield and simple growth technique, it allows for the high aspect ratio diamond membranes to be utilised for a variety of nanophotonics, nanoelectronics and quantum information science processes.

### 3.1.1 Fabrication of diamond membranes

Single crystal diamond membranes were created from a bulk type IIa CVD diamond from Element 6$^{TM}$, with a nitrogen concentration <1ppm. The crystal was implanted with 1 MeV $He^+$ ions to a dose of $5 \times 10^{16}$ ions/cm$^2$. Stopping range of ions in matter (SRIM) simulations predicted a stopping range of 1.71 μm. The implanted diamond was subsequently annealed at 900$^o$C in vacuum to create a thin amorphous carbon layer 1.7 μm below the surface, as shown in Figure 3.1. The amorphous layer enables lift-off of the 1.7 μm thick diamond membrane by electrochemical etching. To selectively remove the graphitic residual, the sample was then immersed in deionised water and electrochemical etching was carried out using a constant forward bias of 60 V. During etching, a positively biased tip was contacted onto the top surface of the diamond while the negatively biased tip was positioned slightly above the substrate. The positive biased contact was coated in a thin layer of PMMA, except for the tip. This allows the injected current to be localised into the bulk diamond sample to etch away the graphitic layer faster. The dissociated diamond membranes were cleaned using a 3:1 (sulphuric acid - hydrogen peroxide) piranha solution and transferred using a liquid droplet onto a Ti coated silica substrate. The diamond membranes range in size from [~50 to 1000] μm × [~100 to 2000] μm in width and length respectively (Figure 3.1). Figure 3.1f shows an optical image of a single crystal diamond membrane with an area of ~ 0.2 mm$^2$ and a thickness of 1.7 μm.

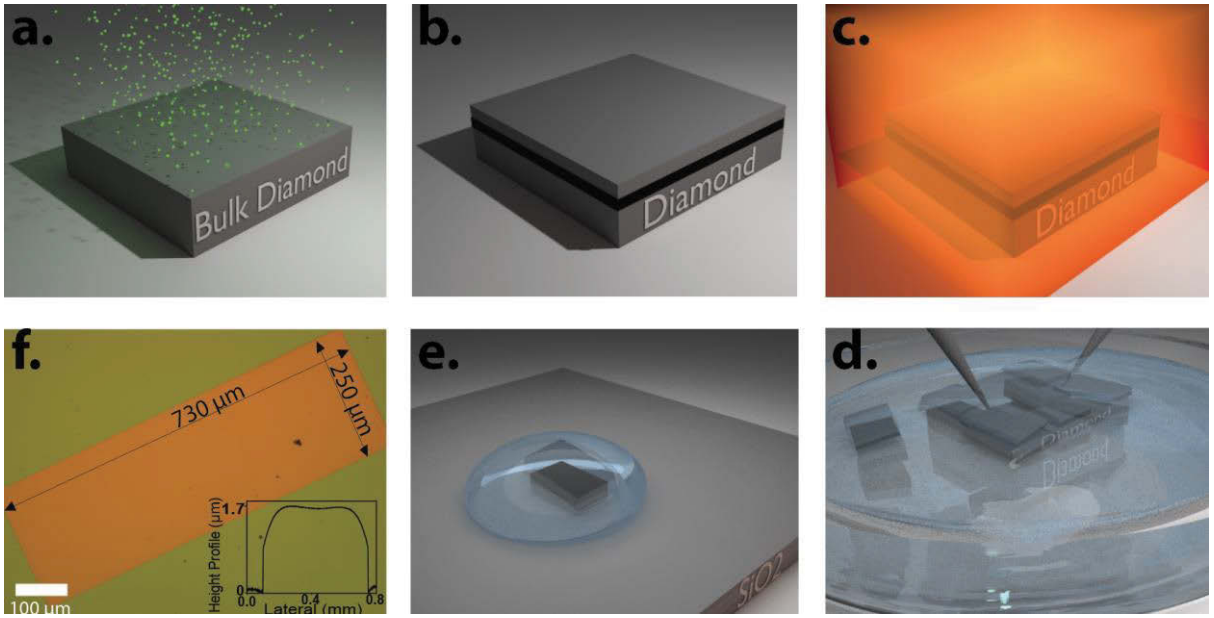


**Figure 3.1.** Schematic of the process used to engineer single crystal diamond membranes. (a) Single crystal, undoped CVD diamond is implanted with $He^+$ ions (1 MeV, $5 \times 10^{16}$ ions/cm$^2$) to create a damaged layer ~ 1.7 µm below the surface (b). (c) The sample is annealed at 900ºC and (d) electrochemically etched to lift off the diamond membranes. (e) The membranes are transferred onto a Ti coated silica substrate using a liquid transfer process. (f) A top-down optical image (false colour) of a membrane that has been lifted off. Inset: height profile that shows the membrane is ~ 1.7 µm thick.

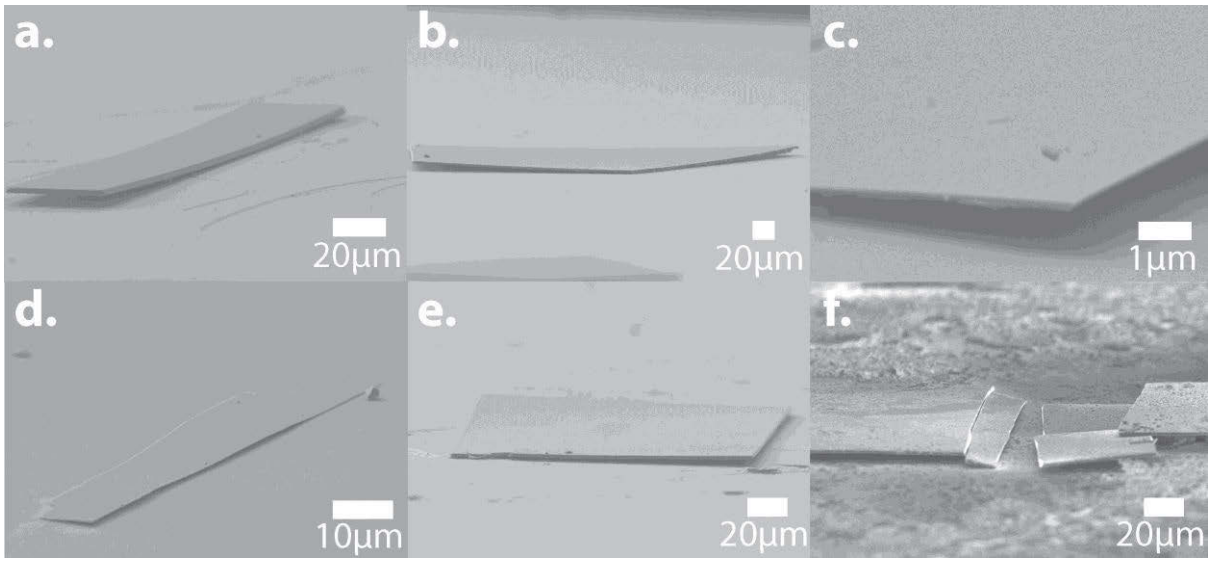


**Figure 3.2.** SEM images of the lifted diamond membranes showing (a-e) the various degrees of induced strain of the diamond membranes to cause curling of the sample. (f) SEM image of a diamond membrane that has shattered due to induced stress from handling the sample.

The lifted off diamond membranes are generally not flat, especially as they increase in size. The inherent strain in the material causes the edges of the membranes to curl at different angles as shown in Figure 3.2, which leads to the extremities of the sample to be suspended in air. The curling of the diamond membranes generates numerous issues for fabrication of devices due to uneven growth and etching. This leads to non-uniform or roughening of the diamond surfaces. Therefore, the diamond membranes need to be flatten down using a layer of PMMA or titanium. The flattening can be achieved by transferring the membranes with tweezers or using a clean piece of silicon or sapphire to press the membrane down. Handling the membranes is also a very delicate process. The diamond membranes are fragile and prone to shattering by handling the samples with tweezers or droplets of water and transferring the membranes between growth and etching procedures (Figure 3.2f).

### 3.1.2 Diamond overgrowth

To incorporate a variety of colour centres, I utilised a MPCVD chamber. The chamber was pumped down to 1x $10^{-6}$ Torr, to remove all atmospheric gasses and cleaned using a hydrogen plasma at 900W with a pressure of 30 Torr for several hours to remove all unwanted contaminants. The diamond membranes are overgrown using a MPCVD chamber (Figure 3.3) with a hydrogen/methane ratio of 100:1 at 60 Torr, a microwave power of 900W for 8 minutes to fabricate a ~100 nm intrinsic single crystal diamond layer. Silicon doping occurs naturally with the silicon source from the substrate and is incorporated into the membrane creating SiV colour centres, shown by the ZPL at 737 nm (Figure 3.3d). Figure 3.4e shows a Scanning Electron Microscopy (SEM) image of an overgrown diamond membrane with a homogeneous single crystal diamond layer.

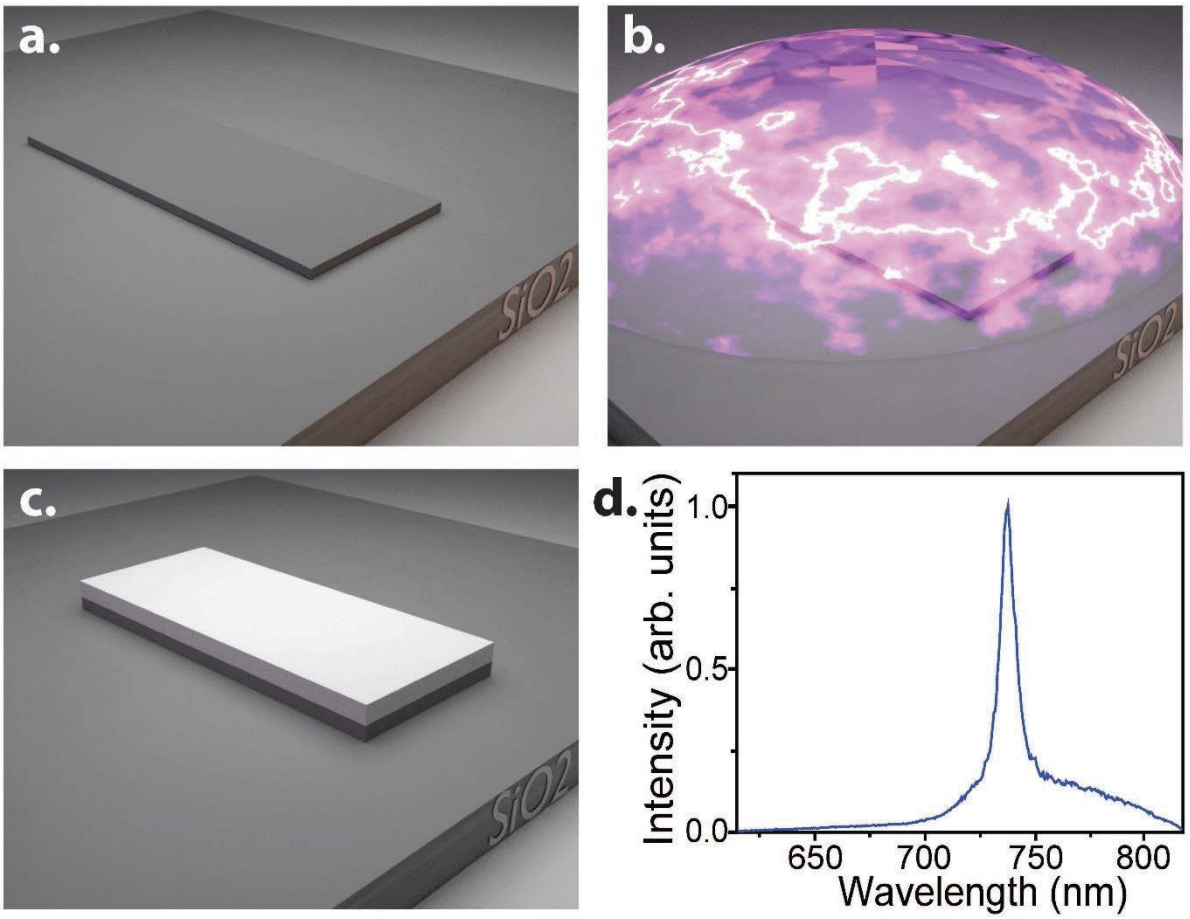


**Figure 3.3.** (a) The transferred diamond membrane is placed on a $SiO_2$ substrate to act as a source for SiV colour centres. (b) The sample is epitaxially overgrown using an MPCVD to create (c) a layer of single crystal diamond. (d) The overgrown layer contains SiV colour centres, as shown by the peak at 737 nm.

### 3.1.3 Flip and thin

It is ideal to fabricate high quality single crystal diamond membrane for engineering of devices. Therefore, the original damaged diamond sample needs to be removed as it may be host to residual sp2 carbon, a rough surface and a damaged lattice structure from ion implantation. To remove the original damaged diamond, the membranes were flipped and placed onto a sapphire substrate to reduce sputtering and masking in the chamber. The membranes were thinned by Inductively Coupled Plasma - Reactive Ion Etching (ICP-RIE) in the presence of tetrafluoromethane ($CF_4$) and oxygen ($O_2$) in a ratio of 1:3 at a pressure of 20 Pa, with a forward power of 200 W for 7 minutes as shown in Figure 3.4b. Using ICP-RIE, thin membranes were reliably produced to achieve thicknesses smaller than 300 nm. Thinning the membranes using

the method ensures that only the high quality overgrown single crystal layer remains. A SEM image of the 300 nm thick diamond membrane is shown in Figure 3.4f, the surface is still relatively clean and can be used as a base for other applications discussed below.

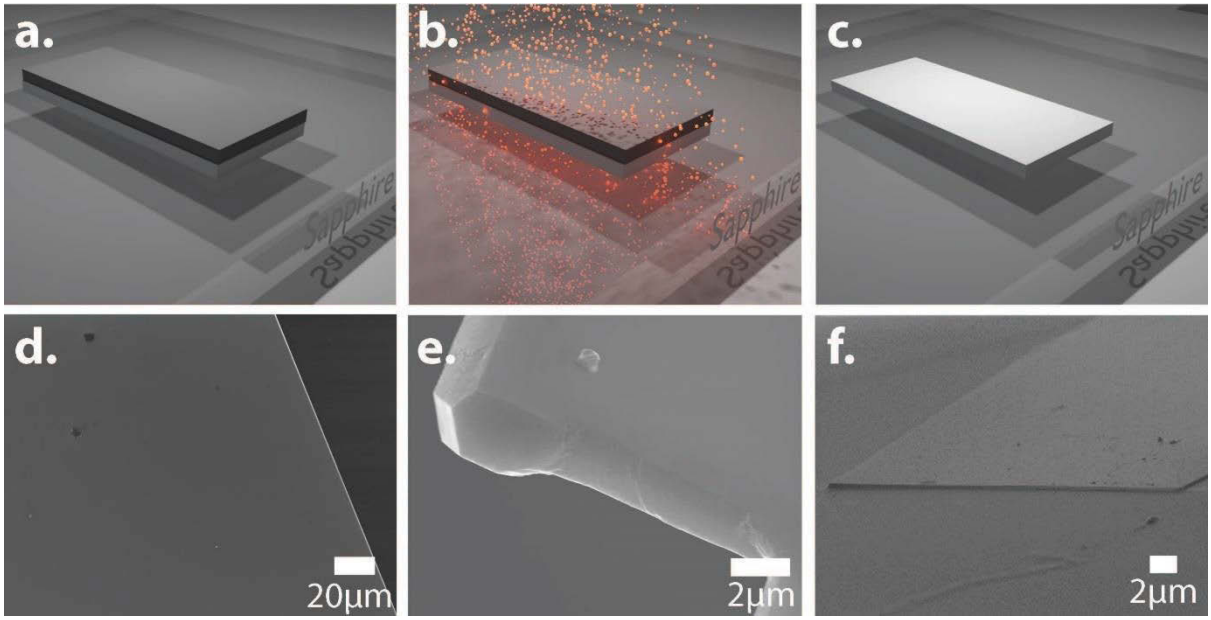


**Figure 3.4.** (a) The membrane is flipped and placed onto a sapphire substrate. (b) The damaged layer is removed by ICP-RIE in the presence of $CF_4$ and $O_2$, leaving (c) only the epitaxially grown single crystal diamond layer. (d) SEM image of the lifted diamond membrane after piranha cleaning. (e) SEM image of the diamond membrane after CVD grown and (f) shows the membrane after ICP-RIE thinning.

The diamond membranes were probed using Raman spectroscopy with a 633 nm HeNe laser. A peak at ~1332 $cm^{-1}$ corresponding to a single crystal diamond is shown in Figure 3.5a with a FWHM of 8.3 $cm^{-1}$ [210]. The surface roughness of the membrane before and after etching was determined by an atomic force microscope (AFM) to be below 3 nm, suitable for photonic and electronic devices (Figure 3.5b). To unambiguously show that diamond overgrowth is indeed a single crystal diamond, the overgrown membranes were transferred to a TEM grid. The typical membrane morphology after etching and epitaxial overgrowth is shown in the TEM micrographs in Figure 3.5c. Select-area electron diffraction confirms the membrane microstructure is a single crystal (Figure 3.5d). The diffraction intensity pattern is indexed to the [001] zone axis of a diamond cubic structure. The measured plane spacing of (200) and (220) planes were 1.275 and 0.903 Å respectively, in good agreement with bulk diamond. TEM

and SAED characterisation were conducted on a FEI Tecnai T20 microscope at 200keV with a LaB 6 filament.

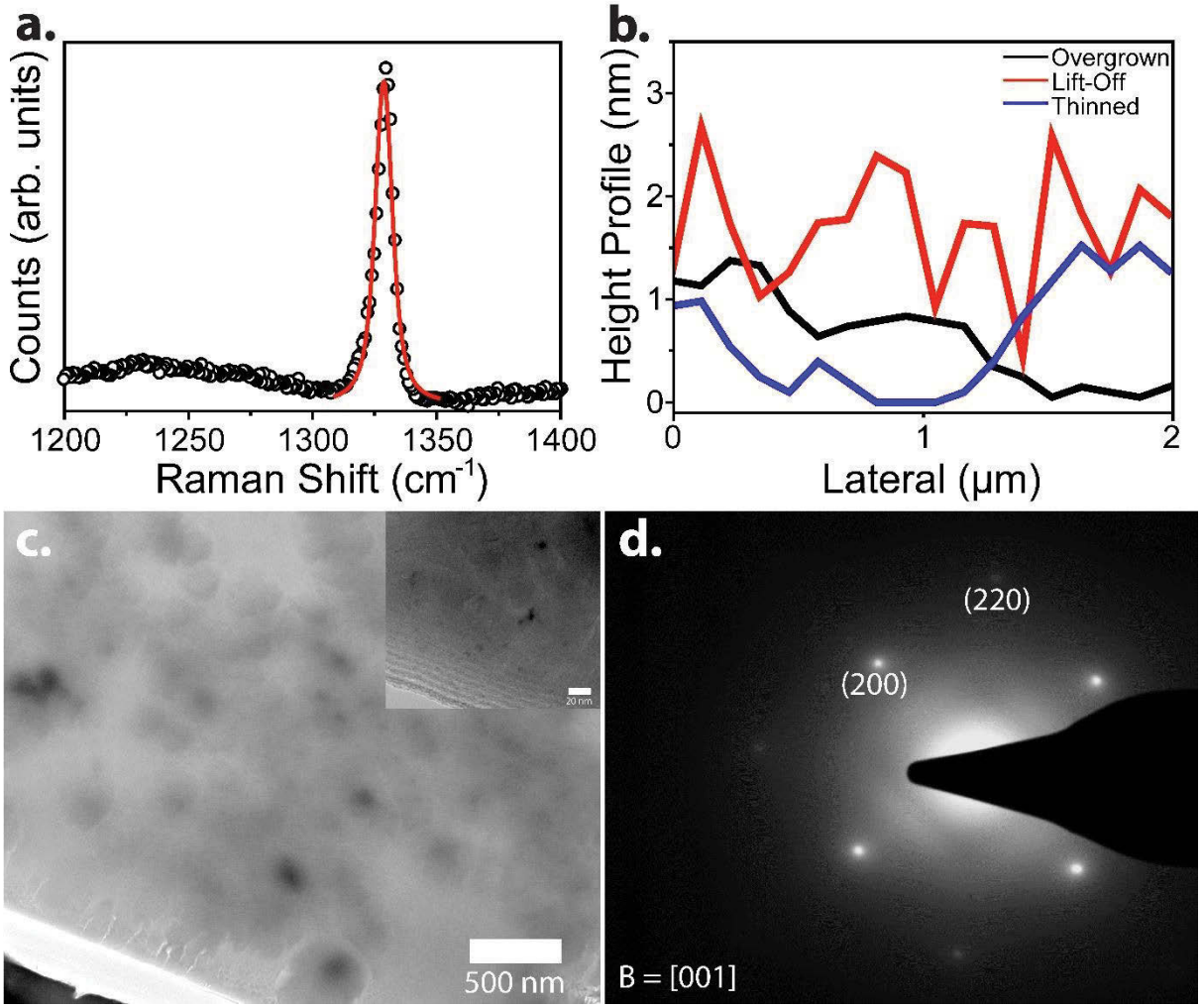


**Figure 3.5**. Structural characterisation. (a) Raman spectroscopy of the diamond membrane using a 633 HeNe laser shows the characteristic single crystal diamond peak at 1332 $cm^{-1}$. The curve was fit with a Voight function to show a FWHM of 8.3 $cm^{-1}$. (b) Lateral AFM scan show the surface roughness of the membrane after lift-off, after thinning and after an overgrowth to be ~2.5 nm, ~1.5 nm and ~ 1.5 nm respectively. (c) TEM image of an overgrown diamond membrane (~250 nm in thickness) transferred to a copper TEM grid. Inset: higher magnification image of edge region. Scale bar 20 nm. (d) Diffraction pattern from the diamond membrane in (c) indexed to the [001] zone axis.

In summary, I reliably fabricated ~300 nm thin, optically active, single crystal diamond membranes. The standalone membranes possess a high aspect ratio and can be positioned onto

a substrate of choice. Finally, I show that the membranes are able to host optically active defects, in particular the SiV colour centre. The fabrication of diamonds membranes is important for advancing diamond device fabrication. The scalability of this process can drive the use of diamond from a laboratory setting into a large variety of devices spanning high power electronics, sensing and photonics such as resonators and waveguides. Membrane fabrication is scalable because the size of the initial bulk diamond can be increased and implanted with $He^+$ ions. The single crystal bulk diamond can then be overgrown with an intrinsic layer (containing SiV or GeV colour centres) and a phosphorus doped layer using CVD techniques. The overgrown bulk diamond can then be patterned with HSQ, EBIE and RIE techniques where is can be subsequently lifted off through electrochemical etching, allowing a defined p-i-n single crystal diamond membrane to be transferred, flipped, and thinned in preparation for electrical stimulation. If a device set-up or processes could be developed to allow the transfer and accurate positioning of multiple diamond membranes, then this will also allow a significantly increased throughput of p-i-n diamond devices for characterization. Currently, the diamond membranes can be lifted off with a 100% success rate. However, the rate of etching varies between ~two to ~eight weeks. This variation in etching rate may be due to a poor electrical etching set-up, i.e. poor contacts, lack of ion channels in the deionised water or inhomogeneity of the initial $He^+$ ion implantation and subsequent annealing. The transferring, growing, flipping, and thinning of the membranes has a success rate of ~80%. The ~20% include the loss or destruction of the membranes through transferring, CVD growth, RIE etching, optical and electrical characterisation. The main cause of diamond membrane loss occurs at the transferring between different substrates and flipping of the diamond membranes. I will discuss in the following chapters why it is that high-aspect ratio diamond membranes are necessary for photonic, optoelectronic and quantum information processes.

Based on the protocols in this chapter, the next step is to use the fabricated diamond membranes for the fabrication of high aspect ratio, vertical nanoscale diamond p-i-n device structures for electrical triggering of SiV colour centres. The diamond planar device fabrication and electrical characteristics, more specifically vertical p-n and p-i-n diamond membranes, is described in Chapter 4, while their optoelectrical properties are discussed in Chapter 5.

# Chapter 4 Single crystal diamond membranes for nanoelectronics

Previously in Chapter 3, I showed a robust and reliable method to fabricate single crystal diamond membranes, explicitly the fabrication of a high quality, surface smooth diamond planar devices. This is taken another step forward in this chapter, where I will discuss how the established protocols to produce high quality single crystal diamond membranes will help to fabricate, p-doped, p-n and p-i-n diode devices and exploit these diamond planar devices for nanoelectronic applications.

The availability of conductive diamond membranes for applications in nanoelectronics so far has remained as an unreachable goal. In this work, I present a complete nanofabrication methodology for engineering high aspect ratio, electrically active single crystal diamond membranes. The membranes have large lateral directions, exceeding ~ 500×500 $\mu m^2$ and are only several hundreds of nanometres thick. I further realise vertical single crystal p-n junctions, made from the diamond membranes that exhibit onset voltages of ~ 10V and a current of several mA. Moreover, I deterministically introduce optically active colour centres into the membranes and demonstrate for the first time a single crystal nanoscale diamond LED. The robust and scalable approach to engineer the electrically active single crystal diamond membranes, offers new pathways for advanced nanophotonics, nanoelectronics and optomechanics devices employing diamond. Igor Aharonovich and Kerem Bray conceived the idea. Kerem Bray and Rodolfo Previdi generated the membranes. Andrew P. Magyar contributed to the electrochemical etch. Hiromitsu Kato, Masahiko Ogura, Toshiharu Makino and Satoshi Yamasaki (AIST, Japan) performed the n-type diamond growth. Kumaravelu Ganesan (University of Melbourne, Australia) carried out the ion implantation. Kerem Bray measured and analysed the PL and electrical measurements. Igor Aharonovich and Milos Toth supervised the work. All the authors discussed and wrote the manuscript.

## 4.1 Introduction

The majority of modern photonic and optoelectronic devices including photodetectors, LEDs, lasers, MEMS and sensors rely on efficient doping (p-type and n-type) for electrical triggering or readout. Many devices also require robust nanofabrication protocols that enable engineering

of nanoscale (tens to hundreds of nanometres) suspended membranes. These membranes are fundamental building blocks of advanced nanophotonic components, such as waveguides or photonic crystal cavities, and also crucial to enable mechanical motion in MEMs [31]–[33], [112], [211].

The exceptional properties of diamond, including excellent thermal conductivity, high young modulus and wide optical transparency [44], [152], [153], [212], [213], make it an ideal platform for a vast majority of these applications. Diamond is also poised to be the leading candidate for modern nano-electronic devices due to its ability to sustain high temperatures and high electric fields before breakdown [214]–[216]. However, broad adoption of diamond-based devices has so far been hindered by a lack of large area conductive diamond membranes and efficient nanoscale p-n junctions. While progress has been made to demonstrate proof of concept experiments and develop nanofabrication protocols to sculpt diamond [31], [205], [209], [217]–[223], large-scale conductive diamond membranes that are suitable for efficient p-n or p-i-n junction engineering are currently beyond reach. This is due, in part, by the challenges associated with epitaxial growth onto non-diamond sacrificial substrates that can be subsequently chemically removed – a process that is well established for silicon and gallium arsenide.

In this chapter, I describe how these barriers were overcome and demonstrate a robust method to fabricate p-type diamond membranes and engineer vertical p-n and p-i-n junctions that are suitable for further development of on-chip nanoelectronic devices. The nanoscale diamond membranes produced in the work have large lateral dimensions, over 500 x 500 $\mu m^2$, excellent electronic properties, and are fabricated using a highly robust and technologically mature process, making them attractive candidates for broad adoption and scalable device fabrication.

### 4.1.1 Fabrication of p-type diamond membranes.

Similarly, to the section 3.1.1, boron doped membranes were created from a bulk boron doped ($\sim 3 \times 10^{20}$atoms/cm$^3$) diamond crystal grown by MPCVD. Boron has been reliably used to achieve p-type doping in diamond [22], [155]. The crystal was implanted with 1 MeV $He^+$ ions and subsequently annealed at 900$^o$C in a vacuum to create a thin amorphous carbon layer. The membranes were selectively removed through electrochemical etching in deionised water with a constant forward bias of 60 V. This optimised implantation and electrochemical etch method leads to the lift off of membranes with high surface area. The diamond membranes were

cleaned using piranha solution and transferred to a silicon substrate coated with ~150 nm of titanium which acts as a sticking layer and a bottom contact for electrical measurements, detailed below in Chapter 4 and Chapter 5. The membranes similarly range in size from [~100 to 600] μm × [~120 to 800] μm.

## 4.2 Characterisation of diamond membranes

To test the electrical properties of the p-type diamond membranes, I measured the current – voltage (I-V) curves for a thick (1.7 μm) and a thinned (~ 200 nm) membrane. An optical image of the latter is shown in Figure 4.1a, while the electrical measurements are presented in Figure 4.1(b, c). As expected, semiconducting behaviour (Schottky junction) is observed from both membranes. The thicker membrane exhibits a forward threshold voltage of ~10 V and a breakdown voltage of -5V, while the thin membrane exhibits a slightly reduced threshold of 8 V. In both cases, currents on the order of ~ mA (~1.5 – 2 A/cm$^2$) are recorded. These values are comparable to bulk and polycrystalline diamond devices [20], [22]. For reference, the inset of Figure 4.1c shows the same measurement performed on an un-doped diamond membrane with the same thickness (200 nm), that results in a small leakage current of several ~ μA (~2 mA/cm$^2$) flowing through the junction. These results confirm that the boron doped diamond membranes maintain their electrical properties even when they are thinned down to several hundred nanometres. A different data set of another boron doped diamond membrane after electrochemical etching and RIE thinning is shown in Figure 4.2. This diamond membrane exhibits a higher threshold and breakdown voltage at ~±20 V with a current of ~200 μA.

For the electrical measurements, the membranes were positioned onto a titanium (~150 nm) coated silicon dioxide wafer. The top contact was titanium/gold metal that was sputtered at a base pressure of 1 x 10$^{-6}$ Torr and a 100 W forward bias, through a lithographic mask (thickness ~ 150 nm and 20 μm diameter). To contact the devices, two xyz nanomanipulators were used, one positioned on top of the membrane and the second one positioned in a close proximity to it. The voltage was generated and controlled using the Keithley 617 electrometer and the current passing through the device was measured using the same tool. The data was recorded using custom-built software. All the measurements were done at room temperature.

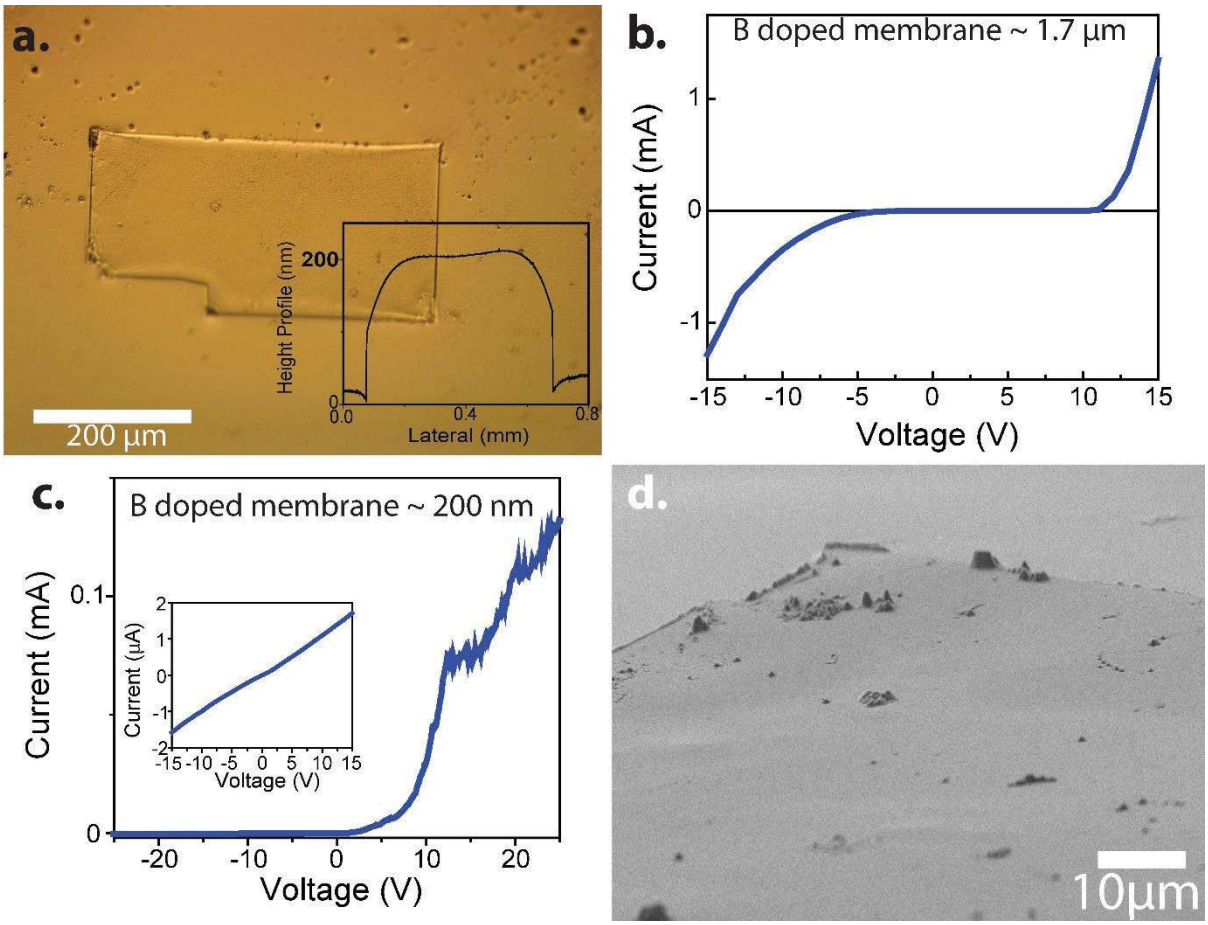


**Figure 4.1.** Boron-doped diamond membranes. (a) Optical image of a thin boron doped diamond membrane. Inset: height profile that confirms the membrane is ~ 200 nm thick. (b) An I-V curve of the lifted off boron doped membrane (~1.7 µm) exhibits a threshold of ~ 10 V. (c) An I-V curve of a 200 nm thick, boron doped membrane exhibits an on-set threshold of ~ 8 V. Both I-V curves show semiconducting behaviour. Inset: IV curve of an undoped diamond membrane showing insulating behaviour with negligible µA currents. (d) SEM image of the diamond membrane.

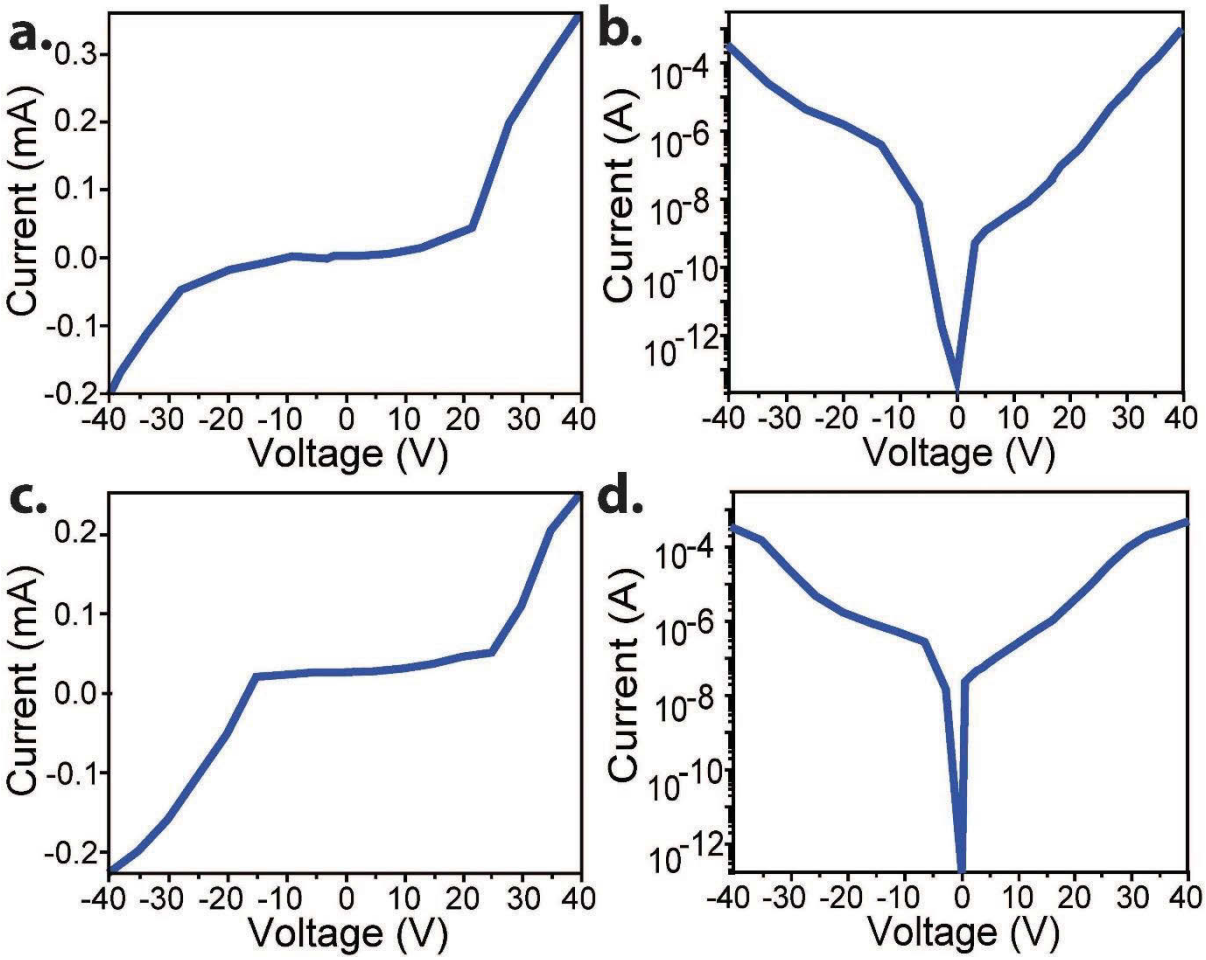


**Figure 4.2.** Electrical measurements of a (a) 1.7 μm boron doped diamond membrane after electrochemical etching, showing a threshold voltage at ~20 V and a breakdown voltage of ~30 V with a current of 0.3 mA. (b) Log (I) vs (V) rectification curve of the boron doped diamond membrane showing a rectification ratio of ~9. (c) An I-V curve of the thinned (~300 nm) boron doped membrane, showing a similar on-set and breakdown voltage along with its (d) Log (I) vs (V) rectification curve with a ratio of ~6.

### 4.2.1 Fabrication of vertical nanoscale p–n junctions

The availability of p-type membranes enables the exploration of p-n junction engineering using the single crystal diamond membranes. To realise the p-n junctions, I employed a modified fabrication protocol in which a 200 nm n-type layer was grown epitaxially using MPCVD on top of $He^+$ ion implanted boron doped single crystal bulk diamond, before the electrochemical etching. For the n-type layer, Phosphine ($PH_3$) diluted with $H_2$ was used for phosphorus doping at a ratio ($PH_3/CH_4$) of 5% and the final doping is $\sim 8 \times 10^{18}$ $cm^{-3}$ of phosphorus atoms. The sample then underwent electrochemical etching to dissociate the p–n diamond membrane that

is ~1.9 μm thick. The p-layer was thinned by ICP-RIE to achieve a total membrane thickness of ~300 nm, as described previously.

### 4.2.2 Characterisation of vertical nanoscale p–n junctions

The overgrown n-type layer was verified using a secondary ion mass spectrometry (SIMS) measurement, to quantify the phosphorus concentration (Figure 4.3). The measurement was done on an epitaxial layer that was grown under identical conditions for a longer time. The doping concentration was determined to be $\sim 1 \times 10^{18}$ atoms/cm$^2$ (blue curve). The red curve represents the detection limit of the boron atoms.

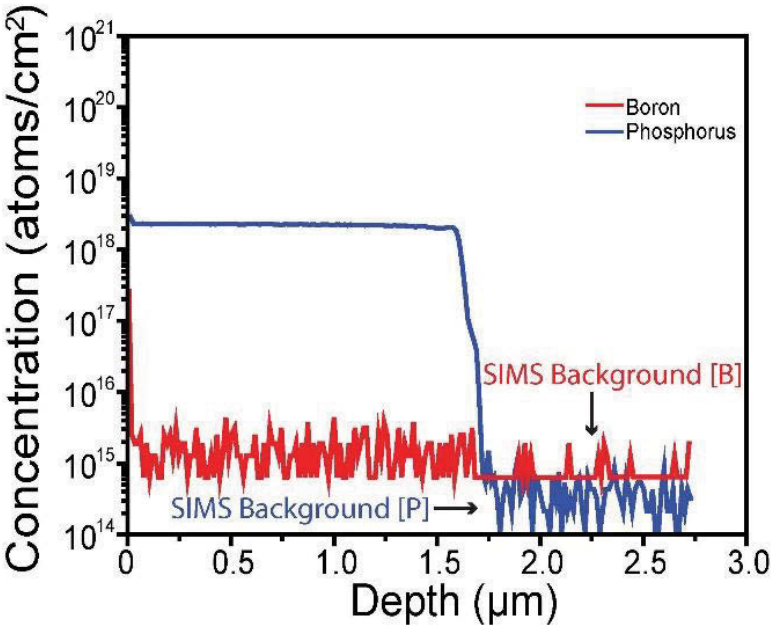


**Figure 4.3.** SIMS analysis from a bulk element 6 doped diamond. Secondary ion mass spectrometry measurement of CVD grown phosphorus doped diamond. Hydrogen, nitrogen, and boron exhibit background noise while Phosphor shows a doping concentration of ~$10^{18}$ atoms/cm$^2$ (blue curve) while the boron shows background noise (red curve.)

The experimental conditions allow a slow growth that achieves uniform n-type doping across the sample. The overgrown diamond was then processed as described previously to produce a single crystal membrane with a total thickness of ~1.9 μm that is a vertical p-n junction (see Figure 4.4(a-b)). An optical image of the membrane is shown in the inset of Figure 4.4(b). It

exhibits diode-like behaviour with a forward threshold voltage of ~ 10 V with ~ mA (~ 3A/cm$^2$) current, and a negligible current (~1×10$^{-7}$ A/cm$^2$) under a reverse bias of > 40V (Figure 4.4c). This leads to an extremely high rectification ratio of ~ 10$^4$ (Figure 4.5) which is ideal for diode fabrication[224], [225]. This value is comparable to bulk diamond devices [22].

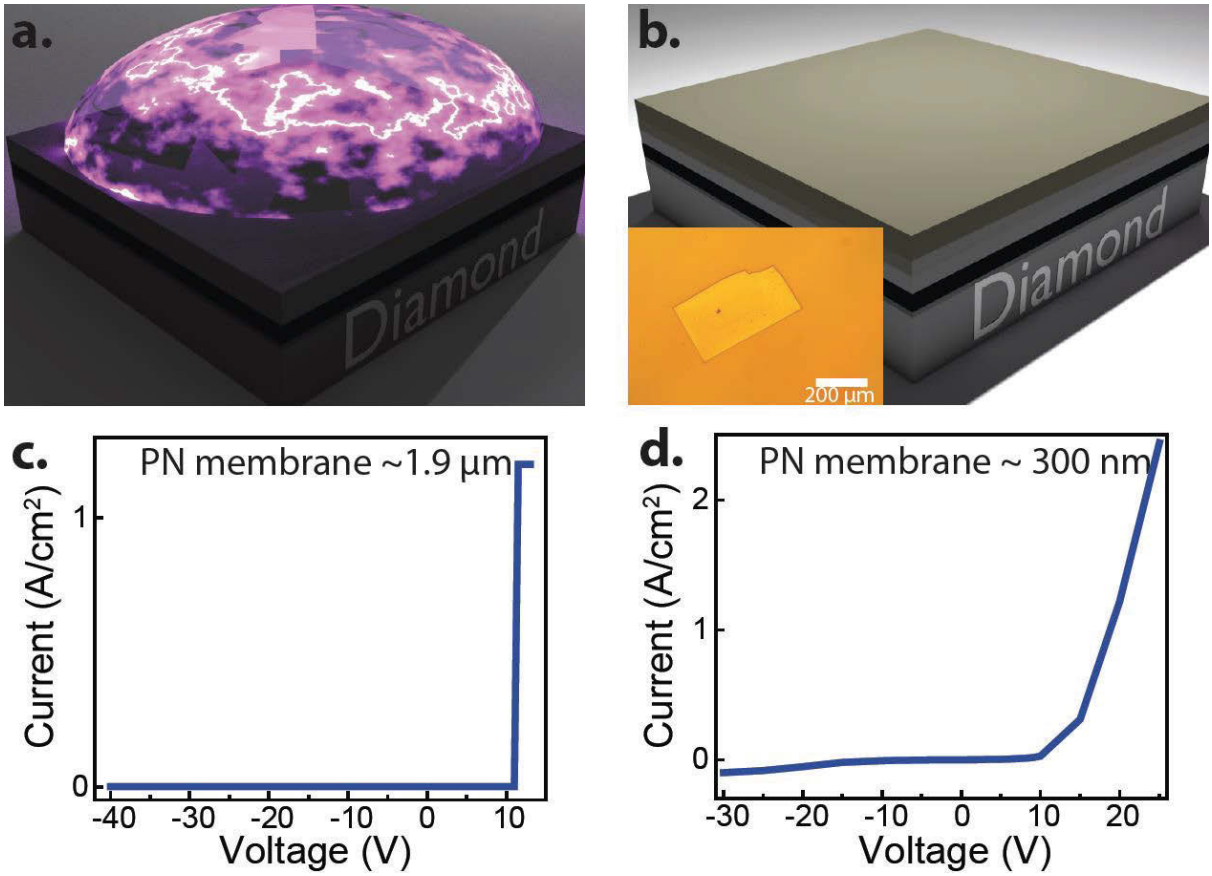


**Figure 4.4.** Engineering of vertical p-n junctions. (a-b) Schematic of the process used to produce single crystal p-n diamond membranes. (a, b) Bulk boron doped diamond that was implanted with He ions to create a graphitic channel is overgrown with diamond to create a phosphorus doped n-type layer represented by the dark green colour in (b). Inset, the lifted-off entire p-n diamond membranes. (c) Electrical measurements of the lifted off, 1.9 µm thick PN membrane showing diode behaviour at ~10 V and (d) an I-V curve of the thinned (~300 nm) p-n membrane, showing a similar on-set voltage.

Upon subsequent thinning of the membrane to ~ 300 nm by RIE (yielding a p-type layer of ~ 100 nm and an n-type layer of ~200 nm), p-n membrane still behaves as a diode with a forward voltage of ~ 8 V with ~ mA (~ 2 A/cm$^2$) current, and negligible current (~2x10$^{-7}$ A/cm$^2$) under

reverse bias (Figure 4.4d). The rectification ratio of the thin membrane is lower, ~ 30, and may be caused by roughening during the RIE process or by heterogeneous boron doping near the p-n interface. Another p-n membrane showed very similar results (Table 4-1) with a rectification ratio of ~10000 and ~20 after electrochemical etching and RIE, respectively (Figure 4.5c, d). To the best of my knowledge, this is the first report of a vertical nanoscale p-n junction engineered within single crystal diamond and is highly promising for nano-electronic applications. Figure 4.5 shows rectification curves from another set of lifted-off and thinned p-n membranes. The lifted off p-n diamond membranes show rectifications ratios ~$10^4$. Unfortunately, upon thinning the p-n membranes show a similar trend as the previously mentioned same, with rectification ratios of ~30 and 20.

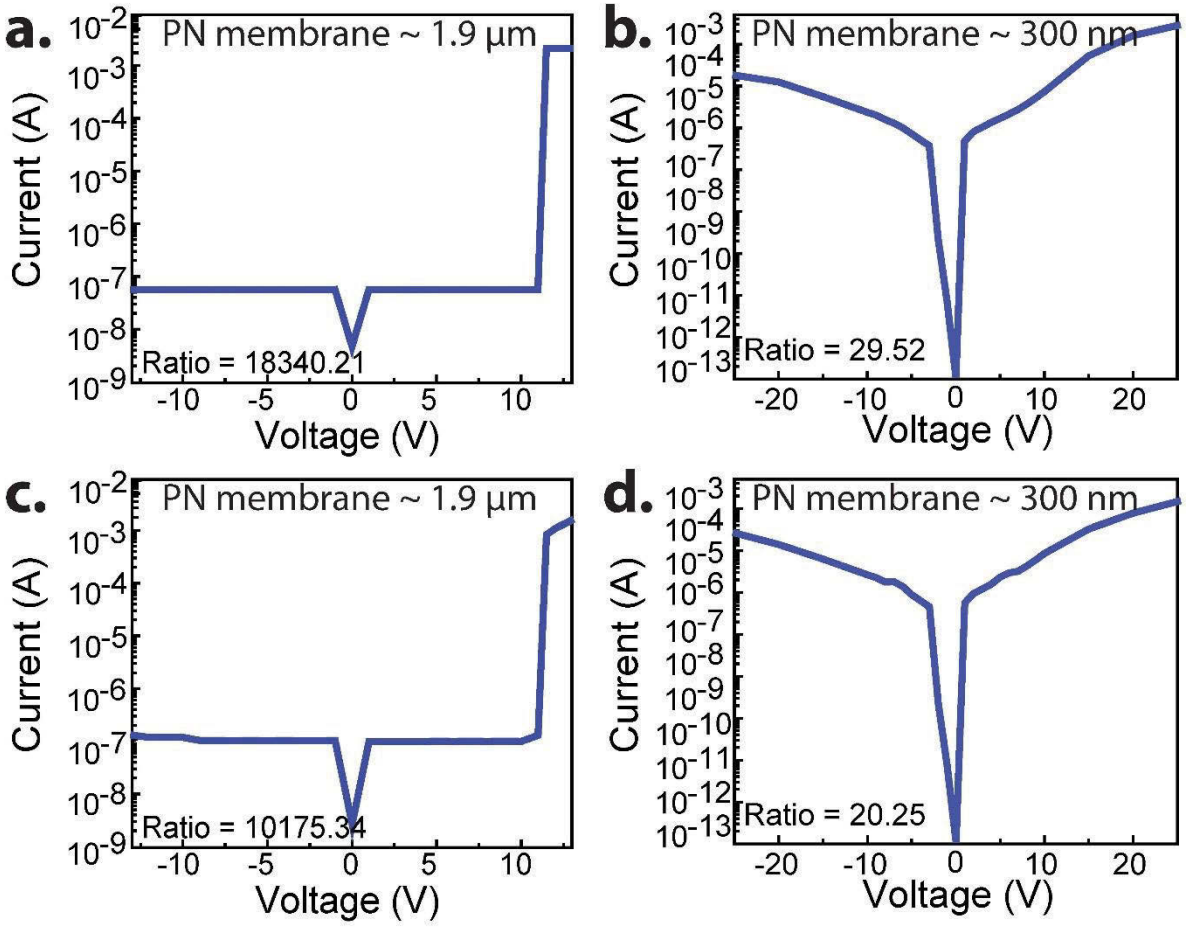


**Figure 4.5**. Log (I) vs (V) rectification curves of (a) 1.9 µm p-n diamond membrane after electrochemical etching, showing a high rectification of ~18300 and (b) a thinned ~ 300 nm p-n membrane showing a rectification ratio of ~30. The ratio was determined by dividing the value at which the current plateaus at an identical forward and reverse bias. (c, d) Another set

of rectification curves from the same 1.9 µm and 300 nm p-n diamond membrane showing rectification ratios of 10100 and 20, respectively.

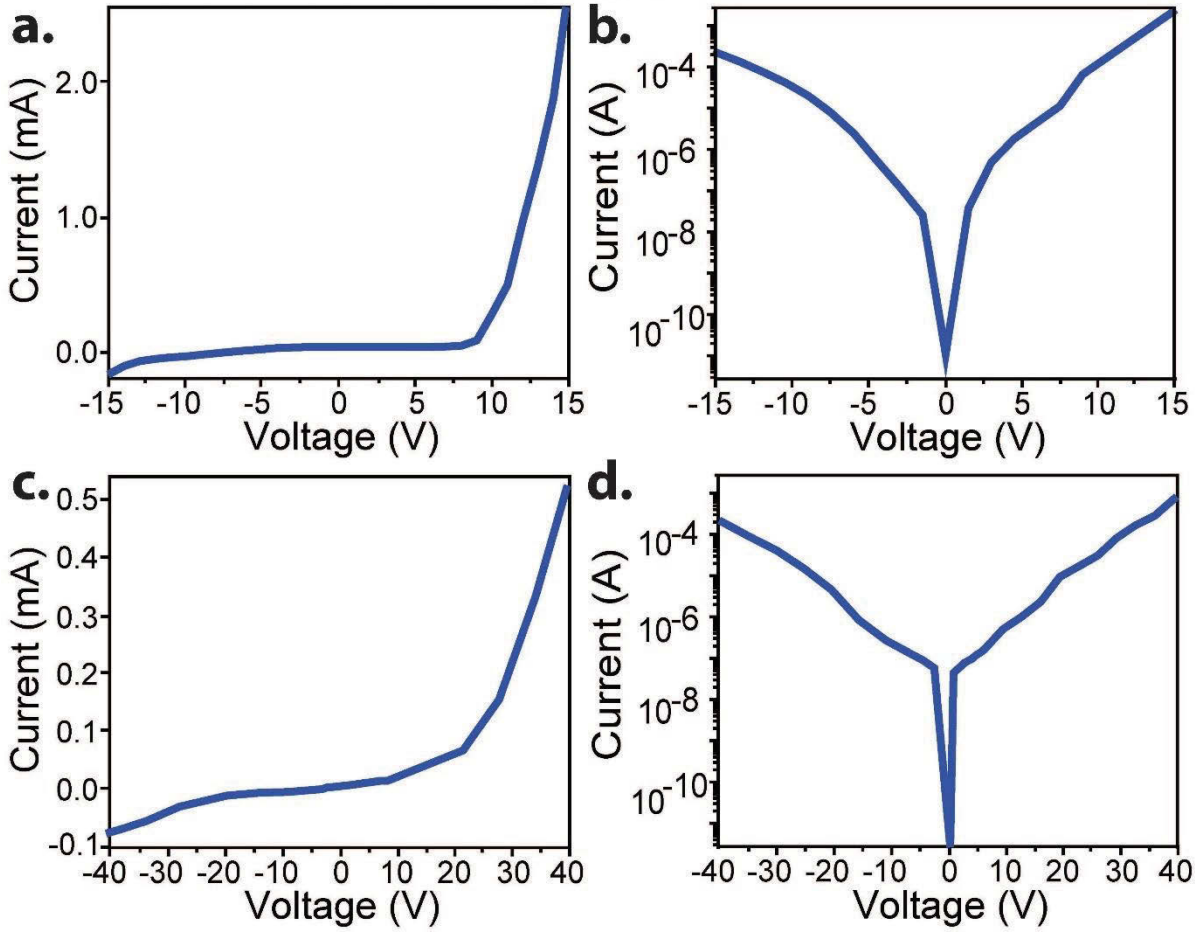


**Figure 4.6.** Electrical measurements of a (a) 1.9 µm p-n diamond membrane after electrochemical etching, showing a threshold voltage at ~8 V and a breakdown voltage of ~10 V with a current of 2 mA. (b) Log (I) vs (V) rectification curve of the p-n diamond membrane showing a rectification ratio of ~25. (c) An I-V curve of the thinned (~300 nm) p-n diamond membrane, showing a threshold voltage of ~ 9 V along with its (d) Log (I) vs (V) rectification curve with a ratio of ~12.

More electrical measurements of the 1.9 µm and ~300 nm p-n diamond membrane are shown in Figure 4.6 and Figure 4.5. The thick p-n diamond membrane shows semiconductor behaviour with a threshold voltage of ~8 V with mA current with a low rectification ratio of ~25 (Figure 4.6a, b). Upon subsequent thinning to 300 nm both the I-V and rectification curve improved slightly, showing a threshold voltage of ~9 V with a breakdown voltage of -30 V and

a rectification ratio of ~12. The low breakdown voltage may be due to non-uniform boron and phosphorous doping, as well as a rough surface. The low current may also be related to a poor contact.

To determine the thickness of the depletion region, ω, of the p-n diamond junction, the following equation was employed,

$$\boldsymbol{\omega = \sqrt{\frac{2\varepsilon_s}{q}\left(\frac{1}{N_A}+\frac{1}{N_D}\right)(\phi_i - V_a)}} \qquad \textbf{Equation 4.1}$$

where $\varepsilon_s$ is the permittivity, $q$ is the electron charge, $N_A$ and $N_B$ are the acceptor ([B] ~$3\times10^{20}$/cm$^3$) and donor ([P] ~$8\text{x}10^{18}$/cm$^3$) concentrations, respectively, $\phi_i$ is the built-in potential (~ 5.5 V) of the device and $V_a$ is the applied voltage (calculation is done for $V_a$ = 0 at equilibrium). Under the experimental conditions, a depletion layer of ~ 21 nm exists. The short depletion layer indicates that only a minimal voltage is needed to overcome this barrier potential and allow for recombination of electrons and holes flowing from the n- and p+ layers respectively and is important for practical devices. Furthermore, the p-n single crystal diamond membrane devices show a maximum electric field,

$$\boldsymbol{\mathcal{E} = \frac{2(\phi_a - V_i)}{w}} \qquad \textbf{Equation 4.2}$$

of ~ 500 MV/m. While this field is not as high as millimetre scale bulk diamond, it is still an order of magnitude greater than silicon (300 kV/m) which is ordinarily used as the base material for nanoelectronic devices. A higher electric field allows the diamond membranes to withstand higher voltages (up to ~ 100 V for a 500 nm vertical device) and stresses before the device electrically breaks down and the material becomes conductive. Overall, the short depletion layer and the high breakdown field make these nanoscale single crystal diamond membranes extremely attractive for real nanoelectronic devices.

### 4.2.3 Characterisation of vertical p–i–ITO junctions

Additionally, there have been a number of groups that have made bulk diamond hybrid devices using doped diamond substrates and transparent n-doped materials [20]. The silicon doping in the intrinsic layer occurs naturally with the silicon source from the substrate incorporates into the membrane. An optical image of the overgrown membrane containing SiV colour centres is

shown in Figure 4.7a and the schematic of the membrane device is shown in Figure 4.7b, confirming the presence of strong SiV luminescence centred at 737 nm. The overall thickness of the SiV containing membrane is ~ 300 nm. To study the electrical properties of these membranes, the p-i membrane was subsequently transferred onto a titanium coated silicon and sputtered with ~100 nm of n-doped indium titanium oxide (ITO) through a defined photolithographic mask. This created the final p-i (Diamond) – n-type (ITO) junction. Figure 4.7c shows the I-V characteristics, with diode-like behaviour and a threshold voltage of ~ 10 V. A semi log IV curve of the hybrid device shows a rectification ratio of $3\times10^3$ (Figure 4.7d). Such hybrid devices can be interesting to explore in conjunction with other semiconductors such as Zinc Oxide (ZnO), which exhibits excellent n-type characteristics for creating of efficient LEDs and heterojunctions.

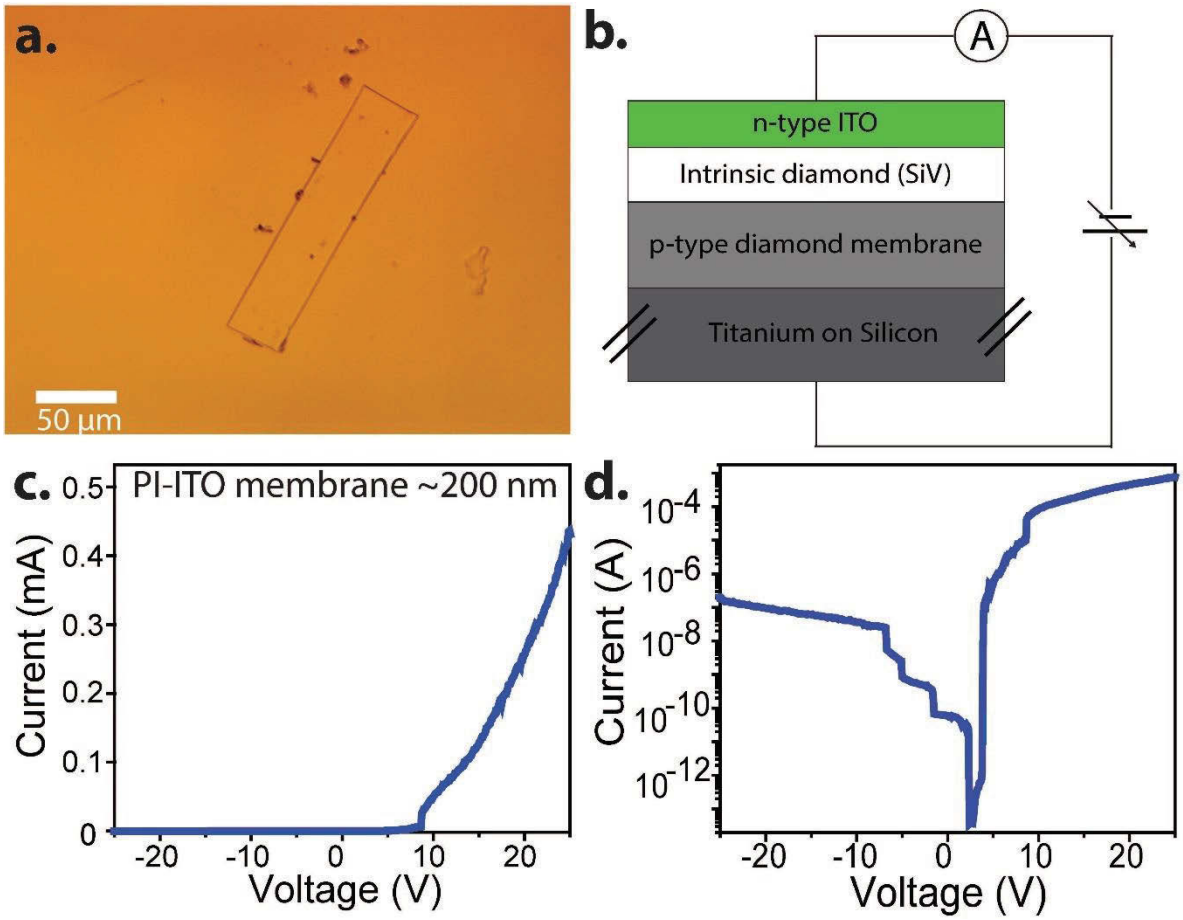


**Figure 4.7.** (a) An optical image of the overgrown membrane (200 nm p-type base with 100 nm of intrinsic layer with SiV centres). (b) Schematic diagram of the hybrid diamond/ITO device. (c) The p-i-ITO membrane is semiconducting with an on-set voltage of ~ 10V. (d) Log

(I) vs (V) rectification curves of a p-i-ITO diamond membrane showing a rectification ratio of ~3000.

For comparison to other diamond devices, a hybrid p-i-n device was fabricated in bulk diamond. The bulk diamond crystal was doped with $\sim 3 \times 10^{20}$ boron atoms/cm$^3$ during MPCVD growth. An intrinsic layer was overgrown in the presence of a silicon source to introduce a uniform ~100 nm layer of SiV colour centres. The diamond crystal was then sputtered with ~100 nm of n-doped ITO through a defined photolithographic mask. This creates the final bulk diamond p-i– n-type (ITO) junction (Figure 4.8a). Figure 4.8b shows the I-V characteristics, with diode-like behaviour and a threshold voltage of ~ 9 V. A semi log IV curve of the hybrid device shows a rectification ratio of ~560. The fabricated hybrid device is comparable to other bulk diamond devices in the literature [21], where it exhibits a higher current but a lower rectification ratio which may be due to a non-high quality diamond surface or inhomogeneous boron doping. Furthermore, it may be due to poor adhesion of the interface layer between the diamond sample and sputtered ITO contact or defects in either layer. This would cause current to flow through the defects and not the colour centres in the intrinsic layer.

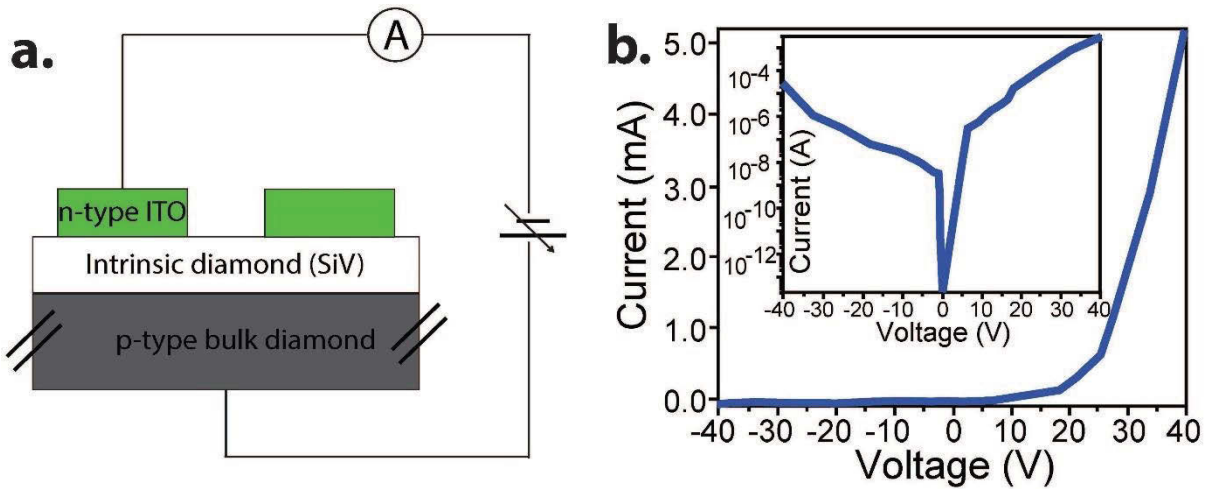


**Figure 4.8.** Electrical measurements of a bulk boron doped diamond. (a) A schematic diagram of the bulk boron doped diamond with an intrinsic layer of SiVs and a sputtered layer of n-type ITO. (b) The p-i-ITO diamond is semiconducting with an on-set voltage of ~ 9V. Inset: Log (I) vs (V) rectification curve of the p-i-ITO bulk diamond showing a rectification ratio of ~560.

### 4.2.4 Characterisation of vertical p–i–n junctions

There exists great potential for the use of diamond membranes within optoelectronic and nanophotonic applications. To realise a working diode device, I fabricated a p-i-n structure into a single crystal diamond membrane containing a uniform layer of SiV colour centres (Figure 4.9). The SiVs colour centres were chosen intentionally, as they are emerging fluorescent defects in diamond that hold great potential for quantum photonic applications[18], [112]. To realise this structure, a $He^+$ ion implanted boron doped single crystal diamond was overgrown in the presence of a silicon source to introduce a 100 nm layer of SiV colour centres (into the intrinsic layer). This growth was performed using a MPCVD chamber with a hydrogen/methane ratio of 100:1 at 60 Torr, a microwave power of 900W for 8 minutes. A 200 nm n-type diamond (~ $8\times10^{18}$ $cm^{-3}$ phosphorous) was subsequently epitaxially overgrown and the sample then underwent electrochemical etching to dissociate the p-i-n diamond membrane as described previously. It should be noted that neither the intrinsic layer nor the n-layer is exposed to the ion damage.

An optical image of the stand-alone p-i-n single crystal membrane device is shown in Figure 4.9a and the schematic illustration of the structure and the device are shown in Figure 4.9b. A schematic energy band diagram is shown in the Figure 4.10. The formed single crystal diamond membrane device displays excellent electrical characteristics, as shown in Figure 4.9c. The diamond membranes exhibit diode-like behaviour with a threshold voltage at ~11 V and negligible current under a reverse bias of > 20V. This was confirmed by the semi-log I-V curve with a high rectification ratio of ~ $10^6$ (Figure 4.9dc). The low threshold voltage is advantageous for efficient device operation and is comparable to many standard nano-optoelectronic devices made of GaN, SiC and ZnO [186], [226], [227]. It is possible that the phosphorous doping of the overgrown n-type diamond layer, may be causing issues with the efficient recombination of species and as an extension won't show electroluminescence of our SiV emitters in the intrinsic layer of the diamond membrane diode. The CVD recipe for uniform n-type growth may be tweaked by manipulating several growth parameters which may lead to a more homogenous doping and/or a higher doping of n-type species to allow for recombination to occur. By modifying the gas rate ratios and gas flow of the phosphorous gas. This will modify the incorporation rate of n-doped species and therefore the doping density of the n-doped layer which may lead to an enhancement of the diamonds electrical properties. It will be a very time-consuming process and can't currently be conducted in-house.

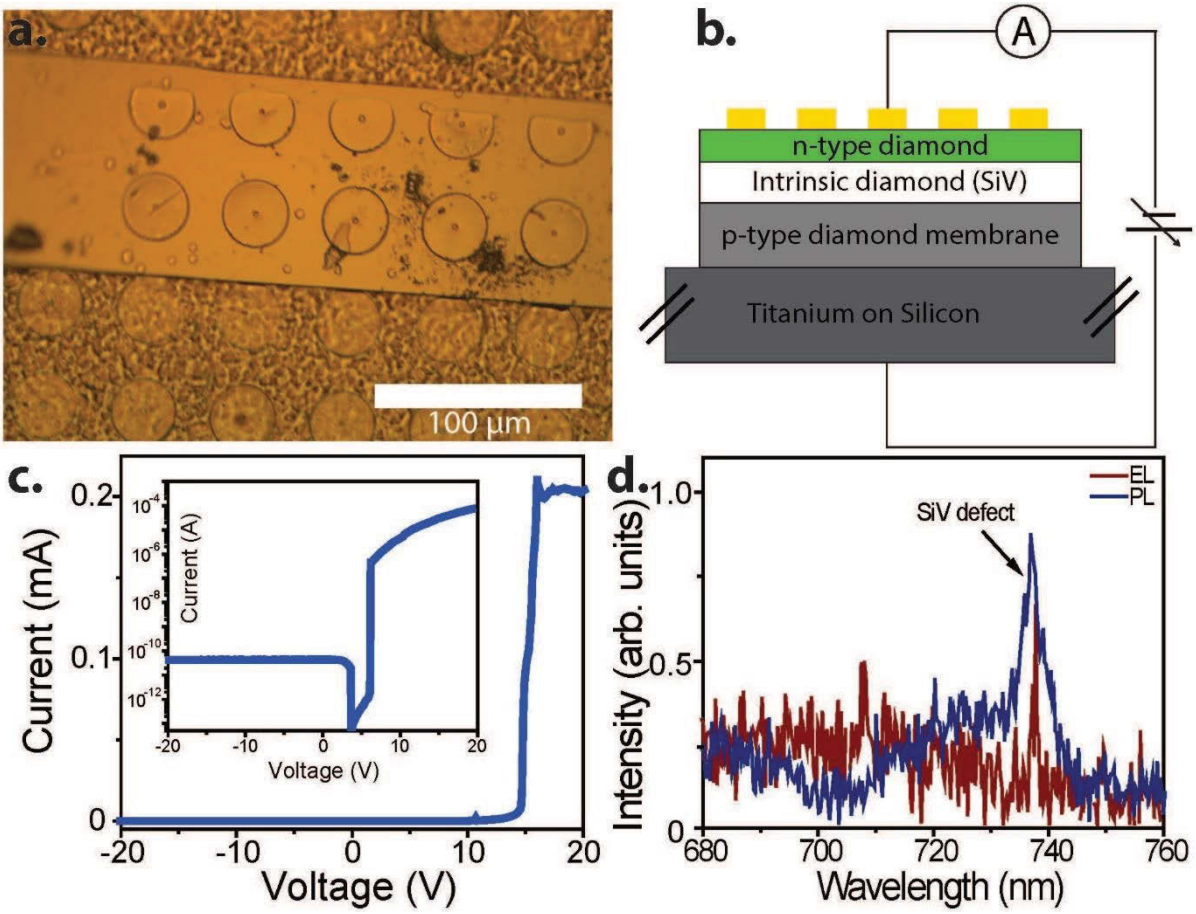


**Figure 4.9.** Vertical standalone single crystal diamond p-i-n device. (a) An optical image of the p-i-n membrane containing a layer of SiV emitters in the intrinsic region. The circles are the metal contacts on the top n-type surface. (b) Schematic diagram of the cross section of the p-i-n diamond device. (c) The p-i-n membrane shows diode-like behaviour with an onset voltage of ~ 11V. Inset: Log (I) vs (V) rectification curve of the p-i-n diamond membrane showing a rectification ratio of ~ $10^6$.

A band diagram of a typical all diamond p-i-n junctions is presented below (Figure 4.10). $W_{Ti}$ corresponds to the work function of titanium, $E_F$ and $E_{EF}$ are the Fermi and effective Fermi level after doping, respectively. $V_O$ is the step-in energy between the bands of the p and n doped diamond regions. The boron and phosphorous energy levels were taken as 0.36 and 0.57 eV, respectively. $E_{FIP}$ and $E_{FIN}$ are the effective Fermi energies for the p-doped and n-doped diamond layers.

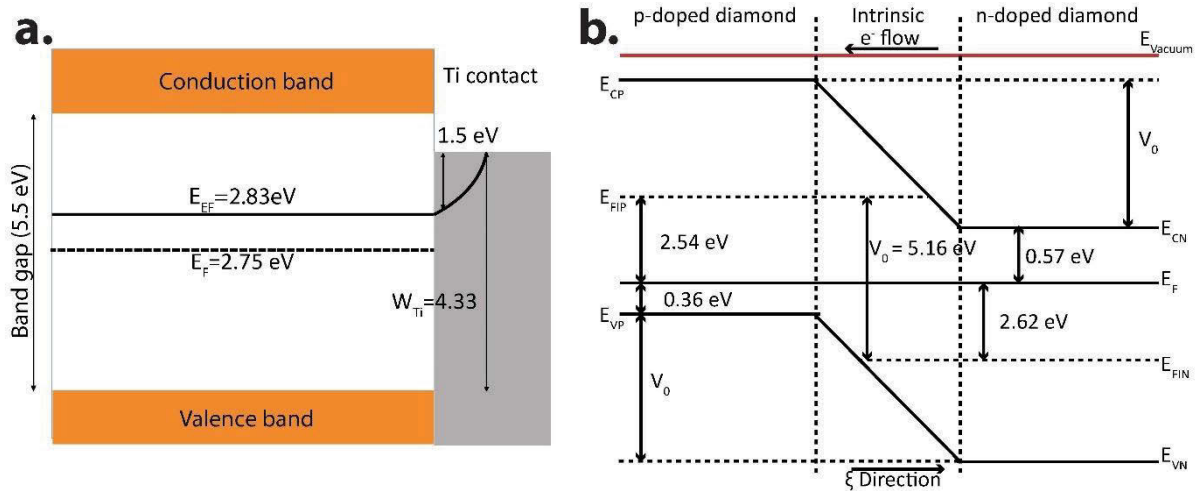


**Figure 4.10.** Band diagram of the p-i-n diamond device. (a) Diagram illustrating when the Titanium comes into contact with the n-layer of the diamond membrane. $E_{EF}$ is the effective fermi level, $E_F$ is the fermi level and $W_{Ti}$ is the work function of titanium. (b) Schematic energy band diagram of the p-i-n diamond membrane at equilibrium. The boron and phosphorous energy levels were taken as 0.36 and 0.57 eV respectively.

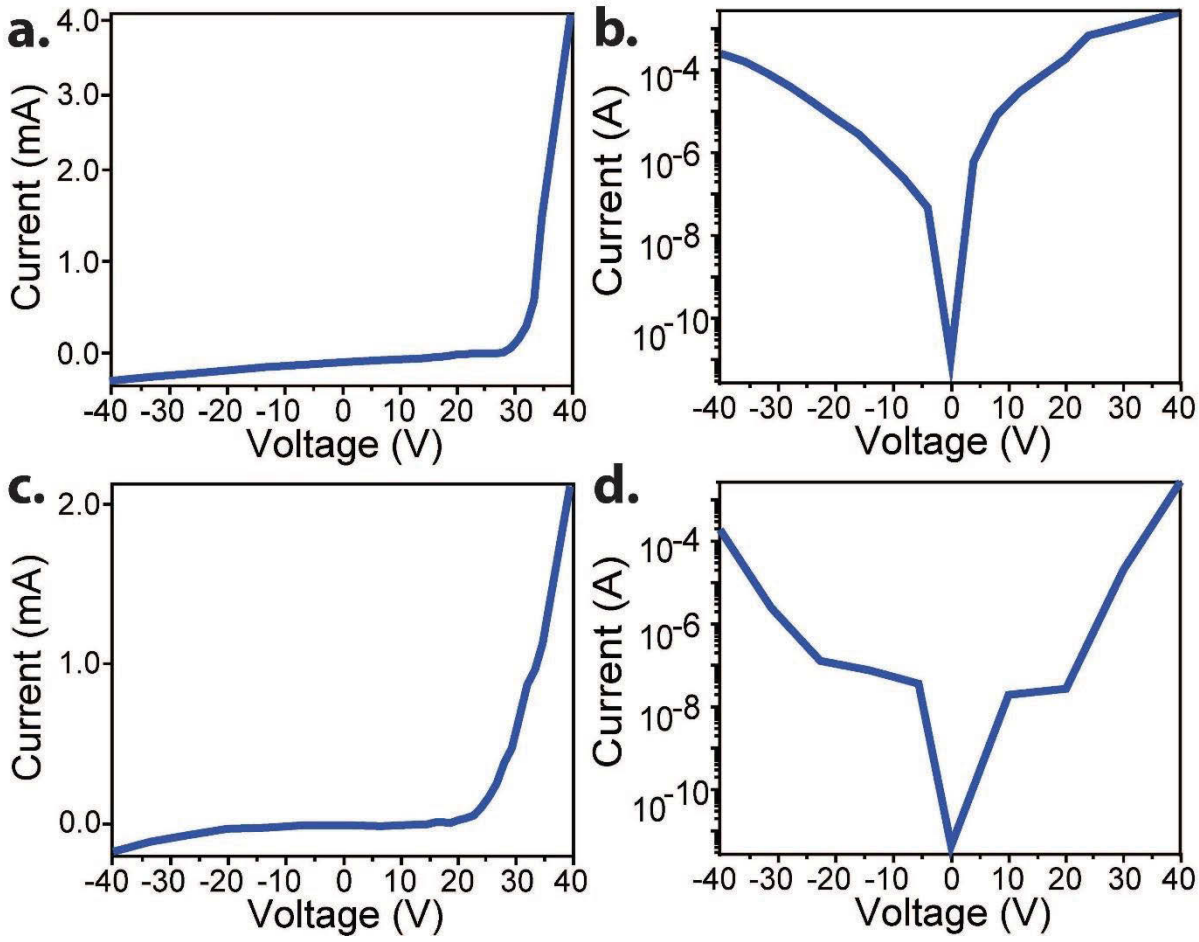


**Figure 4.11.** Electrical measurements of a 2µm thick p-i-n membrane showing semiconducting behaviour with (a) an on-set voltage of ~ 30V. (b) Log (I) vs (V) rectification curves of a p-i-n diamond membrane showing a rectification ratio of ~26. (c) The p-i-n diamond membrane after thinning to ~300 nm, showing an on-set voltage of ~26V and (d) a rectification ratio of ~23.

Not all of the p-i-n diamond devices exhibited exceptional electrical properties. Figure 4.11 shows the electrical measurements of another p-i-n diamond membrane after electrochemical etching and RIE thinning down to ~300 nm. The diamond membranes exhibit semiconductor behaviour with a threshold voltage at ~30 V with a current on the order of mA. Unfortunately, it possesses a high current under reverse bias with a breakdown voltage of ~ -10 V. This is shown in the semi-log I-V curve with a low rectification of ~26 (Figure 4.11b). Upon subsequent thinning down to ~300 nm the I-V curve improved with an onset voltage of ~26 V and a breakdown voltage of ~30 V with mA current. The rectification ratio is still very poor with a ratio of ~23. This may be due to surface roughening through the use of the RIE reactor

and possible non-uniform doping of the p and n doped regions. It may also be caused by the charge mobility across the p-i-n junction due to the low conductivity of phosphorus doped diamond. Phosphorous doped diamond films only have a carrier mobility of ~660 $cm^2$ $V^{-1}$ $s^{-1}$ which is approximately three time slower than boron doped diamond films at ~1800 $cm^2$ $V^{-1}$ $s^{-1}$ [228], [229]. The data from the p-doped, p-n, p-i-ITO and p-i-n devices are summarised in Table 4-1

**Table 4-1.** A summary of the electrical properties of the fabricated diamond membranes in this thesis.

| Material | Threshold voltage (V) | Current (mA) | Rectification ratio | Breakdown voltage (V) | Number of devices |
|---|---|---|---|---|---|
| **Thick p-doped** | ~11 – 20 | ~0.3 – 1.3 | ~9 – 15 | ~5 – 15 | 6 |
| **Thin p-doped** | ~8 – 20 | 0.2 – 0.3 | ~6 – 180 | ~12 – 20 | 6 |
| **Thick p-n** | ~9 – 12 | ~1.0 – 3.0 | ~30 – $10^4$ | 40 | 20 |
| **Thin p-n** | ~8 – 10 | 0.8 – 2.5 | 12 – 35 | 20 | 20 |
| **p-i-ITO** | 9 – 11 | 0.4 – 0.6 | $1\times10^3$ – $3\times10^3$ | 20 – 25 | 30 |
| **p-i-n** | 10 - 30 | 0.3 – 4.0 | ~25 – $10^6$ | 20 | 25 |

The fabricated p-i-n diamond membranes possess an average threshold voltage of ~10 V with a forward bias current of ~4 mA. The current under reverse bias is negligible under a voltage > 40 V. The devices boast a high rectification ratio of $1 \times 10^6$. These properties make them ideal for electrical applications and are comparable to other semiconductor p-i-n diode structures in the literature. For instance, p-i-n ZnO structure has been studied for decades boasting a threshold voltage of ~3.2 V with a forward bias current of up to 80 mA. The device exhibits high breakdown voltages of up to 30 V with negligible current on the order of $1 \times 10^{-7}$A, which leads to high rectification ratios of $8 \times 10^5$ [227]. Furthermore, by embedding InGaN QDs into the intrinsic layer of GaN p-i-n diode, diode-like behaviour has been demonstrated with onset voltages of ~3.5V and a current density up to ~100 mA with breakdown voltages and leakage current of between 4 – 20V and $1 \times 10^{-12}$A, respectively, leading to a rectification ratio of ~2000 [177], [186]. SiC is another readily studied wide band gap material and exhibits a threshold voltage of ~3.1 V with currents in the range of mA. The

diode structures show a very small reverse leakage current of $\sim 1 \times 10^{-10}$A, which leads to very high rectification ratios of $140 \times 10^{6}$ [180], [181], [226]. The fabricated diamond membranes boast higher rectification ratios and similar leakage current, making them an ideal substitute to ZnO and GaN diode devices. The forward bias current of the diamond membranes is lower than the ZnO and GaN devices. The lower current is due to power transport of carries between the n-doped and p-doped region. To improve the transport of carriers through the device the more sophisticated fabrication protocols need to be developed to create a higher quality n-doped single crystal layer and more conductive metal contacts to allow high current densities to flow into the device.

Furthermore, diodes have been engineered out of layered 2D chalcogenide materials such as $MoS_2$ that possesses a lower forward voltage of ~ 0.5 V with 0. 35 - 1 μA current under a positive bias. They also have an unfavourably low breakdown voltage ~1.5 - 10 V with a leakage current of $\sim 5 \times 10^{-8} - 5 \times 10^{-9}$ A [183], [184]. $MoS_2$ is known to have poor optical quality than other group-VIB transition-metal dichalcogenides (TMDs), possibly due to impurities. In contrast, it has been shown previously that monolayer $WSe_2$ has better optical properties compared to other group-VIB TMDs [230], [231]. $WSe_2$ has been shown to possess a threshold voltage of 6.5 V with a current of ~7 nA. The breakdown voltage for this device was not explicitly shown but is >2V [179].

Diode fabrication is not limited to bulk and monolayer materials, it has also been demonstrated for single molecules. For example, single tris(1-phenylisoquinoline)iridium $(Ir(piq)_3)$ molecules [232] were used as emitters inside wide bandgap PMMA and poly(9-vinylcarbazole):2-(4-tert-butylphenyl)-5-(4-biphenylyl)-1,3,4-oxadiazole (PVK:PBD) polymers. Iridium-based emitters are known for their short triplet-state lifetimes compared with other organometallic complexes [233], [234]. These embedded single molecules exhibit a lower forward threshold voltage of ~5 V and a high current of ~100 mA. These types of devices do not possess the same variability as the fabricated diamond membranes, in the sense that they cannot be further processed to create resonators or waveguides as well as they cannot be easily transferred to different substrates or other desired structures.

The fabricated diamond membranes are also comparable to other diamond diode devices that have been fabricated out of polycrystalline and single crystalline diamond. For instance, polycrystalline diamond was grown onto a lightly phosphorous doped silicon substrate using MPCVD then a layer of ITO was magneton sputtered. The device displays a low threshold

voltage of ~1.5 V with a forward bias current of ~60 mA. The diode device exhibits a small breakdown voltage and large current of ~2.5 V and ~8 mA, respectively. This leads to a low rectification ratio of ~10 [20]. Alternatively, bulk single crystal diamond p-i-n structures have been engineered through MPCVD growth of a bulk boron doped diamond crystal with an independently grown intrinsic layer containing either NV or SiV colour centres and a phosphorus doped n-type layer. The bulk diamond diodes show a forward threshold voltage of ~30 – 40 V with 3 – 12 mA current and a breakdown voltage and leakage current of ~43 V and $1 \times 10^{-7}$ A, respectively. This leads to very high rectification ratios of up to $1 \times 10^{9}$ [21], [22]. The data is summarised in Table 4-2 Diamond membranes are the next step in the development of diamond nanoelectronics since they possess similar electrical characteristics to their bulk counterparts and have a high-quality diamond surface. This will allow the realisation of membranes for quantum communication, quantum information processes and on-chip applications.

**Table 4-2.** A summary of the electrical properties of varying diode structures in the literature, compared to the fabricated diamond membranes.

| Material | Threshold voltage (V) | Current (mA) | Rectification ratio | Breakdown voltage (V) | Ref. |
|---|---|---|---|---|---|
| **ZnO** | ~3.2 | 80 | 800000 | 30 | [227] |
| **SiC** | ~3.1 | ~14 | $140 \times 10^6$ | $> 0$ | [226] |
| **GaN** | ~3.5 | ~100 | ~2000 | $> 4 - \sim 20$ | [177], [186] |
| **$MoS_2$** | ~0.5 | $\sim 0.35 \times 10^{-3} - \sim 1 \times 10^{-3}$ | 7 - 1000 | ~1.5 - 10 | [183], [184] |
| **Single molecule** | ~5 | ~100 | n/a | $> 0$ | [234] |
| **$WSe_2$** | 6.5 | $\sim 7 \times 10^{-6}$ | n/a | $> 2$ | [179] |
| **Polycrystalline diamond** | ~1.5 | ~60 | ~10 | ~2.5 | [20] |
| **Bulk diamond** | $\sim 30 - 40$ | $\sim 3 - 12$ | $1 \times 10^4$ $-1 \times 10^9$ | ~43 | [21], [22] |
| **Diamond membranes** | ~10V | ~4 mA | $1 \times 10^6$ | $> 40$ | [160] |

To conclude, I show the first reliable and robust engineering of nanoscale conductive diamond membranes. Moreover, I engineered the first-of-its-kind vertical p-n and p-i-n nanoscale devices using entirely single crystal diamond. The membranes and the devices have high aspect ratio of lateral to vertical dimensions, are standalone and can be positioned onto a substrate of choice. The diamond membrane devices are therefore suitable for a variety of nanophotonic, nanoelectronics and quantum information applications. Their suitability will be shown and discussed in the following chapter, demonstrating EL from nanoscale diamond membrane diodes.

# Chapter 5 Diamond electroluminescence

Building on the work described in Chapter 4, I utilise the fabricated p-n and p-i-n structures for not only electrical but also for optoelectronic applications to create the first nanoscale single crystal diamond diode hosting optically active SiV emitters.

Beyond nanoelectronics, I foresee the great potential of the single crystal diamond membranes diodes for optoelectronic and nanophotonic applications. Single photon sources that show quantized states have a broad range of uses from quantum communication, computation, and metrology. Here I show the realisation of a high-aspect ratio, several hundred nanometres thick, room temperature, electrically driven of the stable $SiV^-$ colour centre in a novel diamond diode. As shown previously, these devices exhibit a low forward threshold voltage with mA current and negligible current under a reverse bias, which leads to a high rectification ratio of $\sim 10^6$. Igor Aharonovich and Kerem Bray conceived the idea. Kerem Bray and Rodolfo Previdi generated the membranes. Hiromitsu Kato, Masahiko Ogura, Toshiharu Makino and Satoshi Yamasaki (AIST, Japan) performed the n-type diamond growth. Kumaravelu Ganesan (University of Melbourne, Australia) carried out the ion implantation. Kerem Bray measured and analysed the PL and EL. Igor Aharonovich and Milos Toth supervised the work.

To demonstrate a working diamond LED, I fabricated a p-i-n structure into a single crystal diamond membrane containing SiV colour centres (section 4.2.4); that display both PL and EL (Figure 5.1). The inclusion of the SiVs into the intrinsic layer between the p- and the n-doped regions allows the recombination process to occur at the SiV centres, thus generating EL signal. Figure 5.1a shows the same p-i-n diamond diode schematic diagram for reference. Figure 5.1b shows the PL and the EL characteristics of the device, recorded at room temperature. The PL was recorded using a 532 nm laser excitation, while the EL was recorded under a forward bias with an injection current of 3 mA. Both the EL and the PL exhibit the desirable emission of the SiV colour centres at ~ 737 nm. The noisy PL signal arises from dislocations in the membrane diamond lattice material during growth. The noise is further enhanced by normalising the data to 1 and comparing it to the EL signal.

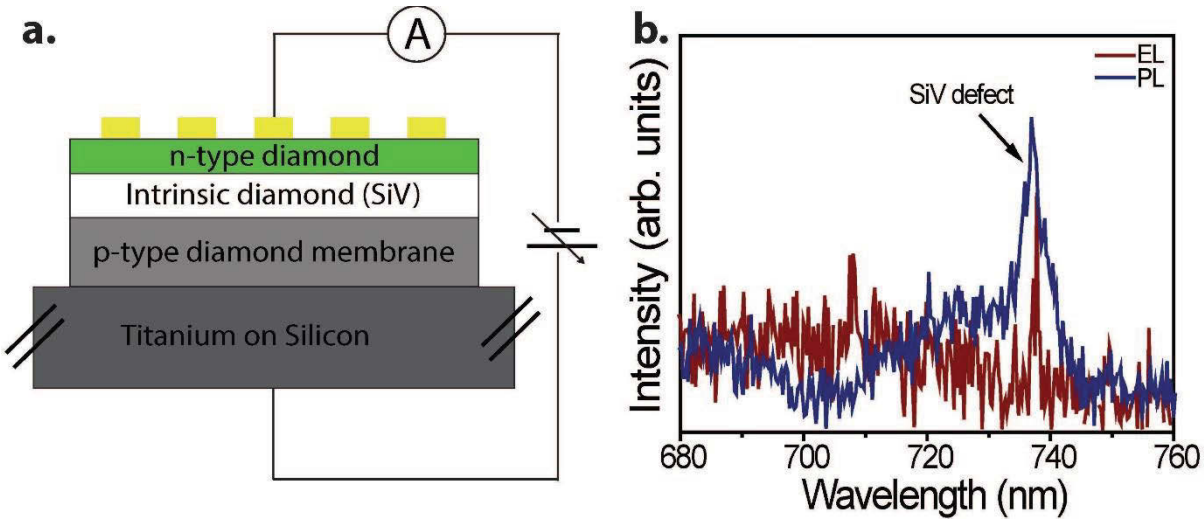


**Figure 5.1.** EL of an all diamond membrane p-i-n diode device. (a) A schematic diagram of the cross section of the p-i-n diamond device, reprinted for clarity. (b) Photoluminescence (blue) and electroluminescence (red) measurements recorded at room temperature showing a characteristic emission from the same SiV colour centre at ~737 nm.

Table 5-1 summarises the literature of diamond membranes and provides the key characteristics of size and optical activity. Notably, the membranes reported in this work are amongst the largest in terms of surface area, while still being relatively thin – on the order of ~ 300 nm thick. Furthermore, the membranes have the advantage of being free standing single crystal diamond that can be transferred and accurately positioned on a substrate of choice. The membranes engineered in the current work also host optically active defects that can be triggered both optically and electrically. In combination, all these attributes are unique and ideal for future fabrication of integrated nanophotonic, optoelectronic and optomechanical circuits using single crystal diamond membranes. Most of the works referenced in Table 5-1 claim to be using membranes. The work most similar to my work are references [204], [205] since they make use of a similar fabrication protocol. The 'no' in the EL column for references [28], [209] means that the presented referenced work did not demonstrate EL upon the characterisation of their materials.

| Length×Width (µm) | Thickness (nm) | PL | EL | Free standing | Ref |
|---|---|---|---|---|---|
| 15 x 3 | 200 | No | No | No | [235] |
| 2000 x 2000 | 3000 | No | No | No | [236] |
| 3000 x 3000 | 2000 | No | No | No | [237] |
| 400 x 400 | 1000 | Yes, (NV) | No | No* | [204], [205] |
| 1100 (diameter) | 1200 | Yes, (NV) | No | No | [238] |
| 300 x 300 | 200 | No | No | Yes | [27] |
| 4500 x 4500 | 15000 | No | No | Yes | [29] |
| 10 x 10 | 200 | Yes, (NV) | No | Yes | [239] |
| 220 x 220 | 200 | Yes (NV, SiV) | No | Yes | [28], [209] |
| 1000 x 500 | 300 | Yes, (SiV) | Yes, (SiV) | Yes | My work |

**Table 5-1.** A table summarising the performance of diamond membranes. The main parameters of size, optical activity (PL), EL and whether the membrane is free standing or attached are provided. *The membrane was attached to a large polycrystalline diamond frame

## 5.1 Improvements for electroluminescence generation

Although I have achieved EL from p-i-n diamond membrane diodes, there are several possible improvements and avenues to obtain a stronger EL signal from the p-i-n diamond membrane devices. I have investigated a variety of potential parameters that could lead to successful electrical triggering of optically active colour centres in diamond with a higher signal to noise

ratio. There are several factors that could be improved, these include reducing the dislocations and defects along the diamond surface which could create more favourable pathways for the current to flow through, reducing the non-homogeneity of SiV defects, varying the types of n-doped and metal contacts, using a pulsed voltage source, increasing the temperature or modifying the structure of the device. I have attempted to address these issues prior to electrical measurements, and the attempts are discussed in detail below.

### 5.1.1 Homogeneous growth of SiV

One of the possible issues preventing EL from being observed is due to the non-homogeneity of optically active colour centres in the diamond membrane. The non-homogeneity may cause the rate of potential recombination sites to be reduced, as it would allow electrons to pass through non-active defect sites in the membrane and recombine elsewhere. To increase the probability of electrical recombination occurring at $SiV^-$ colour centres, the diamond membranes were epitaxially overgrown using an MPCVD reactor with a silicon substrate as a source. The MPCVD reactor was modified to optimise the growing conditions, including by increasing the concentration of the hydrogen/methane plasma by increasing the pressure in the chamber, purging the lines, and pumping the system overnight after a cleaning cycle to remove unwanted species. This allows a higher purity single crystal diamond layer with a uniform layer of active SiV defects to be grown.

### 5.1.2 Smooth surface

A high quality single crystal diamond layer is necessary to prevent the loss of electrons through grain boundaries and other dislocations in the diamond lattice. However, it was observed that a few of the diamond membrane samples possessed a rough overgrown layer after MPCVD epitaxial overgrowth. The dislocations in the diamond surface are possibly due to MPCVD growth on the damaged side of the diamond membrane, *i.e.* where the graphitic layer formed after $He^+$ ion implantation and the presence of sp2 carbon. Also, the dislocations may be due to the presence of residual organic compounds after piranha cleaning or after transferring the membranes between substrates prior to growth. The non-smooth surface caused an array of squares of varying heights to be produced (Figure 5.2). This pattern is possibly due to the previously mentioned micro masking of organics, other contaminants, or a rough surface

causing the diamond planes to grow at different rates. This non-single crystalline surface will cause the electrons to preferentially flow through the deformities, grain boundaries and dislocations on the diamond surface. The grain boundary lattice sites will have more available sp2 sites for recombination to occur away from a SiV defect. To improve the quality of the diamond surface, the diamond samples and equipment need to be cleaned of all unwanted contaminants through both wet and dry-cleaning techniques, which include piranha solution as well as cleaning the sample in a hydrogen or a weak oxygen plasma at high pressure to burn away organics.

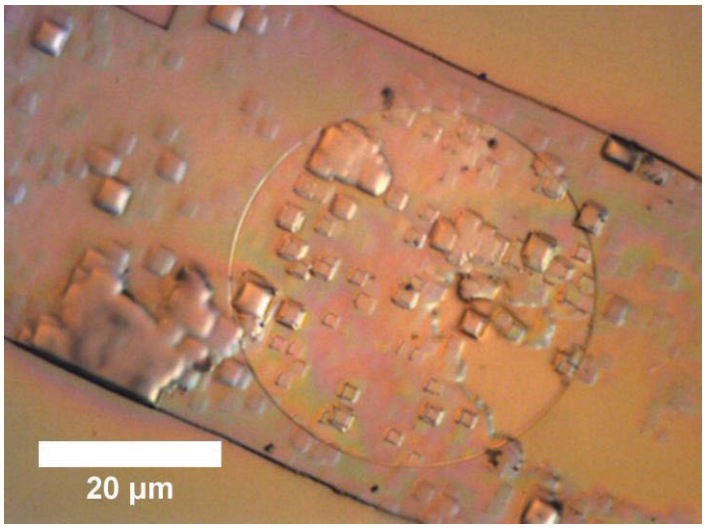


**Figure 5.2.** Rough surface**.** Optical microscopy image of a membrane that underwent MPCVD overgrowth to produce an array of squares of varying dimensions.

### 5.1.3 Variety of thickness

Furthermore, it was theorised that the thickness of the n-doped, p-doped, and intrinsic layer may affect density and probability of recombination of electron-hole pairs, or force recombination to occur deeper in the intrinsic or boron doped layers. To address this in the single crystal p-i-n diamond membrane device, I used ICP-RIE, as described previously, to thin the n-doped and p-doped region to ~100 nm to maintain a consistent thickness in each of the diamond layers.

### 5.1.4 Variety of contacts

In order for the electrons to flow freely and increase the probability that they recombine at a SiV defect, it is imperative to promote efficient electron injection into the diamond membrane. To optimise the configuration of the p-i-n devices, I explored a variety of n-type layers and contacts for use for contacting the diamond membrane devices. I used either single crystal grown n-doped diamond, n-doped ITO or n-doped ZnO as contacts. Both ITO and ZnO are commonly used as n-type contacts for p-i-n junctions [240]. However, ITO is optimal because the sputtered layer is transparent which allows the photons generated by EL to be observed directly by the APDs and CCD camera. Sputtering only a layer of ITO onto the diamond membranes did not yield any EL as shown in Figure 5.3, Figure 5.4 and Figure 5.5. The lack of observed EL may be due to a high activation barrier between the n-doped region and p-doped region impeding the ability of electrons to flow freely and recombine. To rectify this and to increase the injection of current from the power supply, several metal contacts were further sputtered onto the n-doped top surface of the device. The metal layers then underwent annealing at 500$^{o}$C for an hour to create stronger adhesion between the metal contact and the n-doped layer. The sputtered metal contacts included a ~10 nm sticking layer of titanium along with 300 nm of gold and 30 nm of platinum to act as a capping layer. The platinum layer was also replaced with a 300 nm layer of sputtered nickel due to its low resistivity ($6.99 \times 10^{-8}\ \Omega m$) and high conductance ($1.43 \times 10^{7}\ S/m$). With the addition of a nickel metal contact, I observed EL from a p-i-n diamond membrane device as shown in Figure 5.6.

### 5.1.5 Large Voltage sweeping and pulsing

Another way to address the lack of current density or to overcome the energy barrier in the device and to promote recombination is to increase the flow of electrons through the n-doped region of the diamond membrane device. To achieve this, the voltage was increased from between 0 V to +80 V in 1 V steps to increase the probability for electrons to pass through the space charge region and combine with holes. This was repeated under reverse bias as a sanity check and force recombination after charge breakdown between 0 V to – 80 V, to force reverse current flow or breakdown voltage to occur. It was observed that if the device did not show any EL signal under electrical triggering above the threshold voltage (~8 – 10 V) then increasing the voltage would not promote recombination. This leads to the possibility that the

issue is related to the device set up or the high resistivity in the top diode contact inhibiting the current from flowing freely between the injection probe and device.

Furthermore, I experimented with a pulsed bias injection to force high energy, short bursts past the space charge region. Pulsing the voltage in small intervals (on/off pulse width of 5 μs) may allow current to flow more directly into the sample and cause recombination. This was achieved using a 2612B Keithley SMU 2 channels 200V 10A pulsed max - TM170328C1 [154]. However, pulsing the voltage from 0 V - ± 60 V did not produce an EL signal.

### 5.1.6 Z-focal plane

It was hypothesized that the recombination sites may be occurring deeper in the intrinsic layer of the diamond device and may possibly be occurring at an adjacent point in the X-Y plane, differing to where the active colour centre is located through PL analysis. To address this, once an SiV emitter was located by a continuous wave (CW) 532 nm laser source, the focus in the z axis was moved in small increments (~50-100 nm) below the intrinsic layer and ~100-500 nm into the device, (dependent on configuration) to observe if recombination was occurring deeper in the device. When an emitter was located, its signal was optimised in the X, Y and Z confocal planes to enhance the collection efficiency because the optically active surface sites were deep in the intrinsic layer.

Moreover, regardless of whether the SiV emitter did or did not display EL recombination, I proceeded to move around the X-Y plane to observe if recombination was happening at a specific point in proximity or to improve the signal to noise ratio. If an EL signal was not observed, I moved up to ~2μm away from the emitter in both the X and Y planes. This was repeated for each Z-confocal map obtained. Since, the pathway for the electrical circuit would not be straight down into the diamond device, recombination would travel arbitrarily along the diamond lattice until an adequate defect site was met, the randomisation was minimised by scanning additional confocal maps in the X-Y and Z confocal planes.

### 5.1.7 Increase temperature

Additionally, to promote recombination and EL in the diamond membrane devices, the sample was placed on a heating stage at ~ $300^{O}$C. The recombination rate at the optical defect is restricted by the electron density at moderate injection levels. This is known to be minor in n-

doped diamond, due to the high activation energy of diamond. The probability of electron thermal emission from the deep donor states to the conduction band increases with increasing temperature. Therefore, as temperature rises, the density of free electrons in the n-doped layer grows rapidly, as:

$$T^{3/2} \exp\left(-\frac{E_D}{k_B T}\right) \qquad \textbf{Equation 5.1}$$

The photon emission rate from the optical defect also grows rapidly [192], [229], [241]–[243]. Fedyanin and Agio showed that increasing the temperature of a p-n diamond diode can improve the photon emission rate by orders of magnitude, up to ~10M counts/s. To improve the performance of a semiconductor, the opposite, i.e. cooling the device, is usually carried out [186], [189], [244]–[246]. It can be extrapolated that the optical properties of the diamond device can be improved by heating it while it is being electrically triggered. It should be noted that I had not observed any EL signal from the SiV defect by heating it to 300°C. The lack of observed EL signal may be due to one of the previously mentioned reasons *i.e.* poor homogeneity, poor conductance and carrier mobility in the n-doped or p-doped region.

### 5.1.8 Device configuration

I attempted to improve the p-i-n diamond diode by exploring several device configurations. The devices included a 300 nm epitaxially overgrown SiV containing intrinsic diamond layer placed on a p-doped silicon substrate. The sample was patterned using positive resist exposed through a photolithographic mask to create disks of 20 μm in diameter. Several layers were sputtered on top of the diamond device, including ~100 nm of n-doped ITO (Figure 5.3). The ITO layer acts as a transparent conductive contact to promote the injection of current from the probe and recombination of electron – hole pairs. A confocal image of the device is shown in Figure 5.3a. Upon PL excitement of the diamond device several SiV emitters were observed, as shown by the characteristic peak at 737 nm (Figure 5.3b). However, when the sample was electrically pumped no recombination or EL was observed at room temperature or after being heated to 300°C on a hot-stage. For each device configuration, different Z-focal planes were measured, along with points several pixels away from the emitter in X and Y planes, to observe if recombination could be happening elsewhere. Additionally, I employed large voltage sweeps of ± 80 V to induce recombination.

I now show a number of device configurations that exhibit diode like behaviour and PL spectrum of SiV colour centres. For EL, each device underwent a large voltage sweep both with and without a pulsed bias, different Z-confocal planes along with local X and Y were investigated and the temperature was increased to 300ºC.

A thinned down ~300 nm diamond membrane containing a homogeneous layer of SiV colour centres was placed on top of a p-doped silicon substrate. A layer of n-doped ITO was subsequently sputtered to create a p-i-n junction. An optical image of a p-i-n diamond membrane device is shown in Figure 5.3a, where the circles denote the sputtered ITO top contact pattern. The fabricated membrane device displays excellent electrical characteristics, as shown in Figure 5.3b. Diode-like behaviour with a threshold voltage at ~10 V and negligible current under a reverse bias of > 20V was measured. The rectification ratio of the device is moderate as shown by the semi-log I-V curve with a ratio of ~ 500 (inset of Figure 5.3b). A schematic of the fabricated device is shown in Figure 5.3c. The sample was scanned using a 532 nm CW room temperature laser. The confocal map along with the PL spectra exhibiting the SiV ZPL are shown. Upon electrical excitation with a forward bias above the onset voltage and ~mA current, no EL was observed from the sample. The sample was placed on a 300ºC heating stage and no EL was shown (Figure 5.3e).

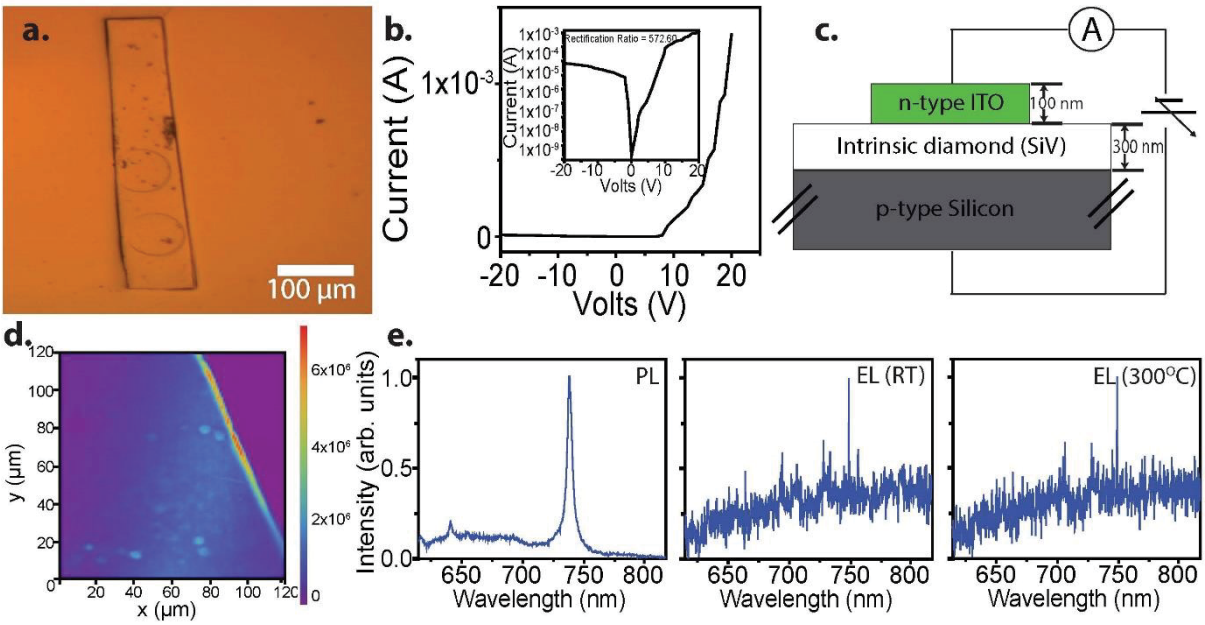


**Figure 5.3.** Characterisation of a vertical $p^-$/silicon-i-$n^+$/ITO device. (a) An optical microscopy image of the diamond membrane device. The circles are the n-type contacts on the membrane. (b) The $p^-$/silicon-i-$n^+$/ITO membrane shows diode-like behaviour with an on-set voltage of

~9V. Inset: Log (I) vs (V) rectification curve of the $p^-$/silicon-i-$n^+$/ITO diamond membrane showing a rectification ratio of ~600. (c) Schematic diagram cross section of the $p^-$/silicon-i-$n^+$/ITO diamond device. The intrinsic diamond layer is 300 nm and the ITO layer is 100 nm thick. (d) A confocal map of the $p^-$/silicon-i-$n^+$/ITO membrane device containing SiV emitters in the intrinsic diamond layer. (e) The PL spectra were collected using a RT CW 532 nm 0.5 mW excitation sources and exhibit the characteristic SiV emission peak at ~737 nm. The EL were recorded from the same points using a positive bias at both RT and $300^OC$ and only show background emission.

A similar configuration was employed for another device; however, the doping of the contracts was modified. ~100 nm of n-doped ITO was sputtered through a photolithographic mask onto an intrinsic diamond membrane containing SiV colour centres, positioned on an n-doped silicon substrate (Figure 5.4). The device was pumped using a CW 532 nm laser. An optical image of the device is shown in Figure 5.4a where the bright circle denotes the sputtered ITO top contact. The fabricated membrane device exhibits similar electrical characteristics, as shown in Figure 5.4b with diode-like behaviour exhibiting a threshold voltage at ~11 V and negligible current under a reverse bias of > 20V was measured. The rectification ratio of the device is moderate as shown by the semi-log I-V curve with a ratio of ~ 2800 (inset of Figure 5.4b). A schematic diagram of the diamond device is shown in Figure 5.4c. The diamond membrane device exhibited several bright SiV colour centres. The device still failed to show EL recombination through electrical triggering both at room temperature and at $300^OC$ (Figure 5.4e).

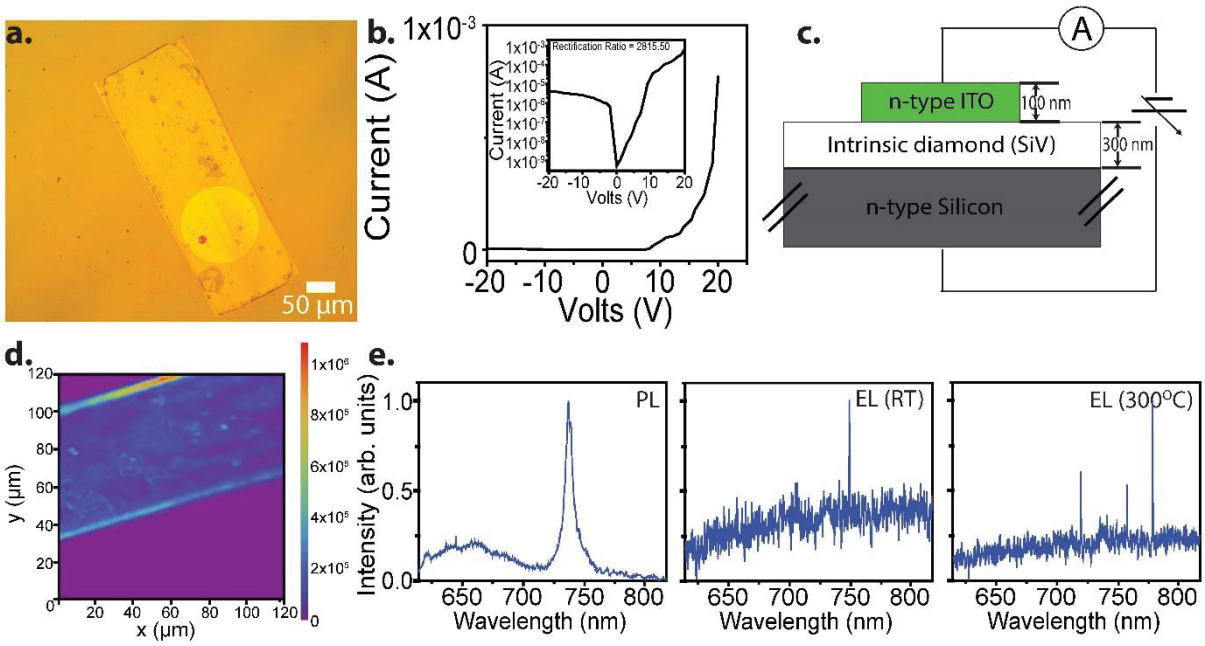


**Figure 5.4.** Characterisation of a vertical $n^+$/silicon-i-$p^-$/ITO diamond device. (a) An optical microscopy image of the diamond membrane device. The circle is the p-type contacts on the membrane. (b) The p-i-n membrane shows diode-like behaviour with an on-set voltage of ~10V. Inset: Log (I) vs (V) rectification curve of the p-i-n diamond membrane showing a rectification ratio of ~2800. (c) Schematic diagram cross section of the $n^+$/silicon-i-$p^-$/ITO diamond device. The intrinsic diamond layer is 300 nm and the ITO layer is 100 nm thick. (d) A confocal map of the $n^+$/silicon-i-$p^-$/ITO membrane device containing a layer of SiV emitters in the intrinsic layer. (e) The PL spectra were collected using a RT CW 532 nm 0.5 mW excitation sources and exhibit the characteristic SiV emission peak at ~737 nm. The EL were recorded from the same points using a positive bias at both RT and 300$^O$C and only show background emission.

An additional p-i-n device was made entirely out of a single crystal diamond membrane, as described in Chapter 4. Furthermore, a ~100 nm of n-doped ITO was sputtered onto the p-i-n diamond membrane to increase the electron flow from the contact probe to the intrinsic layer. An optical image of the diamond membrane device is shown in Figure 5.5a, where the circles denotes the sputtered ITO top contact. The fabricated membrane device exhibits better electrical characteristics, as shown in Figure 5.5b with a forward threshold voltage at ~8 V and negligible current under a reverse bias of > 20V. The device shows diode like before which leads to an extremely high rectification ratio of ~7600 (inset of Figure 5.5b), which is comparable to diamond devices [22]. A schematic diagram of the diamond device is shown in

Figure 5.5c. The device was pumped using a CW 532 nm laser, creating the confocal image which is shown in Figure 5.5d. The diamond membrane device exhibited several SiV colour centres. The device still failed to show EL recombination through electrical triggering both at room temperature and at 300$^{O}$C (Figure 5.5b).

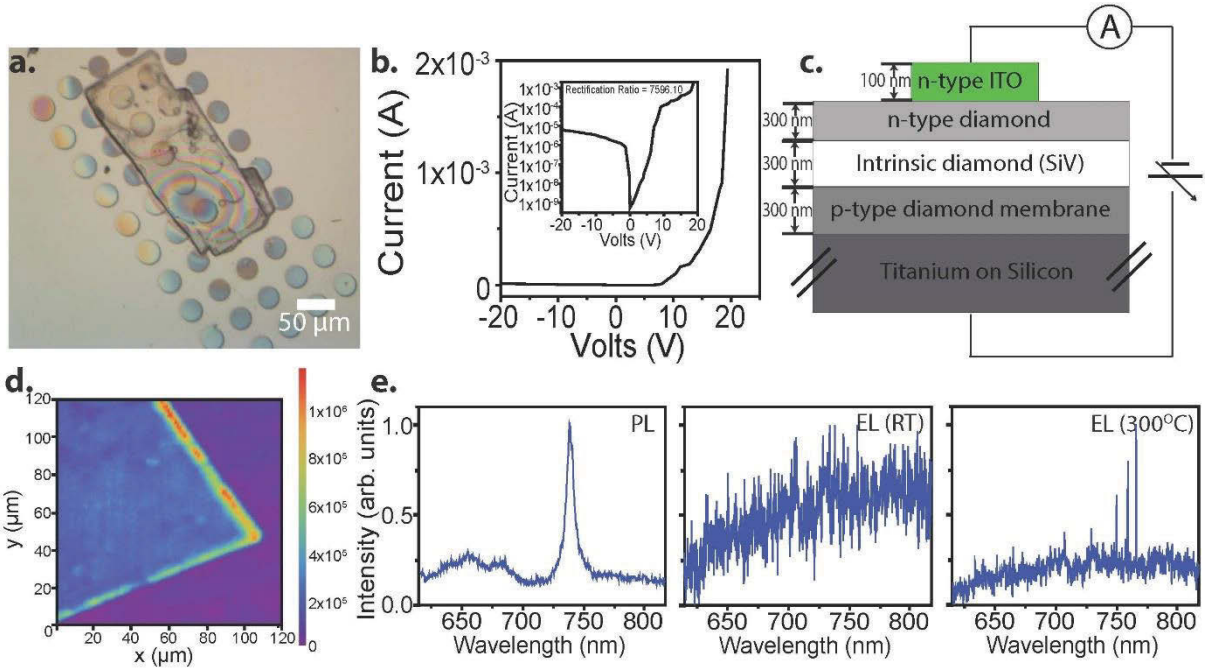


**Figure 5.5.** Characterisation of a vertical p-i-n diamond device. (a) An optical microscopy image of the diamond membrane device. The circles are the n-type contacts on the membrane. (b) The p-i-n membrane shows diode-like behaviour with an on-set voltage of ~9V. Inset: Log (I) vs (V) rectification curve of the p-i-n diamond membrane showing a rectification ratio of ~7600. (c) Schematic diagram cross section of the p-i-n diamond device containing a 300 nm layer of SiV emitters in the intrinsic layer. The sputtered ITO layer is 100 nm thick. (d) A confocal map of the p-i-n membrane device. (e) The PL spectra were collected using a RT CW 532 nm 0.5 mW excitation sources and exhibit the characteristic SiV emission peak at ~737 nm. The EL were recorded from the same points using a positive bias at both RT and 300$^{O}$C and only show background emission.

The reliability and repeatability of the EL signal is high and low, respectively. Once an EL signal is observed in a diamond membrane device, the signal is stable and does not bleach or blink. The EL signal is consistent and remains, unless a very high current is passed through the device causing it to breakdown or 're-wire' the recombination pathways. However, locating an EL signal is difficult and rare because requires extensive probing.

Once an EL signal is located, the spectra are collected for 300 seconds with a voltage above the device's threshold barrier. This is then repeated without a flowing current or voltage, as a sanity check, to collect a background spectrum. The background spectra are subtracted from the devices spectra and analysed. The spectra in Figure 5.1b showed a distinct peak at ~739 nm after background correction. On the other hand, the spectra in Figure 5.3, Figure 5.4 and Figure 5.5 showed a noisy signal after correction and therefore no distinct EL peak from the SiV emitter. The origin of the 680 nm peak could potentially be highly strained $SiV^-$ vacancies. Or potentially contamination from previous germanium growths and be either a strained $GeV^-$ or the $GeV^0$ signal. Contamination from germanium sources is possible but unlikely, because I thoroughly wipe down and plasma clean the chamber when changing sources.

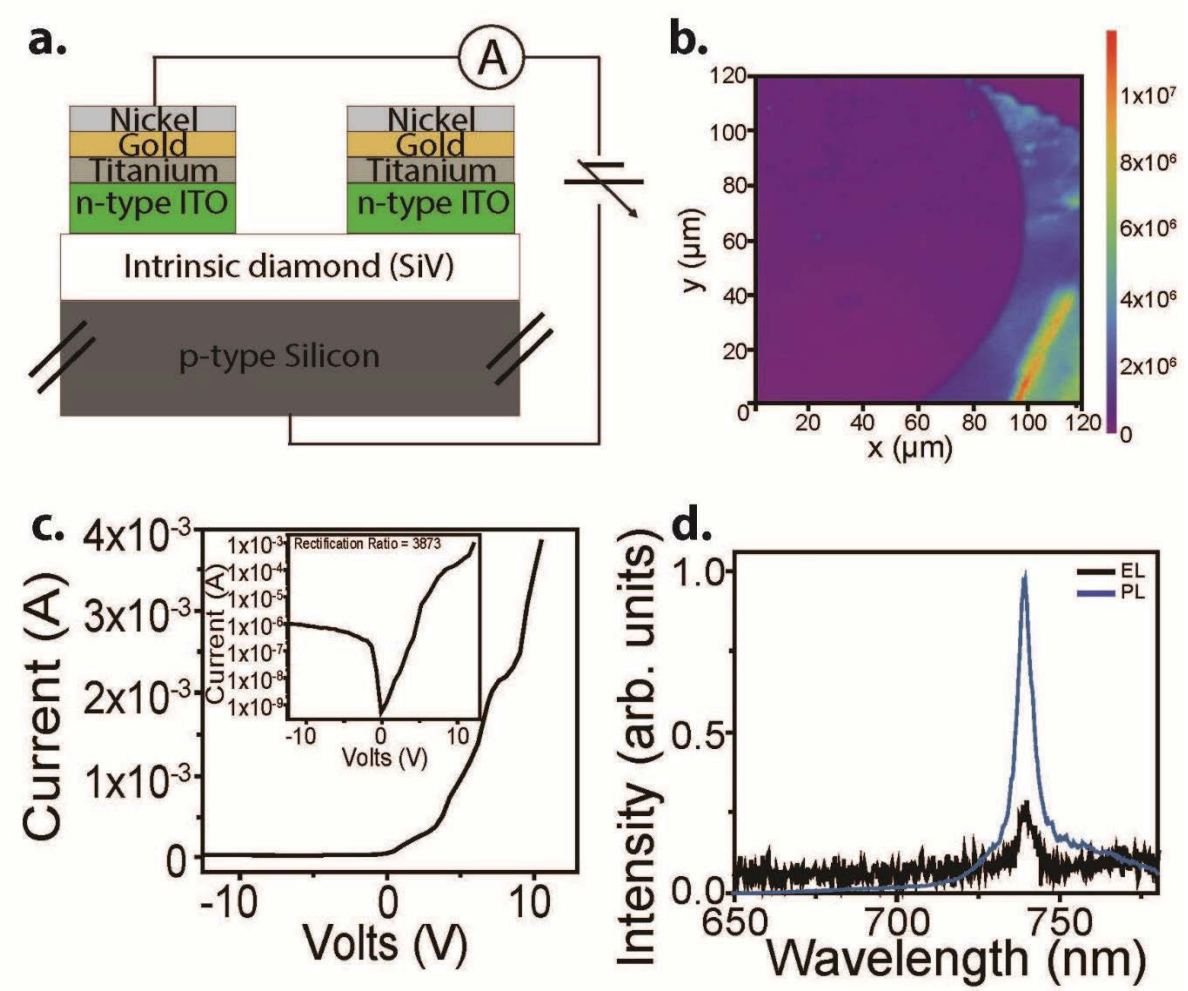


**Figure 5.6.** (a) Schematic cross-sectional diagram of the p-i-n diamond device. The device contains a 300 nm intrinsic layer, ~100 nm of ITO, ~100 nm of titanium, ~30 nm of gold and ~30 nm of nickel. (b) Confocal map of the p-i-n membrane device. (c) Photoluminescence

(Blue) and electroluminescence (black) recorded at room temperature, showing the characteristic emission from the same SiV colour centre at 737 nm.

Finally, a single crystal diamond membrane was overgrown through MPCVD with a source of silicon to create a homogeneous intrinsic layer of SiV colour centres. The membrane was subsequently flipped and thinned down to ~300 nm then transferred to a p-doped silicon substrate to act as a conductive back contact. A 100 nm layer of PMMA was spin coated and exposed onto the diamond membrane to pattern an array of circles, 20 μm in diameter, using EBL. After development, several conductive layers were sputtered using a dual sputterer to increase the current flow into the diamond membrane for recombination. These included ~100 nm of ITO, ~100 nm of Titanium, ~30 nm of gold and ~30 nm of Nickel Figure 5.6a. The unwanted metal and PMMA resist were lifted off and the diamond sample underwent annealing at 300$^{o}$C for an hour to meld the metal layers together to improve contact. The diamond sample was scanned using a CW 532 nm laser, and the resulting confocal map is shown in Figure 5.6b.

The p-i-n single crystal diamond membrane device shows excellent electrical characteristics, as shown in Figure 5.6c. Diode-like behaviour with a threshold voltage at ~5 V and negligible current under a reverse bias of > 10V was measured. This is confirmed by the semi-log I-V curve with a high rectification ratio of ~ $10^4$ (inset of Figure 5.6c). The low threshold voltage is advantageous for efficient device operation and is comparable with many standard nano-optoelectronic devices.

Figure 5.6d shows the PL and EL characteristics of the device, recorded at room temperature. The PL was recorded using a 532 nm laser excitation, while the EL was recorded under a forward bias with an injection current of ~4 mA. Both the EL and the PL exhibit the desirable emission of the SiV colour centres at ~ 737 nm.

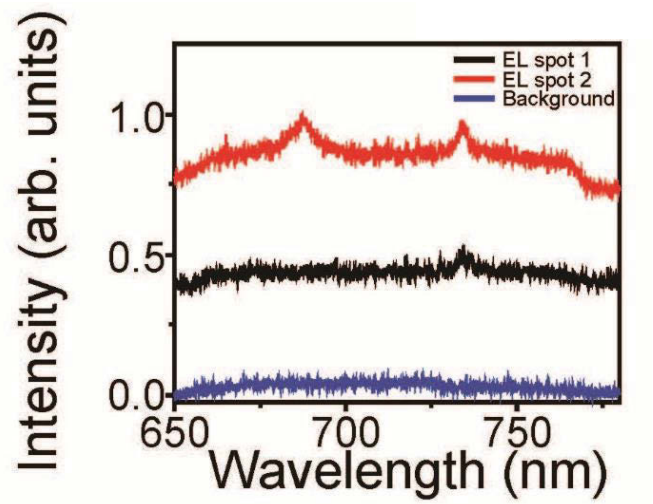


**Figure 5.7.** EL measurement of the p-i-n device shown in Figure 5.6a showing two additional spots that underwent a forward bias of 9 V, a current flow of ~4 mA that were collected for 300 seconds. I observe EL from the intrinsic SiV colour centres as shown by the characteristic peak at 737 nm. Additionally a background spectrum was collected under the same conditions with a current several orders of magnitude smaller, showing no peak. The spectra are shifted for clarity.

Figure 5.7 exhibits additional EL measurements recorded from the device shown in Figure 5.6 with a forward bias of 9 V and a current of ~3.5 mA. The characteristic SiV peak at 737 nm is visible in both areas as shown in the red and black curve. A peak was observed at ~680 nm, of which the origin is not currently known. A background spectrum was recorded without an injection current to show that the peak is not an artefact.

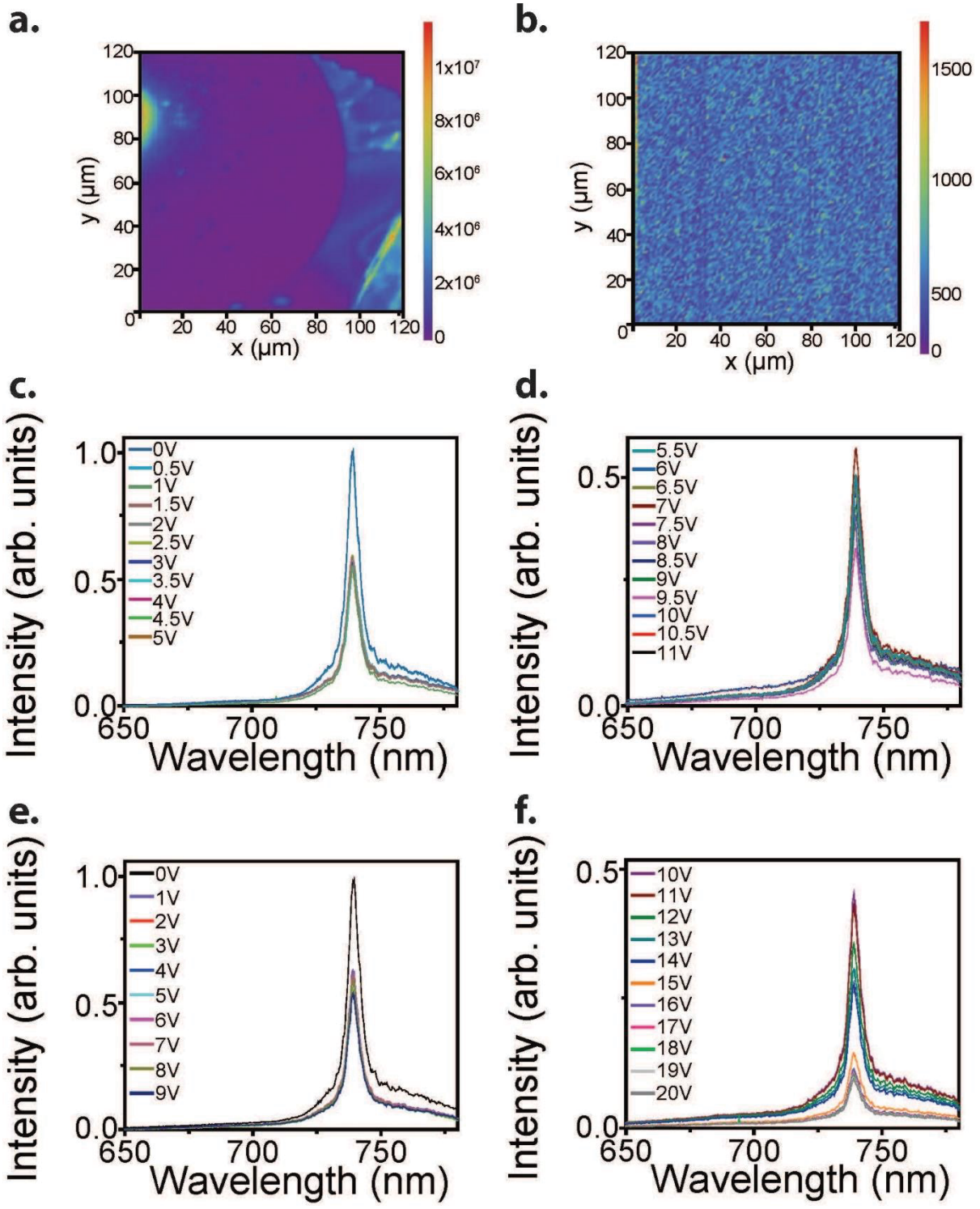


**Figure 5.8.** (a) Confocal map of the membrane device under CW laser and pulsed current excitation. (b) A confocal map collected under a pulsed 9V bias with an on/off pulse with of 5 μs. (c, d) Photoluminescence excitation of a SiV colour centre at a variety of continuous voltages between 0 V and 11 V in 0.5 V steps. (e, f) Photoluminescence excitation of the same emitter under 5 μs on/off pulsed excitation of between 0 V and 20 V in 1 V steps.

The diamond membrane device was pumped with a pulsed voltage with an on/off pulse duration of 5 µs. A confocal map was collected under a pulsed bias both with and without a 532 nm CW sources, to determine if emission could be enhanced or observed the electrical triggering (Figure 5.8a and b respectively). When there is an enhancement in the emission, we would expect to see an increase in the counts from the APD.

Once a strong SiV colour centre was located, it was excited by a CW 532 nm laser source and electrically triggered with either a continuous bias from 0 – 11V in 0.5 V steps (Figure 5.8c) or a pulsed bias from 0 – 20 V in 1 V steps. (Figure 5.8d). Additionally, the sample was consistently checked for mechanical and sample drift by X, Y, and Z tracking before each measurement. As the voltage increased, the maximum intensity of the emitter steadily declined until it reached a minimum fluorescent intensity. By ceasing electrical triggering, the intensity of the SiV emitter increased to the same maximum counts prior to electrical pumping. When the voltage was switched off it took ~2 seconds for the maximum counts to stabilise. The decreasing PL signal may be due to an increased tunnelling rate of charge carriers, specifically electrons because of their lower effective mass. After ~1.5 V, the electrons tunnel faster than they can radiatively recombine [247], leading to the exciton peaks being quenched in the PL spectrum. It may also be possible that there is a charge transfer between the negatively ($SiV^-$) and neutral charged ($SiV^0$) SiV colour centre.

As mentioned previously the SiV centre has a bond centre location with a $D_{3d}$ axis formed by the <111> joining the split-vacancy. The $SiV^0$ centre possesses a ground state electron spin of S=1 and has been theorized by computational studies and characterised by electron paramagnetic resonance (EPR) [248]–[250] and by PL studies [251], [252]. Similarly, to the $SiV^-$, the $SiV^0$ charge state exhibits a high DW factor, with the majority of its photons be emitted by the ZPL at 946 nm. The reason for the unobserved ZPL emission from $SiV^0$ at 946 nm, in the presented thesis, can be attributed to its difficulty to be observed at room temperature [251], [253].

Siddharth Dhomkar *et al*. have shown [254] that $SiV^0$ can efficiently capture photogenerated electrons diffusing through the diamond crystal. While in the presence of conduction band electrons, the SiV defect readily converts from the negative to neutral charged states. To determine the carrier process, the authors used metal electrodes to generate an electric field parallel to the direction of excitation. They observed that as the voltage increased, there was a larger generation of $SiV^-$ close to the positive electrode and a lower formation near the negative electrode. This indicates that free electrons, not holes, form during the red laser illumination

which strongly suggests that SiV centres must have a neutral charge preceding to carrier capture [254]. However, it has also been shown that as the laser moves around the sample any $SiV^0$ the beam produces locally is subsequently transformed into $SiV^-$ remotely via electron capture [254]. This could mean, that the decrease in PL signal with increasing voltage in the fabricated p-i-n diamond devices may not be undergoing charge transfer from the $SiV^-$ to the $SiV^0$ charged states. As the voltage and, subsequently, current increase, there are more free electrons available to combine with potential $SiV^0$ defects in the diamond lattice. This abundance of electrons will be able to transfer their charge to create the negatively charged $SiV^-$ state. Therefore, the decrease in the overall PL intensity could be attributed to an oversaturation of available charge carriers (electrons) to radiatively recombine to emit photons.

The hybrid p-i-n devices (p-type silicon – intrinsic diamond – n-doped ITO/Ti/Au/Ni) appear to perform better than the all single crystal diamond p-i-n devices. This may be due to inactive charge carriers in either the boron doped or phosphorus doped diamond layers which would inhibit charge recombination for the emission of a photon. Also, the p-type silicon, n-doped ITO and metal contacts are readily available commercial products that have undergone rigorous testing, juxtaposed to the recently adapted doped diamond layers. Furthermore, it is ideal to fabricate p-i-n as opposed to p-n diamond diodes due to the inclusion of an intrinsic layer that can host a variety of optically active colour centres for electrical triggering.

To conclude, I show the first robust and reliable engineering of nanoscale conductive diamond membranes. Additionally, I have fabricated a range of p-i-n diamond devices using thin single crystal diamond membranes as an optically active intrinsic layer with various n-doped and metallic contacts to promote electrical triggering. The membranes and the devices have high aspect ratio of lateral to vertical dimensions, are standalone and can be positioned onto a substrate of choice. Finally, I show that the p-i-n single crystal diamond devices can host optically active colour centres – namely the SiV centres that exhibit excellent EL and PL characteristics and therefore are suitable for optoelectronic and photonic applications.

Our work paves the way for numerous exciting new avenues employing the electrically active membranes. For instance, scalable integrated quantum nanophotonics circuits – including waveguides and photonic crystal cavities with electrically driven single photon emitters may become possible[8], [23]. The ability of diamond to host a myriad of colour centres, can be leveraged to realise arrays of nanoscale multicolour LEDs that operate under harsh chemical and physical environments – as diamond is chemically inert. In addition, further advanced NEMS [255] may potentially be realised. The availability of robust single crystal p-n junctions

may lead to engineering of nanoscale diamond field effect transistors with high breakdown voltages to achieve fast nanoelectronic circuits on a single chip. Finally, development of advanced sensing techniques – particularly for DNA translocation [256] where excellent mechanical and electrical properties are needed – may come a reality.

# Chapter 6 Narrowband emitters in nanodiamonds

## 6.1 Localisation of narrowband single photon emitters in nanodiamonds

In addition to the electrical pumping of diamond membranes, I also fabricated diamond nanocrystals and investigated the optical properties and structure of an unknown narrowband emission formed within the grain boundaries. The properties of the narrowband emitters can be further exploited for electrical triggering if a device can be fabricated, as well as coupled to waveguides and other cavities.

Diamond nanocrystals that host room temperature narrowband single photon emitters are highly sought after for applications in quantum information processing and quantum communications and bioimaging. However, current understanding of the origin of these emitters is extremely limited. In this chapter, I demonstrate that the narrowband emitters are point defects localised at extended morphological defects in individual nanodiamonds. In particular, I show that nanocrystals with defects such as twin boundaries and secondary nucleation sites exhibit narrowband emission that is absent from pristine individual nanocrystals grown under the same conditions. Critically, I prove that the narrowband emission lines vanish when extended defects are removed deterministically using highly localised electron beam induced etching. I also report on a bright, highly polarised near infrared single photon emitter embedded in diamond nanocrystals with a narrow, sub-GHz optical linewidth at 10 K. The observed zero-phonon line at ~780 nm is optically stable under low power excitation and blue shifts as the excitation power increases. The results enhance the current understanding of single photon emitters in diamond and are directly relevant to fabrication of novel quantum optics devices and sensors. Igor Aharonovich and Kerem Bray conceived the idea. Kerem Bray and Russell Sandstrom fabricated the nanocrystals. Kerem Bray measured and analysed the photoluminescence data. Cristopher Elbadawi performed EBIE. Martin Fischer and Matthias Schreck (Universität Augsburg, Germany) grew the nanocrystals on Iridium. Matthias Schreck, Olga Shimoni, Charlene Lobo, Milos Toth and Igor Aharonovich supervised the work. All the authors discussed and wrote the manuscript.

### 6.1.1 Narrowband emitters

Colour centres in diamond nanocrystals, and other solid-state single photon emitters (SPE), are attracting major attention in this regard for biolabeling and quantum information technologies which include, quantum communication and sensing applications [9], [37], [264]–[266], [59], [257]–[263]. This is due to their ability to host room temperature, photostable single photon emitters [137] and availability of spin photon interfaces [112], [267], [268]. Whilst there are hundreds of luminescent defects known to be hosted in diamonds, the vast majority of the existing studies focus on several known optically active defects such as the $NV^-$ [269] and $SiV^-$ [18] where their photophysical properties are well understood. As stated previously, the NV centre has a major drawback, as only ~4% of the photons are emitted into the ZPL [270]. This hinders its potential use in scalable nanophotonics devices and demands for sophisticated cavity engineering solutions [150], [271], [272]. As a result, other types of diamond colour centres with narrow lines and high Debye-Waller factors have been recently investigated. These include the SiV centre, [18], [103], [106], [116], [117], [273] the GeV centre, [122]–[124] and other emitters at the NIR spectral range [274]–[276].

Yet, diamonds can host many other colour centres that have not been explored to date [41], [274] and their origin remains unknown. While some of these centres can be engineered using ion implantation techniques, [144] this avenue is not ideal due to the damage caused by ion bombardment [60]. It is therefore highly desirable to understand emitter formation mechanisms in damage-free, scalable, bottom-up techniques such as CVD. During CVD, a growing diamond crystal often incorporates silicon and other impurities [277]. This has been utilised extensively to engineer SiV [18] and other single photon emitters [122], [278] in both individual nanodiamonds as well as polycrystalline films [279][280]. However, the process is stochastic, and improved control over emitter concentrations and distributions is needed. It is imperative to understand the underlying mechanisms and to achieve greater control over the incorporation of narrowband emitters in fluorescent nanodiamonds, which is essential for quantum photonic devices as well as bio-imaging applications. Here I present three independent experiments showing that narrowband, single photon emitters in CVD-grown nanodiamonds (FWHM < 5 nm) are localised predominantly at extended morphological defects, such as twin boundaries and secondary nucleation sites. In this work, I also explore the optical properties and the linewidth of single photon emitters embedded in nanodiamonds grown via CVD. At room temperature, the emitters have linewidths of ~2 THz (~4 nm) and a range of ZPLs at the NIR with extremely high Debye-Waller factors. When cooled down to 10

K, most of the emitters show spectrometer-limited lines. These properties make the emitters extremely promising for a variety of quantum photonic applications. In particular, I show that the emitters exhibit sub-GHz linewidths within NDs, which offers interesting possibilities for the potential realisation of hybrid quantum photonic networks [155], [156]. The insights gained in this work pave the way to controlled engineering of narrowband single photon emitters in diamond.

### 6.1.2 Characterisation of narrowband emitters

The growth of nanodiamonds was performed using a microwave plasma CVD reactor with a hydrogen/methane ratio of 100:1 at 60 Torr, a microwave power of 900 W from 4−6 nm detonation nanodiamond seeds. To achieve reproducible identification of individual nanodiamonds by PL and SEM, a grid pattern was deposited after the growth using standard photolithography procedure (AZ1505 photoresist). This enabled characterisation of the same nanocrystals in both SEM and PL. Figure 6.1a and b show PL spectra recorded from individual defective and pristine nanodiamonds, respectively, grown on a silicon substrate. The insets show the corresponding SEM images of the nanodiamonds and schematic illustrations of their geometries for clarity.

A CW 532 nm laser source (Gem 532™, Laser Quantum Ltd.) was used for excitation and scanning. The laser was directed through a half waveplate. It was focused onto the sample using a high numerical aperture (NA = 0.9, Nikon™) objective lens. Scanning is performed using an X-Y piezo scanning mirror (FSM-300™, Newport Corp.). The collected light is filtered using a 532 nm dichroic mirror (532 nm laser BrightLine™, Semrock Inc.) and an additional long pass filter (Semrock). The signal is then coupled into a graded index fibre, where the fibre aperture serves as a confocal pinhole. A fibre splitter is used to direct the light into a spectrometer (Acton SpectraPro™, Princeton Instrument Inc.) or into two APDs (Excelitas Technologies) for single photon detection. Correlation measurements are done using a time-correlated single photon counting module (PicoHarp300, PicoQuant).

The nanodiamond in Figure 6.1a exhibits morphological defects, while Figure 6.1b shows a nearly perfect nanocrystal with a cuboctahedral symmetry [281]. The PL spectrum from the nearly perfect nanodiamond shown in Figure 6.1b is dominated by the SiV emission at 738 nm. A peak at 630 nm (1.967 eV) was observed in all the studied nanodiamonds.

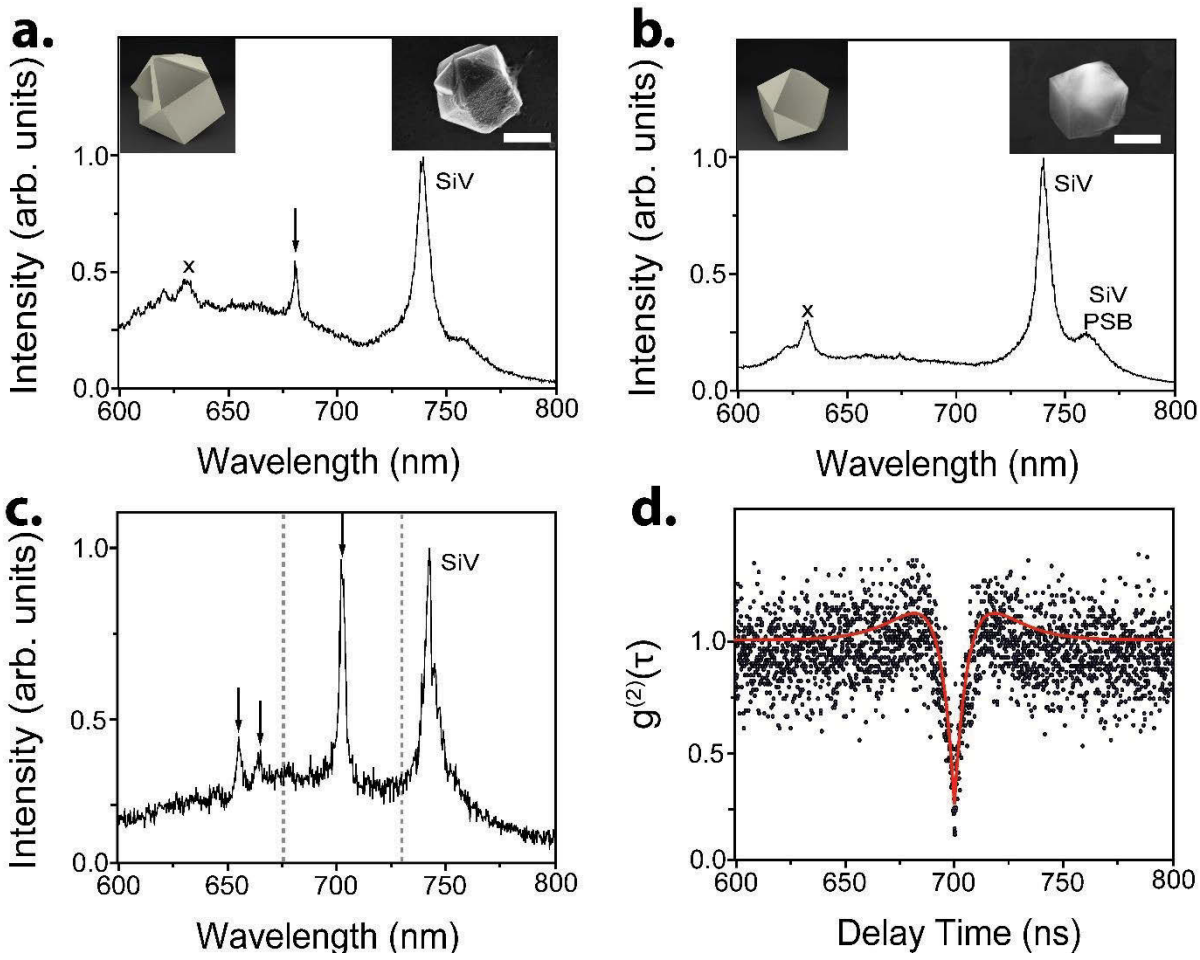


**Figure 6.1.** Nanodiamonds on a silicon substrate. (a) PL spectrum from a single nanodiamond containing morphological defects. (b) PL spectrum from a nearly perfect nanodiamond crystal. Insets in panels a and b are SEM images of the nanodiamonds and schematic illustrations of their geometries. Scale bars in both images are 500 nm. (c) PL spectrum from a different nanodiamond with morphological defects showing a narrow line at ~700 nm. (d) Second-order autocorrelation function $g^2(\tau)$, recorded from the spectral region indicated by dashed lines in panel c. The dip at zero delay time indicates a single photon emitter. The solid red line is a fit to the data. The samples were grown on a silicon substrate, and the strong emission at 738 nm corresponds to the SiV centre. Peak assignments: SiV = silicon vacancy, SiV PSB = silicon vacancy phonon sideband, X = CVD related peak at 630 nm, and the arrows indicate narrow-band emitters studied in this work.

The 630 nm peak is normally observed in CVD diamond films and is especially pronounced in nitrogen-doped films [41]. In the current work, I do not discuss the origin of this particular defect, typically referred as the CVD peak. The results illustrate that morphological defects

correlate with the narrowband emission lines (indicated by an arrow in Figure 6.1a). The morphological defects include major twinning that often occurs between the <111> planes of icosahedral nanodiamonds[282] (seen as dimples between adjacent triangular facets of the nanodiamonds) and secondary nucleation sites, a common morphological defect that forms when a nanodiamond nucleates on a pre-existing crystal, which forms a grain boundary along the nucleation site.

Figure 6.1c shows an additional spectrum recorded from a defective nanodiamond that exhibits a narrow, intense emission line at 700 nm, and Figure 6.1d shows a second order correlation function, $g^{(2)}(\tau)$, which confirms that the line is a single photon emitter (as evidenced by the dip below 0.5 at $g^2(0)$). The autocorrelation measurement (Figure 1d) was performed using a band-pass filter illustrated using grey dotted lines in Figure 6.1c. The data were corrected for background using the equation,

$$\boldsymbol{g_m^2(\tau) = (g^2(\tau) - (1 - \rho^2)]/\rho^2} \qquad \textbf{Equation 6.1}$$

where ρ is the ratio between the emitter signal and the total count rate. In this particular case, 20% of the total signal was background related. The data were fit using a three-level model. Most of the narrowband lines that were observed in the experiments are in fact from single photon emitters indicating that they are point defects that are localised at the extended morphological defects visible in SEM images.

To ascertain whether the narrowband emitters are related to silicon impurities originating from the substrate, nanodiamonds grown on iridium were investigated. Figure 6.2 shows a representative example of a nearly perfect nanodiamond and one that contains morphological defects. A similar trend to that seen in Figure 6.1 is clearly observed. The defective nanodiamond exhibits narrow, sharp PL emission lines, while the nearly perfect nanodiamond shows no emission at all, or in some cases only the very weak nitrogen-related emission at 630 nm. The broadband background emission for the nanodiamond containing morphological defects is attributed to graphitic regions located at the grain boundaries. The absence of the SiV peak is expected as there was no intentional source of silicon in the growth chamber. These results indicate that the narrowband emitters are not related to silicon impurities or associated defect complexes.

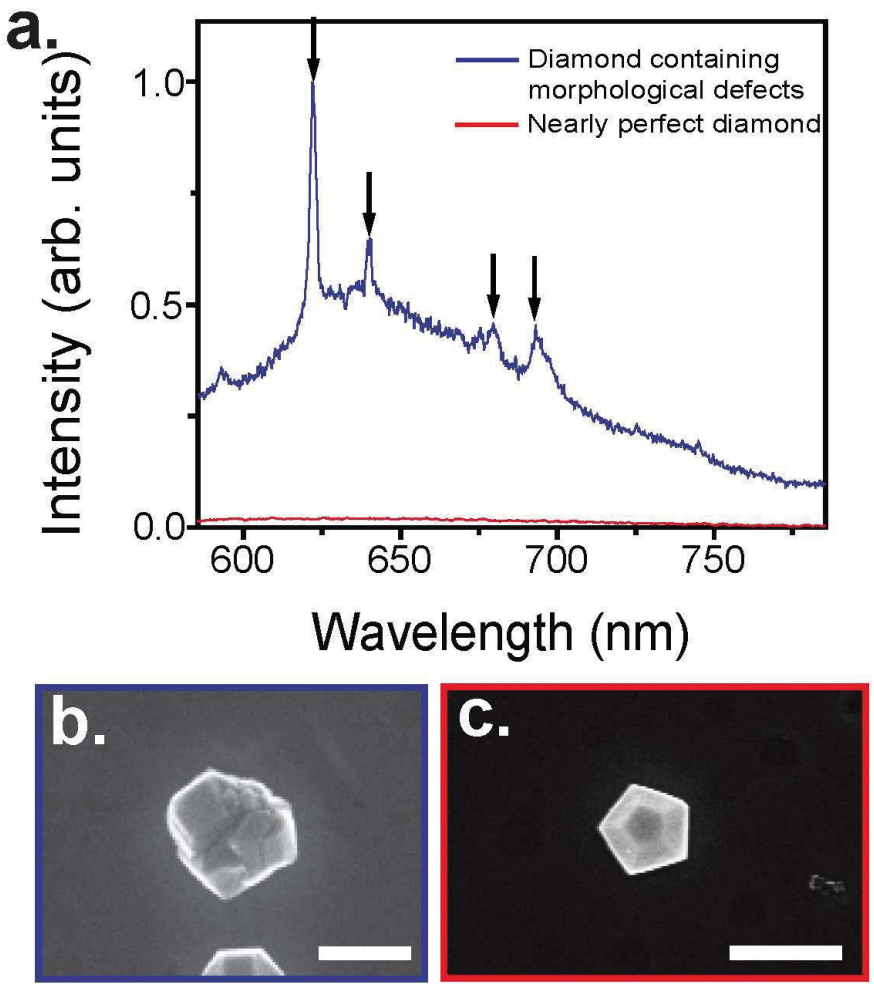


**Figure 6.2.** Nanodiamonds on an iridium substrate. (a) PL spectra recorded from individual nanodiamond that do (blue) and do not (red) contain morphological defects. (b, c) Corresponding SEM images of the defective and pristine nanodiamonds. Scale bars in both images are 500 nm. The spectra were recorded using a fixed excitation power. The arrows indicate narrowband emitters studied in this work.

A statistical survey of 60 individual nanodiamonds, which were studied in detail, on both silicon and iridium substrates revealed that 90% of the investigated nanodiamonds showed a direct correlation between the presence of morphological defects and narrowband peaks. The remaining 10% of the nanodiamonds either contained morphological defects but showed no distinct narrowband emission, or they appeared to be pristine crystals and showed narrowband emissions (in these cases morphological defects may still be present but invisible in SEM images). 53 narrowband emitters were examined and studied throughout the work. Spectral

stability was carried out on every single studied emitter and I observed that each emitter was stable and did not bleach or blink. Additional examples from both the silicon and iridium substrates are shown in Figure 6.3 as well as the histogram of the emitters zero phonon lines and the FWHMs (Figure 6.4).

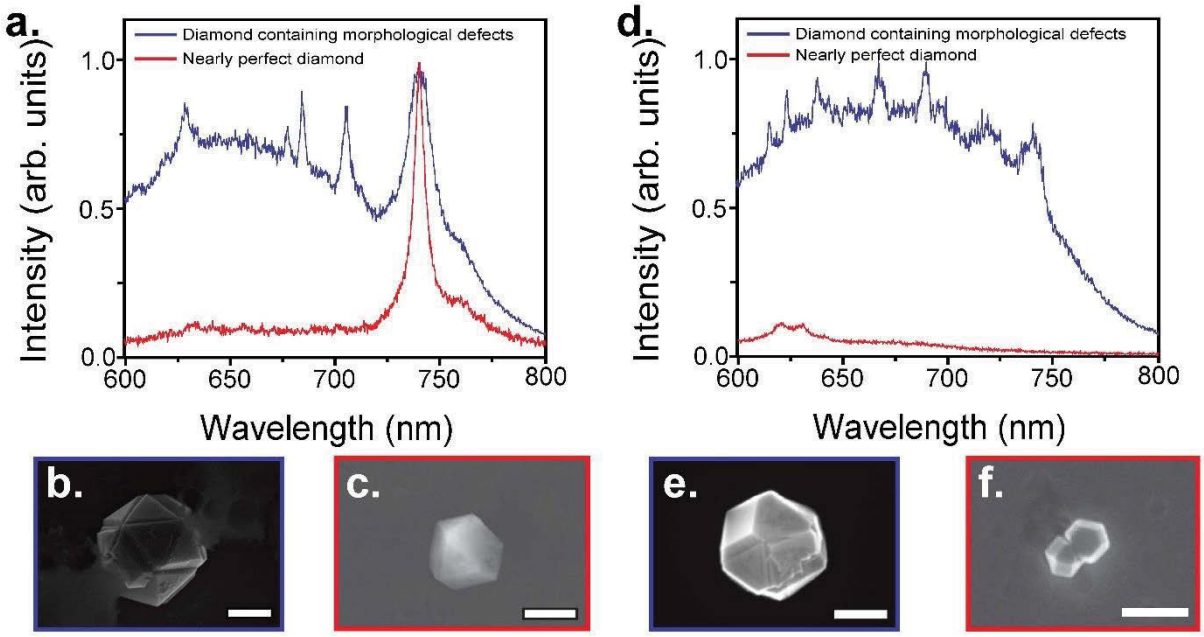


**Figure 6.3.** Two additional examples of photoluminescence spectra recorded from individual nanodiamonds grown on (a) silicon and (d) iridium along with their corresponding SEM images. Nanodiamonds with morphological defects are shown in (b, e), while nearly-perfect nanodiamonds are shown in (c, f). Scale bars on the SEM images are 500 nm. All the spectra were recorded using the same excitation power.

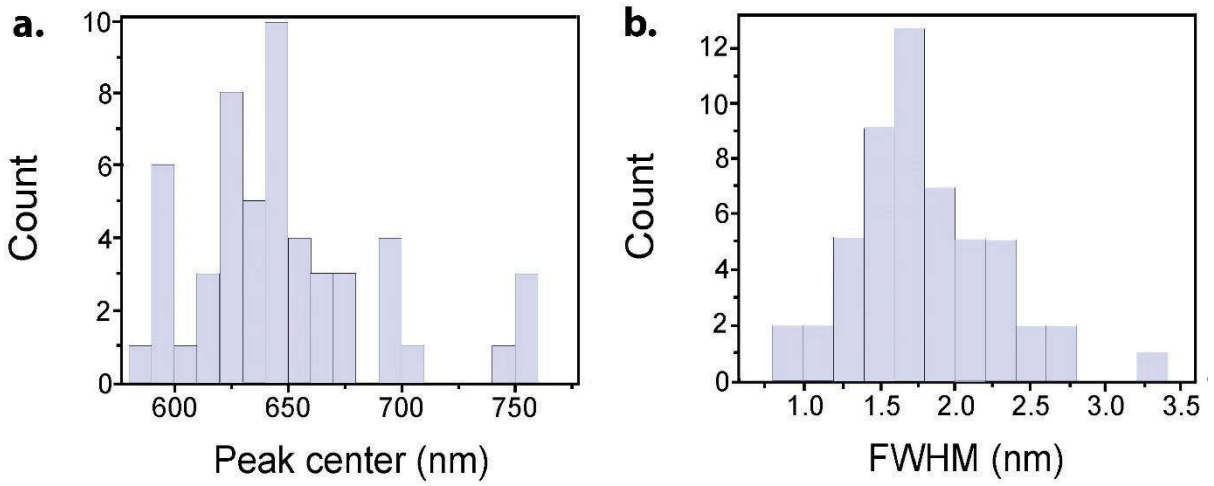


**Figure 6.4.** a) Histogram of wavelength centres from the narrowband emitters. b) Histogram of emission FWHM values from the narrowband emitters

The above experimental results suggest that morphological defects play a critical role in the formation of the localised narrowband emitters. I therefore performed an additional experiment that enabled us to compare PL spectra from nanodiamonds to a single crystal diamond that was grown on a diamond membrane under the same CVD conditions. The single crystal diamond membrane was lifted off type IIA single crystal diamond (Element6 Inc., [N] < 1 ppm) [30]. The membrane was placed on a silicon substrate and subjected to CVD growth under the conditions described earlier, yielding a single crystal diamond over layer with a thickness of ~650 nm. Figure 6.5 a shows a corner of the resulting overgrown membrane and a range of neighbouring nanodiamonds. The nanodiamonds were grown through spontaneous nucleation without seeds and contain multiple structural defects. The inset of Figure 6.5a is an optical image of the original single crystal diamond membrane.

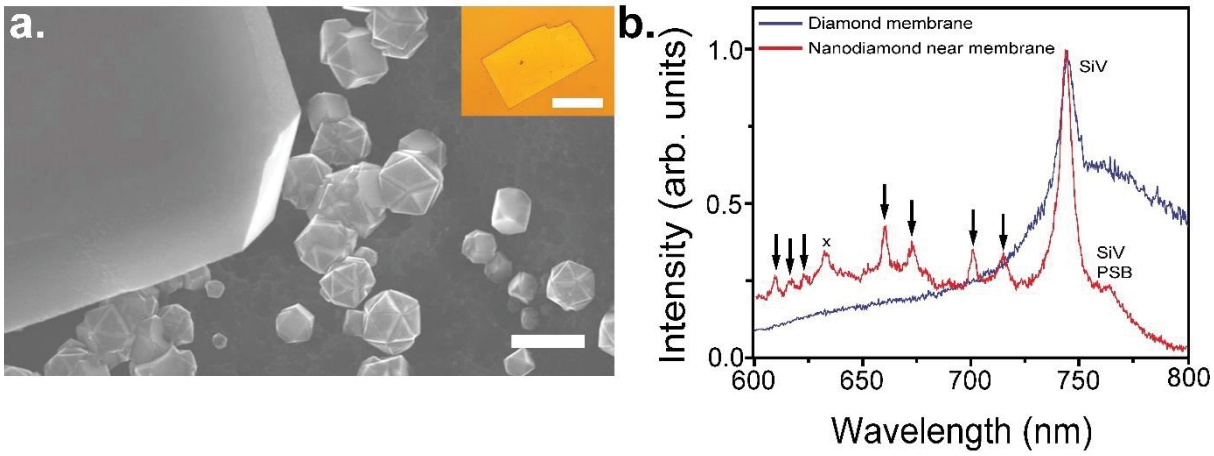


**Figure 6.5.** Comparison between single crystal and nanodiamond growth. (a) SEM image of a corner of the overgrown diamond membrane and nearby nanodiamonds that grew spontaneously on the silicon substrate and contain morphological defects. The scale bar is 2 μm. Inset: optical image of the diamond membrane prior to growth; the scale bar is 200 μm. (b) PL spectra recorded from the membrane and the adjacent nanodiamonds. Spectra normalised to SiV peak. Peak assignments: SiV = silicon vacancy, SiV PSB = silicon vacancy phonon sideband, X = CVD related peak at 630 nm, and the arrows indicate narrowband emitters studied in this work.

As expected, Figure 6.5b shows that both the nanodiamonds and the membrane exhibit a strong SiV emission due to incorporation of silicon atoms from the substrate during growth. However, the overgrown single crystal diamond membrane does not exhibit any narrowband emission lines, while the nanodiamonds exhibit a range of narrowband emitters. This experiment confirms that the narrowband emission lines are related to morphological deformations in the nanodiamonds, likely to be twins or grain boundaries that are not present in the single crystal diamond membrane.

Finally, to prove that the narrowband emitters are indeed localised at morphological defects, I select several nanodiamonds and deterministically removed the morphological defects using electron beam induced etching (EBIE) performed using water vapour as the precursor gas (Figure 6.6) [283]–[285]. EBIE is a chemical dry etch process that is driven and localised by an electron beam. A time-lapse SEM image sequence showing EBIE of a single nanodiamond is shown in Figure 6.7.

EBIE was performed using a customised FEI Field Emission SEM (accelerating voltage = 15kV, beam current = 1.35nA, water vapour pressure = 8 Pa) [286]. The nanodiamonds were located using the SEM. Specific areas of the nanodiamonds were then selectively etched by raster scanning, which also enabled real time imaging of the etched nanodiamonds (Figure 6.7). The etching process is then stopped by blanking the electron beam.

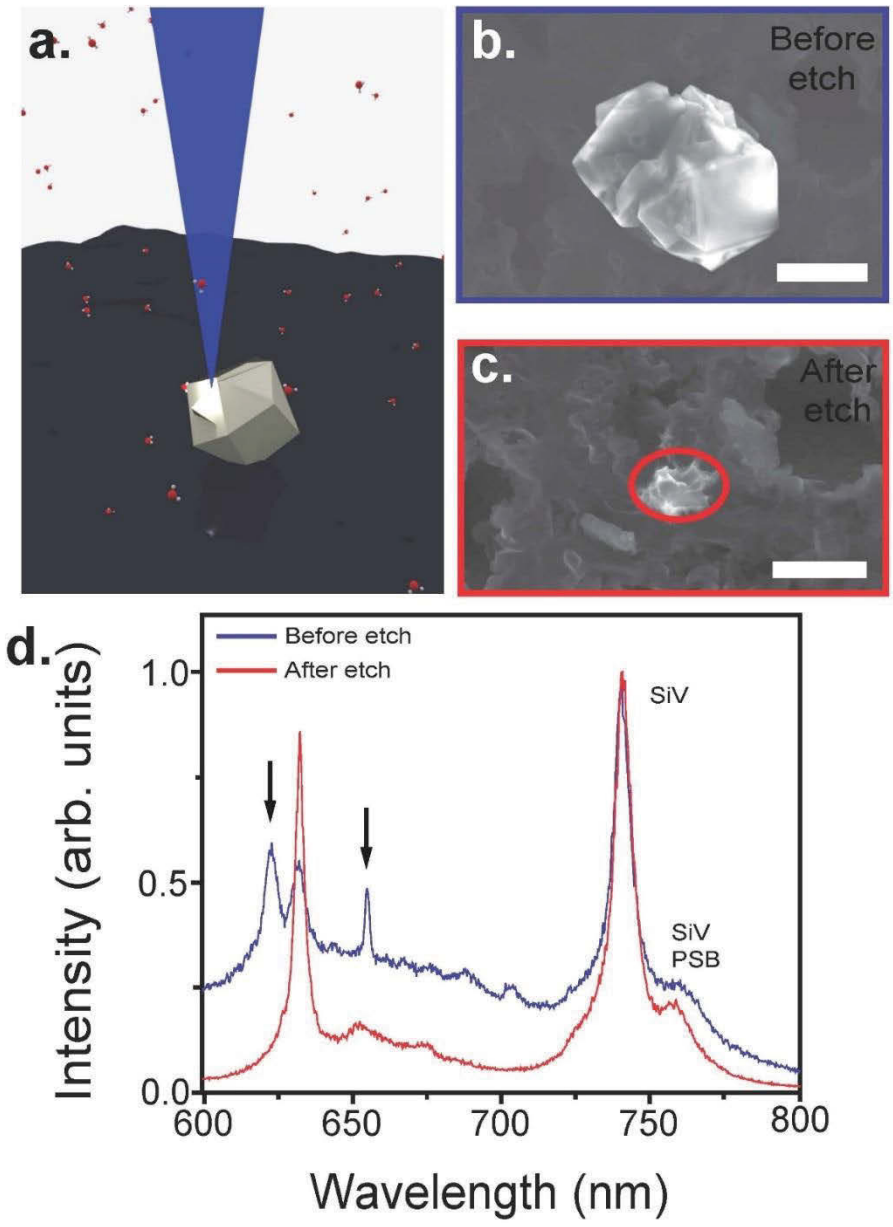


**Figure 6.6.** Deterministic removal of morphological defects from a single nanodiamond. (a) Schematic showing selective etching of an individual nanodiamond. (b, c) SEM images of the diamond crystal before and after electron beam induced etching. The red circle denotes the etched diamond. The contrast around the diamond is the substrate that did not fluoresce. Scale

bars in both images are 500 nm. (d) PL spectra collected before (blue curve) and after (red curve) the etch process. Spectra normalised to SiV peak. Peak assignments: SiV = silicon vacancy, SiV PSB = silicon vacancy phonon sideband, X = CVD related peak at 630 nm, and the arrows indicate narrowband emitters studied in this work.

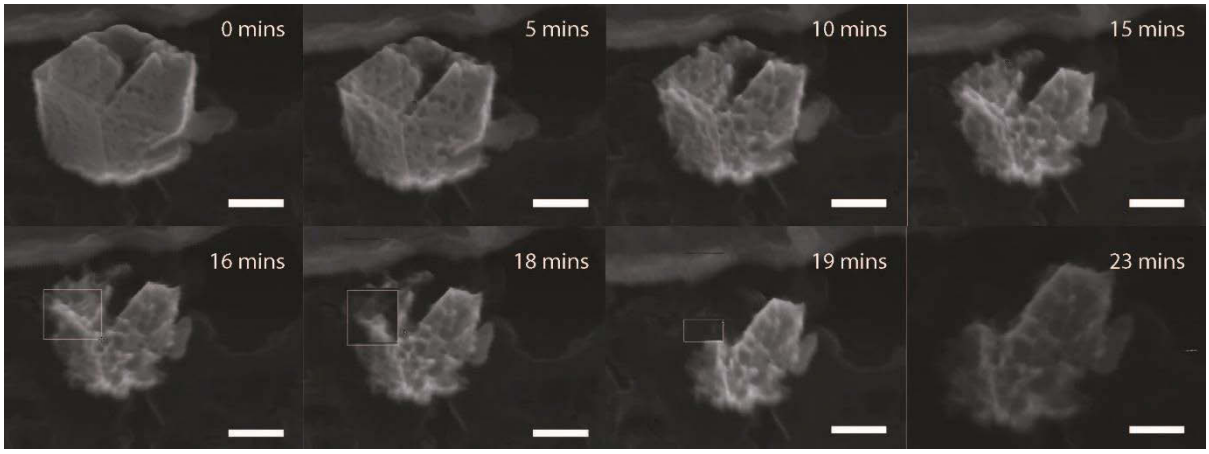


**Figure 6.7.** SEM image sequence showing deterministic EBIE of a CVD grown nanodiamond on a silicon substrate. The scale bar is 500 nm. The bottom row shows reduced-area-EBIE demonstrating selective removal of a specific nanodiamond region.

SEM images of the same nanodiamond taken before and after etching are shown in Figure 6.6b and c, respectively. The residual nanodiamond in Figure 6.6c is circled for clarity and is approximately ~200 nm in size. The narrowband emission lines seen in Figure 6.6d (blue spectrum, taken prior to EBIE) were removed by the EBIE process (red spectrum). Yet, the remaining nanocrystal still exhibits a strong SiV emission (~738 nm), which shows that the nanodiamonds are sufficiently large to host optically active colour centres. These results solidify the hypothesis that the narrowband emissions in fluorescent nanodiamonds are point defects that decorate extended morphological defects such as twin boundaries and secondary nucleation sites.

While I cannot deduce the chemical structure of the narrowband emitters, one can speculate about the importance of nitrogen in the formation of the defects. It is known that residual nitrogen in the gas phase modifies growth, causing twinning and renucleation, due to changes in the growth velocities of different crystallographic planes [287]. Therefore, nitrogen atoms may also be involved in the formed isolated defects that give rise to the narrowband emission

lines. Alternatively, this can result in localised deformations and stresses in the lattice [288] that may create luminescent defect states.

A number of the unknown narrowband emitters may be related to highly strained SiV colour centres. Lindner *et al.* [289] has carried out a comprehensive study on the shift of SiV defects and linewidths in nanodiamond crystals. A CVD grown diamond film on a silicon substrate underwent a wet-milling process. The wet-milling process dissociates the diamond film from the substrate. The film is subsequently crushed using a vibrational mill with steel beads to create diamond particles of 50 nm, 70 nm and 100 nm in diameter. The group investigated the strain and shift of the ZPL in the diamond nanocrystals by characterizing, not only the brightest spots but also the peaks that were barely above noise. The observed ZPLs were split into two distinct groups. Group one exhibits a small shift of ZPL between 738 nm to 741 nm with varying linewidths of ~5 nm – 18 nm. Group two showed a range of ZPL peaks from 715 – 835 nm with linewidths between 1 nm and 5 nm. After their analysis, it has been shown that only six data points exhibit shorter wavelengths than the ideal SiV colour centre, with the shortest being 729 nm. In addition, their data suggested that the ZPL is more likely to be red-shifted than blue-shift, meaning that the narrowband ZPLs shown in Figure 6.4 between ~580 nm – 710 nm are probably not highly strained SiV colour centres but another diamond defect. The mechanisms that contribute to the red shift in ZPL are prominently hydrostatic and uniaxial strain [289]. While the origin of the emitter certainly warrants further work, the localisation of narrowband quantum emitters at morphological deformations offers a fascinating opportunity for controlled localisation of emitters in photonic devices as well as targeted sensing. Once we have a greater understanding regarding the origin and formation of these narrowband emitters, I will need to explore controlled CVD growth parameters and conditions. This would include manipulating gas flows and ratios, chamber pressure, plasma power, time of growth to engineer the narrowband emitters fluoresce at specific wavelengths and be isolated in the crystal.

To summarise, I show convincing evidence for a direct correlation between morphological defects, such as secondary nucleation sites and twin boundaries, and narrowband single photon emitters in nanodiamonds. A survey of nanodiamonds grown on silicon and iridium showed that in 90% of cases, the presence of grain boundaries and crystal twinning correlated with the presence of narrowband emission lines in PL spectra. Single crystal diamond grown under the same conditions did not show any narrowband emitters. Finally, removal of grain boundaries from nanodiamonds using EBIE eliminated the narrowband emission lines. The results are an important step towards understanding of the origin, formation probabilities, and spatial

distributions of single photon emitters in nanodiamonds, which enable the deployment of nanodiamonds in bio-imaging and nanophotonic technologies.

### 6.1.3 Nanodiamonds with photostable, sub-gigahertz linewidth quantum emitters

As mentioned in the previous section, the narrowband emitters in diamond nanocrystals possess sub-GHz linewidths. Utilising narrowband sub-GHz emitters is ideal for communication over large distances while still exploiting low power and lower data rate applications, which is ideal for hybrid quantum photonic and wireless networks. In this work the optical linewidths and optical properties of these narrowband emitters were explored. The emitters show linewidths of ~4 nm with extremely high DW factors. Igor Aharonovich and Toan Trong Tran conceived the idea. Kerem Bray fabricated the nanocrystals. Toan Trong Tran and Mehran Kianinia measured and analysed the PL data. Sejeong Kim, Zai-Quan Xu, Angus Gentle, Bernd Sontheimer (Humboldt University, Berlin), Carlo Bradac and Kerem Bray analysed the data. Igor Aharonovich and Milos Toth supervised the work. All the authors discussed and wrote the manuscript.

Similarly, as described before, the diamond nanocrystals were grown from detonation nanodiamond seeds (diameter 4-6 nm) that were spin coated on a sapphire substrate. The use of sapphire substrates assisted in minimising the incorporation of silicon atoms that would otherwise result in undesired silicon doping. The samples were then loaded into a MPCVD system, and the crystals were grown in mixed gases (hydrogen:methane = 100:1) with a microwave power of 900 W, at 60 Torr of atmospheric pressure for 30 min. Under these conditions, nanodiamonds with diameters of ~0.3–1 μm were grown (Figure 6.8a). A CW tuneable Ti:sapphire laser (M Squared Ltd.) was used for excitation and scanning. The laser was directed through a Glan-Taylor polariser (Thorlabs, Inc.) and an achromatic half-waveplate (Thorlabs, Inc.), and focused onto the sample using a high numerical aperture (NA = 0.95, Nikon) objective lens. The sample stage was enclosed in a high vacuum chamber, equipped with an open-loop liquid helium flow system (ST500, Janis Ltd.). Scanning was performed using an X-Y piezo scanning mirror (FSM-300™). The sample was moved into place via a XYZ cryogenic-grade piezo stage (Attocube, Inc.). The collected light passed through a 90:10 (T:R) beam splitter (Thorlabs, Inc.) and an additional long-pass filter (Semrock) to reject the residual pump.

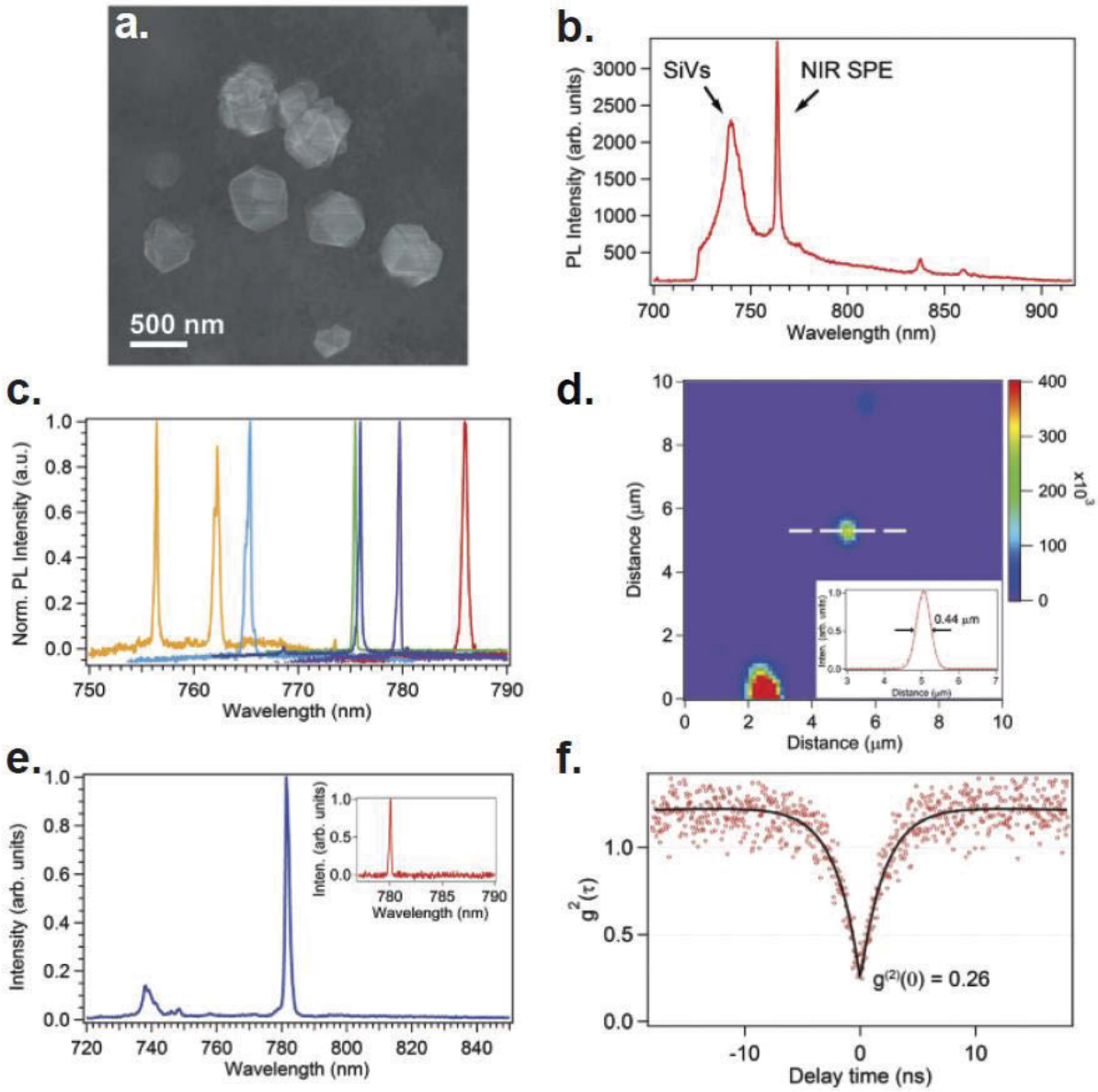


**Figure 6.8.** (a) SEM image showing several MPCVD-grown nanodiamonds on a sapphire substrate. The nanodiamonds are ~0.3– 1 μm in size. (b) A typical PL spectrum showing both SiVs and a near-infrared emitter recorded at room temperature. (c) ZPL distribution of the colour centres in MPCVD-grown nanodiamonds analysed in this study. A 700-nm, CW laser at 300 μW was used to excite the colour centres at 80 K. (d) Confocal PL map recorded with 700-nm laser excitation at 300 μW with a bandpass filter (785 ± 22) nm and acquired at 10 K. The bright spot corresponds to a nanodiamond hosting a single emitter. The bottom inset shows the cross-sectional intensity analysis (dotted line) revealing a FWHM of 0.44 μm, consistent with emission from a point-source. (e) Normalised PL spectrum taken from the colour centre in (d) (blue trace) with a 300 g/mm grating. The inset (red trace) shows a higher resolution spectrum taken from the same emitter (with an 1800 g/mm grating). The measurements were

conducted at 10 K. (f) Second-order autocorrelation function (red open circles) acquired for the emitter with a bandpass filter (785 ± 22) nm. The black solid line is the fitting (see main text) for the $g^{(2)}(0)$ function. The measurement was carried out at 80 K. The value of 0.26, without any background correction, indicates that the emission is from a single emitter.

The signal from the sample was then coupled into a graded-index fibre, where the fibre aperture served as a confocal pinhole. A fibre splitter was used to direct the light to a spectrometer (Andor SR303i), equipped with both a 300 g/mm grating and an 1800 g/mm grating, or to two avalanche photodiodes (Excelitas Technologies$^{TM}$) arranged in a Hanbury-Brown and Twiss interferometer configuration. Correlation measurements were carried out using a time-correlated single-photon counting module (Swabian Time Tagger 20$^{TM}$). The presented $g^{(2)}(\tau = 0)$ curve displayed in Figure 6.8f is not background-corrected.

Lifetime measurements were performed using a 675-nm pulsed laser excitation source (PiL067X$^{TM}$, Advanced Laser Diode Systems GmbH) with a 100-ps pulse width and 10-MHz repetition rate. The optical properties of the emitters were studied using a home-built laser scanning confocal PL microscope equipped with a continuous wavelength tuneable titanium sapphire laser (linewidths, 100 kHz). The sapphire substrate with the grown diamond nanocrystals was mounted onto a cryostat equipped with a high-precision XYZ piezo scanning stage and was cooled to 10 K using liquid helium. The excitation and collection were done via a high numerical aperture (NA = 0.9) objective mounted inside the cryostat, creating an excitation and collection spot size of ~430 nm. The signal collected from the emitters was analysed with both a spectrometer equipped with a high-resolution silicon-based charge coupled device (CCD) camera and HBT interferometer.

## 6.2 Results and discussion

From surveying the confocal PL scans with a 700-nm laser excitation, I observed both ensembles of SiV centres and NIR single emitters (Figure 6.8b). The SiV centres embedded in the nanodiamonds exhibit emission at ~738 nm, whereas the NIR emitter, spectrally separated form SiV centres, emits at various longer wavelengths with sharp ZPLs. All the studied nanodiamonds exhibited SiV emission but not all the nanodiamonds contained the bright isolated NIR emitters. A detailed spectroscopic study of the sample revealed that the nanodiamonds host narrowband colour centres with a ZPL in the range of 756–786 nm (Figure

6.8c). Note that these are not the SiV defects but other NIR emitters. On average, two to three emitters were found in a 60 × 60 μm$^2$ scan area, with the nanodiamond areal density of ~0.0125 particles/μm$^2$ (~45 particles per 60 × 60 μm$^2$). Bright spots that correlate with single emitters embedded in the nanodiamonds are shown in Figure 6.8d. The cross-sectional analysis of each spot shows a Gaussian profile with a FWHM of 0.44 μm, very close to the diffraction-limited point spread function of the confocal system (bottom right inset).

For the remainder of the chapter, I focus on a particular line at 780 nm. The line was selected arbitrarily, with the goal to study centres that emit further in the NIR. Consequently, Figure 6.8e shows the narrow ZPL at 780 nm with a FWHM of ~79 GHz (~0.16 nm) that corresponds to the spectrometer resolution. The inset in Figure 6.8e corresponds to the higher resolution spectrum of the same emitter. The spectra were recorded at 10 K. From the spectrum, a Debye-Waller (DW) factor, DW = IZPL/Itot = 0.87 was deduced, a value higher than that of the nitrogen-vacancy colour centre in diamonds (0.04) and comparable with that of SiV and GeV defects.

To verify that the centre is indeed a single-photon emitter, a second-order autocorrelation function, $g^2(\tau)$, was recorded and is shown in Figure 6.8f. The data are fitted by employing a standard three-level model for the colour centre

$$\boldsymbol{g^2(\tau) = 1 - (1 + a)e^{-\tau/\tau_1} + ae^{-\tau/\tau_2}} \qquad \textbf{Equation 6.2}$$

, where $a$ is the bunching factor, while $\tau_1$ and $\tau_2$ are the lifetimes of the excited and metastable states, respectively. The fit yields a value of 0.26 for $g^{(2)}(0)$, indicating the quantum nature of the emission. The non-zero antibunching dip is due to the timing jitter of the detectors, similarly to previous studies [17], [290], [291]. Under increasing excitation power, a slight photo-bunching was observed, indicating the presence of a third shelving state.

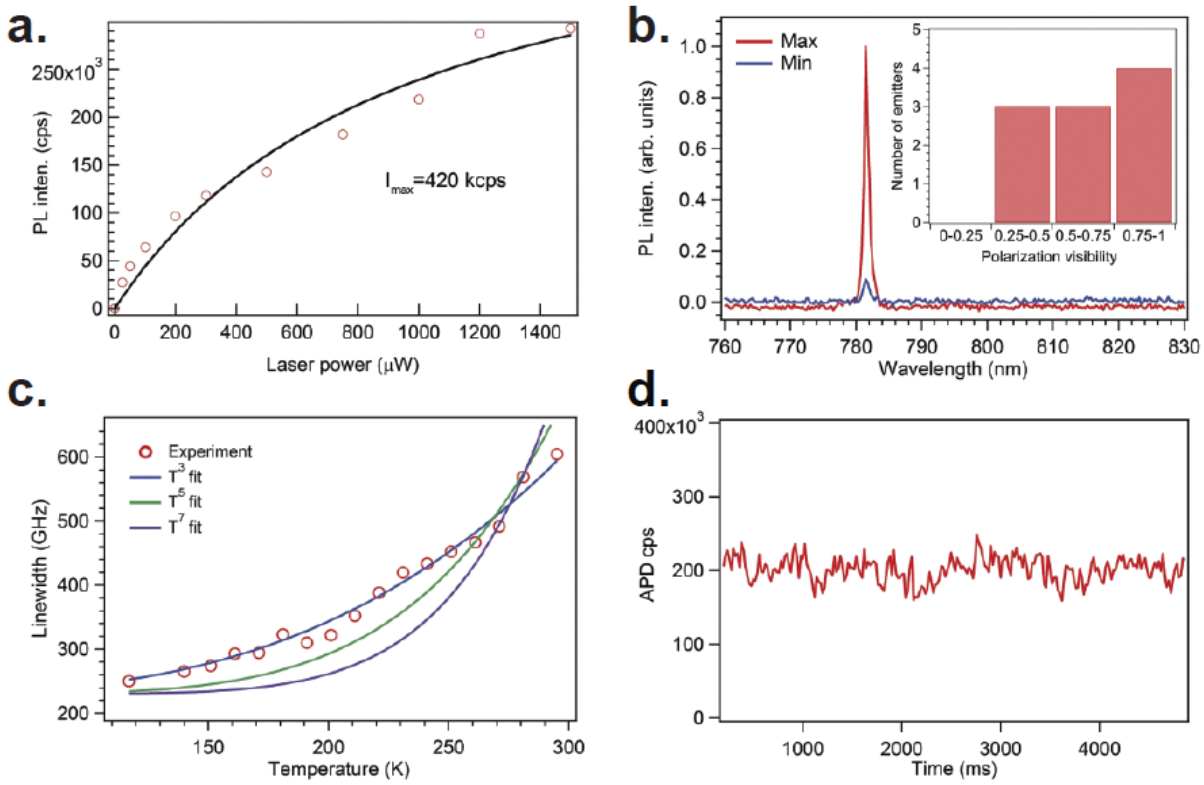


**Figure 6.9.** (a) Power-dependent fluorescence saturation curve (red open circles). The fit (solid red line) produces values of $I_{max}$, $I_{sat}$, and $P_{sat}$ of 420 kcounts/s, 210 kcounts/s, and 960 μW, respectively. The measurement was acquired with a bandpass filter (785 ± 22) nm. (b) Spectra showing maximum (red trace) and minimum (blue trace) emission polarisation from the emitter and taken with the use of a linear polariser. The data were taken using excitation laser power of 300 μW with 5s acquisition time. The visibility was determined to be 0.83. The inset shows a visibility statistic from 10 randomly chosen emitters. (c) Emission linewidth as a function of temperature for the emitter from 117 K to 295 K. The linewidths were obtained by fitting the Lorentzian function to the PL spectra. The experimental data are in red open circles while the blue, green, and purple solid lines are $T^3$, $T^5$, and $T^7$ power law fits, respectively. (d) Emission photostability as a function of time shows stable fluorescence. The bin time is 20 ms, the excitation wavelength and power are 700 nm and 1 mW, respectively. Measurements in (a), (b), and (d) were conducted at 10 K.

Additionally, the brightness and polarisation of the chosen emitter was investigated. The saturation curve for the emitter with the ZPL at ~780 nm is shown in Figure 6.9a. A fitting based on the following equation is used to extract characteristic information about the emitter:

$$\boldsymbol{I = I_{max} \times P/(P + P_{sat})} \qquad \textbf{Equation 6.3}$$

, where $I_{max}$ and $P_{sat}$ are the maximum emission rate and excitation power at which saturation is reached, respectively. The fit produces values for $I_{max}$ , $I_{sat}$ , and $P_{sat}$ of 420 kcounts/s, 210 kcounts/s, and 960 μW, respectively. This level of brightness is superior to that of NV [70] and SiV [102] centres grown on a non-iridium substrate. By rotating a linear polariser at the collection path and measuring the intensity from the ZPL of the emitter, a visibility of 0.83 was obtained with the following expression (Figure 6.9b):

$$\boldsymbol{VIS = \frac{I_{max} - I_{min}}{I_{max} + I_{min}}} \qquad \textbf{Equation 6.4}$$

, where $I_{max}$ and $I_{min}$ are the maximum integrated emission intensity and minimum integrated emission intensity, respectively. A visibility of almost unity indicates that the emission is associated with a single transitional dipole moment. The small deviation (0.17) from unity is attributed to an off-plane angular misalignment of the transition dipole moment with respect to the substrate. Furthermore, a visibility survey taken from 10 randomly chosen emitters (inset Figure 6.9b) shows a distribution of values ranging from 0.29 to 0.92, with the average visibility value of 0.69. These statistical data, therefore, suggest that the orientation of the emitter's dipole moments is random—a typical observation from colour centre embedded nanodiamonds [106].

Next, the linewidth as a function of temperature (117–295 K) was measured for the emitter to understand its phonon-coupling characteristic. Figure 6.9c presents the Lorentzian-fit linewidth values (red open circles) obtained at different temperatures as well as the $T^3$ (blue line), $T^5$ (green line), and $T^7$ (purple line) fits. The $T^3$ dependence describes the experimental data best, suggesting that the linewidth broadening from the emitter is mostly due to the coupling to low-energy phonons [96].

Finally, a temporal PL intensity measurement at 1 mW excitation power to obtain the fluorescence intermittency characteristic of the emitter as shown in Figure 6.9d was carried out. The emitter remained stable even at higher excitation powers.

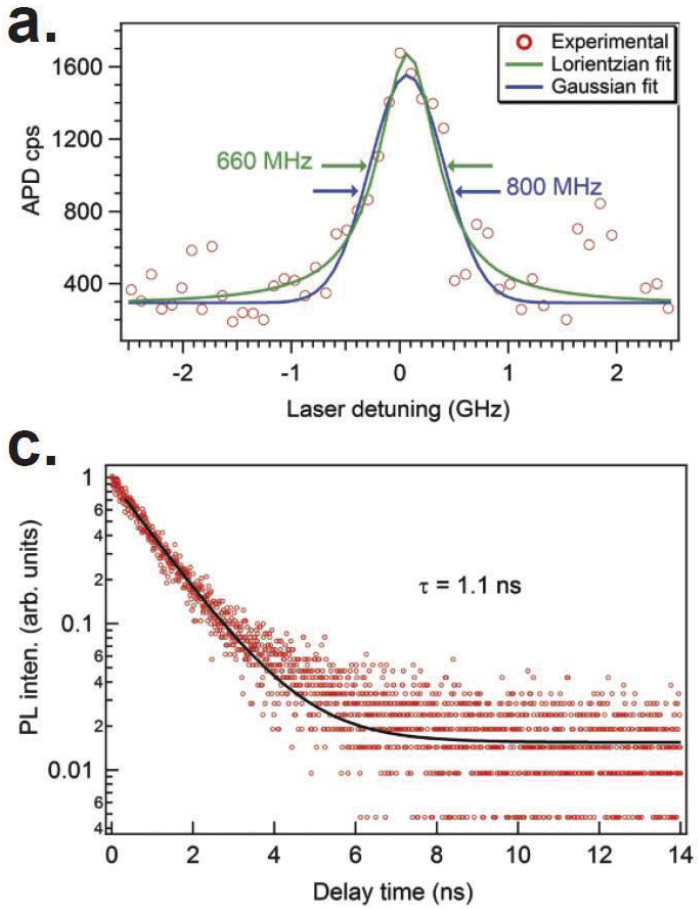


**Figure 6.10.** (a) Resonant photoluminescence excitation measurements on the single emitter with a ZPL peak at 779.61 nm. The excitation power used was 5 μW. Only photons from the PSB were collected using a long-pass filter. The experimental data are plotted as open red circles. The data were fit with either a Lorentzian (green line) or Gaussian (blue line) function. The measurement was done at 10 K. (b) Time-resolved PL measurements (red open circles) of the same single emitter measured at room temperature. A single-exponential fit gives rise to a lifetime of 1.1 ns for the emitter's excited state. The measurement was done with a 675-nm pulsed laser (100 μW, 10-MHz repetition rate, 100-ps pulse width).

To gain more information about the coherent properties of the SPEs and unveil their natural linewidth, resonant excitation measurements were performed. While cross-polarisation schemes are often used for studying quantum dots, [292] they were not practical in the measurement due to the high scattering from the diamond nanocrystals. To filter the excitation laser, a long-pass filter was used to collect only the emitter's phonon side band. Figure 6.10a shows a resonant excitation spectrum recorded at 5 μW with 5-GHz scan range and 70-MHz

resolution of the same SPE as shown in Figure 6.8 (centre wavelength at 779.61 nm or 384.54 THz). A single peak was clearly observed. The data are fit with a Lorentzian profile, producing a FWHM of 660 MHz and as a comparison with a Gaussian line shape, that results in a linewidth of 800 MHz. Using $\chi^2$ as the good-of-fit parameter, values of $6.53 \times 10^6$ and $6.71 \times 10^6$ for Lorentzian and Gaussian fits, respectively was obtained. From the fitting results, the Lorentzian fit arrived at slightly lower $\chi^2$ values than that from the Gaussian fit. The Lorentzian line shape results in a better fit when compared to the Gaussian fit, suggesting that the optical linewidth is less prone to spectral diffusion [12], [293], [294]. However, given the rather close $\chi^2$ values, at this stage, it is hard to conclude whether pure dephasing (*i.e.*, due to phonon interactions) or spectral diffusions are the main contributors to the line broadening.

The excited state lifetime of the emitter was measured using a pulsed laser to find out whether the emitter's linewidth is Fourier-Transform (FT) limited. The results are shown in Figure 6.10b. Using a single-exponential fit, the lifetime of the excited state of the emitter was determined to be $\tau_1 = 1.1$ ns. By applying the expression [10]

$$\boldsymbol{\gamma = 1/2\pi\tau_1} \qquad \textbf{Equation 6.5}$$

, where $\gamma$ and $\tau_1$ are the FT-limited linewidth (natural linewidth) and the excited state's lifetime of the emitter, respectively, a value for $\gamma$ of 145 MHz was estimated. This means that the emitter's linewidth is ~4.5 times broader than the expected value.

The linewidth broadening can arise from numerous factors including ultrafast spectral diffusion due to interaction of the strong emitter dipole with fluctuating electric fields from surrounding defects (inhomogeneous broadening), or alternatively, a homogeneous broadening due to phonon coupling. In addition, spectral diffusion often results in intensity fluctuations, associated with slow frequency jumps, which were not observed in the experiments. Based on these considerations, combined with the more favourable Lorentzian fit, it is concluded that the line broadening is predominantly due to phonon interactions. Similar behaviours were also reported for the SiV [117], [128] and the GeV [124] in diamonds. Despite the line broadening, achieving a sub-GHz linewidth from single emitters in nanodiamonds— particularly at the NIR spectral range—is valuable, as it opens pathways to coupling these emitters to high-quality optical resonators and photonic cavities [295], [296].

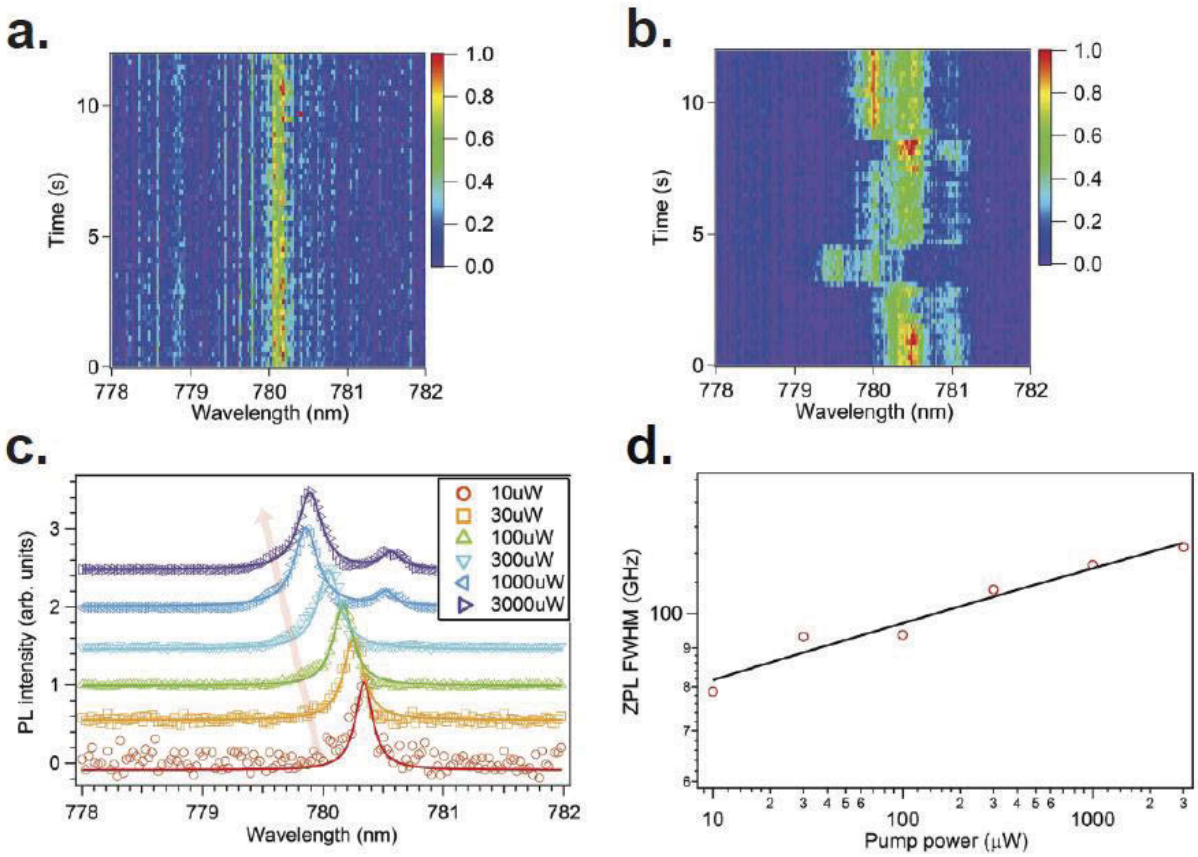


**Figure 6.11.** Spectral stability measurements taken from the emitter at 300 μW (a) and 3 mW (b). All the spectra shown were normalised. (c) Power-induced linewidth broadening measurements for the same emitter with laser power increasing from 10 μW to 3 mW. The open markers and solid lines are experimental and fit data, respectively. The red semitransparent arrow serves as a guide to the eye for the shift in the spectra. (d) Lorentzian-fit FWHM of the linewidth of the emitter with respect to the pump power from (c). The data are fit to a power function. The spectral broadening is evident.

Next, the emitter's linewidth off-resonantly as a function of laser power was measured to determine the photostability of the emitter under increasing excitation power. Figure 6.11a and b show the optical stability of the emitters under a relatively low 300-μW and high 3-mW excitation laser power, respectively. For these measurements, a total of 200 PL spectra were acquired at intervals of 200 ms. At low power (300 μW), almost no spectral diffusion or blinking to a different frequency was witnessed (within the spectrometer resolution). Conversely, at the higher excitation power of ~3 mW, the spectral fluctuation of the ZPL became noticeable. Spectral jumps as large as ~1.5 nm away from the ZPL position were observed, which are several orders of magnitude higher than the measured FWHM of ~660

MHz. This suggests that the emitter is highly susceptible to the strength of the laser electromagnetic field, and it may possess a linear permanent dipole behaviour that may result in spectral diffusion under increased excitation power. Additionally, an increased pumping intensity may result in photoionization—similarly to what occurs with the NV centre [297]. Photoionization will result in a frequency drift and can be evidenced as blinking. Note, however, that the spectral jumps occurred on the time scale of seconds, which means techniques such as dynamic stabilisation using applied electric fields can be employed to stabilise the emitter under high excitation power [80].

In addition to the power induced blinking, the ZPL exhibits broadening as a function of excitation power. Figure 6.11c shows several spectra from the same SPE under increased excitation powers which reveal power broadening and a blue shift in the ZPL spectral positions. Figure 6.11d presents a plot of the FWHM values as a function of power, showing a good fit with a power function that was employed previously for defects in solids [298]. These measurements are also in agreement with previous optical studies on carbon nanotubes, suggesting that the broadening arises from an increase of the local temperature induced by an increase in power of the excitation laser [299].

Amongst colour centres in diamonds, only SiV, GeV, and an unknown NIR defect [294] exhibited narrow lines amenable to resonant excitation. While I cannot categorically exclude that the emitters are highly detuned SiV defects, I do not believe that this is the case for the following reasons: (1) I have not observed splitting into 4 spectral lines at cryogenic temperatures—a typical signature of a single SiV defect, even under high strain environment as reported by Evans *et al.* [129] Indeed, some cases report that not all SiV defects exhibit splitting [96], [300] but majority of them do. In this case, no splitting was observed in any of the lines. (2) The studied emitter's ZPL at ~780 nm is also far from the standard SiV emission centred at 738 nm [18]. While detuned single SiVs were observed at ~750–760 nm range, [91], [301] there is no clear indication that single negatively charged SiVs can have ZPLs farther in the NIR. Previous reports by Neu *et al.* [194] suggested that another NIR transition of the SiV exists, but this is much weaker than the main transition, in stark contrast to our observation as shown in Figure 6.8b. (3) I clearly observed single bright emitters in addition to the ensemble of weak SiVs. While previous reports showed that single SiVs can emit at wavelengths higher than 738 nm, [91], [194] there is no evidence for single-photon emission from these lines when an additional ensemble of SiV emitters is present, nor there is a proof that these additional lines are in fact SiV defects.

The observed emitters in the work could be attributed to Cr-related impurities, as the sample was grown on sapphire, in accordance with a similar procedure reported in previous studies, [302] although previous measurements from these emitters revealed broader GHz lines [294]. The incorporation of chromium can occur during the growth since the plasma slightly etches the sapphire allowing the chromium atoms to diffuse into the diamond during growth. Another viable explanation is the discovered narrowband emitters that appear at secondary nucleation sites and extended defects in CVD-grown nanodiamonds as discussed in the previous section 6.1. As seen from the SEM image in Figure 6.8a, many nanodiamonds possess crystal defects and therefore give rise to the narrowband PL lines, as indeed observed in the experiments. The attribution of these lines to the morphological defects is plausible and offers advantage since such nanodiamonds can be easily grown in standard laboratory settings. This is, for instance, easier than growing nanodiamonds containing GeVs or SiVs as they require specific doping control. The presented emitters are also slightly brighter than the currently available nanodiamonds hosting SiVs (with exception of NDs grown on iridium) and GeVs. While I cannot conclusively identify the origin of the emitters, the production of these emitters from standard growth offers the unique opportunity to explore quantum optics experiments and relevant applications with single nanodiamond emitters in the NIR.

Table 6-1 shows a summary of the optical properties of the investigated narrowband emitters and compares them to other prominent diamond colour centres, mainly the SiV, NV and GeV defects. The narrow band emitter possesses the highest DW factor at 0.85 and boasts a short lifetime of 1.1 ns which is comparable to both the SiV and GeV colour centres. The saturation power, $P_{sat}$, is not as high as the SiV or GeV emitter but is three times brighter than the NV defect.

**Table 6-1** Comparison of optical properties between SiVs, NVs, GeV colour centres and the narrowband emitters [16], [17], [102], [142], [303]–[305].

| **Property** | **Narrowband emitter** | **SiV** | **NV** | **GeV** |
|---|---|---|---|---|
| ZPL (nm) | 780 | 738 | 637 | 602 |
| FWHM (nm) | 0.16 | ~6 | > 100 | 4.5 |
| Lifetime (ns) | 1.1 | 1 | 20 | ~1.4 |
| Photostability | Extremely high | Extremely high | Extremely high | Extremely high |
| Quantum efficiency | -- | 0.05 | 0.7 | -- |
| DW | 0.85 | 0.8 | 0.04 | 0.26 |
| $I_{(max)}$ (kcounts/s) | 420 | 1500 | 5700 | 300 |
| $I_{(sat)}$ (kcounts/s) | 210 | 200 | 252 | 204 |
| $P_{(sat)}$ (μW) | 960 | 6920 | 320 | 1900 |

In conclusion, the study shows promising optical properties of SPEs with ZPLs at the NIR (~780 nm). The resonant excitation measurements suggest that the SPE has a FWHM of ~660 MHz, broadened likely by interactions with phonons. The studied emitter does not show any blinking under resonant excitation and low power excitation. The SPE exhibits high DW factors exceeding 0.85, with fast florescence lifetime and fully polarised emission. These results should stimulate more studies into the promising attributes of NIR emitters in nanodiamonds and their use in quantum photonics applications.

# Chapter 7 Versatile Multicolour Nanodiamond Probes for Biological Intracellular Imaging and Targeted Labelling

This chapter shifts from nanophotonic and optoelectrical applications of diamond samples to biological applications of nanodiamond crystals. Diamond has excellent properties for use in biological applications, namely its biocompatibility due to being made out of carbon, its photostability, and its ease of functionalisation.

Diamond nanoparticles that host bright luminescent centres are attracting attention for applications in bio-labelling and bio-sensing. Beyond their unsurpassed photostability, diamond can host multiple colour centres, from the blue to the near infra-red spectral range. While nanodiamonds hosting nitrogen vacancy defects have been widely employed as bio-imaging probes, production and fabrication of nanodiamonds with other colour centres is a challenge. In this work, a large-scale production of fluorescent nanodiamonds (FNDs) containing a NIR colour centre – namely the SiV defect, and the first demonstration of their uptake and localisation inside cells for bio-imaging is reported. More importantly, the concept of applying different colour centres for multi-colour bio-imaging to investigate intercellular processes is demonstrated. Furthermore, two types of FNDs within cells can be easily resolved by their specific spectral properties, where data shows that SiV FNDs initially dispersed throughout the cell interior while NV FNDs localised prominently in close proximity to the cell nucleus. The reported results are the first demonstration of SiV colour centres and multi-colour labelling with FNDs that can pave the way for the wide-ranging use of FNDs in applications, including bio-sensing, bio-imaging and drug delivery applications. Olga Shimoni and Kerem Bray conceived the idea. Leonard Cheung fabricated the nanocrystals. Kerem Bray and Khondker Rufaka Hossain cultured the cells and performed confocal microscopy. Kerem Bray characterized the nanodiamonds and analysed the data with help from Olga Shimoni. Igor Aharonovich, Stella Valenzuela and Olga Shimoni supervised the work. All the authors discussed and wrote the manuscript.

## 7.1 Introduction

Targeted sub-cellular imaging is crucially important for understanding biological processes and developing new drugs. To this extent, fluorescent probes are sought after for a range of potential applications, from mapping cellular environments, measuring cell temperatures and amino acids concentrations to monitoring drug localisation within the body [93], [306]. Despite numerous advantages, the majority of fluorescent probes, such as quantum dots or fluorescent proteins, exhibit undesirable properties, including blinking, photo-bleaching and/or toxicity, limiting their use for biological imaging [138], [140].

FNDs particles are a promising material for bio-sensing and bio-imaging due to their ability to host a variety of bright, photostable colour centres originated from atomic defects in the carbon lattice [44], [137]. Furthermore, FNDs possess inherent biocompatibility and high surface tuneability [59], [307], [308]. To date, there is abundance of research on the application of FNDs containing NV defects for bio-imaging and drug delivery [35]–[40], [309], [310]. However, NV FNDs have excitation and emission in visible range that can contribute to tissue absorption and auto-fluorescence. Therefore, FNDs with narrowband emission at the NIR spectral range are particularly advantageous to achieve a better signal to noise ratio imaging for long term cellular imaging [311]. In addition, excitation of NIR emitters can be achieved using a longer wavelength, therefore minimising tissue light absorption. Finally, use of NIR luminescent probes is valuable in bio-imaging as it presents a greater tissue penetration depth compared to visible range fluorophores [311].

One defect that meets these criteria is the SiV colour centre in diamond that has narrowband emission at 738 nm. Despite clear advantages of SiV ND properties, reliable fabrication and application of SiV FNDs for sustained biological applications remains a pressing issue and challenge [312].

Herein, I report on a scalable approach for the production of FNDs hosting the SiV emitters, confirm that the fabricated nanoparticles hold NIR fluorescent properties and with sizes compatible for bio-imaging. The SiV colour centre is ideal as it can fluoresce in the near infra-red region, which allows us to excite the sample at higher wavelengths which reduces cell autofluorescence. I further demonstrate the concept of utilisation of FNDs as multi-colour staining for intercellular immunofluorescence. In fact, for the first time I show simultaneous labelling of cell interior using two different types of FNDs, such as containing SiV and NV

defects. Diamond surfaces can be easily modified to attach targeting biomolecules using standard chemical procedures, such as carbodiimide chemistry, to achieve a specific labelling. Additionally, I effectively resolved two types of FNDs within cells by their specific spectral properties, where I find that SiV FNDs dispersed throughout the cell interior, while the NV FNDs localised to the perinuclear region of the cell. Finally, I show long term imaging of FNDs up to 5 hours, where timed uptake of FNDs showed cell induced mechanism of FNDs aggregation. The results are the first demonstration of multi-colour labelling with FNDs that can pave the way for the wide-ranging use of FNDs in applications, including bio-sensing, bio-imaging and drug delivery applications. Furthermore, the SiV colour centre is ideal as it can fluoresce in the NIR region, which allows excitation of the sample at higher wavelengths thus reducing cell autofluorescence.

## 7.2 FNDs in cells

The FND containing NV colour centres were purchased from FND Biotech (Taiwan) with a particle size of ~35 nm. The SiV containing FNDs have been produced via bead-assisted sonication disintegration (BASD) process [91], [259]. The growth of dispersed polycrystalline diamond containing SiV colour centres was performed on a silicon substrate using a MPCVD reactor, with a hydrogen/methane ratio of 50:1 at 50 Torr, a microwave power of 1500 W, equipped with a cooling stage, from 4−6 nm detonation nanodiamond seeds on a silicon wafer. Silicon atoms from substrate were incorporated in a diamond lattice, leading to creation of SiV defect in the diamond nanocrystalline film. The diamond films were further processed to yield diamond nanocrystalline particles. The process of fabrication of FNDs can be up scaled depending on the capacity of the CVD reactor. The unwanted silicon substrates were dissolved in 30% potassium hydroxide (KOH) solution at 89$^{o}$C for several hours. The detached polycrystalline diamond thin films were separated from the KOH solution using a corning filtration system with a 0.22 μm polyethersulfone membrane while leaving the diamond film fragments behind. The separated diamond film fragments were subsequently dissolved in dimethyl sulphoxide (DMSO) to remove the residual KOH crystals. To fabricate individual ND particles, diamond thin film was disintegrated into nanoparticles by BASD process. Specifically, 10 mg of zirconia beads were added to the diamond film solution and subjected to sonication (probe sonicator) for 2 hours with a 2/1 second on/off pulse. The zirconia and DMSO were removed through centrifugation at 4000 rcf. and washed with water three times.

To remove residual zirconia fragments and graphite, the diamond solution then underwent acid reflux with a 1:1 solution of nitric and sulphuric acid within an oil bath at 83$^{o}$C for 24 hours. The acid solution was removed by centrifugation for 30 minutes and replaced with water. The size of the particles was measured using dynamic light scattering (DLS) and were shown to be ~141.01 ± 40.12 nm in diameter with a zeta potential of -17.40 ± 3.60 mV indicating that the FNDs containing SiV colour centres are relatively small and dispersed in solution. The flow of the fabrication process is shown in Figure 7.1. Initially the yield of SiV FNDs was on the order of ~0.5 – 1 mg. After practise and refinement of the process the yield of the SiV FNDs is now on the order of 10s of mg. The initial concentration of the FNDs was determined by weight. A known amount of diamond solution was placed into a tube with known weight. The solution plus the tube was weighed before and after evaporating away the solution, leaving behind only a diamond powder.

Raman spectroscopy unambiguously showed the characteristic diamond peak at 1332cm$^{-1}$ (Figure 7.2) in the fabricated SiV FNDs. To prove that the diamond particles host bright SiV colour centres, the SiV FND dispersion was characterised using a home built scanning confocal microscope using a 532 nm excitation source through a high numerical aperture (NA = 0.9) objective at room temperature (Figure 7.2d). FNDs with NV centres were pre-characterised using the same confocal system. Figure 7.3a shows the photoluminescence spectra, where I observed the characteristic ZPL at 738 nm and at 640 nm for the SiV (red) and NV (blue) colour centres, respectively. NV FNDs produce a broad red fluorescence rending from 640 nm to 730 nm, while SiV FNDs show a sharp narrow peak ranging between 735 nm to 760 nm. It can be clearly seen that these two types of FNDs can be distinguished using their spectral characteristics.

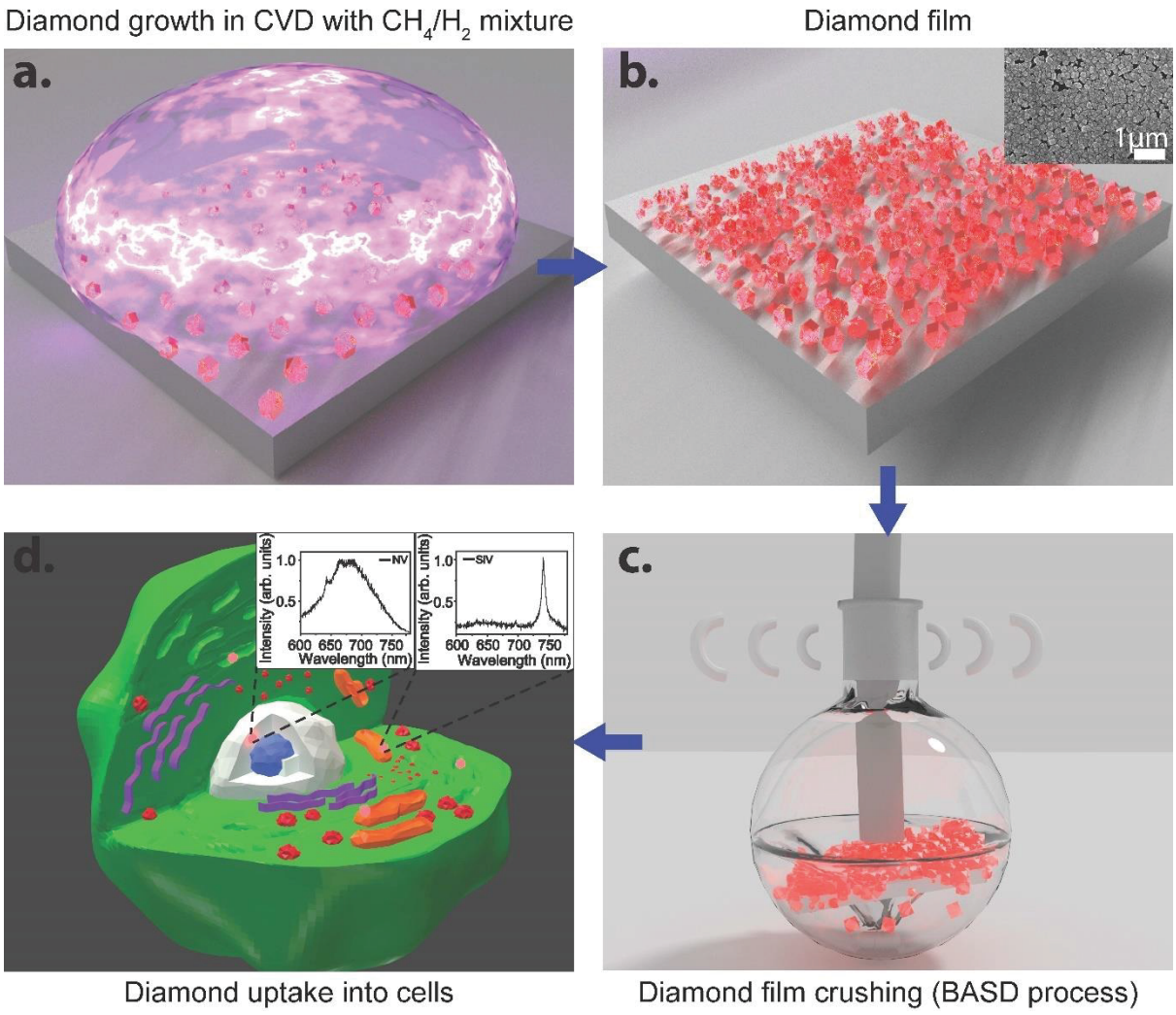


**Figure 7.1.** Synthesis of SiV containing FNDs. (a) Silicon substrate seeded with detonation nanodiamond (4-5 nm) is subjected to CVD plasma using a standard hydrogen/methane gas mixture to produce highly dense polycrystalline diamond thin film. (b) SEM micrograph (inset) shows diamond thin film of SiV containing FNDs crystals. The CVD diamond film was isolated and was subjected to the BASD process. (c) To remove residual particles and graphite, the diamond solution then underwent strong acid reflux for 24 hours, washed through centrifugation with water to produce SiV FNDs in solution for use in intracellular bio-imaging (d).

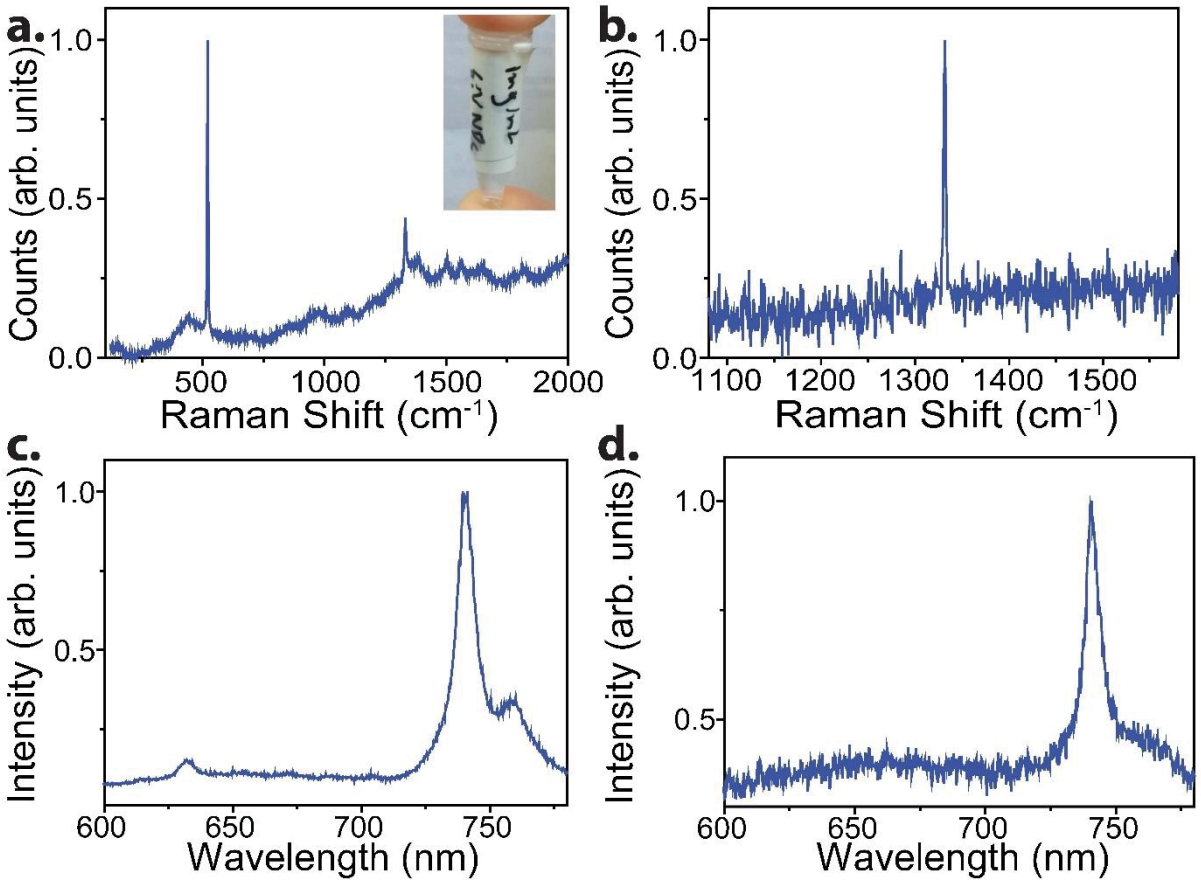


**Figure 7.2.** Characterisation of fabricated diamond films and particles. (a) Raman spectra of CVD grown diamond particles with a 633 HeNe laser. It shows the characteristic silicon and diamond peak at 520 $cm^{-1}$ and 1333 $cm^{-1}$ respectively. Inset: Photo of the processed CVD grown particles in aqueous solution. (b) Raman spectra of processed FNDs after purification, exhibiting the Raman diamond peak at 1333 $cm^{-1}$. (c) Photoluminescence spectra of CVD grown diamond particles at RT using a 532 nm excitation source, it shows the characteristic SiV emission at 738 nm. (d) Photoluminescence spectra of processed FNDs showing that they still host bright SiV colour centres.

The size and zeta potential of the fabricated FNDs were characterised by Zetasizer Nano ZS (Malvern Instruments Ltd) instrument (Figure 7.3b). The measurements of hydrodynamic size show the FNDs to be 141.1 ± 49.4 nm and 44.8 ± 13.7 nm in diameter with a zeta potential of -17.4 ± 3.7 mV and -45.4 ± 21.2 mV for the diamonds containing SiV and NV colour centres, respectively (Table 7-1). The origin of negatively charged zeta potential is due to oxidation treatments that FNDs were subjected during the purification processes that produced oxygen-

containing groups, such as carboxylic, hydroxyl or ester groups. The results confirm that the ND samples are relatively small, stable and dispersed in aqueous solution that is suitable for bio-applications. By upscaling the fabrication of FNDs hosting varying colour centres and modifying the surface, FNDs may be applied to investigate cellular processes in living organisms.

**Table 7-1.** Characterisation of various FNDs samples through DLS using a 633 nm HeNe laser source. Standard deviation was calculated based on measurements of at least three different samples

| Sample | Size distribution by Number (nm) | Size distribution by Volume (nm) | Zeta Potential (mV) |
|---|---|---|---|
| **NV FNDs** | 44.8 ± 13.7 | 60.9 ± 25.8 | - 45.4 ± 21.2 |
| **NV FNDs – TAT** | 68.6 ± 22.0 | 99.3 ± 59.7 | + 32.8 ± 5.6 |
| **SiV FNDs** | 141.1 ± 49.4 | 153.1 ±39.3 | -17.4 ± 3.7 |

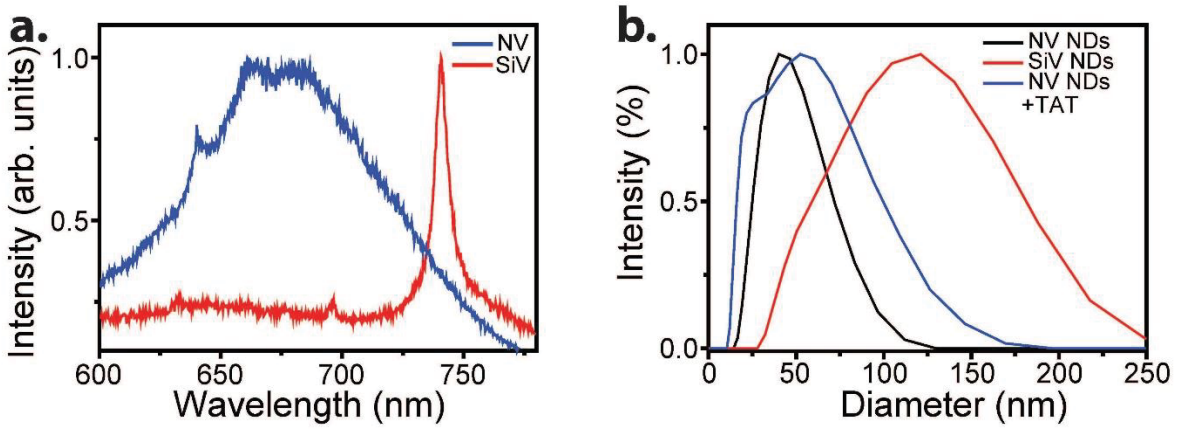


**Figure 7.3.** Characterisation of different types of FNDs. (a) Normalised, typical room temperature spectra of SiV (red) and NV (blue) colour centres under a 532 nm excitation source. Two spectra can be clearly separated based on their optical properties. (b) Particle size distribution by number of SiV (red), NV (black) and NV containing FNDs with TAT (blue) showing sizes <150 nm in diameter.

Once I established the robust fabrication of the SiV containing FNDs, I proceeded to use them in bio-labelling. The goal of this work was to demonstrate multiple, distinct intracellular targeting via conjugation of FNDs with targeting species. To this end, I utilised the convenience of carbon surface functionality to attach functional biomolecules to achieve biologically active nanoprobes. Specifically, FNDs containing NV defects were conjugated with trans-activating transcriptional activator (TAT, China Peptides Ltd, 1mg/mL) peptides using carbodiimide chemistry. TAT peptide is a small basic cell penetrating peptide (CPP) derived from HIV-1 [313], and is known for successful cell membrane penetrating functionality that is effective at delivering materials of varying sizes from small particles to proteins into primary and other cells [314]–[316]. To create the NV FNDs-TAT complex 300 µL of 1 mg/mL solution of FNDs containing NV colour centres was mixed with 5 µL of 10 mg/mL 1-Ethyl-3-(3-dimethylaminopropyl) carbodiimide (EDC) and 50 µL of 10 mg/mL N-Hydroxysuccinimide (NHS). After sonication 200 µL of 2.5 mg/mL of TAT peptides in HEPES buffer was added then sonicated for an additional 2 hours to ensure complete surface coverage. The successful conjugation was monitored by zeta potential charge change from -45.4 ± 21.2 mV to +32.8 ± 5.6 mV due to multiple positively charged lysine residues on the peptide chain. On the other hand, the bare SiV containing FNDs can be used to target endosomes.

Chinese Hamster Ovary epithelial cells (CHO-K1) were grown in Dulbecco's Modified Eagle Medium: Nutrient Mixture F-12 (DMEM/F12 Glutamax, Life Technologies) at 37$^{o}$C in 5% $CO_2$ incubator for a couple of days to reach ~ 80% confluency. To lift off these adherent cells from the plastic container, ~2 mL of 5 mM Ethylenediaminetetraacetic acid (EDTA) in serum-free media (DMEM/F12) was added to cover the cells for 2-5 minutes at room temperature. Lifted cells were diluted with ~10 mL of 5% Foetal Bovine Serum (FBS) in DMEM/F12, transferred to a 15 mL falcon tube, and centrifuged at 1200 rpm for 4 minutes. 1/10 of the cells were split and transferred into a new flask. The cells are then grown for the desired time (1-3 days) at 37$^{O}$C + 5% $CO_2$.

The macrophages were prepared by using the monoblast-like human histiocytic lymphoma cell line U937 which was induced by using phorbol 12-myristate 13-acetate (PMA, Sigma Aldrich) at concentrations of 8-16 ng/ml to undergo differentiation into macrophages. U937 cells were cultured in RPMI media supplemented with 10% heat-inactivated FBS at 37$^{o}$C + 5% $CO_2$ incubator.

The cells were incubated with either FNDs with NV defects or SiV containing FNDs, at concentrations ranging from 5 µg/mL - 100 µg/mL and their viability subsequently assessed to

understand the effect of nanodiamonds on the cultured cells. Cell viability was determined by the AlamarBlue (7-Hydroxy-3H-phenoxazin-3-one 10-oxide) assay (Life Technologies, Australia) according to the manufacturer instructions. The absorbance of cells with AlamarBlue reagent and various diamond concentrations in addition to controls was measured at 600 nm using a microplate reader. Alamarblue was chosen because it is a quick, easy, and accurate out of the box method to determine cell viability. AlamarBlue exploits the natural abilities of cells to reduce resazurin to the fluorescent molecule, resorufin. Resazurin is the active ingredient of AlamarBlue, it is cell permeable, nontoxic compound that is nonfluorescent. When added to cells, resazurin is reduced to resorufin, which produces a bright red fluorescence. Viable cells continuously convert resazurin to resorufin, thereby allowing for a quantitative measure of cell cytotoxicity and viability[317].

CHO-K1 cells were grown in DMEM-F12 Glutamax cell culture medium, supplemented with 5% FBS, and the resultant cell suspension (~$1x10^5$ cells/mL) were dispersed into 96-well plates and incubated overnight to allow for cell adherence. The required concentrations of FNDs were added dropwise into 1 mL of cell media and incubated with the CHO-K1 cells at 37ºC for 3 hours. Cells without FNDs, grown under identical conditions were used as controls.

The monoblast-like human histiocytic lymphoma cell line U937 can be induced by phorbol 12-myristate 13-acetate (PMA) at concentrations of 8-16 ng/ml to undergo differentiation into macrophages. U937 cells were cultured in RPMI supplemented with 10% heat-inactivated FBS at 37ºC + 5% $CO_2$. To assess cell viability, $0.2 \times 10^6$ U937 cells were seeded into 24 well plates (BD Siosciences, USA) such that they were 70-80% confluent at the time of assay. 15 ng/ml PMA solution was added to each well and cells were incubated for 48 hours at 37ºC + 5% $CO_2$. The cells were then subsequently washed with PBS and replaced with fresh media and allowed to grow for another 4 hours, after which NV and SiV containing FNDs were incubated with macrophage cells at concentrations ranging from 5 μg/mL - 100 μg/mL. Macrophages were incubated with the FNDs at 37ºC + 5% $CO_2$ for 3 hours. Cells alone, grown under identical conditions were used as controls. 200 μL of 1 mg/ml of TAT peptide dispersed in 800 μL of DMEM/F12 media served as an additional control for cell viability with only TAT peptide.

Figure 7.4 shows the percentage (%) of cell viability following exposure to varying FNDs concentrations after 4 hours of incubation. Additionally, to assess the effect of FNDs over a sustained exposure time, the samples were measured after 24 hours (Figure 7.4b). The cell

viability percentage was determined by the absorbance of the FNDs in cells divided by the absorbance of the control. Error bars represent standard deviation between at least three independent measured samples. Cell viability studies demonstrated that at the tested concentrations of FNDs, two different types of cells, CHO-K1 cell line and U937 macrophages, show good viability after 4h and even after 24h (Figure 7.4). Interestingly, in some cases the cells appear to have increased cell growth as seen by the increased viability (which is directly proportional to cell number), e.g. Figure 7.4c, macrophage cells exposed to NV FNDs at 5μg/mL, which may indicate that the NDs were capable of stimulating cell replication. Tested concentrations of FNDs were below 100 μg/mL in accordance with multiple published studies using similar nanoparticles [318]–[320]. A student t-test conclusively shows that fluctuations in cell viability were not statistically significant, indicating that the FNDs are non-toxic to the cells at the tested concentrations.

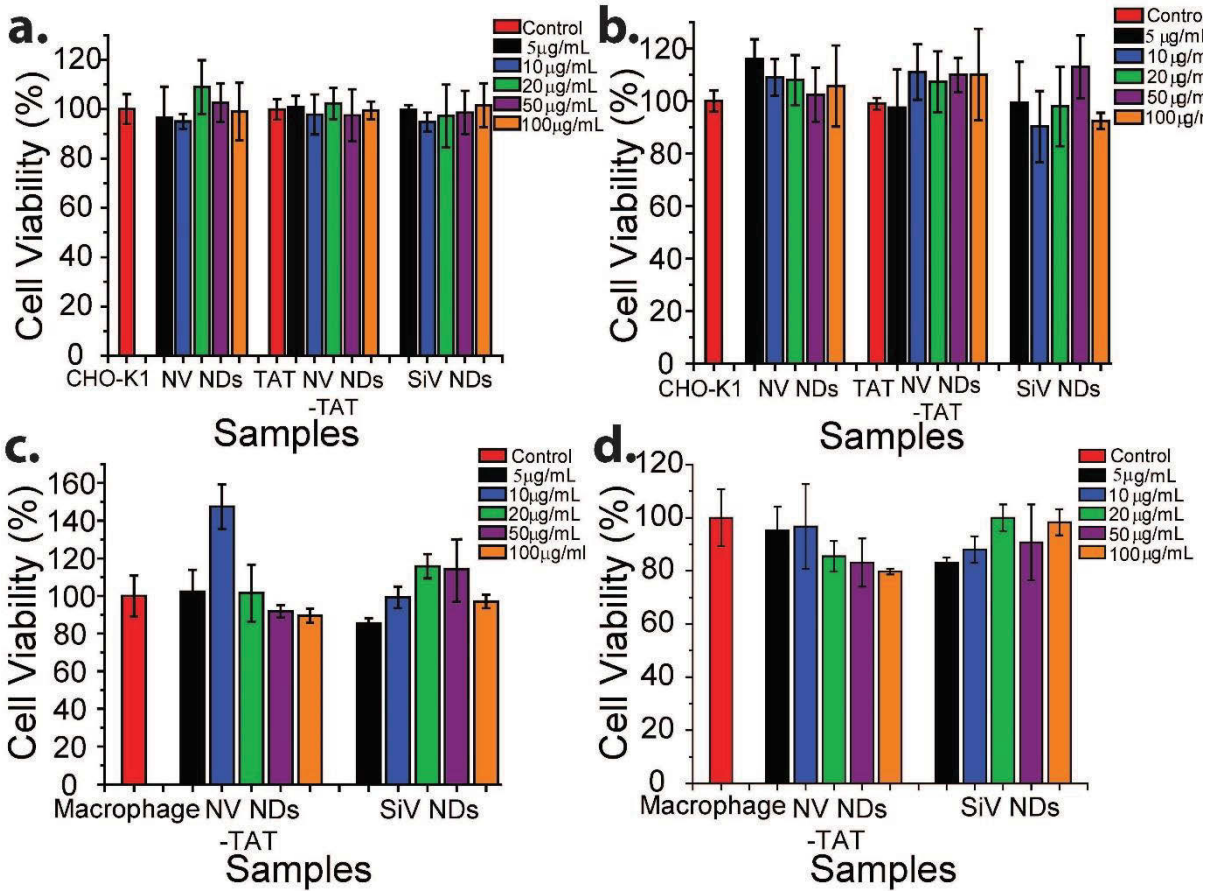


**Figure 7.4.** A cell viability assay for FNDs samples of varying concentrations (5 μg/mL – 100 μg/mL) in CHO-K1 and macrophage cells with controls after (a and c) 4 and (b and d) 24 hours of incubation at 37$^{O}$C. The small fluctuations are not statistically significant, indicating that the

FNDs are non-toxic to the CHO-K1 and macrophage cells. Error bars represents standard deviation of at least three different samples (SD, n=3).

Biological imaging studies were then performed on the two cell lines that were individually incubated with 50 μg/mL of FNDs solutions in cell media (37°C + 5% $CO_2$). After cells had reached confluency, they were split as described previously. ~0.5 x $10^6$ cells with cell media were transferred to a 35 mm Fluorodish cell culture dish purchased from World Precision Instruments (WPI). The cells were incubated overnight at 37ºC + 5% $CO_2$ to reach optimal confluency and to allow the cells to adhere to the surface of the imaging dish. 60 μL of the 50 μg/mL of FNDs was transferred to the imaging dish and incubated for an additional 2-3 hours to ensure uptake of the FNDs. The media was removed and replaced with 1 mL of 4% paraformaldehyde in PBS and incubated at room temperature for 15 minutes. The sample was then washed three times with 1 mL of PBS for 2-5 minutes. To allow for fluorescence labelling of cell interior, 1 mL of permeabilisation solution (0.5% Triton X-100) was added and incubated at room temperature for 15 minutes. The sample was subsequently washed and replaced with 1 mL of blocking solution (3% BSA in DPBS) for one hour to reduce the amount of nonspecific binding in the sample, replaced with 1 mL of specific primary antibodies (LAMP-1, Life Technologies) diluted 1:1000 in a blocking solution and incubated for one hour at room temperature. The sample was washed and replaced with 1mL of Alexa Fluor 488-labeled secondary antibody diluted 1:1000 in PBS and incubated for one hour in the dark at room temperature. The sample was then washed and 2 drops of NucBlue (nucleus staining reagent) was added prior to confocal imaging. The samples were then excited by a Coherent OBIS 561 nm CW excitation source, the signal was then passed through a photo-multiplier tube/spectrometer with a collection range from ~570 nm to 740 nm for confocal microscopy cellular studies. Typically, 50 μg/mL of FNDs (SiV or NV-TAT or 50:50 ratio of SiV with NV-TAT) were mixed with cell media, added drop wise to the growing cell culture and incubated for 3 hours. The cells were subsequently fixed with a 4% paraformaldehyde/PBS solution, stained with a nucleus stain, NucBlue (Life Technologies, Australia), and subsequently imaged using an A1 Nikon confocal scanning laser microscope at room temperature equipped with 405 nm, 488 nm and 561 nm excitation laser sources.

The two types of FNDs – namely the ones containing the NV centres and the ones containing the SiV centres, can be individually distinguished based on their spectral differences (Figure

7.5). Explicitly, NV FNDs produce emission in the 620-720 nm region as a distinguished broad peak (Figure 7.5 b, c), while SiV FNDs generate a sharp peak in the region of 720-750 nm (Figure 7.5 d). The fluorescence of FNDs is stable with no photobleaching effect, this is useful for undertaking studies over time to help in understanding complex biological processes happening inside cells. Furthermore, excitation with 561 nm laser allowed us to avoid a large amount of auto-fluorescence that is usually generated by use of blue laser, such as 475 nm, for excitation of NV defects in diamond.

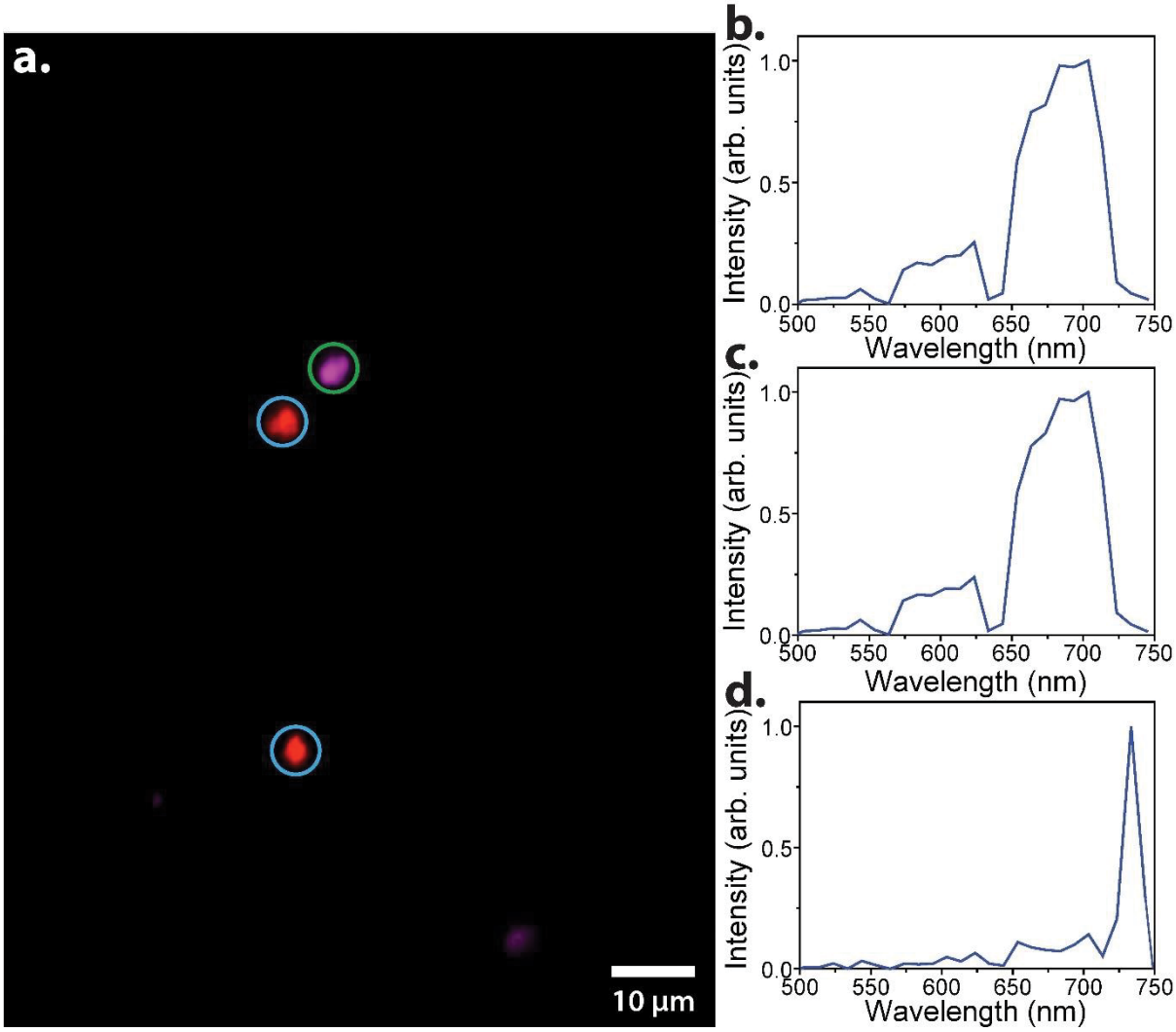


**Figure 7.5.** Confocal laser scanning microscopy of fixed CHO-K1 cells. Cells containing FNDs hosting (a) both SiV and NV-TAT were imaged using confocal microscopy using a 561 nm excitation collected by a spectrometer. The NV (blue circles) and SiV (green circles) colour centres are labelled for clarity. Scale bar 10 µm. Spectra were obtained from the circled FNDs and exhibited a strong (b, c) NV and (d) SiV emission. The NDs containing NV defects have a red false colour while the SiV defects have a purple false colour.

Figure 7.6 (a-d) shows the efficient uptake of FNDs hosting SiV colour centres (50 μg/mL) from cell media into the cells after 3 hours of incubation. Confocal microscopy revealed that the internalisation is relatively spontaneous, without additional chemical or mechanical force. Additionally, upon comparing confocal images of the control and cells containing FNDs with NV centres (Figure 7.6) I observed that the cell nucleus appears to remain healthy and undamaged following the introduction of FNDs. Previous studies by others have demonstrated that internalisation of FNDs occurs through endocytosis, specifically via micropinocytosis [319][321]. It can be seen that SiV FNDs appear to spread over the entire cell cytoplasm (Figure 7.6 (b-d)), while NV FNDs with TAT peptide are localised to discrete areas (Figure 7.6 (e-h)) at the same time point. As both types of FNDs have been well dispersed in cell media prior to cellular uptake, it is most likely that the nanoparticles are processed differently once inside cells. FNDs hosting NV colour centres would be internalised via a different non-receptor mediated process as their surface is conjugated with the TAT peptide (Figure 7.6 e-h) with highly positive charge leading to faster cellular response.

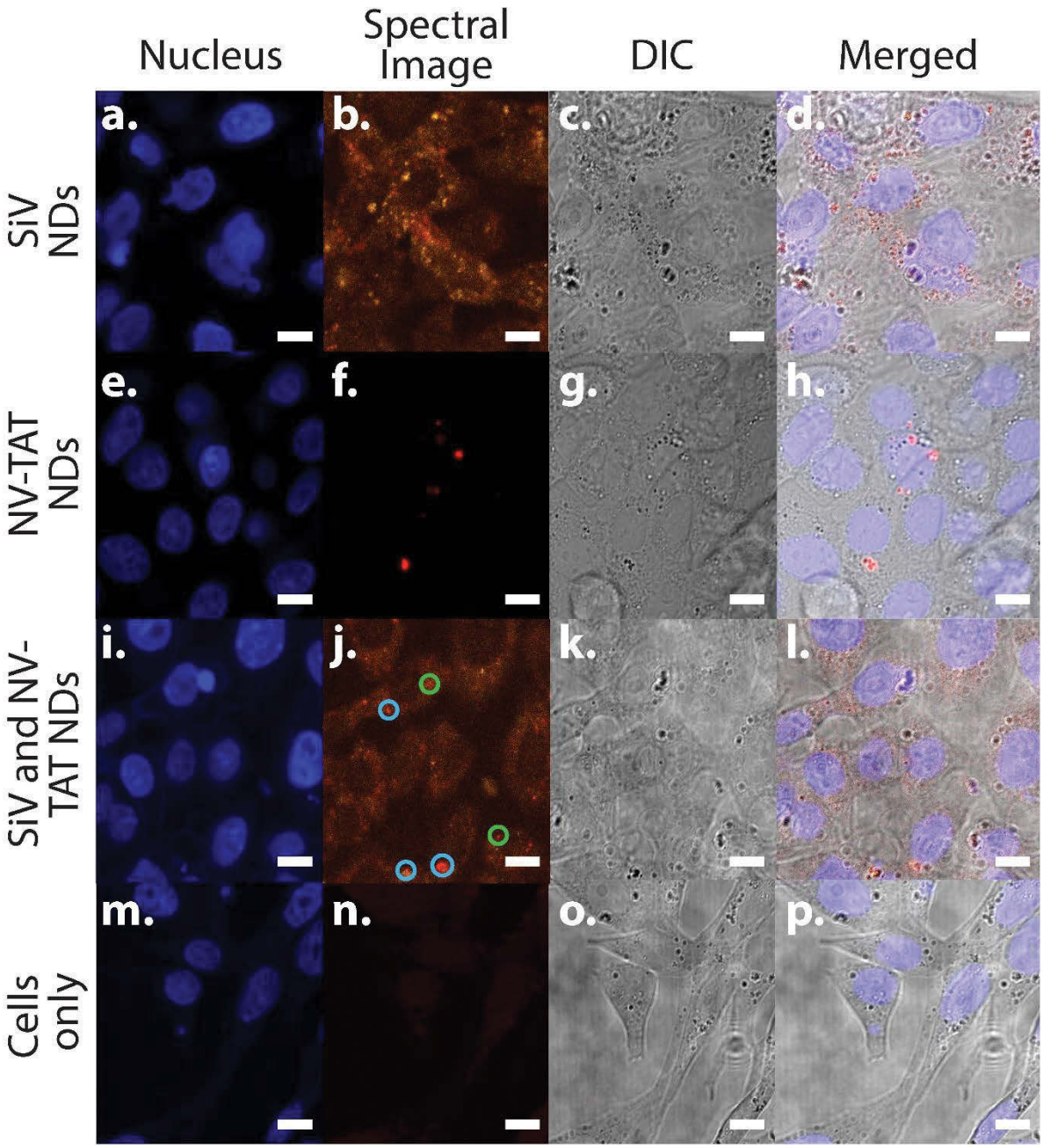


**Figure 7.6.** Confocal laser scanning microscopy of fixed CHO-K1 cells. Cells containing FNDs hosting SiV (a-d), NV (e-h), both SiV and NV-TAT (i-l) and control CHO-K1 cells (m-p) were imaged using confocal microscopy. 405 nm excitation (a, e, i, m) shows the NucBlue stained nucleus of the cells. 561 nm excitation collected by a spectrometer (b, f, l, n) shows the bright emission from the various FNDs colour centres (localised red spheres). A number of the NV (blue circles) and SiV (green circles) colour centres are labelled for clarity. The NV emitters preferentially accumulate at the periphery of the nucleus, while the SiV emitters are

dispersed throughout the cell cytoplasm. A wide field image (c, g, k, o) and merged (d, h, l, p) image shows the cellular membranes and scanned area of interest. The scale bars are 10 μm.

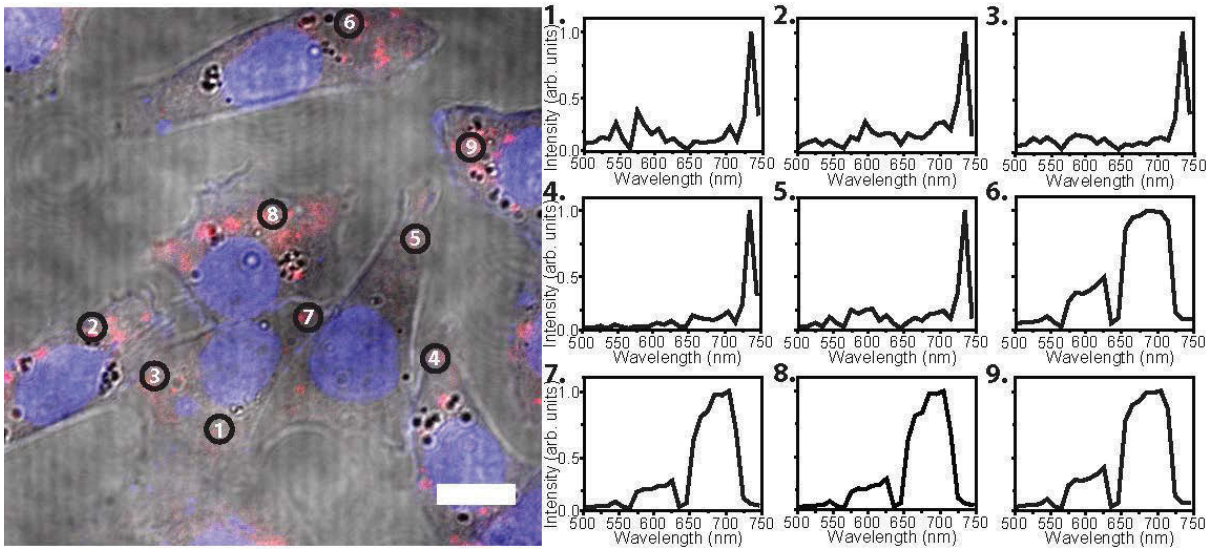


**Figure 7.7.** Bright field image merged with fluorescence confocal laser scanning microscopy imaged of fixed CHO-K1 cells. Cells containing FNDs hosting both SiV and NV-TAT were imaged using confocal microscopy equipped with a 561 nm excitation laser and emission collected by a spectrometer. Randomly selected 9 spots were characterised to reveal their spectral signatures. Spectra were obtained from the circled FNDs number 1, 2, 4 and 5 represent SiV NDs spectral emission, while spectra from spots number 6, 7, 8 and 9 are originated from NV NDs emission. Scale bar is 10 μm.

The NV FND-TAT particles in conjunction with bare SiV containing FNDs (50:50 ratio) incubated together with cells allow the dual tagging of CHO-K1 cells. I provide detailed spectral analysis of the nanoparticles inside the cells (Figure 7.7), where spectral emission of each fluorescent region clearly identifies the type of FNDs. Consequently, Figure 7.6 (i-l) shows successful dual tagging of the CHO-K1 cells containing FNDs hosting either SiV or NV colour centres. Each red spot in Figure 7.6 was confirmed by spectral analysis distinction to be FNDs containing either NV or SiV colour centres (only a few were labelled for clarity). It can be clearly seen that the NV FNDs (blue circles) preferentially accumulate at the periphery of the nucleus, while the SiV FNDs (green circles) are dispersed throughout the cell cytoplasm.

On the contrary, Figure 7.6 (m-p) show the control and the non-treated CHO-K1 cells with no fluorescence.

To further extend the work, I also show that all the types of FNDs internalise efficiently into macrophages. Figure 7.9 unambiguously shows the positions of the FNDs in the representative 3D reconstructed confocal z-stack, where individual images from different channels (blue, red, and wide field) taken at varying heights are spliced together to create a 3D rendering of the sample. The obtained z-stack images confirm that the FNDs are being internalised by the cells, with NV FNDs-TAT accumulate in perinuclear area, but are not entering the nucleus of the cells. Again, SiV FNDs were observed individually spread in the cytoplasmic area of cells. This shows that the FND particles can be used as dual tags in a cellular environment with no significant damage observed. More 3D reconstructed images can be found in the Figure 7.10 (CHO K1) and Figure 7.11 (U937 macrophages).

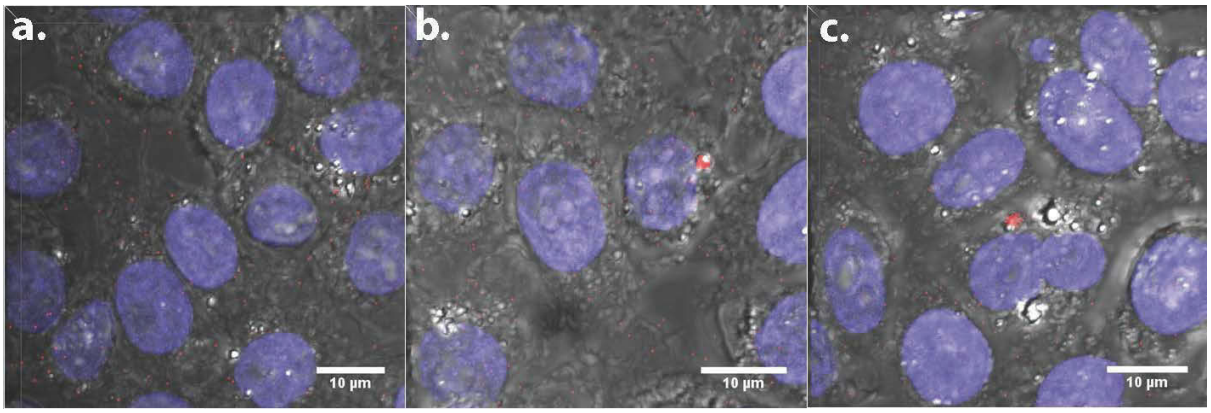


**Figure 7.8.** 3D reconstruction of confocal raster scan of CHO-K1 cells hosting (a) SiV (b) NV (c) both SiV and NV-TAT containing FNDs. 405 nm laser excitation (a, e, i, m) shows the NucBlue stained nucleus of the cells, 561 nm laser excitation was used to reduce cell auto-fluorescence and maximise the collected signal from the FNDs particles. Different angle from the 3D reconstruction of CHO-K1 cells can be seen in Figure 7.10.

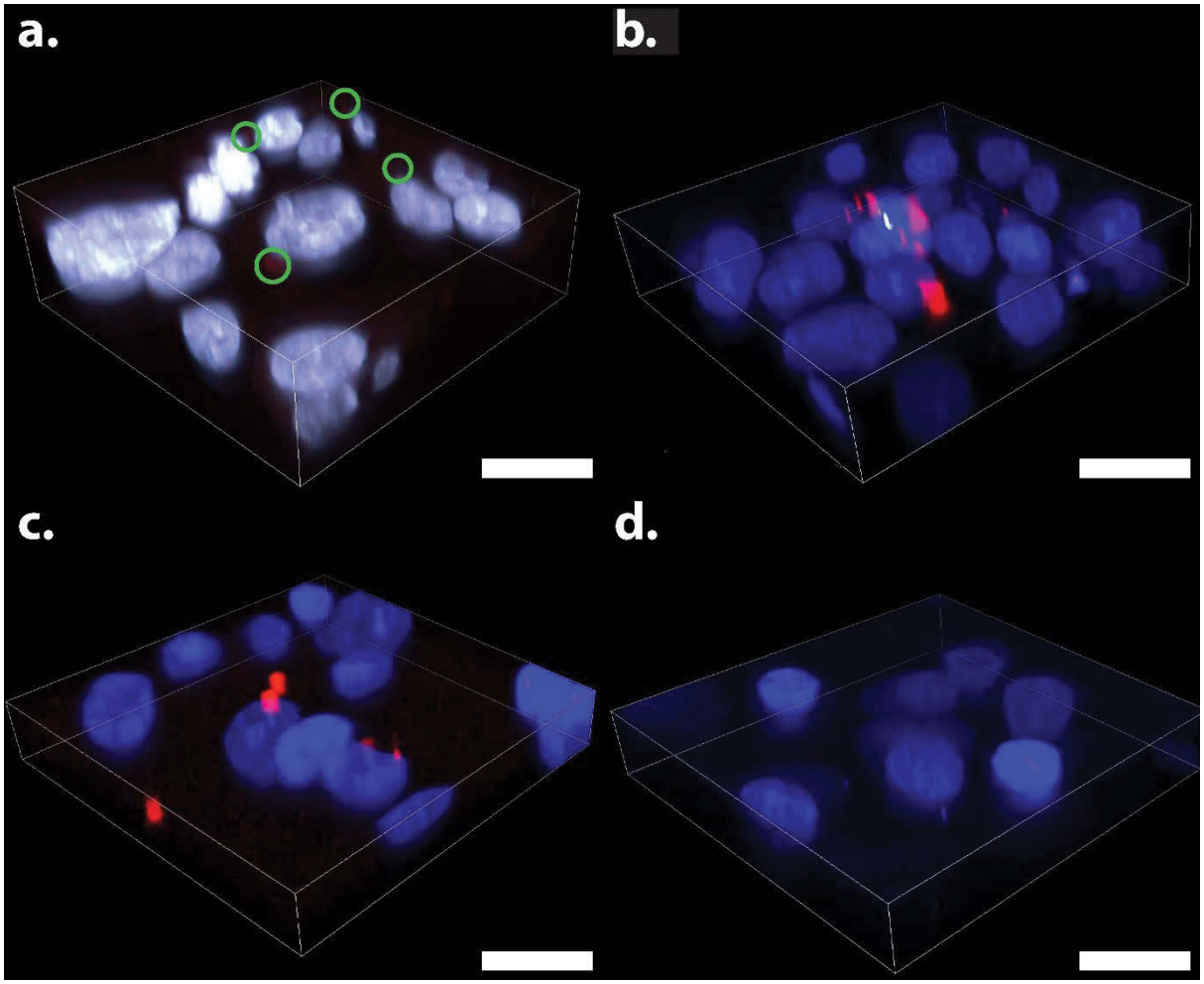


**Figure 7.9.** 3D z-stack of CHO-K1 cells hosting FNDs. 3D constructed z-stack images of CHO-K1 cells hosting (a) SiV (b) NV (c) SiV and NV-TAT containing FNDs and (d) control cells were imaged under 561 nm excitation to reduce cell auto fluorescence and maximise the collected signal from the FNDs particles. Scale bar 20 μm.

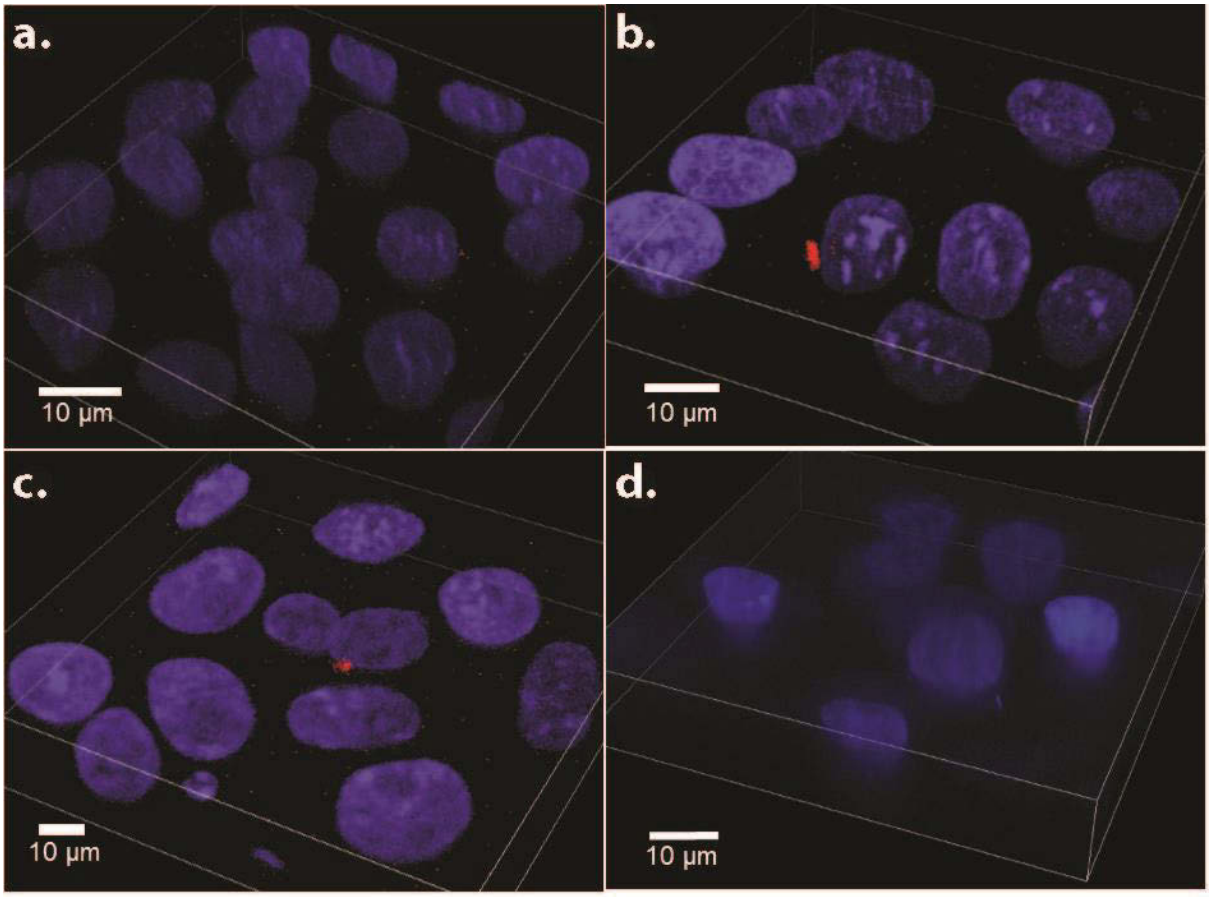


**Figure 7.10.** 3D reconstruction of confocal raster scan of CHO-K1 cells hosting (a) SiV (b) NV (c) both SiV and NV-TAT containing FNDs and (d) control cells. 405 nm laser excitation shows the NucBlue stained nucleus of the cells, while 561 nm laser excitation was used to maximise the collected signal from the FNDs particles. Fluorescence from SiV FNDs is dispersed throughout the cell except nucleus, while fluorescence from NV-TAT FNDs is clearly segregated in a perinuclear area of cells.

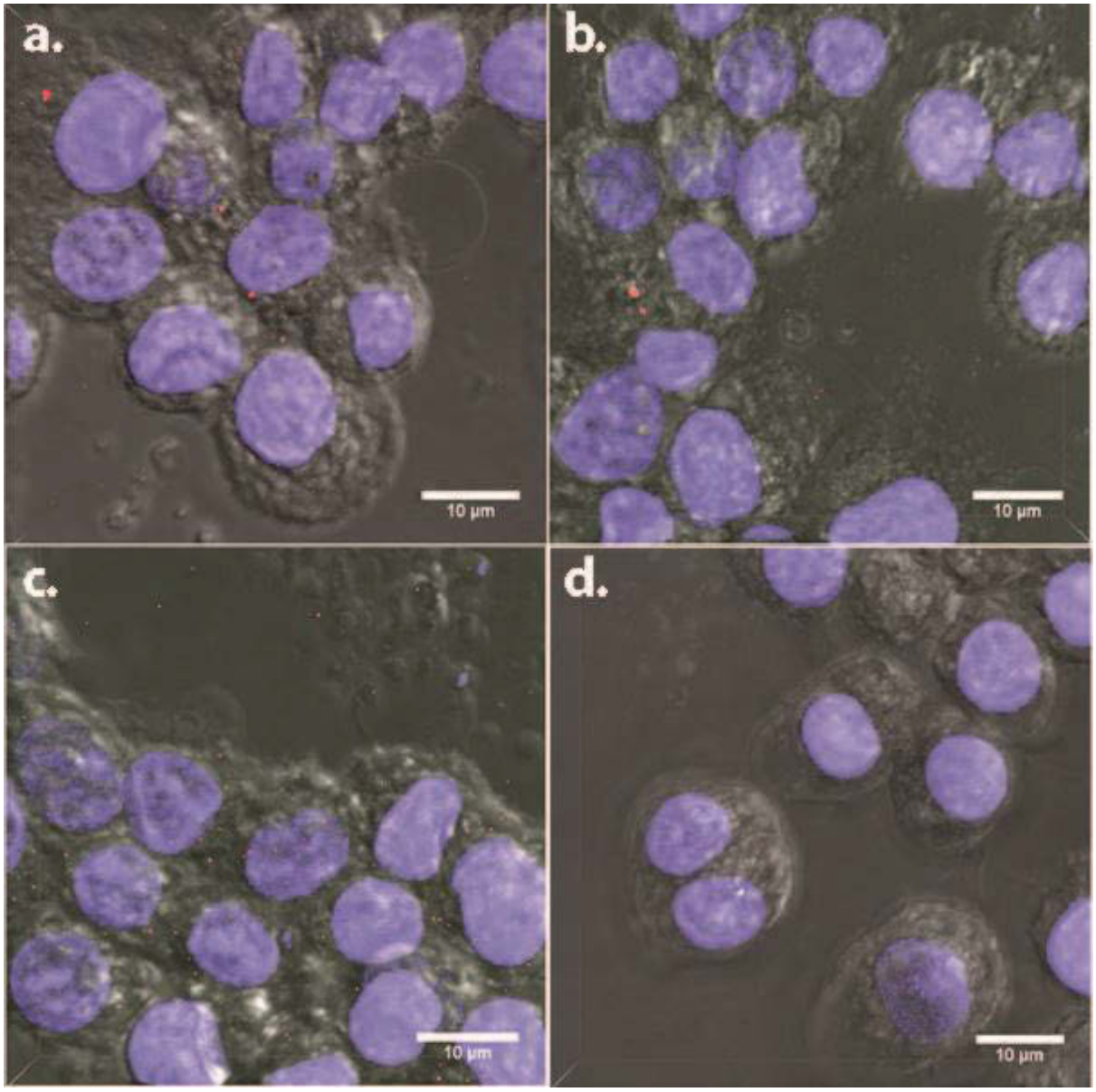


**Figure 7.11.** 3D reconstruction of confocal raster scan of U937 cells induced to macrophages hosting (a) SiV (b) NV (c) both SiV and NV-TAT containing FNDs and (d) control cells. 405 nm laser excitation shows the NucBlue stained nucleus of the cells, while 561 nm laser excitation was used to maximise the collected signal from the FNDs particles. Fluorescence from both FNDs is dispersed throughout the cell except nucleus.

The efficiency of uptake for the FNDs particles into the CHO-K1 cells was also studied. A 50 µL solution of FNDs containing either NV or SiV colour centres was introduced into the cultured CHO-K1 cells as described previously, then subsequently fixed and stained after 5, 30, 60, 180 and 300 minutes of incubation at 37°C. Figure 7.12 (a-e) shows confocal images

of the cells after the various times of incubation. After 5 minutes of incubation, Figure 7.12a show individual FNDs dispersed throughout the cell interior while a small number of FNDs have been successfully internalised by the CHO-K1 cells. Figure 7.12 (a-e) shows that the FNDs particles are efficiently up taken into the cells after 2 hours (between 1 and 3 hours of incubation) in accordance with other reports [319], [322]. Previous studies demonstrated that FNDs are internalised via endocytic pathways, where the particles are engulfed, then suspended within small vesicles (endosomes). It has been shown for other cell lines that the FNDs are usually trapped in endosomes for an hour prior to translocation to the cytoplasm [321]. This did not appear to be the case here, as the FNDs appear to accumulate in subcellular vesicles. As the time increases from 5 to 300 minutes, I further observed that the FND particles are agglomerating inside the cell. This timed subcellular processing has been recently described for other type of inorganic nanoparticles (gold nanoparticles) [323]. Cells initially uptake individual nanoparticles engulfed in earlier endosomes, followed by vesicular clustering and matursation, nanoparticles accumulate in late endosomes and further led into lysosomes. Such subcellular processing is indicative for intracellular trafficking of external material. In this case, after 300 minutes, the FNDs form large aggregates in the perinuclear area, the same area where lysosomes are located inside CHO-K1 cells. It is a known phenomenon that some types of nanoparticles induce a process of autophagy [324]–[326], in which cells can induce autophagy pathways to eliminate these extraneous particles. Further studies are required to confirm the fate of these particles. Despite it, controlled agglomeration of nanoparticles can lead to novel applications in drug delivery applications including controlled and sustained release of a drug into biological systems [327]. Ideally, for cellular uptake I would like the FNDs to be as small as possible, to be non-invasive in the cellular system while their fluorescent properties are still reliable and efficient, and they are still able to efficiently be conjugated to various proteins for cellular targeting. The size of the FNDs will modify the uptake mechanisms. If the FNDs are too large, they may not be able to traverse the cell membrane and, therefore, the cell may not uptake the particles. It is possible that the FNDs could undergo a different uptake mechanism and be eaten by the cell or be transported to another region. The uptake of FNDs into cells has not be studied extensively and is currently beyond the scope of this PhD.

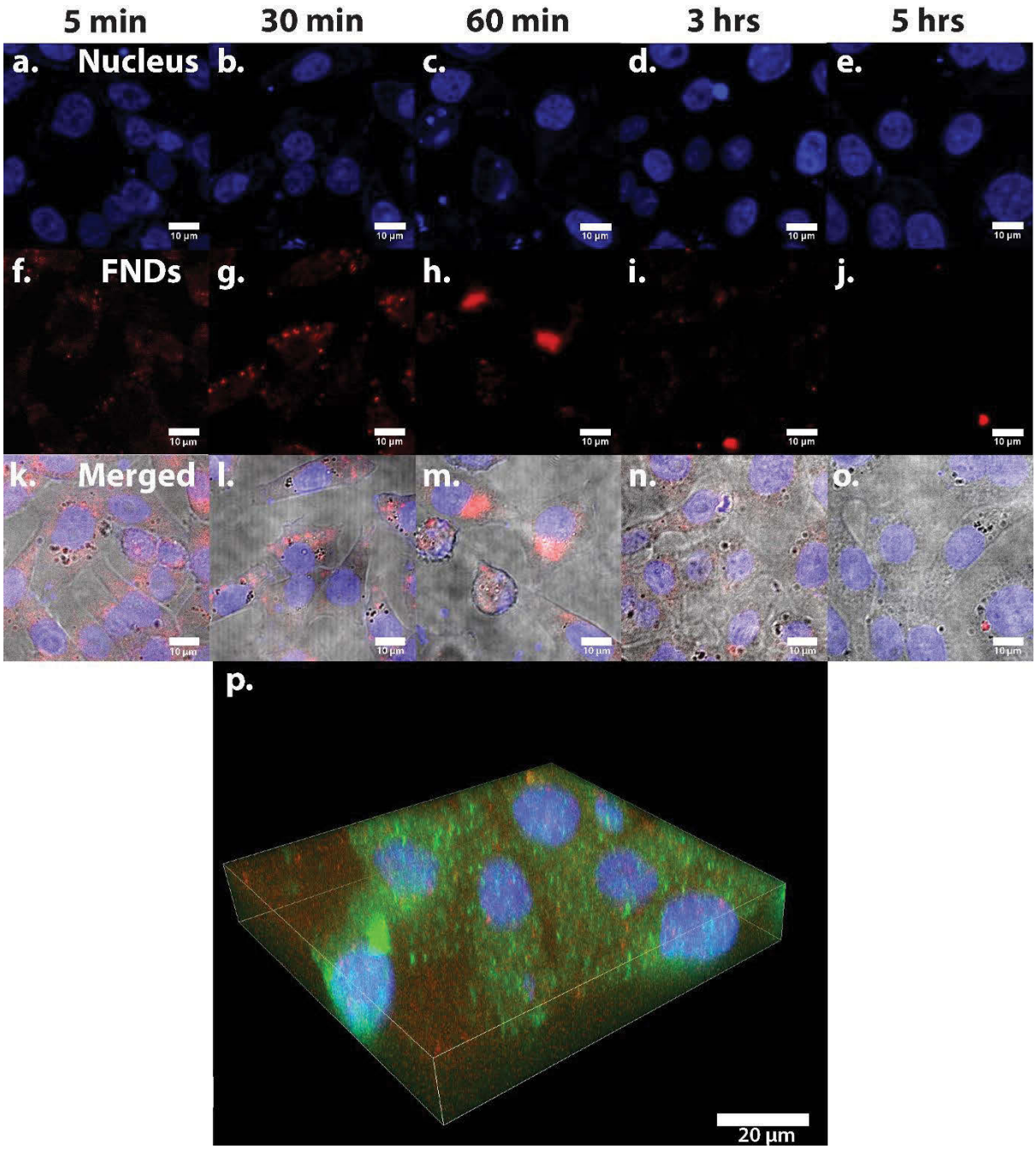


**Figure 7.12.** Uptake time study for FNDs hosting NV and SiV colour centres. The cells hosting the FNDs particles were fixed after (a) 5 min, (b) 30 min, (c) 60 min, (d) 180 min and (e) 300 min, they were imaged with a 561 nm excitation source. The top line shows only the nucleus of the cells stained with the blue stain (NucBlue). The second row shows fluorescence emission from only the FNDs inside the CHO-K1 cells (as confirmed by spectral analysis). The third row is an overlay of the first two rows (nucleus and FNDs only) along with a wide field image showing the outline of the cells with grey lines. The FNDs are initially dispersed (a) but over time agglomerate near the cell nucleus (b-e). Scale bar 10 µm. Co-localisation study of FNDs

against primary LAMP1 (f) proteins stained the endosomes or lysosomes. Secondary anti-mouse Alexa Fluor 488 antibodies were used to visualise primary LAMP1. Scale bar 20 μm.

To better determine the endosomal localisation of the FNDs within the cells, co-localisation staining studies were undertaken using antibodies against LAMP1 (Lysosomal-associated membrane protein). Co-localisation or degree of overlap of two images, between the ND fluorescence and the cells is determined through a number of statistical parameters. LAMP1 primarily stains the late endosomes or lysosomes (Figure 7.12f). The various imaging channels for the nucleus, stain and FNDs (blue, green, and red) were compared using a number of parameters, Pearsons's coefficient, Costes, Manders coefficient and Li's Intensity Correlation Quotient (ICQ) using Fiji (ImageJ). The Pearsons's coefficient calculates the degree of overlap between the pixels in the red (FNDs) and green (fluorescent biomarker) colour channels using the equation [328]:

$$\boldsymbol{r = \frac{\sum(red\ intensity - average\ red)\times(green\ intensity - average\ green)}{\sqrt{\sum(red\ intensity - average\ red)^2 \times \sum(green\ intensity - average\ green)^2}}} \quad \textbf{Equation 7-1}$$

The confidence of co-localisation between two colour channels, the stained channel and NIR FND channel, according to the Pearson correlation, perfect correlation equals to 1, perfect negative correlation equals to -1 and 0 denotes the absence of a relationship or is equivalent to random noise.

The Manders coefficients M1/M2 is a secondary check on the validity of the test and tends towards 1; it describes the degree of overlapping between the red and green pixels between the particles and stain respectively. M1 is the ratio of the summed intensities of pixels from the green image for which the intensity in the red channel is above zero to the total intensity in the green channel and M2 is conversely for red, using the equation below where $R_{i,coloc}$ is the intensity of a particular pixel and $R_{i,total}$ is the total intensity of the channel, similarily, $G_{i,}$ for the green channel.

$$\boldsymbol{M_R = \frac{\sum_i R_{i,coloc}}{\sum_i R_{i,total}}}\ \boldsymbol{, M_G = \frac{\sum_i G_{i,coloc}}{\sum_i G_{i,total}}} \quad \textbf{Equation 7-2}$$

The Costes method uses a similar approach but randomises one channel and repeats the comparison iteration 100 times to determine the degree of overlap. The Costes method tends towards 95% when there is co-localisation between two images.

Li's ICQ is the degree of how well the Li's ICQ equation fits to the experimental intensities in the green and red channels and tends towards 0.5, where $R_i$ is the pixels intensity and $r$ is the mean intensity of the channel, similarly for $G_i$ and $g$.

$$\boldsymbol{Li's\ ICQ = \frac{(R_i - r)(G_i - g)}{\sum (R_i - r)(G_i - g)} - 0.5} \qquad \textbf{Equation 7-3}$$

To unambiguously confirm the co-localisation of fluorescence, I performed co-localisation tests (Table 7-2)**,** Pearson's coefficient, Manders Coefficient, Costes P-value, and Li's intensity correction quotient (ICQ)).

The Pearson's R value for the LAMP1 is 0.82 indicates moderate to strong co-localisation of intensity distributions between the LAMP1 and FND particles. The Manders' M1 and M2 values indicate significant overlap between the red and green pixels for the samples, except for control sample, as expected. Additional confirmation of co-localisation is Li's ICQ, which indicates moderate co-localisation between the LAMP1 stain and FNDs (0.312) samples. Taking all the evidence together, I conclude that the FNDs localise to the lysosome organelles (LAMP1) in the CHO-K1 (Table 7-2).

**Table 7-2.** Co-localisation test for control and stained cells. The LAMP1 shows co-localisation as the Pearson's R value tends towards 1.

| Sample | Pearson's R (no Threshold) | Pearson's R (below/above Threshold) | Manders' M1/M2 | Costes P-Value | Li's ICQ |
|---|---|---|---|---|---|
| **Cells only (Red vs Green)** | 0.00 | -0.00/-0.04 | 0.01/0.27 | 0.98 | 0.112 |
| **LAMP1 (Red vs Green)** | 0.82 | 0.70/0.15 | 1.00/1.00 | 1.00 | 0.312 |

In conclusion, I demonstrated large scale production of FNDs containing NIR emitters (SiV) suitable for biological labelling. I further show convincing evidence for co-localised uptake of FNDs containing SiV or NV colour centres into cells with no apparent toxicity and can be visualised using a standard confocal set-up. FNDs promote cell-induced aggregation of nanoparticles over time that most likely correlates to an autophagy process inside cells. Finally, co-localisation study demonstrates that after a prolong incubation the FNDs are located inside

late endosomes/lysosome. The results provide an important stepping stone for the effective use of FNDs multi-colour bio-imaging applications, showing that FNDs are a promising bio-imaging research tool.

# Chapter 8 Summary and Outlook

This work featured spectroscopic, electrical and biological studies of defect-based emission from diamond nanocrystals and diamond membranes. The first part of the thesis reports on the fabrication and characterisation of diamond membrane devices. The devices include single crystal diamond p-n and p-i-n structures as well as hybrid p-i-n structures. Various photophysical properties of the SiV emitters in the diamond membranes were investigated at room temperature showing electroluminescence and the possibility for optoelectronic applications. The second part of the thesis deals with the investigation of narrowband emitters in diamond nanocrystals, determining their origin and cooling the emitters to cryogenic temperatures to investigate their narrow, sub-GHz optical linewidths. This part of the thesis enhances our understanding of the optophysical properties of novel single photon emitters in diamond for quantum optic devices and sensor applications. Finally, I explored the use of diamond nanocrystals for bio-imaging in two cell lines, showing relevance of defect-induced fluorescence of NDs for biological applications. In this chapter I summarise relevant findings and results discussed throughout the thesis. Finally, an outlook is provided to motivate additional work on the topics with possible future directions for potential applications.

The main conclusions which are drawn from the thesis are summarised below:

1. High quality diamond membranes were fabricated using ion implantation and electrochemical lift-off techniques. The membranes were subsequently overgrown by MPCVD and thinned by ICP-RIE to create a high aspect ratio, 300 nm thin single crystal diamond membrane.
2. Fluorescent defects were efficiently incorporated into the diamond membranes during MPCVD growth and the high-quality diamond material remained post thinning as shown by TEM and AFM analysis.
3. Numerous p-n and p-i-n devices were successfully fabricated consisting entirely of single crystal diamond and their electrical properties were quantified. The p-doped and n-doped region consisted of $\sim 3 \times 10^{20}$cm$^{-3}$ of boron atoms and $\sim 8 \times 10^{18}$ cm$^{-3}$ of phosphorus atoms, respectively. The intrinsic layer is comprised of a uniform layer of SiV colour centres. The devices showed moderate to high current outputs at voltages comparable to other devices in the literature. Furthermore, they showed high rectification ratios of $\sim 10^6$.

4. EL from the p-i-n devices has been demonstrated. A voltage of 10 V is applied to the device generating a 4 mA current along with characteristic ZPL emission of the SiV colour centre at 737 nm. This is the first time electrical triggering of SiV has been observed in a nanoscale single crystal diamond device.
5. The origin of narrowband emitters in diamond nanocrystals was investigated. They were determined to be point defects localised at extended morphological defects in individual nanodiamonds. I showed that the twin boundaries and secondary nucleation sites exhibit the narrowband emission and is absent from pristine individual nanocrystals. Furthermore, I was able to deterministically remove the grain boundaries using EBIE, proving that the source of the narrowband emission lines originates from morphological defects.
6. The narrowband emitters were also investigated at cryogenic temperatures (10K). They show promising optical properties with ZPL at ~780 nm in the NIR. The emitter was shown to be optically stable with low power excitation and blue shifts as the power is increased. It offers the ability to promote more studies on the attributes of NIR emitters in nanodiamonds for quantum photonic applications.
7. Spectroscopy studies were carried out on FNDs containing SiV defects that were up taken into CHO-K1 and macrophage cell lines. This was the first demonstration of *in situ* bio-imaging of SiV colour centres. Additionally, I showed simultaneous multi-colour bio-imaging of NV and SiV FNDs to investigate intracellular processes. I showed that the SiV FNDs are initially dispersed throughout the interior of the cell while the NV-TAT FNDs localise near the nucleus of the cell.

## 8.1 Outlook

There is a lot of interest in researching various single emitting defects and device configurations for quantum applications. Diamond possesses many unique and sought-after properties that will allow it to excel for use in photonic and optoelectronic applications, and many more. Even with the large amount of progress, there are still several bottlenecks and obstacles to overcome.

In the future, more robust n-type and p-type doping of diamond would need to be achieved to allow a more efficient transfer of electrons through the diamond defects to increase photon collection. Additionally, a more reliable way to introduce single SiV or GeV emitters into the

intrinsic layer of diamond without causing damage would lead to the excitation of single photon emitters through electrical triggering. Upon addressing these issues, it would lead to highly transformative devices for quantum optics and electrical components. The reliable and robust engineering of nanoscale, conductive, single crystal diamond membranes demonstrates the first nanoscale diamond LED and highlights their use for optoelectrical applications. While electrical excitation from diamond containing SiV ensembles in nanoscale devices is demonstrated in this thesis, there is still single photon electroluminescence that needs to be explored. Accordingly, the next necessary step is to electrically trigger SiV centres in diamond to generate electrically driven single photons [22]. By achieving this, I can pursue electrically driven single photon emitters from arrays imbedded in the diamond membrane devices.

The scientific community is currently searching for alternative systems to the most popular NV centre in diamond. The new emitters will need to possess an optical spin read out associated and far greater optical properties [329]. Given the recent efforts on GeV and other diamond colour centres, investigating them for electroluminescent cavities and device is promising due to their ideal, narrow luminescent ZPLs. This narrow ZPL will allow the emitter to be tuned as well as coupled to a variety of devices for quantum applications and possibly be an alternative for the popular $NV^-$ colour centre. I therefore oversee that the extension of the work on diamond membrane devices will include the exploitation of GeV colour centres in p-i-n devices for optoelectronic applications.

With the reliable fabrication of the thin diamond membranes, it would be ideal to fabricate ring resonators or photonic crystal cavities because the diamond membranes have a high refractive index and would be isolated from the substrate due to an air gap. Furthermore, the membranes can be moved and positioned onto either a substrate or device of choice, allowing them to be highly versatile. Therefore, to utilise diamond-based emitters for quantum optics applications, it is highly desirable to fabricate photonic crystal cavities with high quality (Q) factors. Demonstrating not only high Q-factors to fine tune the emission and also electrically triggering diamond membrane based photonic crystal cavities will endow an all diamond platform suitable to quantum technologies.

Future work will involve incorporation of various colour centres into the ring resonators to out couple the emission to other wires or antennas and to focus the light for on-a-chip processes. It will accelerate the integration of new colour centres in diamond with scalable photonic devices to achieve on-chip quantum nanophotonic circuitry.

Exploiting diamond for biological applications, especially utilising the emission of the SiV defect which emits in the NIR is highly desirable to avoid tissue autofluorescence to interfere with the diamond signal. Further work might include exploration of other NIR-emitting defects in nanodiamonds for further colour multiplexing and application of nanodiamonds as imaging probes. Nanodiamonds with various colour centres can be further utilised to understand intracellular processes.

Diamond is a leading material in exploiting and managing quantum effects and is moving from the laboratory to commercial products. Generation of single photon emitters that can be excited electrically will push forth the design of efficient and scalable integrated quantum nanophotonic circuits which include photonic crystal cavities and waveguides. The application of diamond knows no bounds as it is a highly versatile material and will eventually find its way into a myriad of devices and applications.

# Bibliography

[1] W. Lu and C. M. Lieber, “Nanoelectronics from the bottom up,” *Nat. Mater.*, vol. 6, no. 11, pp. 841–850, 2007.

[2] I. Aharonovich, J. C. Lee, A. P. Magyar, D. O. Bracher, and E. L. Hu, “Bottom-up engineering of diamond micro- and nano-structures,” *Laser Photonics Rev.*, vol. 7, no. 5, pp. 61–65, 2013.

[3] N. Gisin, G. Ribordy, W. Tittel, and H. Zbinden, “Quantum cryptography,” *Rev. Mod. Phys.*, vol. 74, no. 1, pp. 145–195, 2002.

[4] D. D. Awschalom, R. Epstein, and R. Hanson, “The diamond age of spintronics.,” *Sci. Am.*, vol. 297, no. 4, pp. 84–91, 2007.

[5] S. L. Mouradian, T. Schröder, C. B. Poitras, L. Li, J. Goldstein, E. H. Chen, M. Walsh, J. Cardenas, M. L. Markham, D. J. Twitchen, M. Lipson, and D. Englund, “Scalable Integration of Long-Lived Quantum Memories into a Photonic Circuit,” *Phys. Rev. X*, vol. 5, no. 3, p. 031009, 2015.

[6] E. Knill, “Quantum computing,” *Nature*, vol. 463, no. January, pp. 441–443, 2010.

[7] K. Kieling, T. Rudolph, and J. Eisert, “Percolation, renormalization, and quantum computing with nondeterministic gates,” *Phys. Rev. Lett.*, vol. 99, no. 13, pp. 2–5, 2007.

[8] J. L. O’Brien, A. Furusawa, and J. Vuckovic, “Photonic quantum technologies,” *Nat. Photonics*, vol. 3, pp. 687–695, 2009.

[9] P. Lodahl, S. Mahmoodian, and S. Stobbe, “Interfacing single photons and single quantum dots with photonic nanostructures,” *Rev. Mod. Phys.*, vol. 87, no. 2, pp. 347–400, 2015.

[10] S. Buckley, K. Rivoire, and J. Vučković, “Engineered quantum dot single-photon sources,” *Reports Prog. Phys.*, vol. 75, no. 12, 2012.

[11] T. E. Northup and R. Blatt, “Quantum information transfer using photons,” *Nat. Photonics*, vol. 8, no. 5, pp. 356–363, 2014.

[12] B. Lounis and M. Orrit, “Single-photon sources,” *Reports Prog. Phys.*, vol. 68, no. 5, pp. 1129–1179, 2005.

[13] R. Alléaume, F. Treussart, G. Messin, Y. Dumeige, J. F. Roch, A. Beveratos, R. Brouri-Tualle, J. P. Poizat, and P. Grangier, "Experimental open-air quantum key distribution with a single-photon source," *New J. Phys.*, vol. 6, pp. 1–14, 2004.

[14] L. Childress and R. Hanson, "Diamond NV centers for quantum computing and quantum networks," *MRS Bull.*, vol. 38, no. 2, pp. 134–138, 2013.

[15] F. Jelezko and J. Wrachtrup, "Read-out of single spins by optical spectroscopy," *J. Phys. Condens. Matter*, vol. 16, no. 30, 2004.

[16] C. Wang, C. Kurtsiefer, H. Weinfurter, and B. Burchard, "Single photon emission from SiV centres in diamond produced by ion implantation," *J. Phys. B At. Mol. Opt. Phys.*, vol. 39, no. 1, pp. 37–41, 2006.

[17] E. Neu, M. Agio, and C. Becher, "Photophysics of single silicon vacancy centers in diamond: implications for single photon emission," *Opt. Express*, vol. 20, no. 18, pp. 19956–19971, Jul. 2012.

[18] E. Neu, D. Steinmetz, J. Riedrich-Möller, S. Gsell, M. Fischer, M. Schreck, and C. Becher, "Single photon emission from silicon-vacancy colour centres in chemical vapour deposition nano-diamonds on iridium," *New J. Phys.*, vol. 13, no. 2, p. 025012, Feb. 2011.

[19] I. Aharonovich, "Novel single photon emitters based on color centers in diamond," no. November, 2010.

[20] X. Liang, L. Wang, M. Xiangyang, D. Li, P. Cheng, D. Yang, J. Chen, and T. Sekiguchi, "Enhanced red electroluminescence from a polycrystalline diamond film/Si heterojunction structure," *Appl. Phys. Lett.*, vol. 90, no. 16, pp. 16–19, 2007.

[21] A. M. Berhane, S. Choi, H. Kato, T. Makino, N. Mizuochi, S. Yamasaki, and I. Aharonovich, "Electrical excitation of silicon-vacancy centers in single crystal diamond," *Appl. Phys. Lett.*, vol. 106, no. 17, 2015.

[22] N. Mizuochi, T. Makino, H. Kato, D. Takeuchi, M. Ogura, H. Okushi, M. Nothaft, P. Neumann, A. Gali, F. Jelezko, J. Wrachtrup, and S. Yamasaki, "Electrically driven single-photon source at room temperature in diamond," *Nat. Photonics*, vol. 6, no. 5, pp. 299–303, 2012.

[23] B. Ellis, M. A. Mayer, G. Shambat, T. Sarmiento, J. Harris, E. E. Haller, and J. Vučković, "Ultralow-threshold electrically pumped quantum-dot photonic-crystal

nanocavity laser," *Nature*, vol. 5, pp. 297–300, 2011.

[24] R. M. Stevenson, C. L. Salter, J. Nilsson, A. J. Bennett, M. B. Ward, I. Farrer, D. A. Ritchie, and A. J. Shields, "Indistinguishable entangled photons generated by a light-emitting diode," *Phys. Rev. Lett.*, vol. 108, no. 4, pp. 1–5, 2012.

[25] E. M. Purcell, H. C. Torrey, and R. V. Pound, "Resonance Absorption by Nuclear Magnetic Moments in a Solid," *Phys. Rev.*, vol. 69, no. 37, pp. 37–38, 1946.

[26] C. Su, A. D. Greentree, and L. C. L. Hollenberg, "Towards a picosecond transform-limited nitrogen-vacancy based single photon source," *Opt. Express*, vol. 16, no. 9, pp. 2722–2725, 2008.

[27] B. a. Fairchild, P. Olivero, S. Rubanov, A. D. Greentree, F. Waldermann, R. a. Taylor, I. Walmsley, J. M. Smith, S. Huntington, B. C. Gibson, D. N. Jamieson, and S. Prawer, "Fabrication of ultrathin single-crystal diamond membranes," *Adv. Mater.*, vol. 20, no. 24, pp. 4793–4798, 2008.

[28] A. P. Magyar, D. Bracher, J. C. Lee, I. Aharonovich, and E. L. Hu, "High quality SiC microdisk resonators fabricated from monolithic epilayer wafers," *Appl. Phys. Lett.*, vol. 104, no. 5, p. 051109, Feb. 2014.

[29] V. S. Bormashov, S. A. Terentiev, S. G. Buga, S. A. Tarelkin, A. P. Volkov, D. V. Teteruk, N. V. Kornilov, M. S. Kuznetsov, and V. D. Blank, "Thin large area vertical Schottky barrier diamond diodes with low on-resistance made by ion-beam assisted lift-off technique," *Diam. Relat. Mater.*, vol. 75, pp. 78–84, 2017.

[30] J. C. Lee, A. P. Magyar, D. O. Bracher, I. Aharonovich, and E. L. Hu, "Fabrication of thin diamond membranes for photonic applications," *Diam. Relat. Mater.*, vol. 33, pp. 45–48, 2013.

[31] B. J. M. Hausmann, I. B. Bulu, P. B. Deotare, M. McCutcheon, V. Venkataraman, M. L. Markham, D. J. Twitchen, and M. Lončar, "Integrated high-quality factor optical resonators in diamond," *Nano Lett.*, vol. 13, no. 5, pp. 1898–1902, 2013.

[32] Y. Tao, J. M. Boss, B. A. Moores, and C. L. Degen, "Single-crystal diamond nanomechanical resonators with quality factors exceeding one million," *Nat. Commun.*, vol. 5, pp. 1–8, 2014.

[33] E. R. MacQuarrie, M. Otten, S. K. Gray, and G. D. Fuchs, "Cooling a Mechanical Resonator with a Nitrogen-Vacancy Center Ensemble Using a Room Temperature

Excited State Spin-Strain Interaction," *Nat. Publ. Gr.*, vol. 8, pp. 1–10, 2016.

[34] G. Sittas, H. Kanda, I. Kiflawi, and P. M. Spear, "Growth and characterization of Si-doped diamond single crystals grown by the HTHP method," *Diamond and Related Materials*, vol. 5, no. 6–8. pp. 866–869, May-1996.

[35] C.-C. Fu, H.-Y. Lee, K. Chen, T.-S. Lim, H.-Y. Wu, P.-K. Lin, P.-K. Wei, P.-H. Tsao, H.-C. Chang, and W. Fann, "Characterization and application of single fluorescent nanodiamonds as cellular biomarkers.," *Proc. Natl. Acad. Sci. U. S. A.*, vol. 104, no. 3, pp. 727–732, 2007.

[36] G. Balasubramanian, A. Lazariev, S. R. Arumugam, and D. W. Duan, "Nitrogen-Vacancy color center in diamond-emerging nanoscale applications in bioimaging and biosensing," *Curr. Opin. Chem. Biol.*, vol. 20, no. 1, pp. 69–77, 2014.

[37] T. D. Merson, S. Castelletto, I. Aharonovich, A. Turbic, T. J. Kilpatrick, and A. M. Turnley, "Nanodiamonds with silicon vacancy defects for nontoxic photostable fluorescent labeling of neural precursor cells.," *Opt. Lett.*, vol. 38, no. 20, pp. 4170–3, Oct. 2013.

[38] A. Alhaddad, M. P. Adam, J. Botsoa, G. Dantelle, S. Perruchas, T. Gacoin, C. Mansuy, S. Lavielle, C. Malvy, F. Treussart, and J. R. Bertrand, "Nanodiamond as a vector for siRNA delivery to Ewing sarcoma cells," *Small*, vol. 7, no. 21, pp. 3087–3095, 2011.

[39] J. Li, Y. Zhu, W. Li, X. Zhang, Y. Peng, and Q. Huang, "Nanodiamonds as intracellular transporters of chemotherapeutic drug," *Biomaterials*, vol. 31, no. 32, pp. 8410–8418, 2010.

[40] L. P. McGuinness, Y. Yan, A. Stacey, D. a Simpson, L. T. Hall, D. Maclaurin, S. Prawer, P. Mulvaney, J. Wrachtrup, F. Caruso, R. E. Scholten, and L. C. L. Hollenberg, "Quantum measurement and orientation tracking of fluorescent nanodiamonds inside living cells," *Nat. Nanotechnol.*, vol. 6, no. 6, pp. 358–363, Jun. 2011.

[41] A. M. Zaitsev, *Optical Properties of Diamond*. Berlin: Springer, 2001.

[42] C. Becher, "Fluorescent nanoparticles: Diamonds from outer space.," *Nat. Nanotechnol.*, vol. 9, no. 1, pp. 16–7, 2014.

[43] N. N. Lepeshkin, R. R. Hancock, M. a. Lewis, R. M. Boysel, M. Quesada, R. Welty, a. R. Bleier, J. Treichler, R. E. Slusher, R. W. Boyd, J. E. Heebner, Q.-H. Park, A. Schweinsberg, G. W. Wicks, a. S. Baca, and J. E. Fajardo, "Nanofabrication of optical

structures and devices for photonics and biophotonics," *Journal of Modern Optics*, vol. 50, no. 15–17. pp. 2543–2550, 2003.

[44] I. Aharonovich, A. D. Greentree, and S. Prawer, "Diamond photonics," *Nat. Photonics*, vol. 5, no. 7, pp. 397–405, 2011.

[45] R. Kaur and I. Badea, "Nanodiamonds as novel nanomaterials for biomedical applications: Drug delivery and imaging systems," *International Journal of Nanomedicine*, vol. 8. pp. 203–220, 2013.

[46] Y. Y. Hui and H.-C. Chang, "Recent Developments and Applications of Nanodiamonds as Versatile Bioimaging Agents," *J. Chinese Chem. Soc.*, vol. 61, no. 1, pp. 67–76, Jan. 2014.

[47] Y. Xing and L. Dai, "Nanodiamonds for nanomedicine.," *Nanomedicine (Lond).*, vol. 4, no. 2, pp. 207–218, 2009.

[48] C. Gaillard, H. a. Girard, C. Falck, V. Paget, V. Simic, N. Ugolin, P. Bergonzo, S. Chevillard, and J. C. Arnault, "Peptide nucleic acid–nanodiamonds: covalent and stable conjugates for DNA targeting," *RSC Adv.*, vol. 4, no. 7, p. 3566, 2014.

[49] Z.-Y. Lien, T.-C. Hsu, K.-K. Liu, W.-S. Liao, K.-C. Hwang, and J.-I. Chao, "Cancer cell labeling and tracking using fluorescent and magnetic nanodiamond," *Biomaterials*, vol. 33, no. 26, pp. 6172–6185, 2012.

[50] O. a. Shenderova, V. V. Zhirnov, and D. W. Brenner, "Carbon Nanostructures," *Critical Reviews in Solid State and Materials Sciences*, vol. 27, no. 3–4. pp. 227–356, 2002.

[51] a. Y. Vul', A. E. Aleksenskiy, and A. . Dideykin, "Detonation nanodiamonds: technology, properties and applications," *Nanosci. Nanotechnologies*, 2009.

[52] I. I. T. Center, "Nanodiamond Research," 2013. [Online]. Available: http://www.itc-inc.org/nanodiamond.html. [Accessed: 27-Jul-2015].

[53] V. Y. Dolmatov, "Detonation synthesis ultradispersed diamonds: properties and applications," *Russian Chemical Reviews*, vol. 70, no. 7. pp. 607–626, 2007.

[54] eVince Technology, "Why Diamond Is Better Than Anything Else," 2014. [Online]. Available: available: http://www.evincetechnology.com/whydiamond.html. [Accessed: 27-Jul-2015].

[55] R. M. Wood, "Optical properties of diamond: a data handbook," *Optics and Lasers in*

*Engineering*, vol. 42, no. 2. pp. 241–243, 2004.

[56] "opto.e-technik." [Online]. Available: http://www-opto.e-technik.uni-ulm.de/lehre/cs/III_V_map_a.jpg.

[57] A. T. Collins, "The detection of colour-enhanced and synthetic gem diamonds by optical," *Diam. Relat. Mater.*, vol. 12, pp. 1976–1983, 2003.

[58] I. Aharonovich, S. Castelletto, D. a Simpson, C.-H. Su, a D. Greentree, and S. Prawer, "Diamond-based single-photon emitters," *Reports on Progress in Physics*, vol. 74, no. 7. p. 076501, 2011.

[59] V. N. Mochalin, O. Shenderova, D. Ho, and Y. Gogotsi, "The properties and applications of nanodiamonds," *Nat. Nanotechnol.*, vol. 7, no. 1, pp. 11–23, Jan. 2011.

[60] R. Kalish, "Ion-implantation in diamond and diamond films: doping, damage effects and their applications," *Applied Surface Science*, vol. 117–118. pp. 558–569, 1997.

[61] J.-M. Cui, X.-D. Chen, L.-L. Fan, Z.-J. Gong, C.-W. Zou, F.-W. Sun, Z.-F. Han, and G.-C. Guo, "Generation of Nitrogen-Vacancy Centers in Diamond with Ion Implantation," *Chinese Phys. Lett.*, vol. 29, no. 3, p. 036103, 2012.

[62] W. V. Smith, P. P. Sorokin, I. L. Gelles, and G. J. Lasher, "Electron-spin resonance of nitrogen donors in diamond," *Phys. Rev.*, vol. 115, no. 6, pp. 1546–1552, 1959.

[63] K. Iakoubovskii and G. J. Adriaenssens, "Optical transitions at the substitutional nitrogen centre in diamond," *Journal of Physics: Condensed Matter*, vol. 12, no. 6. pp. L77–L81, 2000.

[64] D. Fattal, R. G. Beausoleil, C. Santori, P. Tamarat, P. Neumann, J. Rabeau, P. Olivero, A. D. Greentree, S. Prawer, F. Jelezko, and P. Hemmer, "Coherent Population Trapping of Single Spins in Diamond under Optical Excitation," vol. 247401, no. December, pp. 1–4, 2006.

[65] M. Kayci, H. Chang, and A. Radenovic, "Electron spin resonance of nitrogen-vacancy defects embedded in single nanodiamonds in an ABEL trap.," *Nano Lett.*, 2014.

[66] E. A. Wilson, N. B. Manson, and C. Wei, "Perturbing an electromagnetic induced transparency within an inhomogeneously broadened transition," *Phys. Rev. A - At. Mol. Opt. Phys.*, vol. 67, no. 2, p. 10, 2003.

[67] C. Wei and N. B. Manson, "Observation of the dynamic Stark effect on

electromagnetically induced transparency," *Phys. Rev. A - At. Mol. Opt. Phys.*, vol. 60, no. 3, pp. 2540–2546, 1999.

[68] R. Brouri, A. Beveratos, J.-P. Poizat, and P. Grangier, "Photon antibunching in the fluorescence of individual color centers in diamond," vol. 25, no. 17, pp. 1294–1296, 2000.

[69] I. Aharonovich, S. Castelletto, D. a. Simpson, a. D. Greentree, and S. Prawer, "Photophysics of chromium-related diamond single-photon emitters," *Phys. Rev. A - At. Mol. Opt. Phys.*, vol. 81, no. 4, pp. 1–7, 2010.

[70] A. Beveratos, R. Brouri, T. Gacoin, J. P. Poizat, and P. Grangier, "Nonclassical radiation from diamond nanocrystals," *Phys. Rev. A - At. Mol. Opt. Phys.*, vol. 64, no. 6, p. 4, 2001.

[71] F. M. Hossain, M. W. Doherty, H. F. Wilson, and L. C. L. Hollenberg, "Ab initio electronic and optical properties of the N-V- center in diamond," *Phys. Rev. Lett.*, vol. 101, no. 22, pp. 1–4, 2008.

[72] C. D. CLARK and C. A. NORRIS, "Photoluminescence associated with the 1.673, 1.944 and 2.498 eV centres in diamond," *J. Phys. C Solid State Phys.*, vol. 4, pp. 2223–2229, 1971.

[73] C. Kurtsiefer, S. Mayer, P. Zarda, and H. Weinfurter, "Stable solid-state source of single photons," *Phys. Rev. Lett.*, vol. 85, no. 2, pp. 290–293, 2000.

[74] H. Hanzawa, Y. Nisida, and T. Kato, "Measurement of decay time for the NV centre in Ib diamond with a picosecond laser pulse," *Diam. Relat. Mater.*, vol. 6, no. 11, pp. 1595–1598, 1997.

[75] P. Neumann, R. Kolesov, V. Jacques, J. Beck, J. Tisler, a. Batalov, L. Rogers, N. B. Manson, G. Balasubramanian, F. Jelezko, and J. Wrachtrup, "Excited-state spectroscopy of single NV defects in diamond using optically detected magnetic resonance," *New J. Phys.*, vol. 11, 2009.

[76] J. Tisler, G. Balasubramanian, B. Naydenov, R. Kolesov, B. Grotz, R. Reuter, J. P. Boudou, P. A. Curmi, M. Sennour, A. Thorel, M. Börsch, K. Aulenbacher, R. Erdmann, P. R. Hemmer, F. Jelezko, and J. Wrachtrup, "Fluorescence and spin properties of defects in single digit nanodiamonds," *ACS Nano*, vol. 3, no. 7, pp. 1959–1965, 2009.

[77] T. S. Lim, C. C. Fu, K. C. Lee, H. Y. Lee, K. Chen, W. F. Cheng, W. W. Pai, H. C.

Chang, and W. Fann, “Fluorescence enhancement and lifetime modification of single nanodiamonds near a nanocrystalline silver surface,” *Phys. Chem. Chem. Phys.*, vol. 11, no. 10, pp. 1508–1514, 2009.

[78] J. Wrachtrup and F. Jelezko, “Processing quantum information in diamond,” *J. Phys. Condens. Matter*, vol. 18, no. 21, 2006.

[79] A. T. Collins, M. F. Thomaz, and M. I. B. Jorge, “Luminescence decay time of the 1 . 945 eV centre in type,” *J. Phys. C Solid State Phys.*, vol. 16, pp. 2177–2181, 1983.

[80] V. M. Acosta, C. Santori, A. Faraon, Z. Huang, K. M. C. Fu, A. Stacey, D. A. Simpson, K. Ganesan, S. Tomljenovic-Hanic, A. D. Greentree, S. Prawer, and R. G. Beausoleil, “Dynamic stabilization of the optical resonances of single nitrogen-vacancy centers in diamond,” *Phys. Rev. Lett.*, vol. 108, no. 20, pp. 6–11, 2012.

[81] E. R. Schmidgall, S. Chakravarthi, M. Gould, I. R. Christen, K. Hestroffer, F. Hatami, and K. M. C. Fu, “Frequency Control of Single Quantum Emitters in Integrated Photonic Circuits,” *Nano Lett.*, vol. 18, no. 2, pp. 1175–1179, 2018.

[82] Oxford Instruments, “Plasma Enhanced Chemical Vapour Deposition (PEECVD),” 2014. [Online]. Available: http://www.oxford-instruments.com/products/etching-deposition-and-growth/plasma-etch-deposition/pecvd. [Accessed: 27-Jul-2015].

[83] V. S. Vavilov, A. A. Gippius, A. M. Zaitsev, B. V. Deryagin, B. V. Spitsyn, and A. E. Aleksenko, “Investigation of the cathodoluminescence of epitaxial diamond films,” *Sov. Phys. Semicond.*, vol. 14, no. 9, pp. 1078–1079, 1980.

[84] A. Boogaard, *Plasma-enhanced chemical vapor deposition of silicon dioxide*. 2011.

[85] S. Prawer, “Ion implantation of diamond and diamond films,” *Diam. Relat. Mater.*, vol. 4, no. 5–6, pp. 862–872, 1995.

[86] T. Feng and B. D. Schwartz, “Characteristics and origin of the 1.681 eV luminescence center in chemical-vapor-deposited diamond films,” *J. Appl. Phys.*, vol. 73, no. 3, pp. 1415–1425, 1993.

[87] A. Turukhin, C. Liu, A. Gorokhovsky, R. Alfano, and W. Phillips, “Picosecond photoluminescence decay of Si-doped chemical-vapor-deposited diamond films,” *Phys. Rev. B - Condens. Matter Mater. Phys.*, vol. 54, no. 23, pp. 16448–16451, 1996.

[88] C. Hepp, T. Müller, V. Waselowski, J. N. Becker, B. Pingault, H. Sternschulte, D.

Steinmüller-Nethl, A. Gali, J. R. Maze, M. Atatüre, and C. Becher, "Electronic structure of the silicon vacancy color center in diamond," *Phys. Rev. Lett.*, vol. 112, no. 3, 2014.

[89] A. Gali and J. R. Maze, "Ab initio study of the split silicon-vacancy defect in diamond: Electronic structure and related properties," *Phys. Rev. B - Condens. Matter Mater. Phys.*, vol. 88, no. 23, pp. 1–7, 2013.

[90] C. D. Clark, H. Kanda, I. Kiflawi, and G. Sittas, "Silicon defects in diamond," *Phys. Rev. B*, vol. 51, no. 23, pp. 16681–16688, 1995.

[91] E. Neu, C. Arend, E. Gross, F. Guldner, C. Hepp, D. Steinmetz, E. Zscherpel, S. Ghodbane, H. Sternschulte, D. Steinmüller-Nethl, Y. Liang, a. Krueger, and C. Becher, "Narrowband fluorescent nanodiamonds produced from chemical vapor deposition films," *Appl. Phys. Lett.*, vol. 98, no. 24, p. 243107, 2011.

[92] E. Gu, W. Y. Chen, J. Gu, P. Burridge, and J. C. Wu, "Molecular imaging of stem cells: Tracking Survival, biodistribution, tu-morigenicity, and immunogenicity," *Theranostics*, vol. 2, no. 4. pp. 335–345, 2012.

[93] Y. Urano, "Novel live imaging techniques of cellular functions and in vivo tumors based on precise design of small molecule-based 'Activatable' fluorescence probes," *Curr. Opin. Chem. Biol.*, vol. 16, no. 5–6, pp. 602–608, Dec. 2012.

[94] I. I. Vlasov, A. S. Barnard, V. G. Ralchenko, O. I. Lebedev, M. V. Kanzyuba, A. V. Saveliev, V. I. Konov, and E. Goovaerts, "Nanodiamond photoemitters based on strong narrow-band luminescence from silicon-vacancy defects," *Adv. Mater.*, vol. 21, no. 7, pp. 808–812, 2009.

[95] A. A. Basov, M. Rähn, M. Pärs, I. I. Vlasov, I. Sildos, A. P. Bolshakov, V. G. Golubev, and V. G. Ralchenko, "Spatial localization of Si-vacancy photoluminescent centers in a thin CVD nanodiamond film," *Phys. Status Solidi Appl. Mater. Sci.*, vol. 206, no. 9, pp. 2009–2011, 2009.

[96] E. Neu, C. Hepp, M. Hauschild, S. Gsell, M. Fischer, H. Sternschulte, D. Steinmüller-Nethl, M. Schreck, and C. Becher, "Low-temperature investigations of single silicon vacancy colour centres in diamond," *New J. Phys.*, vol. 15, no. 111, 2013.

[97] J. Walkert and J. Walker, "Optical absorption and luminescence in diamond," *Reports Prog. Phys.*, vol. 42, no. 10, p. 1605, 1979.

[98] T. Gaebel, I. Popa, A. Gruber, M. Domhan, F. Jelezko, and J. Wrachtrup, "Stable single-

photon source in the near infrared," *New J. Phys.*, vol. 6, pp. 1–7, 2004.

[99] E. Neu, D. Steinmetz, J. Riedrich-Möller, S. Gsell, M. Fischer, M. Schreck, and C. Becher, "Single photon emission from silicon-vacancy colour centres in chemical vapour deposition nano-diamonds on iridium," *New J. Phys.*, vol. 13, 2011.

[100] A. T. Collins, L. Allers, C. J. H. Wort, and G. A. Scarsbrook, "The Annealing of Radiation-Damage in Debeers Colorless Cvd Diamond," *Diam. Relat. Mater.*, vol. 3, no. 4–6, pp. 932–935, 1994.

[101] E. Neu, M. Fischer, S. Gsell, M. Schreck, and C. Becher, "Fluorescence and polarization spectroscopy of single silicon vacancy centers in heteroepitaxial nanodiamonds on iridium," *Phys. Rev. B - Condens. Matter Mater. Phys.*, vol. 84, no. 20, pp. 1–9, 2011.

[102] L. J. Rogers, K. D. Jahnke, T. Teraji, L. Marseglia, C. Müller, B. Naydenov, H. Schauffert, C. Kranz, J. Isoya, L. P. McGuinness, and F. Jelezko, "Multiple intrinsically identical single-photon emitters in the solid state," *Nat. Commun.*, vol. 5, pp. 1–2, 2014.

[103] U. Jantzen, A. B. Kurz, D. S. Rudnicki, C. Schäfermeier, K. D. Jahnke, U. L. Andersen, V. A. Davydov, V. N. Agafonov, A. Kubanek, L. J. Rogers, and F. Jelezko, "Nanodiamonds carrying silicon-vacancy quantum emitters with almost lifetime-limited linewidths," *New J. Phys.*, vol. 18, no. 7, 2016.

[104] A. Sipahigil, K. D. Jahnke, L. J. Rogers, T. Teraji, J. Isoya, A. S. Zibrov, F. Jelezko, and M. D. Lukin, "Indistinguishable photons from separated silicon-vacancy centers in diamond," *Phys. Rev. Lett.*, vol. 113, no. 11, 2014.

[105] B. L. Green, S. Mottishaw, B. G. Breeze, A. M. Edmonds, U. F. S. D'Haenens-Johansson, M. W. Doherty, S. D. Williams, D. J. Twitchen, and M. E. Newton, "Neutral Silicon-Vacancy Center in Diamond: Spin Polarization and Lifetimes," *Phys. Rev. Lett.*, vol. 119, no. 9, pp. 1–6, 2017.

[106] T. Müller, C. Hepp, B. Pingault, E. Neu, S. Gsell, M. Schreck, H. Sternschulte, D. Steinmüller-Nethl, C. Becher, and M. Atatüre, "Optical signatures of silicon-vacancy spins in diamond," *Nat. Commun.*, vol. 5, 2014.

[107] V. A. Nadolinny, A. P. Yelisseyev, J. M. Baker, M. E. Newton, D. J. Twitchen, S. C. Lawson, O. P. Yuryeva, and B. N. Feigelson, "A study of 13C hyperfine structure in the EPR of nickel-nitrogen-containing centres in diamond and correlation with their optical properties," *J. Phys. Condens. Matter*, vol. 11, no. 38, pp. 7357–7376, 1999.

[108] A. Yelisseyev, S. Lawson, I. Sildos, A. Osvet, V. Nadolinny, B. Feigelson, J. M. Baker, M. Newton, and O. Yuryeva, "Effect of HPHT annealing on the photoluminescence of synthetic diamonds grown in the Fe-Ni-C system," *Diam. Relat. Mater.*, vol. 12, no. 12, pp. 2147–2168, 2003.

[109] I. Kratochvílová, A. Kovalenko, F. Fendrych, V. Petráková, S. Záliš, and M. Nesládek, "Tuning of nanodiamond particles' optical properties by structural defects and surface modifications: DFT modelling," *Journal of Materials Chemistry*, vol. 21, no. 45. p. 18248, 2011.

[110] J. R. Rabeau, Y. L. Chin, S. Prawer, F. Jelezko, T. Gaebel, and J. Wrachtrup, "Fabrication of single nickel-nitrogen defects in diamond by chemical vapor deposition," *Appl. Phys. Lett.*, vol. 86, no. 13, pp. 1–3, 2005.

[111] E. Wu, J. R. Rabeau, G. Roger, F. Treussart, H. Zeng, P. Grangier, S. Prawer, and J. F. Roch, "Room temperature triggered single-photon source in the near infrared," *New J. Phys.*, vol. 9, 2007.

[112] A. Sipahigil, R. E. Evans, D. D. Sukachev, M. J. Burek, J. Borregaard, M. K. Bhaskar, C. T. Nguyen, J. L. Pacheco, H. A. Atikian, C. Meuwly, R. M. Camacho, F. Jelezko, E. Bielejec, H. Park, M. Lončar, and M. D. Lukin, "An integrated diamond nanophotonics platform for quantum-optical networks," *Science (80-. ).*, vol. 354, no. 6314, pp. 847–850, 2016.

[113] N. Kalb, A. A. Reiserer, P. C. Humphreys, J. J. W. Bakermans, and S. J. Kamerling, "Entanglement Distillation between Solid-State Quantum Network Nodes," vol. 932, no. June, pp. 1–8, 2017.

[114] N. Aslam, M. Pfender, P. Neumann, R. Reuter, A. Zappe, F. F. De Oliveira, A. Denisenko, H. Sumiya, S. Onoda, J. Isoya, and J. Wrachtrup, "Nanoscale nuclear magnetic resonance with chemical resolution," *Science (80-. ).*, vol. 357, no. 6346, pp. 67–71, 2017.

[115] J. L. Zhang, H. Ishiwata, T. M. Babinec, M. Radulaski, K. Müller, K. G. Lagoudakis, J. Dahl, R. Edgington, V. Soulière, G. Ferro, A. a. Fokin, P. R. Schreiner, Z.-X. Shen, N. a. Melosh, and J. Vučković, "Hybrid Group IV Nanophotonic Structures Incorporating Diamond Silicon-Vacancy Color Centers," pp. 1–20, 2015.

[116] J. N. Becker, J. Görlitz, C. Arend, M. Markham, and C. Becher, "Ultrafast all-optical

coherent control of single silicon vacancy colour centres in diamond," *Nat. Commun.*, vol. 7, pp. 1–6, 2016.

[117] Y. Zhou, A. Rasmita, K. Li, Q. Xiong, I. Aharonovich, and W. B. Gao, "Coherent control of a strongly driven silicon vacancy optical transition in diamond," *Nat. Commun.*, vol. 8, pp. 1–7, 2017.

[118] C. Arend, J. N. Becker, H. Sternschulte, D. Steinmüller-Nethl, and C. Becher, "Photoluminescence excitation and spectral hole burning spectroscopy of silicon vacancy centers in diamond," *Phys. Rev. B*, vol. 94, no. 4, pp. 1–7, 2016.

[119] K. D. Jahnke, A. Sipahigil, J. M. Binder, M. W. Doherty, M. Metsch, L. J. Rogers, N. B. Manson, M. D. Lukin, and F. Jelezko, "Electron-phonon processes of the silicon-vacancy centre in diamond," *New J. Phys.*, vol. 17, 2015.

[120] M. K. Bhaskar, D. D. Sukachev, A. Sipahigil, R. E. Evans, M. J. Burek, C. T. Nguyen, L. J. Rogers, P. Siyushev, M. H. Metsch, H. Park, F. Jelezko, M. Lončar, and M. D. Lukin, "Quantum Nonlinear Optics with a Germanium-Vacancy Color Center in a Nanoscale Diamond Waveguide," pp. 1–5, 2016.

[121] K. N. Boldyrev, B. N. Mavrin, and M. N. Popova, "Bright luminescence of diamonds with Ge-V centers," *Journal of Luminescence*, Elsevier B.V., 2017.

[122] T. Iwasaki, F. Ishibashi, Y. Miyamoto, Y. Doi, S. Kobayashi, T. Miyazaki, K. Tahara, K. D. Jahnke, L. J. Rogers, B. Naydenov, F. Jelezko, S. Yamasaki, S. Nagamachi, T. Inubushi, N. Mizuochi, and M. Hatano, "Germanium-Vacancy Single Color Centers in Diamond," *Sci. Rep.*, vol. 5, no. 1, p. 12882, Oct. 2015.

[123] V. G. Ralchenko, V. S. Sedov, A. A. Khomich, V. S. Krivobok, S. N. Nikolaev, S. S. Savin, I. I. Vlasov, and V. I. Konov, "Observation of the Ge-vacancy color center in microcrystalline diamond films," *Bull. Lebedev Phys. Inst.*, vol. 42, no. 6, pp. 165–168, Jun. 2015.

[124] P. Siyushev, M. H. Metsch, A. Ijaz, J. M. Binder, M. K. Bhaskar, D. D. Sukachev, A. Sipahigil, R. E. Evans, C. T. Nguyen, M. D. Lukin, P. R. Hemmer, Y. N. Palyanov, I. N. Kupriyanov, Y. M. Borzdov, L. J. Rogers, and F. Jelezko, "Optical and microwave control of germanium-vacancy center spins in diamond," *Phys. Rev. B*, vol. 96, no. 8, pp. 1–5, 2017.

[125] Y. N. Palyanov, I. N. Kupriyanov, Y. M. Borzdov, A. F. Khokhryakov, and N. V.

Surovtsev, “High-Pressure Synthesis and Characterization of Ge-Doped Single Crystal Diamond,” *Cryst. Growth Des.*, vol. 16, no. 6, pp. 3510–3518, 2016.

[126] S. Ditalia Tchernij, T. Herzig, J. Forneris, J. Küpper, S. Pezzagna, P. Traina, E. Moreva, I. P. Degiovanni, G. Brida, N. Skukan, M. Genovese, M. Jakšić, J. Meijer, and P. Olivero, “Single-photon-emitting optical centers in diamond fabricated upon Sn implantation,” pp. 1–10.

[127] T. Iwasaki, Y. Miyamoto, T. Taniguchi, P. Siyushev, M. H. Metsch, F. Jelezko, and M. Hatano, “Tin-Vacancy Quantum Emitters in Diamond,” *Phys. Rev. Lett.*, vol. 119, no. 25, pp. 1–6, 2017.

[128] K. Li, Y. Zhou, A. Rasmita, I. Aharonovich, and W. B. Gao, “Nonblinking Emitters with Nearly Lifetime-Limited Linewidths in CVD Nanodiamonds,” *Phys. Rev. Appl.*, vol. 6, no. 024010, pp. 1–7, 2016.

[129] R. E. Evans, A. Sipahigil, D. D. Sukachev, A. S. Zibrov, and M. D. Lukin, “Narrow-Linewidth Homogeneous Optical Emitters in Diamond Nanostructures via Silicon Ion Implantation,” *Phys. Rev. Appl.*, vol. 5, no. 4, pp. 1–8, 2016.

[130] L. J. Rogers, O. Wang, Y. Liu, L. Antoniuk, C. Osterkamp, V. A. Davydov, V. N. Agafonov, A. B. Filipovski, F. Jelezko, and A. Kubanek, “Single SiV$^-$ centers in low-strain nanodiamonds with bulk-like spectral properties and nano-manipulation capabilities,” *ArXiv*, pp. 1–10, Feb. 2018.

[131] D. D. Sukachev, A. Sipahigil, C. T. Nguyen, M. K. Bhaskar, R. E. Evans, F. Jelezko, and M. D. Lukin, “The silicon-vacancy spin qubit in diamond: quantum memory exceeding ten milliseconds and single-shot state readout,” no. c, pp. 1–5, 2017.

[132] J. N. Becker, B. Pingault, D. Groß, M. Gündoğan, N. Kukharchyk, M. Markham, A. Edmonds, M. Atatüre, P. Bushev, and C. Becher, “All-Optical Control of the Silicon-Vacancy Spin in Diamond at Millikelvin Temperatures,” *Phys. Rev. Lett.*, vol. 120, no. 5, pp. 1–6, 2018.

[133] M. J. Burek, C. Meuwly, R. E. Evans, M. K. Bhaskar, A. Sipahigil, S. Meesala, B. MacHielse, D. D. Sukachev, C. T. Nguyen, J. L. Pacheco, E. Bielejec, M. D. Lukin, and M. Lončar, “Fiber-coupled diamond quantum nanophotonic interface,” *Phys. Rev. Appl.*, vol. 8, no. 2, pp. 1–10, 2017.

[134] T. Schröder, S. Mouradian, J. Zheng, M. E. Trusheim, M. Walsh, E. H. Chen, L. Li, I.

Bayn, and D. Englund, “Review Article: Quantum Nanophotonics in Diamond,” pp. 1–23, 2016.

[135] J. Riedrich-mo, C. Arend, C. Pauly, F. Mu, M. Fischer, S. Gsell, M. Schreck, and C. Becher, “Deterministic Coupling of a Single Silicon-Vacancy Color Center to a Photonic Crystal Cavity in Diamond,” *Nano Lett.*, vol. 14, pp. 5281–5287, 2014.

[136] S. D. Tchernij, T. Herzig, J. Forneris, J. Küpper, S. Pezzagna, P. Traina, E. Moreva, I. P. Degiovanni, G. Brida, N. Skukan, M. Genovese, M. Jakšić, J. Meijer, and P. Olivero, “Single-Photon-Emitting Optical Centers in Diamond Fabricated upon Sn Implantation,” *ACS Photonics*, vol. 4, no. 10, pp. 2580–2586, 2017.

[137] I. Aharonovich and E. Neu, “Diamond Nanophotonics,” *Adv. Opt. Mater.*, pp. 1–18, 2014.

[138] U. Resch-Genger, M. Grabolle, S. Cavaliere-Jaricot, R. Nitschke, and T. Nann, “Quantum dots versus organic dyes as fluorescent labels.,” *Nat. Methods*, vol. 5, no. 9, pp. 763–775, 2008.

[139] Y. Xing and J. Rao, “Quantum dot bioconjugates for in vitro diagnostics & in vivo imaging.,” *Cancer Biomark.*, vol. 4, no. 6, pp. 307–319, 2008.

[140] J. Geys, A. Nemmar, E. Verbeken, E. Smolders, M. Ratoi, M. F. Hoylaerts, B. Nemery, and P. H. M. Hoet, “Acute toxicity and prothrombotic effects of Quantum dots: Impact of surface charge,” *Environ. Health Perspect.*, vol. 116, no. 12, pp. 1607–1613, 2008.

[141] S. Mahendra, H. Zhu, V. L. Colvin, and P. J. Alvarez, “Quantum dot weathering results in microbial toxicity,” *Environ. Sci. Technol.*, vol. 42, no. 24, pp. 9424–9430, 2008.

[142] R. Schirhagl, K. Chang, M. Loretz, and C. L. Degen, “Nitrogen-vacancy centers in diamond: nanoscale sensors for physics and biology,” *Annu. Rev. Phys. Chem.*, vol. 65, pp. 83–105, 2014.

[143] I. Aharonovich, S. Castelletto, D. A. Simpson, C. H. Su, A. D. Greentree, and S. Prawer, “Diamond-based single-photon emitters,” *Reports Prog. Phys.*, vol. 74, no. 7, 2011.

[144] S. Pezzagna, D. Rogalla, D. Wildanger, J. Meijer, and A. Zaitsev, “Creation and nature of optical centres in diamond for single-photon emission—overview and critical remarks,” *New J. Phys.*, vol. 13, no. 3, p. 035024, 2011.

[145] B. Lounis and W. E. Moerner, “Single photons on demand from a single molecules at

room temperature," *Nature*, vol. 407, no. 28, pp. 491–493, 2000.

[146] C. Toninelli, K. Early, J. Bremi, A. Renn, S. Goetzinger, and V. Sandoghdar, "Near-infrared single-photons from aligned molecules in ultrathin crystalline films at room temperature," vol. 18, no. 7, pp. 23986–23991, 2010.

[147] A. Beveratos, S. Kühn, R. Brouri, T. Gacoin, J. P. Poizat, and P. Grangier, "Room temperature stable single-photon source," *Eur. Phys. J. D*, vol. 18, no. 2, pp. 191–196, 2002.

[148] R. Hanbury Brown and R. Q. Twiss, "Correlation between photons in two coherent beams of light," *Nature*, no. 4497, pp. 27–29, Mar. 1956.

[149] J. Riedrich-Möller, L. Kipfstuhl, C. Hepp, E. Neu, C. Pauly, F. Mücklich, A. Baur, M. Wandt, S. Wolff, M. Fischer, S. Gsell, M. Schreck, and C. Becher, "One- and two-dimensional photonic crystal microcavities in single crystal diamond," *Nat. Nanotechnol.*, vol. 7, p. 69, Nov. 2011.

[150] B. J. M. Hausmann, B. Shields, Q. Quan, P. Maletinsky, M. McCutcheon, J. T. Choy, T. M. Babinec, A. Kubanek, A. Yacoby, M. D. Lukin, and M. Lončar, "Integrated diamond networks for quantum nanophotonics," *Nano Lett.*, vol. 12, no. 3, pp. 1578–1582, 2012.

[151] J. Isberg, J. Hammersberg, E. Johansson, T. Wikström, D. J. Twitchen, A. J. Whitehead, S. E. Coe, and G. A. Scarsbrook, "High carrier mobility in single-crystal plasma-deposited diamond.," *Science*, vol. 297, no. 5587, pp. 1670–1672, Sep. 2002.

[152] C. J. H. Wort and R. S. Balmer, "Diamond as an electronic material," *Materials Today*, vol. 11, no. 1–2. Elsevier Ltd, pp. 22–28, 2008.

[153] S. Koizumi, K. Watanabe, M. Hasegawa, and H. Kanda, "Ultraviolet Emission from a Diamond pn Junction," *Science (80-. ).*, vol. 292, no. June, pp. 1899–1901, 2001.

[154] T. Makino, K. Yoshino, N. Sakai, K. Uchida, S. Koizumi, H. Kato, D. Takeuchi, M. Ogura, K. Oyama, T. Matsumoto, H. Okushi, and S. Yamasaki, "Enhancement in emission efficiency of diamond deep-ultraviolet light emitting diode," *Appl. Phys. Lett.*, vol. 99, no. 6, pp. 25–28, 2011.

[155] J. Achard, F. Silva, R. Issaoui, O. Brinza, A. Tallaire, H. Schneider, K. Isoird, H. Ding, S. Koné, M. A. Pinault, F. Jomard, and A. Gicquel, "Thick boron doped diamond single crystals for high power electronics," *Diam. Relat. Mater.*, vol. 20, no. 2, pp. 145–152,

2011.

[156] H. Kato, T. Makino, S. Yamasaki, and H. Okushi, “n-type diamond growth by phosphorus doping on (0 0 1)-oriented surface,” *J. Phys. D. Appl. Phys.*, vol. 40, no. 20, pp. 6189–6200, Oct. 2007.

[157] T. Iwasaki, Y. Hoshino, K. Tsuzuki, H. Kato, T. Makino, and M. Ogura, “High-Temperature Operation of Diamond Junction Field-Effect Transistors With Lateral p-n Junctions,” vol. 34, no. 9, pp. 1175–1177, 2013.

[158] A. Lohrmann, S. Pezzagna, I. Dobrinets, P. Spinicelli, V. Jacques, J. F. Roch, J. Meijer, and A. M. Zaitsev, “Diamond based light-emitting diode for visible single-photon emission at room temperature,” *Appl. Phys. Lett.*, vol. 99, no. 25, 2011.

[159] N. Mizuochi, T. Makino, H. Kato, D. Takeuchi, M. Ogura, H. Okushi, M. Nothaft, P. Neumann, A. Gali, F. Jelezko, J. Wrachtrup, and S. Yamasaki, “Electrically driven single-photon source at room temperature in diamond,” vol. 6, no. April, pp. 299–303, 2012.

[160] K. Bray, H. Kato, R. Previdi, R. Sandstrom, K. Ganesan, M. Ogura, T. Makino, S. Yamasaki, A. P. Magyar, M. Toth, and I. Aharonovich, “Single crystal diamond membranes for nanoelectronics,” *Nanoscale*, vol. 10, no. 8, pp. 4028–4035, 2018.

[161] S. Pezzagna, B. Naydenov, F. Jelezko, J. Wrachtrup, and J. Meijer, “Creation efficiency of nitrogen-vacancy centres in diamond,” *New J. Phys.*, vol. 12, 2010.

[162] Y. Doi, T. Makino, H. Kato, D. Takeuchi, M. Ogura, H. Okushi, H. Morishita, T. Tashima, S. Miwa, S. Yamasaki, P. Neumann, J. Wrachtrup, Y. Suzuki, and N. Mizuochi, “Deterministic Electrical Charge-State Initialization of Single Nitrogen-Vacancy Center in Diamond,” vol. 011057, pp. 1–11, 2014.

[163] H. Kato, M. Wolfer, C. Schreyvogel, M. Kunzer, W. Müller-Sebert, H. Obloh, S. Yamasaki, and C. Nebel, “Tunable light emission from nitrogen-vacancy centers in single crystal diamond PIN diodes,” *Appl. Phys. Lett.*, vol. 102, no. 15, pp. 1–5, 2013.

[164] S. F. Joannopoulos J.D, Pierre R. Villeneuve, “Photonic crystals:putting a new twist on light,” *Nature*, vol. 386. p. 7, 1997.

[165] A. Scherer, O. Painter, J. Vuckovic, M. Loncar, and T. Yoshie, “Photonic crystals for confining, guiding, and emitting light,” *IEEE Trans. Nanotechnol.*, 2002.

[166] Y. N. Zhang, Y. Zhao, and R. Q. Lv, "A review for optical sensors based on photonic crystal cavities," *Sensors Actuators, A Phys.*, vol. 233, pp. 374–389, 2015.

[167] J. B. Wright, S. Liu, G. T. Wang, Q. Li, A. Benz, D. D. Koleske, P. Lu, H. Xu, L. Lester, T. S. Luk, I. Brener, and G. Subramania, "Multi-colour nanowire photonic crystal laser pixels," *Sci. Rep.*, vol. 3, pp. 16–19, 2013.

[168] G. Shambat, B. Ellis, J. Petykiewicz, M. A. Mayer, A. Majumdar, T. Sarmiento, J. S. Harris, E. E. Haller, and J. Vuckovic, "Electrically Driven Photonic Crystal Nanocavity Devices," *IEEE J. Sel. Top. Quantum Electron.*, vol. 18, no. 6, pp. 1700–1710, 2012.

[169] A. Majumdar, J. Kim, J. Vuckovic, and F. Wang, "Electrical control of silicon photonic crystal cavity by graphene," *Nano Lett.*, vol. 13, no. 2, pp. 515–518, 2013.

[170] X. Gan, R. J. Shiue, Y. Gao, K. F. Mak, X. Yao, L. Li, A. Szep, D. Walker, J. Hone, T. F. Heinz, and D. Englund, "High-contrast electrooptic modulation of a photonic crystal nanocavity by electrical gating of graphene," *Nano Lett.*, vol. 13, no. 2, pp. 691–696, 2013.

[171] M. Haurylau, S. P. Anderson, K. L. Marshall, and P. M. Fauchet, "Electrical modulation of silicon-based two-dimensional photonic bandgap structures," *Appl. Phys. Lett.*, vol. 88, no. 6, pp. 22–25, 2006.

[172] S. W. Leonard, J. P. Mondia, H. M. Van Driel, O. Toader, S. John, K. Busch, a. Birner, U. Gosele, and V. Lehmann, "Tunable two-dimensional photonic crystals using liquid-crystal infiltratio," *Phys. Rev. B*, vol. 61, no. 4, pp. 2389–2392, 2000.

[173] D. McPhail, M. Straub, and M. Gu, "Electrical tuning of three-dimensional photonic crystals using polymer dispersed liquid crystals," *Appl. Phys. Lett.*, vol. 86, no. 5, pp. 1–3, 2005.

[174] P. E. Barclay, K. M. C. Fu, C. Santori, and R. G. Beausoleil, "Chip-based microcavities coupled to nitrogen-vacancy centers in single crystal diamond," *Appl. Phys. Lett.*, vol. 95, no. 19, pp. 4–7, 2009.

[175] P. E. Barclay, C. Santori, K.-M. Fu, R. G. Beausoleil, and O. Painter, "Coherent interference effects in a nano-assembled optical cavity-QED system," vol. 17, no. 10, pp. 2012–2014, 2008.

[176] C. Santori, P. E. Barclay, K.-M. C. Fu, R. G. Beausoleil, S. Spillane, and M. Fisch, "Nanophotonics for quantum optics using nitrogen-vacancy centers in diamond,"

*Nanotechnology*, vol. 21, no. 27, p. 274008, 2010.

[177] S. Deshpande, T. Frost, A. Hazari, and P. Bhattacharya, "Electrically pumped single-photon emission at room temperature from a single InGaN/GaN quantum dot," *Appl. Phys. Lett.*, vol. 105, no. 14, 2014.

[178] Z. Yuan, B. E. Kardynal, R. M. Stevenson, A. J. Shields, C. J. Lobo, K. Cooper, N. S. Beattie, D. A. Ritchie, and M. Peppe, "Electrically Driven Single-Photon Source," *Science (80-. ).*, vol. 295, no. 5552, pp. 102–105, Jan. 2002.

[179] J. S. Ross, P. Klement, A. M. Jones, N. J. Ghimire, J. Yan, D. G. Mandrus, T. Taniguchi, K. Watanabe, K. Kitamura, W. Yao, D. H. Cobden, and X. Xu, "Electrically tunable excitonic light-emitting diodes based on monolayer WSe2 p–n junctions," *Nat. Nanotechnol.*, vol. 9, no. 4, pp. 268–272, 2014.

[180] I. A. Khramtsov, A. A. Vyshnevyy, and D. Y. Fedyanin, "Enhancing the brightness of electrically driven single-photon sources using color centers in silicon carbide," *npj Quantum Inf.*, vol. 4, no. 1, p. 15, 2018.

[181] M. Ikeda, T. Hayakawa, S. Yamagiwa, H. Matsunami, and T. Tanaka, "Fabrication of 6H-SiC light-emitting diodes by a rotation dipping technique: Electroluminescence mechanisms," *J. Appl. Phys.*, vol. 50, no. 12, pp. 8215–8225, 1979.

[182] L. Zhang, Y.-J. Yu, L.-G. Chen, Y. Luo, B. Yang, F.-F. Kong, G. Chen, Y. Zhang, Q. Zhang, Y. Luo, J.-L. Yang, Z.-C. Dong, and J. G. Hou, "Electrically driven single-photon emission from an isolated single molecule," *Nat. Commun.*, vol. 8, no. 1, p. 580, 2017.

[183] R. S. Sundaram, M. Engel, A. Lombardo, R. Krupke, A. C. Ferrari, P. Avouris, and M. Steiner, "Electroluminescence in single layer MoS2," *Nano Lett.*, vol. 13, no. 4, pp. 1416–1421, 2013.

[184] Y. Ye, Z. Ye, M. Gharghi, H. Zhu, M. Zhao, Y. Wang, X. Yin, and X. Zhang, "Exciton-dominant electroluminescence from a diode of monolayer MoS2," *Appl. Phys. Lett.*, vol. 104, no. 19, 2014.

[185] P. Michler, A. Kiraz, C. Becher, and W. V Schoenfeld, "A Quantum Dot Single-Photon Turnstile Device," vol. 290, no. December, pp. 2282–2286, 2000.

[186] S. Deshpande, J. Heo, A. Das, and P. Bhattacharya, "Electrically driven polarized single-photon emission from an InGaN quantum dot in a GaN nanowire," *Nat. Commun.*, vol.

4, p. 1675, 2013.

[187] S. Choi, A. M. Berhane, A. Gentle, C. Ton-that, M. R. Phillips, and I. Aharonovich, "Electroluminescence from Localized Defects in Zinc Oxide: Toward Electrically Driven Single Photon Sources at Room Temperature," *ACS Appl. Mater. Interfaces*, vol. 7, no. 10, pp. 5619–5623, 2015.

[188] C. Sandorfy, E. North-holland, Z. Yuan, B. E. Kardynal, R. M. Stevenson, A. J. Shields, C. J. Lobo, K. Cooper, N. S. Beattie, D. A. Ritchie, and M. Pepper, "Electrically Driven Single-Photon Source," vol. 295, no. January, 2002.

[189] Sze, *Physics of Semiconductor Devices Physics of Semiconductor Devices*. 1995.

[190] M. J. Cristea, "Unified model for p-n junction Current-voltage characteristics," *Cent. Eur. J. Eng.*, vol. 1, no. 1, pp. 113–116, 2011.

[191] A. J. Shields, "Semiconductor quantum light sources," *Nat. Photonics*, vol. 1, no. 4, pp. 215–223, 2007.

[192] D. Y. Fedyanin and M. Agio, "Ultrabright single-photon source on diamond with electrical pumping at room and high temperatures," *New J. Phys.*, vol. 18, no. 7, p. 073012, 2016.

[193] D. D. Awschalom, L. C. Bassett, A. S. Dzurak, E. L. Hu, and J. R. Petta, "Quantum spintronics: Engineering and manipulating atom-like spins in semiconductors," *Science (80-. ).*, vol. 339, no. 6124, pp. 1174–1179, 2013.

[194] E. Neu, R. Albrecht, M. Fischer, S. Gsell, M. Schreck, and C. Becher, "Electronic transitions of single silicon vacancy centers in the near-infrared spectral region," *Phys. Rev. B - Condens. Matter Mater. Phys.*, vol. 85, no. 24, pp. 1–8, 2012.

[195] L. J. Rogers, K. D. Jahnke, M. W. Doherty, A. Dietrich, L. P. McGuinness, C. Müller, T. Teraji, H. Sumiya, J. Isoya, N. B. Manson, and F. Jelezko, "Electronic structure of the negatively charged silicon-vacancy center in diamond," *Phys. Rev. B - Condens. Matter Mater. Phys.*, vol. 89, no. 23, pp. 1–8, 2014.

[196] S. L. Mouradian and D. Englund, "A tunable waveguide-coupled cavity design for scalable interfaces to solid-state quantum emitters," *APL Photonics*, vol. 2, no. 4, p. 046103, 2017.

[197] S. Schietinger, M. Barth, T. Aichele, and O. Benson, "Plasmon-enhanced single photon

emission from a nanoassembled metal-diamond hybrid structure at room temperature.," *Nano Lett.*, vol. 9, no. 4, pp. 1694–1698, 2009.

[198] K. J. Vahala, "Optical microcavities," *Nature*, vol. 424, no. 6950, pp. 839–846, 2003.

[199] A. Faraon, C. Santori, Z. Huang, V. M. Acosta, and R. G. Beausoleil, "Coupling of nitrogen-vacancy centers to photonic crystal cavities in monocrystalline diamond," *Phys. Rev. Lett.*, vol. 109, no. 3, pp. 2–6, 2012.

[200] A. Faraon, P. E. Barclay, C. Santori, K. M. C. Fu, and R. G. Beausoleil, "Resonant enhancement of the zero-phonon emission from a colour centre in a diamond cavity," *Nat. Photonics*, vol. 5, no. 5, pp. 301–305, 2011.

[201] M. J. Burek, N. P. De Leon, B. J. Shields, B. J. M. Hausmann, Y. Chu, Q. Quan, A. S. Zibrov, H. Park, M. D. Lukin, and M. Lončar, "Free-standing mechanical and photonic nanostructures in single-crystal diamond," *Nano Lett.*, vol. 12, no. 12, pp. 6084–6089, 2012.

[202] N. R. Parikh, J. D. Hunn, E. McGucken, M. L. Swanson, C. W. White, R. a. Rudder, D. P. Malta, J. B. Posthill, and R. J. Markunas, "Single-crystal diamond plate liftoff achieved by ion implantation and subsequent annealing," *Appl. Phys. Lett.*, vol. 61, no. 26, pp. 3124–3126, 1992.

[203] I. Aharonovich, J. C. Lee, A. P. Magyar, B. B. Buckley, C. G. Yale, D. D. Awschalom, and E. L. Hu, "Homoepitaxial growth of single crystal diamond membranes for quantum information processing," *Adv. Mater.*, vol. 24, no. 10, 2012.

[204] A. H. Piracha, P. Rath, K. Ganesan, S. Kühn, W. H. P. Pernice, and S. Prawer, "Scalable Fabrication of Integrated Nanophotonic Circuits on Arrays of Thin Single Crystal Diamond Membrane Windows," *Nano Lett.*, vol. 16, no. 5, pp. 3341–3347, May 2016.

[205] A. H. Piracha, K. Ganesan, D. W. M. Lau, A. Stacey, L. P. McGuinness, S. Tomljenovic-Hanic, and S. Prawer, "Scalable fabrication of high-quality, ultra-thin single crystal diamond membrane windows.," *Nanoscale*, vol. 8, pp. 6860–6865, 2016.

[206] R. S. Balmer, J. R. Brandon, S. L. Clewes, H. K. Dhillon, J. M. Dodson, I. Friel, P. N. Inglis, T. D. Madgwick, M. L. Markham, T. P. Mollart, N. Perkins, G. a Scarsbrook, D. J. Twitchen, a J. Whitehead, J. J. Wilman, and S. M. Woollard, "Chemical vapour deposition synthetic diamond: materials, technology and applications.," *J. Phys. Condens. Matter*, vol. 21, no. 36, p. 364221, 2009.

[207] S. Tomljenovic-Hanic, M. J. Steel, C. M. de Sterke, and J. Salzman, "Diamond based photonic crystal microcavities," *Opt. Express*, vol. 14, no. 8, p. 3556, 2006.

[208] A. P. Magyar, J. C. Lee, A. M. Limarga, I. Aharonovich, F. Rol, D. R. Clarke, M. Huang, and E. L. Hu, "Fabrication of thin, luminescent, single-crystal diamond membranes," *Appl. Phys. Lett.*, vol. 99, no. 8, 2011.

[209] I. Aharonovich, J. C. Lee, A. P. Magyar, B. B. Buckley, C. G. Yale, D. D. Awschalom, and E. L. Hu, "Homoepitaxial growth of single crystal diamond membranes for quantum information processing," *Adv. Mater.*, vol. 24, no. 10, pp. OP54-OP59, Mar. 2012.

[210] G. Faggio, G. Messina, S. Santangelo, G. Prestopino, I. Ciancaglioni, and M. Marinelli, "Raman scattering in boron-doped single-crystal diamond used to fabricate Schottky diode detectors," *J. Quant. Spectrosc. Radiat. Transf.*, vol. 113, no. 18, pp. 2476–2481, Dec. 2012.

[211] J. Bochmann, A. Vainsencher, D. D. Awschalom, and A. N. Cleland, "Nanomechanical coupling between microwave and optical photons," *Nat. Phys.*, vol. 9, no. 11, pp. 712–716, 2013.

[212] H. Watanabe, C. E. Nebel, and S. Shikata, "Isotopic Homojunction Band Engineering from Diamond," *Science (80-. ).*, vol. 342, no. June, pp. 1425–1428, 2009.

[213] M. V Hauf, P. Simon, M. Seifert, A. W. Holleitner, M. Stutzmann, and J. A. Garrido, "Low dimensionality of the surface conductivity of diamond," *Phys. Rev. B - Condens. Matter Mater. Phys.*, vol. 89, no. 11, pp. 1–5, 2014.

[214] S. Shikata, "Single crystal diamond wafers for high power electronics," *Diam. Relat. Mater.*, vol. 65, pp. 168–175, 2016.

[215] T. Matsumoto, H. Kato, K. Oyama, T. Makino, M. Ogura, D. Takeuchi, T. Inokuma, N. Tokuda, and S. Yamasaki, "Inversion channel diamond metal-oxide-semiconductor field-effect transistor with normally off characteristics," *Sci. Rep.*, vol. 6, no. 1, p. 31585, 2016.

[216] H. Schneider, J. L. Sanchez, and J. Achard, "2005 European Conference on Power Electronics and Applications."

[217] P. Rath, S. Khasminskaya, C. Nebel, C. Wild, and W. H. P. Pernice, "Diamond-integrated optomechanical circuits," *Nat. Commun.*, vol. 4, p. 1690, 2013.

[218] S. Drijkoningen, S. D. Janssens, P. Pobedinskas, S. Koizumi, M. K. Van Bael, and K. Haenen, "The pressure sensitivity of wrinkled B-doped nanocrystalline diamond membranes," *Sci. Rep.*, vol. 6, no. 1, p. 35667, Dec. 2016.

[219] A. R. Krauss, O. Auciello, D. M. Gruen, A. Jayatissa, A. Sumant, J. Tucek, D. C. Mancini, N. Moldovan, A. Erdemir, D. Ersoy, M. N. Gardos, H. G. Busmann, E. M. Meyer, and M. Q. Ding, "Ultrananocrystalline diamond thin films for MEMS and moving mechanical assembly devices," *Diam. Relat. Mater.*, vol. 10, no. 11, pp. 1952–1961, 2001.

[220] F. Buja, A. V. Sumant, J. Kokorian, and W. M. van Spengen, "Electrically conducting ultrananocrystalline diamond for the development of a next generation of micro-actuators," *Sensors Actuators A Phys.*, vol. 214, pp. 259–266, 2014.

[221] J. V. Macpherson, "A practical guide to using boron doped diamond in electrochemical research," *Phys. Chem. Chem. Phys.*, vol. 17, no. 5, pp. 2935–2949, 2015.

[222] P. Rath, S. Ummethala, C. Nebel, and W. H. P. Pernice, "Diamond as a material for monolithically integrated optical and optomechanical devices," *Phys. Status Solidi*, vol. 15, p. n/a-n/a, 2015.

[223] B. Khanaliloo, H. Jayakumar, A. C. Hryciw, D. P. Lake, H. Kaviani, and P. E. Barclay, "Single-Crystal Diamond Nanobeam Waveguide Optomechanics," *Phys. Rev. X*, vol. 5, no. 4, pp. 041051-1-041051-21, Dec. 2015.

[224] J. E. Butler, M. W. Geis, K. E. Krohn, J. Lawless, S. Deneault, T. M. Lyszczarz, D. Flechtner, and R. Wright, "Exceptionally high voltage Schottky diamond diodes and low boron doping," *Semicond. Sci. Technol.*, vol. 18, no. 3, pp. S67–S71, 2003.

[225] T. Makino, S. Tanimoto, H. Kato, N. Tokuda, M. Ogura, D. Takeuchi, K. Oyama, H. Ohashi, H. Okushi, and S. Yamasaki, "Diamond Schottky p-n diode with high forward current density and fast switching operation," *Appl. Phys. Lett.*, vol. 94, pp. 1–3, Sep. 2009.

[226] A. Lohrmann, N. Iwamoto, Z. Bodrog, S. Castelletto, T. Ohshima, T. J. Karle, A. Gali, S. Prawer, J. C. McCallum, and B. C. Johnson, "Single-photon emitting diode in silicon carbide," *Nat. Commun.*, vol. 6, p. 7783, Jul. 2015.

[227] Y.-S. Choi, J.-W. Kang, D.-K. Hwang, and S.-J. Park, "Recent Advances in ZnO-Based Light-Emitting Diodes," *IEEE Trans. Electron Devices*, vol. 57, no. 1, pp. 26–41, Jan.

2010.

[228] M. Katagiri, J. Isoya, S. Koizumi, and H. Kanda, “Lightly phosphorus-doped homoepitaxial diamond films grown by chemical vapor deposition,” *Appl. Phys. Lett.*, vol. 85, no. 26, pp. 6365–6367, 2004.

[229] H. Kato, T. Makino, S. Yamasaki, and H. Okushi, “N-type diamond growth by phosphorus doping on (0 0 1)-oriented surface,” *J. Phys. D. Appl. Phys.*, vol. 40, no. 20, pp. 6189–6200, 2007.

[230] W. Zhao, Z. Ghorannevis, L. Chu, M. Toh, C. Kloc, P.-H. Tan, and G. Eda, “Evolution of Electronic Structure in Atomically Thin Sheets of WS 2 and WSe 2,” *ACS Nano*, vol. 7, no. 1, pp. 791–797, Jan. 2013.

[231] A. M. Jones, H. Yu, N. J. Ghimire, S. Wu, G. Aivazian, J. S. Ross, B. Zhao, J. Yan, D. G. Mandrus, D. Xiao, W. Yao, and X. Xu, “Optical generation of excitonic valley coherence in monolayer WSe2,” *Nat. Nanotechnol.*, vol. 8, no. 9, pp. 634–638, Sep. 2013.

[232] G. J. Hedley, A. Ruseckas, and I. D. W. Samuel, “Ultrafast intersystem crossing in a red phosphorescent indium complex,” *J. Phys. Chem. A*, vol. 113, no. 1, pp. 2–4, 2009.

[233] H. Yersin, “Highly Efficient OLEDs with Phosphorescent Materials,” *Highly Effic. OLEDs with Phosphorescent Mater.*, no. 3, pp. 1–438, 2008.

[234] M. Nothaft, S. Höhla, F. Jelezko, N. Frühauf, J. Pflaum, and J. Wrachtrup, “Electrically driven photon antibunching from a single molecule at room temperature,” *Nat. Commun.*, vol. 3, p. 628, 2012.

[235] T. M. Babinec, J. T. Choy, K. J. M. Smith, M. Khan, and M. Lončar, “Design and focused ion beam fabrication of single crystal diamond nanobeam cavities,” *J. Vac. Sci. Technol. B*, vol. 29, no. 010601, pp. 1–6, 2010.

[236] M. Pomorski, B. Caylar, and P. Bergonzo, “Super-thin single crystal diamond membrane radiation detectors,” *Appl. Phys. Lett.*, vol. 103, no. 11, 2013.

[237] J. Suk, H. Kim, W. C. Lim, J. Yune, S. Moon, J. A. Eliades, J. Kim, J. Lee, and J. Song, “Fabrication of thin diamond membranes by using hot implantation and ion-cut methods,” *Appl. Phys. Lett.*, vol. 110, no. 10, 2017.

[238] S. Ali Momenzadeh, F. F. De Oliveira, P. Neumann, D. D. Bhaktavatsala Rao, A.

Denisenko, M. Amjadi, Z. Chu, S. Yang, N. B. Manson, M. W. Doherty, and J. Wrachtrup, "Thin Circular Diamond Membrane with Embedded Nitrogen-Vacancy Centers for Hybrid Spin-Mechanical Quantum Systems," *Phys. Rev. Appl.*, vol. 6, no. 2, 2016.

[239] J. S. Hodges, L. Li, M. Lu, E. H. Chen, M. E. Trusheim, S. Allegri, X. Yao, O. Gaathon, H. Bakhru, and D. Englund, "Long-lived NV - spin coherence in high-purity diamond membranes," *New J. Phys.*, vol. 14, 2012.

[240] C. X. Wang, G. W. Yang, H. W. Liu, Y. H. Han, J. F. Luo, C. X. Gao, and G. T. Zou, "Experimental analysis and theoretical model for anomalously high ideality factors in ZnO/diamond p-n junction diode," *Appl. Phys. Lett.*, vol. 84, no. 13, pp. 2427–2429, 2004.

[241] J. Chevallier, C. Saguy, M. Barbé, F. Jomard, D. Ballutaud, T. Kociniewski, B. Philosoph, B. Fizgeer, and S. Koizumi, "Improvement of the electrical properties of compensated phosphorus-doped diamond by high temperature annealing," *Phys. Status Solidi Appl. Mater. Sci.*, vol. 202, no. 11, pp. 2141–2147, 2005.

[242] I. Stenger, M. A. Pinault-Thaury, T. Kociniewski, A. Lusson, E. Chikoidze, F. Jomard, Y. Dumont, J. Chevallier, and J. Barjon, "Impurity-to-band activation energy in phosphorus doped diamond," *J. Appl. Phys.*, vol. 114, no. 7, 2013.

[243] R. Sauer, N. Teofilov, K. Thonke, and S. Koizumi, "Donor-related cathodoluminescence in phosphorus-doped CVD diamond," *Diam. Relat. Mater.*, vol. 13, no. 4–8, pp. 727–731, 2004.

[244] M. J. Conterio, N. Sköld, D. J. P. Ellis, I. Farrer, D. A. Ritchie, and A. J. Shields, "A quantum dot single photon source driven by resonant electrical injection," *Appl. Phys. Lett.*, vol. 103, no. 16, 2013.

[245] T. Heindel, C. Schneider, M. Lermer, S. H. Kwon, T. Braun, S. Reitzenstein, S. Höfling, M. Kamp, and A. Forchel, "Electrically driven quantum dot-micropillar single photon source with 34% overall efficiency," *Appl. Phys. Lett.*, vol. 96, no. 1, pp. 2012–2015, 2010.

[246] S. Deshpande and P. Bhattacharya, "An electrically driven quantum dot-in-nanowire visible single photon source operating up to 150 K," *Appl. Phys. Lett.*, vol. 103, no. 24, 2013.

[247] T. Lu, Z. Ma, C. Du, Y. Fang, H. Wu, Y. Jiang, L. Wang, L. Dai, H. Jia, W. Liu, and H. Chen, "Temperature-dependent photoluminescence in light-emitting diodes," *Sci. Rep.*, vol. 4, pp. 1–7, 2014.

[248] K. Iakoubovskii and A. Stesmans, "Characterization of Defects in as-Grown CVD Diamond Films and HPHT Diamond Powders by Electron Paramagnetic Resonance," *Phys. Status Solidi*, vol. 186, no. 2, pp. 199–206, 2001.

[249] A. M. Edmonds, M. E. Newton, P. M. Martineau, D. J. Twitchen, and S. D. Williams, "Electron paramagnetic resonance studies of silicon-related defects in diamond," *Phys. Rev. B - Condens. Matter Mater. Phys.*, vol. 77, no. 24, pp. 1–11, 2008.

[250] J. P. Goss, R. Jones, and S. J. Breuer, "The Twelve-Line 1 . 682 eV Luminescence Center in Diamond and the Vacancy-Silicon Complex," pp. 3041–3044, 1996.

[251] U. F. S. D'Haenens-Johansson, A. M. Edmonds, B. L. Green, M. E. Newton, G. Davies, P. M. Martineau, R. U. A. Khan, and D. J. Twitchen, "Optical properties of the neutral silicon split-vacancy center in diamond," *Phys. Rev. B - Condens. Matter Mater. Phys.*, vol. 84, no. 24, pp. 1–14, 2011.

[252] U. F. S. D'Haenens-Johansson, A. M. Edmonds, M. E. Newton, J. P. Goss, P. R. Briddon, J. M. Baker, P. M. Martineau, R. U. A. Khan, D. J. Twitchen, and S. D. Williams, "EPR of a defect in CVD diamond involving both silicon and hydrogen that shows preferential alignment," *Phys. Rev. B - Condens. Matter Mater. Phys.*, vol. 82, no. 15, pp. 1–10, 2010.

[253] B. C. Rose, D. Huang, Z. Zhang, A. M. Tyryshkin, S. Sangtawesin, S. Srinivasan, L. Loudin, M. L. Markham, A. M. Edmonds, D. J. Twitchen, S. A. Lyon, and N. P. De Leon, "Observation of an environmentally insensitive solid state spin defect in diamond," vol. 03.

[254] S. Dhomkar, P. R. Zangara, J. Henshaw, and C. A. Meriles, "On-Demand Generation of Neutral and Negatively Charged Silicon-Vacancy Centers in Diamond," *Phys. Rev. Lett.*, vol. 120, no. 11, p. 117401, 2018.

[255] K. L. Ekinci and M. L. Roukes, "Nanoelectromechanical systems," *Rev. Sci. Instrum.*, vol. 76, no. 6, 2005.

[256] G. F. Schneider, S. W. Kowalczyk, V. E. Calado, G. Pandraud, H. W. Zandbergen, L. M. K. Vandersypen, and C. Dekker, "DNA Translocation through Graphene

Nanopores," *Nano Lett.*, vol. 10, no. 8, pp. 3163–3167, Aug. 2010.

[257] V. Vaijayanthimala, P. Y. Cheng, S. H. Yeh, K. K. Liu, C. H. Hsiao, J. I. Chao, and H. C. Chang, "The long-term stability and biocompatibility of fluorescent nanodiamond as an in vivo contrast agent," *Biomaterials*, vol. 33, no. 31, pp. 7794–7802, 2012.

[258] D. Ho, C. K. Wang, and E. K. Chow, "Nanodiamonds : The intersection of nanotechnology , drug development , and personalized medicine," *Sci. Adv.*, vol. 1, no. August, p. e1500439, 2015.

[259] S. Heyer, W. Janssen, S. Turner, Y. G. Lu, W. S. Yeap, J. Verbeeck, K. Haenen, and A. Krueger, "Toward deep blue nano hope diamonds: Heavily boron-doped diamond nanoparticles," *ACS Nano*, vol. 8, no. 6, pp. 5757–5764, 2014.

[260] a. Ermakova, G. Pramanik, J.-M. Cai, G. Algara-Siller, U. Kaiser, T. Weil, Y.-K. Tzeng, H. C. Chang, L. P. McGuinness, M. B. Plenio, B. Naydenov, and F. Jelezko, "Detection of a Few Metallo-Protein Molecules Using Color Centers in Nanodiamonds," *Nano Lett.*, vol. 13, no. 7, pp. 3305–3309, 2013.

[261] P. Neumann, I. Jakobi, F. Dolde, C. Burk, R. Reuter, G. Waldherr, J. Honert, T. Wolf, a. Brunner, J. H. Shim, D. Suter, H. Sumiya, J. Isoya, and J. Wrachtrup, "High-precision nanoscale temperature sensing using single defects in diamond," *Nano Lett.*, vol. 13, no. 6, pp. 2738–2742, 2013.

[262] H. S. Knowles, D. M. Kara, and M. Atatüre, "Observing bulk diamond spin coherence in high-purity nanodiamonds," *Nat. Mater.*, vol. 13, no. 1, pp. 21–25, 2013.

[263] M. E. Trusheim, L. Li, A. Laraoui, E. H. Chen, H. Bakhru, T. Schröder, O. Gaathon, C. a Meriles, and D. Englund, "Scalable fabrication of high purity diamond nanocrystals with long-spin-coherence nitrogen vacancy centers," *Nano Lett.*, vol. 14, no. 1, pp. 32–36, 2014.

[264] I. Aharonovich, D. Englund, and M. Toth, "Solid-state single-photon emitters," *Nature Photonics*, vol. 10, no. 10. Nature Publishing Group, pp. 631–641, 2016.

[265] M. J. Holmes, K. Choi, S. Kako, M. Arita, and Y. Arakawa, "Room-temperature triggered single photon emission from a III-nitride site-controlled nanowire quantum dot," *Nano Lett.*, vol. 14, no. 2, pp. 982–986, 2014.

[266] H. Wang, Y. He, Y. H. Li, Z. E. Su, B. Li, H. L. Huang, X. Ding, M. C. Chen, C. Liu, J. Qin, J. P. Li, Y. M. He, C. Schneider, M. Kamp, C. Z. Peng, S. Höfling, C. Y. Lu, and

J. W. Pan, “High-efficiency multiphoton boson sampling,” *Nat. Photonics*, vol. 11, no. 6, pp. 361–365, 2017.

[267] E. Togan, Y. Chu, a S. Trifonov, L. Jiang, J. Maze, L. Childress, M. V. G. Dutt, a S. Sørensen, P. R. Hemmer, a S. Zibrov, and M. D. Lukin, “Quantum entanglement between an optical photon and a solid-state spin qubit.,” *Nature*, vol. 466, no. 7307, pp. 730–734, 2010.

[268] H. Bernien, B. Hensen, W. Pfaff, G. Koolstra, M. S. Blok, L. Robledo, T. H. Taminiau, M. Markham, D. J. Twitchen, L. Childress, and R. Hanson, “Heralded entanglement between solid-state qubits separated by three metres,” *Nature*, vol. 497, no. 7447, pp. 86–90, 2013.

[269] M. W. Doherty, N. B. Manson, P. Delaney, and L. C. L. Hollenberg, “The negatively charged nitrogen-vacancy centre in diamond: the electronic solution,” *New J. Phys.*, vol. 13, no. 2, p. 025019, 2011.

[270] F. Jelezko and J. Wrachtrup, “Single defect centres in diamond: A review,” *Phys. Status Solidi Appl. Mater. Sci.*, vol. 203, no. 13, pp. 3207–3225, 2006.

[271] S. L. Mouradian and D. Englund, “A tunable waveguide-coupled cavity design for scalable interfaces to solid-state quantum emitters,” *APL Photonics*, vol. 2, no. 4, p. 046103, 2017.

[272] D. Englund, B. Shields, K. Rivoire, F. Hatami, J. Vučković, H. Park, and M. D. Lukin, “Deterministic coupling of a single nitrogen vacancy center to a photonic crystal cavity,” *Nano Lett.*, vol. 10, no. 10, pp. 3922–3926, 2010.

[273] B. Pingault, D. D. Jarausch, C. Hepp, L. Klintberg, J. N. Becker, M. Markham, C. Becher, and M. Atatüre, “Coherent control of the silicon-vacancy spin in diamond,” *Nat. Commun.*, vol. 8, no. May, pp. 1–7, 2017.

[274] D. Gatto Monticone, P. Traina, E. Moreva, J. Forneris, P. Olivero, I. P. Degiovanni, F. Taccetti, L. Giuntini, G. Brida, G. Amato, and M. Genovese, “Native NIR-emitting single colour centres in CVD diamond,” *New J. Phys.*, vol. 16, pp. 1–27, 2014.

[275] P. Siyushev, V. Jacques, I. Aharonovich, F. Kaiser, T. Müller, L. Lombez, M. Atatüre, S. Castelletto, S. Prawer, F. Jelezko, and J. Wrachtrup, “Low-temperature optical characterization of a near-infrared single-photon emitter in nanodiamonds,” *New J. Phys.*, vol. 11, 2009.

[276] T. Müller, I. Aharonovich, L. Lombez, Y. Alaverdyan, A. N. Vamivakas, S. Castelletto, F. Jelezko, J. Wrachtrup, S. Prawer, and M. Atatüre, "Wide-range electrical tunability of single-photon emission from chromium-based colour centres in diamond," *New J. Phys.*, vol. 13, 2011.

[277] J. Achard, F. Silva, O. Brinza, a. Tallaire, and a. Gicquel, "Coupled effect of nitrogen addition and surface temperature on the morphology and the kinetics of thick CVD diamond single crystals," *Diam. Relat. Mater.*, vol. 16, no. 4–7 SPEC. ISS., pp. 685–689, 2007.

[278] S. Castelletto, A. Edmonds, T. Gaebel, and J. Rabeau, "Production of Multiple Diamond-Based Single-Photon Sources," *J. Sel. Top. Quantum Electron.*, vol. 18, no. 6, pp. 1792–1798, 2012.

[279] R. G. Sandstrom, O. Shimoni, A. a. Martin, and I. Aharonovich, "Study of narrowband single photon emitters in polycrystalline diamond films," *Appl. Phys. Lett.*, vol. 105, no. 18, p. 181104, 2014.

[280] V. G. Ralchenko, V. S. Sedov, A. A. Khomich, V. S. Krivobok, S. N. Nikolaev, S. S. Savin, I. I. Vlasov, and V. I. Konov, "Observation of the Ge-vacancy color center in microcrystalline diamond films," *Bull. Lebedev Phys. Inst.*, vol. 42, pp. 165–168, 2015.

[281] A. S. Barnard, "Shape-Dependent Confinement of the Nanodiamond Band Gap," *Cryst. Growth Des.*, vol. 9, no. 11, pp. 4860–4863, 2009.

[282] D. Shechtman, A. Feldman, and J. Hutchison, "High-order twin boundaries in chemical vapor deposited diamond," *Mater. Lett.*, vol. 17, pp. 211–216, 1993.

[283] A. a Martin, M. Toth, and I. Aharonovich, "Subtractive 3D Printing of Optically Active Diamond Structures.," *Sci. Rep.*, vol. 4, p. 5022, 2014.

[284] J. Taniguchi, I. Miyamoto, N. Ohno, and S. Honda, "Electron Beam Assisted Chemical Etching of Single Crystal Diamond Substrates," *Jpn. J. Appl. Phys.*, vol. 35, no. Part 1, No. 12B, pp. 6574–6578, 1996.

[285] A. A. Martin, A. Bahm, J. Bishop, I. Aharonovich, and M. Toth, "Dynamic Pattern Formation in Electron-Beam-Induced Etching," *Phys. Rev. Lett.*, vol. 115, no. 25, p. 255501, Dec. 2015.

[286] M. Toth, C. J. Lobo, W. R. Knowles, M. R. Phillips, M. T. Postek, and A. E. Vladár, "Nanostructure Fabrication by Ultra-High-Resolution Environmental Scanning Electron

Microscopy," *Nano Lett.*, vol. 7, no. 2, pp. 525–530, Feb. 2007.

[287] W. Müller-Sebert, E. Wörner, F. Fuchs, C. Wild, and P. Koidl, "Nitrogen induced increase of growth rate in chemical vapor deposition of diamond," *Appl. Phys. Lett.*, vol. 759, no. 1996, p. 759, 1995.

[288] L. Bergman and R. J. Nemanich, "Raman and photoluminescence analysis of stress state and impurity distribution in diamond thin films," *J. Appl. Phys.*, vol. 78, no. 11, pp. 6709–6719, 1995.

[289] S. Lindner, A. Bommer, A. Muzha, A. Krueger, L. Gines, S. Mandal, O. Williams, E. Londero, A. Gali, and C. Becher, "Strongly inhomogeneous distribution of spectral properties of silicon-vacancy color centers in nanodiamonds," pp. 1–23, 2018.

[290] S. Kalliakos, Y. Brody, A. Schwagmann, A. J. Bennett, M. B. Ward, D. J. P. Ellis, J. Skiba-Szymanska, I. Farrer, J. P. Griffiths, G. A. C. Jones, D. A. Ritchie, and A. J. Shields, "In-plane emission of indistinguishable photons generated by an integrated quantum emitter," *Appl. Phys. Lett.*, vol. 104, no. 22, 2014.

[291] R. B. Patel, A. J. Bennett, K. Cooper, P. Atkinson, C. A. Nicoll, D. A. Ritchie, and A. J. Shields, "Postselective two-photon interference from a continuous nonclassical stream of photons emitted by a quantum dot," *Phys. Rev. Lett.*, vol. 100, no. 20, pp. 1–4, 2008.

[292] D. Englund, A. Majumdar, A. Faraon, M. Toishi, N. Stoltz, P. Petroff, and J. Vučković, "Resonant excitation of a quantum dot strongly coupled to a photonic crystal nanocavity," *Phys. Rev. Lett.*, vol. 104, no. 7, pp. 1–4, 2010.

[293] Y. Shen, T. M. Sweeney, and H. Wang, "Zero-phonon linewidth of single nitrogen vacancy centers in diamond nanocrystals," no. September 2007, pp. 2007–2009, 2008.

[294] P. Siyushev, V. Jacques, I. Aharonovich, F. Kaiser, T. Müller, L. Lombez, M. Atatüre, S. Castelletto, S. Prawer, F. Jelezko, and J. Wrachtrup, "Low-temperature optical characterization of a near-infrared single-photon emitter in nanodiamonds," *New J. Phys.*, vol. 11, 2009.

[295] O. Benson, "Assembly of hybrid photonic architectures from nanophotonic constituents," *Nature*, vol. 480, no. 7376, pp. 193–199, 2011.

[296] A. W. Schell, H. Takashima, S. Kamioka, Y. Oe, M. Fujiwara, O. Benson, and S. Takeuchi, "Highly efficient coupling of nanolight emitters to a ultra-wide tunable nanofibre cavity," *Sci. Rep.*, vol. 5, pp. 1–5, 2015.

[297] N. Aslam, G. Waldherr, P. Neumann, F. Jelezko, and J. Wrachtrup, "Photo-induced ionization dynamics of the nitrogen vacancy defect in diamond investigated by single-shot charge state detection," *New J. Phys.*, vol. 15, 2013.

[298] X. Li, G. D. Shepard, A. Cupo, N. Camporeale, K. Shayan, Y. Luo, V. Meunier, and S. Strauf, "Nonmagnetic Quantum Emitters in Boron Nitride with Ultranarrow and Sideband-Free Emission Spectra," *ACS Nano*, vol. 11, no. 7, pp. 6652–6660, 2017.

[299] C. Galland, A. Högele, H. E. Türeci, and A. Imamoğlu, "Non-Markovian decoherence of localized nanotube excitons by acoustic phonons," *Phys. Rev. Lett.*, vol. 101, no. 6, pp. 1–4, 2008.

[300] H. Sternschulte, K. Thonke, R. Sauer, P. C. Münzinger, and P. Michler, "1.681-eV luminescence center in chemical-vapor-deposited homoepitaxial diamond films," *Phys. Rev. B*, vol. 50, no. 19, pp. 14554–14560, 1994.

[301] J. Benedikter, H. Kaupp, T. Hümmer, Y. Liang, A. Bommer, C. Becher, A. Krueger, J. M. Smith, T. W. Hänsch, and D. Hunger, "Cavity-Enhanced Single-Photon Source Based on the Silicon-Vacancy Center in Diamond," *Phys. Rev. Appl.*, vol. 7, no. 2, pp. 1–12, 2017.

[302] I. Aharonovich, S. Castelletto, D. A. Simpson, A. Stacey, J. McCallum, A. D. Greentree, and S. Prawer, "Two-level ultrabright single photon emission from diamond nanocrystals," *Nano Lett.*, vol. 9, no. 9, pp. 3191–3195, 2009.

[303] S. Häußler, G. Thiering, A. Dietrich, N. Waasem, T. Teraji, J. Isoya, T. Iwasaki, M. Hatano, F. Jelezko, A. Gali, and A. Kubanek, "Photoluminescence excitation spectroscopy of SiV- and GeV- color center in diamond," 2017.

[304] T. T. Tran, M. Kianinia, K. Bray, S. Kim, Z. Xu, A. Gentle, B. Sontheimer, C. Bradac, and I. Aharonovich, "Nanodiamonds with photostable, sub-gigahertz linewidths quantum emitters," *ArXiv*, vol. 116103, pp. 1–11, 2017.

[305] N. H. Wan, B. J. Shields, D. Kim, S. Mouradian, B. Lienhard, M. Walsh, H. Bakhru, T. Schröder, and D. Englund, "Efficient Extraction of Light from a Nitrogen-Vacancy Center in a Diamond Parabolic Reflector," *Nano Lett.*, vol. 18, no. 5, pp. 2787–2793, 2018.

[306] T. Wu, Y. Tzeng, W.-W. Chang, C. Cheng, Y. Kuo, C. Chien, H. Chang, and J. Yu, "Tracking the engraftment and regenerative capabilities of transplanted lung stem cells

using fluorescent nanodiamonds," *Nat. Nanotechnol.*, vol. 8, no. 9, pp. 682–689, 2013.

[307] W. W. Hsiao, Y. Y. Hui, P. Tsai, and H. Chang, "Fluorescent Nanodiamond: A Versatile Tool for Long-Term Cell Tracking, Super-Resolution Imaging, and Nanoscale Temperature Sensing," *Acc. Chem. Res.*, vol. 49, no. 3, pp. 400–407, Mar. 2016.

[308] I. P. Chang, K. C. Hwang, J. A. Ho, C.-C. Lin, R. J. R. Hwu, and J.-C. Horng, "Facile Surface Functionalization of Nanodiamonds," *Langmuir*, vol. 26, no. 5, pp. 3685–3689, Mar. 2010.

[309] K. Bray, R. Previdi, B. C. Gibson, O. Shimoni1, and I. Aharonovich, "Enhanced photoluminescence from single nitrogen-vacany defects in nanodiamonds coated with phenol-ionic complexes," *Nanoscale*, vol. 7, no. 11, pp. 4869–4874, 2015.

[310] D. A. Simpson, J. Tetienne, J. M. McCoey, K. Ganesan, L. T. Hall, S. Petrou, R. E. Scholten, and L. C. L. Hollenberg, "Magneto-optical imaging of thin magnetic films using spins in diamond," *Sci. Rep.*, vol. 6, no. 1, p. 22797, 2016.

[311] P. Reineck and B. C. Gibson, "Near-Infrared Fluorescent Nanomaterials for Bioimaging and Sensing," *Adv. Opt. Mater.*, vol. 5, no. 2, 2017.

[312] I. I. Vlasov, A. a Shiryaev, T. Rendler, S. Steinert, S.-Y. Lee, D. Antonov, M. Vörös, F. Jelezko, A. V Fisenko, L. F. Semjonova, J. Biskupek, U. Kaiser, O. I. Lebedev, I. Sildos, P. R. Hemmer, V. I. Konov, A. Gali, and J. Wrachtrup, "Molecular-sized fluorescent nanodiamonds.," *Nat. Nanotechnol.*, vol. 9, no. 1, pp. 54–8, 2014.

[313] A. D. Frankel and C. O. Pabo, "Cellular uptake of the tat protein from human immunodeficiency virus," *Cell*, vol. 55, no. 6, pp. 1189–1193, 1988.

[314] S. Fawell, J. Seery, Y. Daikh, C. Moore, L. L. Chen, B. Pepinsky, and J. Barsoum, "Tat-mediated delivery of heterologous proteins into cells.," *Proc. Natl. Acad. Sci. U. S. A.*, vol. 91, no. 2, pp. 664–668, 1994.

[315] S. A. Moschos, S. W. Jones, M. M. Perry, A. E. Williams, J. S. Erjefalt, J. J. Turner, P. J. Barnes, B. S. Sproat, M. J. Gait, and M. A. Lindsay, "Lung delivery studies using siRNA conjugated to TAT(48-60) and penetratin reveal peptide induced reduction in gene expression and induction of innate immunity," *Bioconjug. Chem.*, vol. 18, no. 5, pp. 1450–1459, 2007.

[316] S. Lim, W.-J. Kim, Y.-H. Kim, S. Lee, J.-H. Koo, J.-A. Lee, H. Yoon, D.-H. Kim, H.-J. Park, H.-M. Kim, H.-G. Lee, J. Yun Kim, J.-U. Lee, J. Hun Shin, L. Kyun Kim, J. Doh,

H. Kim, S.-K. Lee, A. L. M. Bothwell, M. Suh, and J.-M. Choi, "dNP2 is a blood–brain barrier-permeable peptide enabling ctCTLA-4 protein delivery to ameliorate experimental autoimmune encephalomyelitis," *Nat. Commun.*, vol. 6, p. 8244, Sep. 2015.

[317] Thermo Fisher Scientific, "alamarBlue – Reliable and Accurate Cell Health Indicator." [Online]. Available: https://www.thermofisher.com/au/en/home/brands/molecular-probes/key-molecular-probes-products/alamarblue-rapid-and-accurate-cell-health-indicator.html#how. [Accessed: 13-Dec-2018].

[318] V. K. A. Sreenivasan, W. A. Wan Razali, K. Zhang, R. R. Pillai, A. Saini, D. Denkova, M. Santiago, H. Brown, J. Thompson, M. Connor, E. M. Goldys, and A. V. Zvyagin, "Development of Bright and Biocompatible Nanoruby and Its Application to Background-Free Time-Gated Imaging of G-Protein-Coupled Receptors," *ACS Appl. Mater. Interfaces*, vol. 9, no. 45, pp. 39197–39208, 2017.

[319] O. Faklaris, V. Joshi, T. Irinopoulou, P. Tauc, M. Sennour, H. Girard, C. Gesset, J. C. Arnault, A. Thorel, J. P. Boudou, P. A. Curmi, and F. Treussart, "Photoluminescent diamond nanoparticles for cell labeling: Study of the uptake mechanism in mammalian cells," *ACS Nano*, vol. 3, no. 12, pp. 3955–3962, 2009.

[320] Y.-A. Huang, C.-W. Kao, K.-K. Liu, H.-S. Huang, M.-H. Chiang, C.-R. Soo, H.-C. Chang, T.-W. Chiu, J.-I. Chao, and E. Hwang, "The effect of fluorescent nanodiamonds on neuronal survival and morphogenesis.," *Sci. Rep.*, vol. 4, p. 6919, 2014.

[321] Z. Chu, K. Miu, P. Lung, S. Zhang, S. Zhao, and H. Chang, "Rapid endosomal escape of prickly nanodiamonds : implications for gene delivery," *Sci. Rep.*, vol. 5, pp. 1–8, 2015.

[322] N. Prabhakar, M. H. Khan, M. Peurla, H. C. Chang, P. E. Hänninen, and J. M. Rosenholm, "Intracellular Trafficking of Fluorescent Nanodiamonds and Regulation of Their Cellular Toxicity," *ACS Omega*, vol. 2, no. 6, pp. 2689–2693, 2017.

[323] M. Liu, Q. Li, L. Liang, J. Li, K. Wang, J. Li, M. Lv, N. Chen, H. Song, J. Lee, J. Shi, L. Wang, R. Lal, and C. Fan, "Real-Time visualization of clustering and intracellular transport of gold nanoparticles by correlative imaging," *Nat. Commun.*, vol. 8, 2017.

[324] V. R. Lopes, V. Loitto, J. N. Audinot, N. Bayat, A. C. Gutleb, and S. Cristobal, "Dose-dependent autophagic effect of titanium dioxide nanoparticles in human HaCaT cells at

non-cytotoxic levels," *J. Nanobiotechnology*, vol. 14, no. 1, 2016.

[325] D. Huang, H. Zhou, and J. Gao, "Nanoparticles modulate autophagic effect in a dispersity- dependent manner," *Sci. Rep.*, vol. 5, no. 14361, pp. 1–10, 2015.

[326] A. R. Mishra, J. Zheng, X. Tang, and P. L. Goering, "Silver nanoparticle-induced autophagic-Lysosomal disruption and NLRP3-inflammasome activation in HepG2 cells is size-dependent," *Toxicol. Sci.*, vol. 150, no. 2, pp. 473–487, 2016.

[327] E. Panzarini and L. Dini, "Nanomaterial-induced autophagy: A new reversal MDR tool in cancer therapy?," *Molecular Pharmaceutics*, vol. 11, no. 8. pp. 2527–2538, 2014.

[328] J. Adler and I. Parmryd, "Quantifying colocalization by correlation: The pearson correlation coefficient is superior to the Mander's overlap coefficient," *Cytom. Part A*, vol. 77, no. 8, pp. 733–742, 2010.

[329] J. R. Weber, W. F. Koehl, J. B. Varley, A. Janotti, B. B. Buckley, C. G. Van De Walle, D. D. Awschalom, C. G. Van de Walle, D. D. Awschalom, C. G. Van De Walle, D. D. Awschalom, C. G. Van de Walle, and D. D. Awschalom, "Quantum computing with defects," *Proc. Natl. Acad. Sci. U. S. A.*, vol. 107, no. 19, pp. 8513–8, 2010.